



Durham E-Theses

The effect of stress & fractures on fluid flow in crystalline rocks, Cumbria, UK

Reeves, Helen J.

How to cite:

Reeves, Helen J. (2002) *The effect of stress & fractures on fluid flow in crystalline rocks, Cumbria, UK*, Durham theses, Durham University. Available at Durham E-Theses Online:
<http://etheses.dur.ac.uk/1076/>

Use policy

The full-text may be used and/or reproduced, and given to third parties in any format or medium, without prior permission or charge, for personal research or study, educational, or not-for-profit purposes provided that:

- a full bibliographic reference is made to the original source
- a [link](#) is made to the metadata record in Durham E-Theses
- the full-text is not changed in any way

The full-text must not be sold in any format or medium without the formal permission of the copyright holders.

Please consult the [full Durham E-Theses policy](#) for further details.

The Effect of Stress & Fractures on Fluid Flow in Crystalline Rocks, Cumbria, UK.

The copyright of this thesis rests with the author.
No quotation from it should be published without
his prior written consent and information derived
from it should be acknowledged.

Helen J. Reeves

Volume I of III



7 JUL 2003

**A thesis submitted to the University of Durham,
Department of Geological Sciences,
for the degree of Doctor of Philosophy
in the Faculty of Science.**

September 2002

ALL MISSING PAGES ARE BLANK

IN

ORIGINAL

Abstract

The analysis of drill core or borehole image logs from a fractured rock mass, typically reveals the presence of hundreds to thousands of fractures in which a network of fluid flow paths can be difficult to define. Production logging, for example, demonstrates that only a relatively small proportion of fracture pathways contribute to flow in the borehole. Stress has long been known to be a significant control upon fluid flow within fractured rocks. Recent research has indicated that it is often fractures that undergo localized shear failure which experience preferential flow.

The present study examines borehole data from the Borrowdale Volcanics Group, one of the most intensely examined crystalline fractured rock masses in the world. The dataset was acquired as part of UK NIREX's scientific investigations into Sellafield, as a potential site for the deep underground disposal of intermediate level radioactive waste. A comprehensive dataset of fractures, *in situ* stress measurements and fluid flow indicators were gathered during the drilling and geophysical logging of twenty-eight deep boreholes at Sellafield. A new compilation, cross-correlation and analysis of this dataset permits definition of hydraulically conductive fractures that are distinct from the overall fracture population. Fractures in a state of stress close to localized shear failure can act as potentially active faults. The ratio of the induced shear to normal stress component (coefficient of friction) indicates how close a fracture is to failure, with elevated values indicating a state of critical stress. Small-scale shear along these fracture surfaces as a result of being critically stressed can lead to fracture aperture dilation and an increase in the fracture permeability. Integration with production logging data and other well records, indicates a strong correspondence between the occurrence of flow and those fractures that are orientated at approximately 30-40° to the minimum horizontal stress orientation.

The findings of this study are relevant to a wide range of problems, including the flow of hydrocarbons through fractured reservoirs, the migration of contaminants through fractured rocks and the abstraction of water from fractured aquifers.

Contents.

	Page No.
Abstract	ii
Contents	iii
List of Figures, Plates & Tables	vi
List of Abbreviations & Symbols	ix
Declaration	x
Copyright & Intellectual Property Rights	x
Acknowledgements	xi
1. Introduction	1
1.1 Preamble	1
1.2 Aims & Objectives	2
1.3 Thesis Structure	2
1.4 Background & History of Sellafield	4
1.4.1 Deep Borehole Investigations	9
1.4.2 Surface Investigations	10
2. Literature Review	14
2.1 Introduction	14
2.2 Mechanics & Techniques for <i>In Situ</i> Stress Determination	14
2.2.1 Introduction	14
2.2.2 Mechanics for <i>In Situ</i> Stress Determination	14
2.2.3 Techniques for <i>In Situ</i> Stress Determination	17
2.2.3.1 Indirect Methods	20
2.2.3.2 Direct Methods	20
2.2.3.3 Borehole Methods	22
2.3 Regional Stress Map	40
2.3.1 Introduction	40
2.3.2 World Stress Map	40
2.3.3 European Stress Map	42
2.3.4 UK Stress Map	43
2.4 Characterisation of Discontinuities	46
2.4.1 Biased Sampling of Discontinuities	57
2.5 Hydrogeological Characterisation	57
2.6 Stress, Fractures & Flow	58

3. Geological & Hydrogeological Setting	67
3.1 Geology – Introduction	67
3.1.1 Regional/District Geology	67
3.1.2 Site Geology	71
3.1.2.1 Ordovician	76
3.1.2.2 Carboniferous	77
3.1.2.3 Permian & Triassic	81
3.1.2.4 Quaternary	86
3.1.3 PRZ Geology	89
3.2 Hydrogeology	89
3.2.1 Regional/District Hydrogeology	89
3.2.2 Site Hydrogeology	90
3.2.2.1 Ordovician	93
3.2.2.2 Carboniferous	94
3.2.2.3 Permian Brockram	94
3.2.2.4 Permian St Bees Shale & Evaporite Group	97
3.2.2.5 Triassic Sherwood Sandstone Group	97
3.2.2.6 Triassic Mercia Mudstone Group	99
3.2.2.7 Quaternary	99
3.2.3 PRZ Hydrogeology	99
4. Regional Stress Map	103
4.1 Introduction	103
4.2 Acquisition of <i>In Situ</i> Stress Data	103
4.2.1 Preliminary Acquisition of <i>In Situ</i> Stress Data	108
4.2.2 Main Acquisition of <i>In Situ</i> Stress Data	110
4.3 Presentation of Data	111
4.3.1 Presentation of Preliminary <i>In Situ</i> Stress Data	111
4.3.2 Presentation of Main <i>In Situ</i> Stress Data	111
4.4 Analysis & Assessment of Results	114
4.4.1 Analysis & Assessment of Preliminary Results	114
4.4.2 Analysis & Assessment of Main Results	119
5. Characterisation of Discontinuities	136
5.1 Introduction	136
5.2 Flow Zone Data	136
5.3 <i>In Situ</i> Stress Data	142
5.3.1 Flow Zones	142
5.3.1.1 Flow Zones - Acquisition of <i>In Situ</i> Stress Data	142
5.3.1.2 Flow Zones - <i>In Situ</i> Stress Data	143
5.3.1.3 Flow Zones - Assessment of <i>In Situ</i> Stress Data	143
5.3.2 Short Interval Test (SIT) Zone	146
5.3.2.1 SIT Zone - Acquisition of <i>In Situ</i> Stress Data	146
5.3.2.2 SIT Zone - Presentation of Data	147
5.3.2.3 SIT Zone - Assessment of Data	147
5.4 Discontinuity Orientation Data	156
5.4.1 Validation of Discontinuity Data - Acquisition of Data	156
5.4.2 Validation of Discontinuity Data - Presentation of Data	160
5.4.3 Validation of Discontinuity Data - Assessment of Data	160

6. In Situ Stress, Fracture Systems & Groundwater Flow Pathways	167
6.1 Introduction	167
6.2 Integration of Discontinuity Data & <i>In Situ</i> Stress Data	169
6.2.1 Introduction	169
6.2.2 Acquisition of Data	170
6.2.3 Presentation of Data	173
6.2.3.1 Flow Zones	173
6.2.3.2 SIT Zone	173
6.2.4 Assessment of Data	175
6.2.4.1 Flow Zones	175
6.2.4.2 SIT Zone	176
6.3 Integration of all Discontinuity Data, <i>In Situ</i> Stress Data, Flow Data, Geological Data & Geophysical Data	182
6.3.1 Introduction	182
6.3.2 Production of Log(s)	186
6.3.3 Presentation of Composite Log	189
6.3.4 Assessment of Log	189
7. Discussion & Synthesis	194
7.1 Introduction	194
7.2 Regional stress regime within the BVG at Sellafield	195
7.2.1 Assessment of tools used for breakout analysis	195
7.2.2 Filtering of raw image log data	198
7.2.3 Distribution of breakout results	198
7.3 Characterisation & Interaction of In Situ Stresses, Discontinuities & Flow of Fluid at Sellafield	201
7.3.1 Characterisation	201
7.3.2 Interaction	202
8. Conclusions	214
9. Recommendations	220
References	223
Appendices	241(VI)
Appendix 1: Over Sized a) Tables & b) Figures	V I
Appendix 2: Software Manuals	V II
Appendix 3: Software Guides - Stress Map Analysis	V II
Appendix 4: Breakout Roses - Tools Analysis	V II
Appendix 5: Breakout, Discontinuity Roses & Stress Profiles – BVG Stress Map	V II
Appendix 6: Flow Zone & SIT Data	V II
Appendix 7: Software Guides - Flow Zone & SIT Stress Analysis	V II
Appendix 8: Breakout & Discontinuity Roses - Flow Zone & SIT Stress Analysis	V II/III
Appendix 9: Discontinuity Roses & Stereonets - Tools Analysis	V III
Appendix 10: Critical Stress Data - Flow Zone & SIT Stress Analysis	V III
Appendix 11: Nirex's Composite Logs & Summary Charts of the PRZ boreholes	V III

List of Figures.

- Figure 1.1** – Locations and scales of the Sellafield Study Areas.
Figure 1.2 – Location of PRZ, RCF & deep boreholes drilled at Sellafield.
Figure 2.1 – 3D coordinate system of a six-component stress tensor.
Figure 2.2 – The three states of stress encountered within the Earth.
Figure 2.3 – Stress tensor in a rock mass.
Figure 2.4 – Model used in the calculation of the modified Kirsch solution.
Figure 2.5 – Graphical representation of stress intensification around borehole.
Figure 2.6 – Variation of circumferential stress acting at the borehole wall.
Figure 2.7 – Representation of a four-arm dipmeter caliper log.
Figure 2.8a – Image of the borehole televiewer AMWF and TTWF.
Figure 2.8b – Image of the borehole televiewer from the KTB pilot borehole.
Figure 2.9 – A section of core, FMI and UBI imagery demonstrating breakout.
Figure 2.10 – Four common geometries identified using a dipmeter caliper.
Figure 2.11 – The World Stress Map displaying the orientations of σ_{Hmax} .
Figure 2.12 – The European Stress Map displaying the orientations of σ_{Hmax} .
Figure 2.13 – The UK Stress Map displaying the orientations of σ_{Hmax} .
Figure 2.14 – Summary of the *in situ* stress measurements in the UK.
Figure 2.15 – The distinctions between the major types of natural discontinuities.
Figure 2.16a/b – Discontinuities imaged on a) FMI and b) UBI AMWF log.
Figure 2.16c – Illustration of how a discontinuity's orientation is calculate.
Figure 2.17 – Assumed relationship between permeability and stress regime.
Figure 2.18 – 3D sketch of cubic stress element on an inclined discontinuity plane.
Figure 2.19 – Dilation of a discontinuity when sheared.
Figure 3.1a/b – Map showing the (a) regional and (b) district geological setting.
Figures 3.2 – Named structural features in the District at the top of the BVG
Figure 3.3 – Site scale Sub-Quaternary Geological map and cross-sections.
Figure 3.4a – Lithostratigraphy of the BVG in the Sellafield site.
Figure 3.4b – Lithostratigraphy of the BVG the PRZ area.
Figure 3.4c – Lithostratigraphy of the BVG the Calder Hall area.
Figure 3.5 – Lithostratigraphy of the Carboniferous in the Sellafield site.
Figure 3.6 – Lithostratigraphy of the Permian in the Sellafield site.
Figure 3.7 – Borehole correlation of the Triassic strata in the Sellafield site.
Figure 3.8 – Onshore a) District and b) Site Quaternary domains map of Sellafield.
Figure 3.9 – Cross-section of Sellafield site showing groundwater regimes.
Figure 4.1 - A schematic cross-sectional view of a borehole.
Figure 4.2 a/b – Map of the breakout (σ_{Hmin}) results in the a) site and b) PRZ.
Figure 4.3 a/b – Map of the σ_{Hmax} breakout results in the a) site and b) PRZ.
Figure 4.4 a/b – Map of the discontinuity orientation rose in the a) site and b) PRZ.
Figure 4.5 – A section of FMI and UBI, AMWF image log showing breakout.
Figure 4.6 – Summary of all the UBI (AMWF) filtered and unfiltered breakout roses.
Figure 4.7 – Brereton *et al.*, 1997 breakout rose diagram using BHTV AMWF logs.
Figure 4.8 – Comparison of breakout results & discontinuity results.
Figure 4.9 – X plot of mean discontinuity orientation vs mean σ_{Hmin} direction.
Figure 4.10 – Examples of the three types of stress profiles identified.
Figure 4.11 – Stress profiles of the boreholes where faults and rotations identified.
Figure 4.12 – Stress profiles of the boreholes that showed rotation in Figure 4.2a.
Figure 5.1 – Schlumberger's Modular Dynamic Tester.
Figure 5.2 – Transmissivity profile from the SIT zone (634 - 790 mbRT).
Figure 5.3 – Production log for Sellafield borehole RCF3 (635–850 mbRT).

List of Figures (continued).

- Figure 5.4** – Permian-Triassic breakout and discontinuity results for FZ analysis.
- Figure 5.5** – BVG breakout and discontinuity results for FZ analysis.
- Figure 5.6** – Cross plot of the discontinuity orientation vs breakout data for the FZ.
- Figure 5.7** – Frequency plot of σ_{Hmin} for all the flowing and non-flowing areas.
- Figure 5.8** – A selection of the breakout and discontinuity results for SIT zones
- Figure 5.9** – Frequency plot of the orientation of discontinuities in borehole RCF3.
- Figure 5.10** – Frequency plot of discontinuities in flowing to non-flowing areas.
- Figure 5.11** – Results of discontinuity data generated by imagery logs from RCF3.
- Figure 5.12** – Graph of the percentage of discontinuities in each discontinuity.
- Figure 6.1** – Graph of the derived stress and pressure magnitudes versus depth.
- Figure 6.2** – Diagram of the Permian-Triassic & BVG “critical stress” analysis.
- Figure 6.3** – “Critical stress” analysis for all the flowing and non-flowing areas.
- Figure 6.4** – “Critical stress” analysis where a pore pressure magnitude altered.
- Figure 6.5a/b** – Composite log of a) all BVG & b) SIT zone in borehole RCF3.
- Figure 6.6a/b** – Composite log of a) all BVG & b) SIT zone in RCF3 (no MSFL).
- Figure 6.7** – Test log of PFF point data and all smoothed PFF synthetic logs.
- Figure 6.8** – Log of PFFS data presented in TBSK log style.
- Figure 6.9a/b** – Composite log of a) all BVG & b) SIT zone with PFFS log in RCF3.
- Figure 6.10** - Composite log of SIT zone with stress log in RCF3 .
- Figure 7.1** – Frequency plot of the PFF orientation in flowing and non-flowing areas.

List of Plates.

- Plates 3.1a/b** – Satellite Landsat images of Sellafield a) region and b) district.

List of Tables.

- Table 1.1** – Sellafield scientific investigations.
- Table 1.2** – Sellafield Deep Boreholes.
- Table 2.1** – Criteria for recognizing breakout on four-arm dipmeter logs.
- Table 2.2** – Borehole circumference coverage of an electrical imaging tool.
- Table 2.3** – Geophysical techniques available for fracture detection.
- Table 2.4** – Summary of suggested methods used in hydrogeological investigations.
- Table 3.1** – Geological history of the Sellafield Region.
- Table 3.2** – Stratigraphic succession for the Sellafield site area.
- Table 3.3** – Summary of the Diagenetic Episodes encountered at Sellafield.
- Table 3.4** – Borehole hydraulic conductivity determinations from EMP.
- Table 3.5** – Mineralisation Episodes encountered at Sellafield.
- Table 3.6** – Hydrogeological units in the Sherwood Sandstone Group.
- Table 3.7** – Descriptions of Quaternary hydrogeological domains.
- Table 4.1** – Depths, deviation and geology of the top hundred meters of the BVG.
- Table 4.2** – Sample of Output Data File Created from *Breaking*.
- Table 4.3** – Results from the preliminary *in situ* stress investigation of the BVG.
- Table 4.4** – Results from the main *in situ* stress investigation of the BVG.
- Table 4.5** – Results from the discontinuity analysis of the BVG.
- Table 4.6** – Representative results for boreholes 10A, 11A, 12A, 14A and RCF1.
- Table 4.7** – Comparison of mean breakout and discontinuity orientation data.
- Table 4.8** – Summary of type of stress profile and the number of faults encountered.
- Table 5.1** – Eight areas that demonstrated an increase in transmissivity in SIT zone.
- Table 5.2** – Results of flow zone stress analysis.
- Table 5.3** – Results from stress analysis for flowing and non-flowing areas.
- Table 5.4** – Results from detail stress analysis over the SIT zone.
- Table 5.5** – Example of database generated from the picking of discontinuities.
- Table 5.6** – Discontinuity type classification with respect to coverage.
- Table 5.7** – The results of the dip azimuth orientation rose plots from the FMI & UBI.
- Table 5.8** – Results of the % of discontinuities encountered by each imagery tool.
- Table 6.1** – Summary of stress parameters determined from various stress analyses
- Table 6.2** – FZ *StressIt* analysis for borehole 2, 5, 8A, 11A, RCF3, RCM1 & RCM2.
- Table 6.3** – Results of SIT Zone *StressIt* analysis for Sellafield borehole RCF3.
- Table 6.4** – Rock mass characterisation data for some of the lithology at Sellafield.
- Table 6.5** – Logs and data used as basis for production of composite logs.
- Table 6.6** – Table showing the various smoothing amounts used on the PFF data.
- Table 7.1** – Summary of the ϕ_{peak} from the direct shear tests and the derived μ .
- Table 7.2** – Depths, orientation & σ_{Hmin} values for the flowing and non-flowing PFF.

List of Abbreviations & Symbols.

Abbreviations

Nirex = UK Nuclear Industry Radioactive Waste Executive
ILW = Intermediate Level Waste
LLW = Low Level Waste
PRZ = Potential Repository Zone
RCF = Rock Characterization Facility
EMP = Environmental Pressure Measurement
FST = Full Sector Tests
DET = Discrete Extraction Tests
mbRT = meters below Rotary Table
maOD = meters above Ordnance Datum
FM = Focal Mechanism
WSM = World Stress Map
BHTV = Borehole Televiewer
UBI = Ultrasonic Borehole Imager
AMWF = reflected Amplitude Waveform
TTWF = Two-way Travel Time Waveform
EMEX = Emitter Exciter
FMS = Formation Micro-Scanner
FMI = Fullbore Formation MicroImager
BVG = Borrowdale Volcanic Group
ESM = European Stress Map
BGS = British Geological Survey
FZ = Flow Zones
PFF = Potentially Flowing Features
ECC = Eccentricity
D = Diameter
A = Angle
NDGD = Nirex Digital Geoscience Database
MDT = Modular Dynamic Tester
SIT = Short Interval Test
UCS = Unconfined Compressive Strength
GR = Gamma Ray
CALI = Caliper
LLD = Deep Laterlog
LLS = Shallow Laterlog
MSFL = Micro Spherically Focused Log
REFC = Stoneley Wave Refraction Coefficient
RQD = Rock Quality Design
RMR = Rock Mass Rating
Q = Q-System

EMPK = Environmental Pressure Measurement hydraulic conductivity
TBSK = Short Interval Test hydraulic conductivity
FLZN = Flow Zones locations
PFFS = Potentially Flowing Features Smooth log
SHMX = σ_{Hmax} log
DST = Direct Shear Test
1 2 3 = Principal reference frame
max = Maximum value
min = Minimum value
x y z = Cartesian reference frame
' = Effective value
r θ r θ = Polar reference frame

Symbols

τ = shear stress
 σ or σ_N = normal stress
 $S S_H S_v$ = far-field stresses
 $\sigma_1 \sigma_2 \sigma_3$ = principal stresses
 $\sigma_H \sigma_v$ = horizontal and vertical stress
 ρ = mean density of overburden
g = gravitational acceleration
z = depth
R = distance from center of borehole
r = radius
Pp = pore pressure
 θ = angle
 σ_r = radial stress
 σ_θ = circumferential/hoop stress
 τ_θ = shear stress
m/h = meters per hour
" = inches
 α = dip angle
cm = centimeters
 μm = micrometre
 μ = coefficient of friction
 β_{ij} = Direction cosines
km = kilometers
 ms^{-1} = meters per second
 $^\circ$ = degrees
 ϕ_{peak} = peak friction angle

Declaration.

No portion of the work referred to in this thesis has been submitted in support of an application for another degree or qualification of this or any other university or other institute of learning.

Copy & Intellectual Property Rights.

(1) Copyright in text of this thesis rests with the Author. Copies (by any process) either in full, or of extracts, may be made only in accordance with instructions given by the Author and lodged in the University of Durham Library. Details may be obtained from the librarian. This page must form part of any such copies made. Further copies (by any process) of copies made in accordance with such instructions may not be made without the permission (in writing) of the Author.

(2) The ownership of any intellectual property rights which may be described in this thesis is vest in the University of Durham, subject to any prior agreement to the contrary, and may not be made available for use by third parties without the written permission of the University, which will prescribe the terms and conditions of any such agreement.

Further information on the conditions under which disclosure and exploitation may take place is available from the Head of the Department of Geological Sciences.

Acknowledgements.

Many people and organisations have helped and contributed to the development of this project and in the production of this thesis.

Firstly and most importantly, I thank my family, particularly my parents & Iain for their help, support and guidance during the good and more frequently bad times. I would never have continued and completed without their help and support.

I owe a huge debt of gratitude to Dr Chris Evans, Dr Rob Cuss and Andy Kingdon at the British Geological Survey (BGS). Adopting me half way through my research (after being abandoned by my first supervisor before even starting my PhD). Chris took over as my scientific supervisor, mentor and all round provider of data, software and computing facilities during my research. Without his help this research would have never developed. Chris was also entrusted with the task of reading and editing this thesis. Rob Cuss has also helped and guided me through my writing up over the last couple of months and been a great aid in expanding my knowledge of rock mechanics and *in situ* stress.

I also wish to thank Dr Steve Rogers (formerly of the BGS, now at Golder Associates) who, along with the BGS staff, was instrumental in helping me with my research and gaining additional BGS University Collaboration funding for the many trips to the BGS that I have made over the past 3 years.

My thanks are also due to Dr. Bob Holdsworth who took over as my primary supervisor at Durham and was given all my chapters to read. Additional thanks are also due to Dr. Neil Goult who helped and guided me in my first year of research at Durham.

Data availability and help of numerous staff from UK Nirex and the BGS are also gratefully acknowledged.

Since joining the BGS in March 2002, a great amount of encouragement, help and advice has been given by my line manager, Tony Morigi. He has encouraged and aided me in the final stages of my thesis.

The Natural Environment Research Council (NERC), the BGS University Collaboration Fund and the Leverhulme Trust all contributed financially to this work.

1. - Introduction

1.1 Preamble: *In Situ* Stress, Discontinuities & Flow

Discontinuities in rock masses are of great interest to the Petroleum Industry when dealing with fractured reservoirs, to the environmental sector concerned with the migration of contaminants through fractured rocks and to the water industry when dealing with the abstraction of water from fractured aquifers. All these differing industries are trying to analyse and subsequently model fractured rock masses, so that hydraulically conductive (flowing) and hydraulically non-conductive (non-flowing) discontinuities can be identified.

Discontinuities have been recognized as playing an important role in controlling hydraulic properties of rock masses by providing permeable conduits for fluids (Finkbeiner *et al.*, 1997). Analysis of drill core or borehole imagery logs may reveal the presence of hundreds or even thousands of discontinuities. However production logging and experience demonstrates that only a relatively small proportion of these discontinuities contribute to flow in the borehole (e.g. Long *et al.*, 1991). The identification, orientation and distribution of discontinuities (section 2.4) and their relationship to the current stress field (section 2.6) are of great importance in order to properly characterize these complex fractured rock masses. One key to understanding these geological environments is firstly to have a good understanding of the regional stress regime (section 2.2 & 2.3). Once identified, further complex analysis and modeling can be undertaken. The stress regime dictates how discontinuities are formed and subsequently develop.

One area of recent research, by Barton *et al.* (1995), has suggested that stress plays an important role in controlling the flow of fluid within a fractured rock mass (section 2.6). Barton *et al.* (1995) calculated the resultant shear (τ) and normal (σ_n) stresses acting on discontinuity planes. They concluded that discontinuities, which had a ratio of shear to normal stress greater than the

coefficient of friction (μ), should be classed as 'critically' stressed for frictional failure. Barton *et al.* (1995) specifically proposed that 'critically' stressed discontinuities had much higher permeabilities than discontinuities not 'critically' stressed.

1.2 Aims & Objectives

The main aim of this study was to further the knowledge and understanding of the stress regime at Sellafield and how it affects the flow of fluid within the fractured rock mass.

The first objective of this study was to investigate the regional stress regime within the Borrowdale Volcanic Group (BVG) at Sellafield.

The second objective was to investigate the flow of fluid within the fractured rock masses of the BVG and Permian-Triassic rocks, by applying the ideas developed by Barton *et al.* (1995). This investigation focuses on a diagnostic technique to identify flowing and non-flowing discontinuities and help explain why some discontinuities flow and others do not.

1.3 Thesis Structure

This introduction outlines the aims, objectives and structure of this thesis and the background to the UK Nirex Ltd Sellafield data set used in this investigation (discussed below – section 1.4). **Chapter Two** introduces and defines the terms and concepts that are used later in the thesis. This includes: the mechanics and techniques used in the regional stress determination, the characterization of discontinuities (geologically and hydrogeologically) and the modeling of fluid flowing discontinuities.

Chapter Three outlines the geological and hydrogeological setting of the Sellafield area. Discussion is divided up into the regional, district and site studies that were undertaken by Nirex.

Chapter Four introduces the investigation into the regional stress regime encountered at Sellafield. The techniques used to analyse and investigate the stress regime at Sellafield are explained and discussed. The ability to detect breakouts from the various geophysical downhole-imaging tools is evaluated and discussed. The developments of a technique to eliminate the effects of discontinuities' noise is outlined and is applied to permit observations to be made. The results are then used to examine the relationship between stress fields and discontinuities.

Chapter Five starts by introducing the detailed information obtained by Nirex, used to identify flowing and non-flowing zones (section 1.2 & 1.2.1). Techniques used to collect data on the state of *in situ* stress and discontinuities' attributes within these zones from downhole geophysical imagery are then presented. This information was obtained in order to be able to investigate the relationship between the flow of fluid through a fractured rock mass and the prevailing stress field.

Chapter Six uses the hydrogeological, in-situ stress and discontinuity data generated and presented in Chapter 5 to investigate the relationship between the flow of fluid through a fractured rock mass and the prevailing stress field in the BVG and Permo-Triassic rocks at Sellafield. In the second part of this chapter, the geological, hydrogeological, in-situ stress and discontinuity data from Sellafield are integrated to form composite borehole logs. These visual compilations aid in the identification of hydraulically conductive (flowing) from hydraulically non-conductive (non-flowing) discontinuities from simple visual pattern analysis.

Chapter Seven is a general discussion and synthesis concerning the key issues identified in Chapters Four, Five and Six. **Chapter Eight** gives the general conclusions to the thesis. Finally, **Chapter Nine** briefly explores some areas that have been identified for further potential research.

1.4 Background & History of Sellafield

The Sellafield region, west Cumbria, was the focus of the UK's most extensive and thorough site characterisation study from 1989 to 1997 (Gutmanis *et al.*, 1998). The UK Nuclear Industry Radioactive Waste Executive (known as UK Nirex Ltd and referred to as Nirex after here) undertook this work as part of their scientific programme into assessing whether the rocks in the Sellafield region would be suitable as a deep repository for the storage and containment of solid intermediate-level (ILW) and low-level (LLW) radioactive waste.

Sellafield and Dounreay, Caithness, were selected in 1989 by Nirex following an extensive site selection exercise carried out across the UK (Chaplow, 1996). Desk studies of existing geological and geophysical data were completed and two boreholes were drilled at each site together with a number of new geological and geophysical surveys. Nirex announced in July 1991 that it was to concentrate its investigations solely at Sellafield (Chaplow, 1996). The main difference between the suitability of the two sites was that 60% of the waste destined for the repository arose from British Nuclear Fuels' operations at Sellafield (Chaplow, 1996). Thus transportation costs could be minimized if a repository was sited close to Sellafield.

The location of the proposed Sellafield repository was on the west coast of Cumbria, at Longlands Farm, between the Sellafield Nuclear Power Plant and the village of Gosforth.

Because of the diverse requirements for geological information, a hierarchical approach was adopted for data acquisition and interpretation (Bowden *et al.*, 1998). Investigations were initially undertaken on a regional, district and site scale (Figure 1.1).

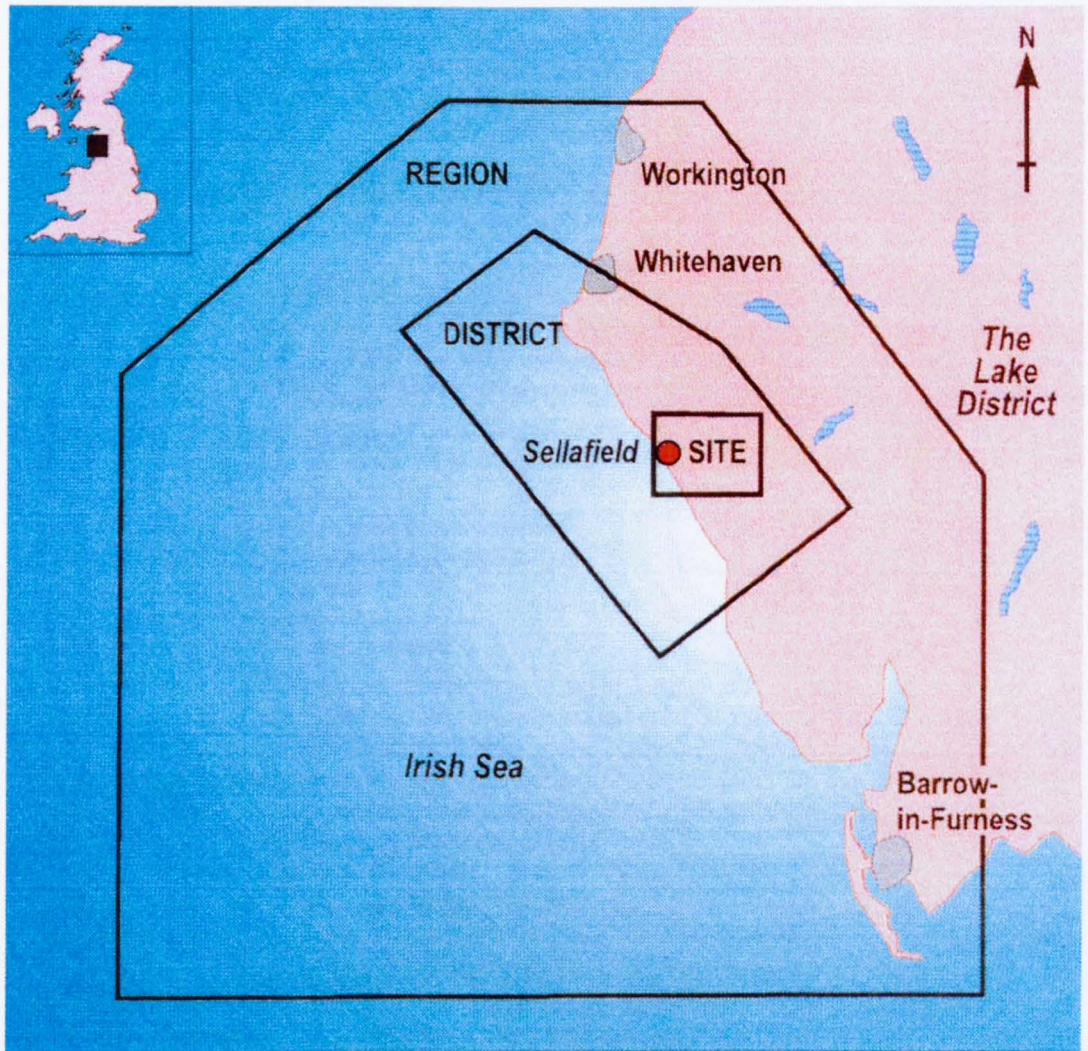
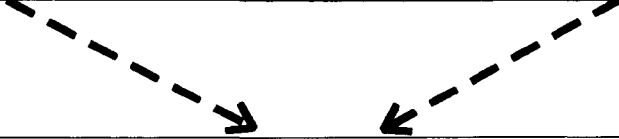


Figure 1.1 - Location and scales of the Sellafield study areas (NIREX, 1997g)

The three scales had a wide range of site characterisation activities that involved the general acquisition of geological, geophysical, geotechnical, hydrogeological and geochemical data. These studies provided important background information to enable the construction of a three-dimensional picture of the geological and hydrogeological conditions encountered at the site. The site characterisation activities were divided between deep borehole investigations and surface based investigations. Sections 1.1.1 and 1.1.2 discuss these investigations in further detail.

More detailed geological and hydrogeological characterisation studies were undertaken in the site area. This area was subsequently sub-divided into the Potential Repository Zone (PRZ) and within that the Rock Characterization Facility (RCF), (Figure 1.2). The RCF was an area that had been proposed for the construction of an underground rock laboratory where further detailed underground characterisation and *in situ* testing of the geology and hydrogeology was to be carried out. During 1995/96, a public inquiry was held into Nirex's proposals to construct the RCF. On March 17th 1997 the Secretary of State for the Environment announced that he had decided to dismiss the appeal by Nirex against the decision by Cumbria County Council to refuse permission for the construction of an RCF (NIREX, 1997e). This decision subsequently meant that Nirex's scientific investigations at Sellafield were terminated. This also meant that the United Kingdom's progression into finding a possible solution to the increasing problem of radioactive waste storage and disposal was halted. Nirex's scientific investigations at Sellafield have greatly advanced the geological and hydrogeological knowledge of the West Cumbrian District, the findings of which are discussed in sections 3.1 and 3.2.

Surface Investigations	Deep Borehole Investigations
<p>Regional geological mapping (lithologies and fractures)</p> <p>Shallow boreholes for regional hydrogeological surveys</p> <p>Regional long-term monitoring of hydrology & meteorology</p> <p>Regional studies of Quaternary deposits</p> <p>Regional, district & site geophysical surveys (onshore & offshore)</p>	<p>Continuous drilling and coring of 29 boreholes</p> <p>Lithological and fracture logging of 29 boreholes</p> <p>Specialist testing within boreholes (geophysical, geotechnical, hydrogeological & geochemical)</p> <p>Specialist testing in between boreholes (geophysical & hydrogeological)</p> <p>Long-term monitoring of groundwater pressures</p>



Detailed multi-disciplinary interpretation studies

Table 1.1 – Sellafield scientific investigations.

1.4.1 Deep Borehole Investigations

During the scientific investigations at Sellafield, 29 deep boreholes (Table 1.1, Figure 1.2) were drilled by Nirex totalling some 27,500 meters depth (Bowden *et al.*, 1998). In addition, further information was also obtained through the refurbishment of two existing boreholes, Boonwood and Holmrook 13, which had been drilled previously for mineral exploration (Bowden *et al.*, 1998). Locations of each borehole are shown in Figure 1.2.

In all of the boreholes, a standard suite of data acquisition techniques were used, including:

- Continuous coring of boreholes with over a 99% recovery rate (Chaplow, 1996);
- Detailed geological (lithological, discontinuity, mineralogical and geotechnical) logging of the core (Chaplow, 1996);
- Sampling, testing and analysis of the borehole core to determine the geological, mineralogical, geochemical and mechanical properties of the rocks (Chaplow, 1996);
- Geophysical wireline logging of the boreholes;
- *In situ* stress analysis (breakout analysis, hydrofrac analysis and/or overcoring);
- *In situ* hydraulic testing of the groundwater system in order to characterise the average hydraulic properties of the rock mass at varying scales, from detailed 1-2m tests (carried out solely in borehole RCF3, section 5.2) to general tests over several thousands of metres, and varying depths (e.g. environmental pressure measurement tests (EMP), full sector tests (FST), discrete extraction tests (DET) (Sutton, 1996);
- Sampling and analysis of the groundwater geochemistry (NIREX, 1997d).

On a selected number of boreholes within the PRZ area, cross-hole seismic tomography was undertaken (boreholes 2 – 4, 5 – 2, 2 – RCF3, 5 – RCF3, RCF1 – RCM3, RCF2 – RCM2) to assist in the definition of faults and fractures between borehole pairs for input into the three-dimensional structural models (Bowden *et al.*, 1998). Cross-hole pump tests in the Ordovician basement between boreholes 2 and 4 were carried out to characterise and sample the flowing features and to establish the connectivity of the fractures both within borehole 2 and between borehole 2 and 4 (Sutton *et al.*, 1996).

1.4.2 Surface Investigations

Surface investigations were carried out simultaneously with the deep borehole investigations, as part of Nirex's scientific investigations at Sellafield. To complement the long-term deep borehole hydrogeological monitoring program, a surface-based network of monitoring sites collected data on the hydrological and meteorological conditions (Bowden *et al.*, 1998). This extensive array of shallow boreholes was drilled by the National Rivers Authority (now part of the Environment Agency), British Nuclear Fuels Ltd., and Nirex. The data collected from this array helped to define the groundwater system around Sellafield, particularly the recharge and discharge aspects, and allowed a groundwater conceptual model (section 3.2.1) to be developed and validated (Sutton, 1996).

Detailed geological mapping of the Sellafield region, district, site and PRZ was carried out to characterise the stratigraphy and structure on each scale. In addition, lithological and fracture mapping studies were carried out in the Lower Palaeozoic basement (Bowden *et al.*, 1998). In the Quaternary, initial desk studies were followed by a programme of mapping pitting and logging (NIREX, 1997h). Twenty exposures in drift were examined and forty-nine trial pits were excavated across the Sellafield area for detailed logging, sampling and testing (Bowden *et al.*, 1998).

Borehole ID	OS National Grid Reference			Drilled Length (mbRT)	Trajectory
	Eastings	Northing	Elevation (maOD)		
BH1	303202.2	502706.1	21.2	786.6	Vertical
BH1A	303202.2	502706.1	21.2	1184.6	Deviated
BH2	305542.9	503412.1	60.2	1604.1	Vertical
BH3	302596.3	502646.3	9.1	1944	Vertical
BH4	305639.2	503457	68.6	1254.1	Vertical
BH5	305169.6	503457	80.6	1254.1	Vertical
BH7A	303856.8	504903	46.9	1003.9	Vertical
BH7B	303854	504853	46.9	474.9	Vertical
BH8A	307208	504982.9	163	996.2	Vertical
BH8B	307213.8	505014.6	163	245	Vertical
BH9	308525.4	504268.8	116.4	496.1	Vertical
BH10A	304312.1	503061.1	35.5	1602.8	Vertical
BH10B	304268.3	503080.3	35.7	252.3	Vertical
BH10C	304342.8	503094.4	35.6	253	Vertical
BH11A	306791.9	501663	44.6	1164	Vertical
BH12A	304933.5	502643.9	38.5	1143.9	Vertical
BH13A	304520.9	500146.2	18.5	1745	Vertical
BH13B	304505.8	500184.1	18.5	295	Vertical
BH14A	302486.2	505692	41.2	868	Vertical
BH16	303964.2	502318.9	37.3	591.3	Vertical
RCF1	305794.6	503907.4	95.9	1143.8	Deviated
RCF2	305506.1	504170.2	94.9	1144.3	Deviated
RCF3	305564.9	503931.9	84.5	986.3	Vertical
RCM1	305568.3	503961.5	84.5	986.2	Vertical
RCM2	305597.9	503491.9	84.5	985	Vertical
RCM3	305785	503896	95.9	1028.8	Deviated
PRZ1	305475.4	503424.7	60.2	775.3	Inclined
PRZ2	305660.3	503443.7	68.5	560	Inclined
PRZ3	305186.3	503852.2	84.9	775	Inclined

Table 1.2 – Sellafield deep boreholes (from Bowden *et al.*, 1998).

Geophysical surveys were commissioned or acquired by Nirex both onshore and offshore. These surveys have included some 1950 kilometres of seismic reflection surveys and 8500 kilometres of airborne magnetic and radiometric surveys (Chaplow, 1996). Gravity data have been collected along many of the seismic lines. In addition specialist surveys were undertaken including: a three-dimensional seismic reflection trial survey of part of the PRZ; a Controlled Source Audio Magneto Telluric Survey within the site area; and a range of non-seismic geophysical surveys techniques that were used to assess their applicability to characterising the Quaternary deposits and the sub-Quaternary structure (Bowden *et al.*, 1998).

2. – Literature Review & Previous Work

2.1 Introduction

This chapter introduces and defines the terms and concepts that will be used later in this thesis. The following will be discussed: the mechanics and techniques used in regional stress determination; the characterization of discontinuities (geologically and hydrogeologically); and the modeling of flowing discontinuities.

2.2 Mechanics & Techniques for *In Situ* Stress Determination

2.2.1 Introduction

In situ stress refers to the present day crustal stresses within a rock mass. The advancement in the understanding of *in situ* stress within the Earth's crust has developed rapidly over the last fifty years. In the past traditional methods in determining crustal stress have been costly or yield unreliable results and hence the availability of accurate measurements has, until recently, been very limited (Brereton *et al.*, 1990). Improvements in the understanding of this area of stress determination have developed from a need to know the geomechanical responses of rock masses affected by earthquakes, underground mining for minerals, underground disposal of waste or the drilling of boreholes for engineering purposes, hydrocarbon or geothermal resources.

2.2.2 Mechanics for *In Situ* Stress Determination

A stress is a force per unit area acting on a surface, which may be real or imagined. Within the Earth this force must be considered in three-dimensions, and therefore it is envisioned as a series of forces acting on the faces of a cube in an isotropic rock mass (Figure 2.1a). The state of stress acting on this cube is determined by means of a six-component stress tensor (Figure 2.1a), whose magnitudes are related to an arbitrarily orientated, three-dimensional coordinate system (Jaeger, 1969).

Calculation and measurement of the *in situ* stress field can be greatly simplified if the effects of shear stress acting on the surfaces of the cube are eliminated. By rotating the three-dimensional coordinate system into parallelism with the three principal normal stress directions (S_1 , S_2 and S_3), this unique situation can be obtained (Figure 2.1b).

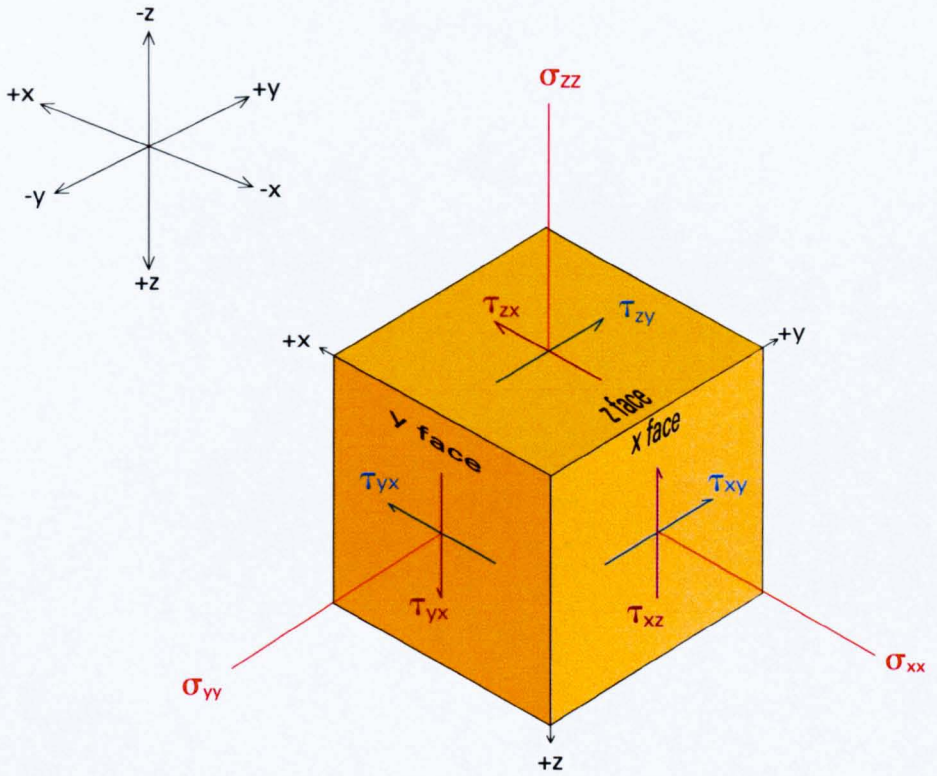
The stress tensor of the cube can therefore be defined by determining the magnitudes and orientation of the three orthogonal principal stresses. The principal stresses in this thesis are divided up into the far-field stresses (S_1 , S_2 and S_3) and *in situ* stresses (σ_1 , σ_2 and σ_3). The far-field stresses are stresses that are unperturbed in a rock mass (pre-borehole). The *in situ* stresses are far-field stresses that have been perturbed by the drilling of boreholes in a rock mass (post-borehole).

In most near-surface geological settings (depth <5km), one of the principal stresses is assumed to be a vertical stress (S_v) and the other two are the horizontal maximum (S_{Hmax}) and minimum stress (S_{Hmin}). This is assumed on the basis that there should be no shear stress existing in the plane of the earth's surface (Anderson, 1951). As the majority of *in situ* stress analyses are generally conducted where there is little topography, it seems geologically reasonable to assume that one of the principal stresses is caused by the weight of the overlying overburden acting vertically (Figure 2.3). In a borehole the integration of the geophysical wireline density log allows σ_v to be determined:

$$\sigma_v = \rho g z$$

Where ρ is the mean density of the overburden; g is gravitational acceleration and z is the depth within the Earth in meters.

A)



B)

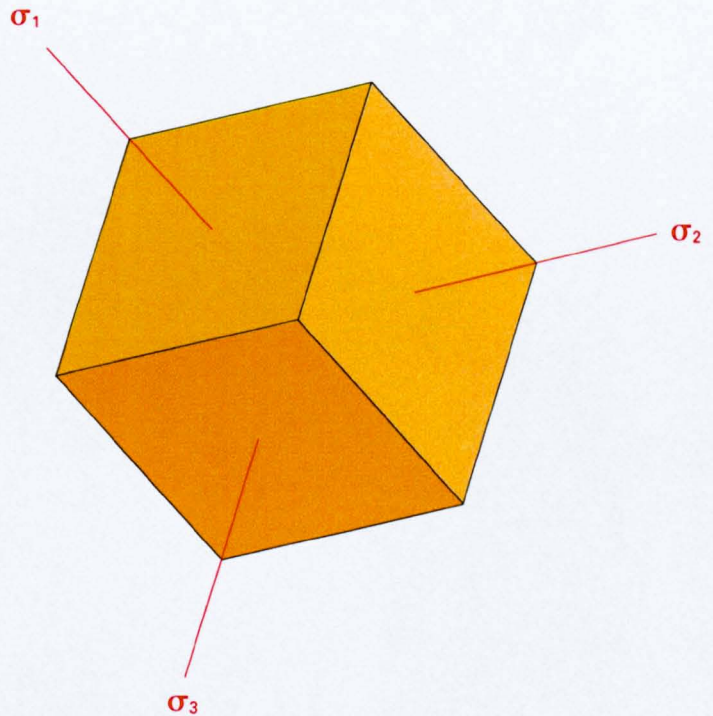


Figure 2.1 - Three-dimensional coordinate system of a) six-component stress tensor on an element cube in an isotropic medium b) rotation of the three-dimensional coordinate system into parallelism with the three principal normal stress directions (adapted from NIREX, 1997a and Priest, 1993).

Within the earth there are three states of stress that can be encountered (Figure 2.2):

- The normal faulting regime – $S_v > S_{Hmax} > S_{Hmin}$
- The strike slip faulting regime – $S_{Hmax} > S_v > S_{Hmin}$
- The thrust faulting regime – $S_{Hmax} > S_{Hmin} > S_v$

These are known as the Anderson classification of stress regimes (Anderson, 1951).

At all but the shallowest depths, S_1 , S_2 and S_3 are compressive and in most locations, of different magnitudes (Gay, 1980). When forces act on rock mass within the earth, they deform in order to maintain the equilibrium of the forces and support the load acting on rock mass. Materials show a combination of elastic, plastic, brittle and/or ductile behavior on a range of intrinsic material controls (e.g. mineralogy, grain size etc) and extrinsic environmental controls (pressure, temperature, strain rate etc). Twiss and Moores (1992) provides a good summary of these deformation processes.

2.2.3 Techniques for *In Situ* Stress Determination

In situ stress is difficult to measure directly. There is a wide variety of stress measurement techniques in use, both in industry and by research workers. These techniques also provide a wide range of scales at which stresses are measured, from the rock core scale of the order of a few centimeters, through the borehole methods which sample scales of the order of several meters, up to the earthquake focal mechanism methods which sample stresses up to perhaps the thickness of the crust (Edwards, 1997).

The main *in situ* stress determination techniques are discussed below and have been divided up into indirect methods, borehole methods and direct methods. Methods that are not used in this research will be only described briefly. Further detailed reviews of the available methods used for *in situ* stress analysis are provided in McGarr and Gay (1978), Zoback and Zoback (1980), Gough and Gough (1987) and Engelder (1993).

**FAULT REGIMES
IN THE LITHOSPHERE**

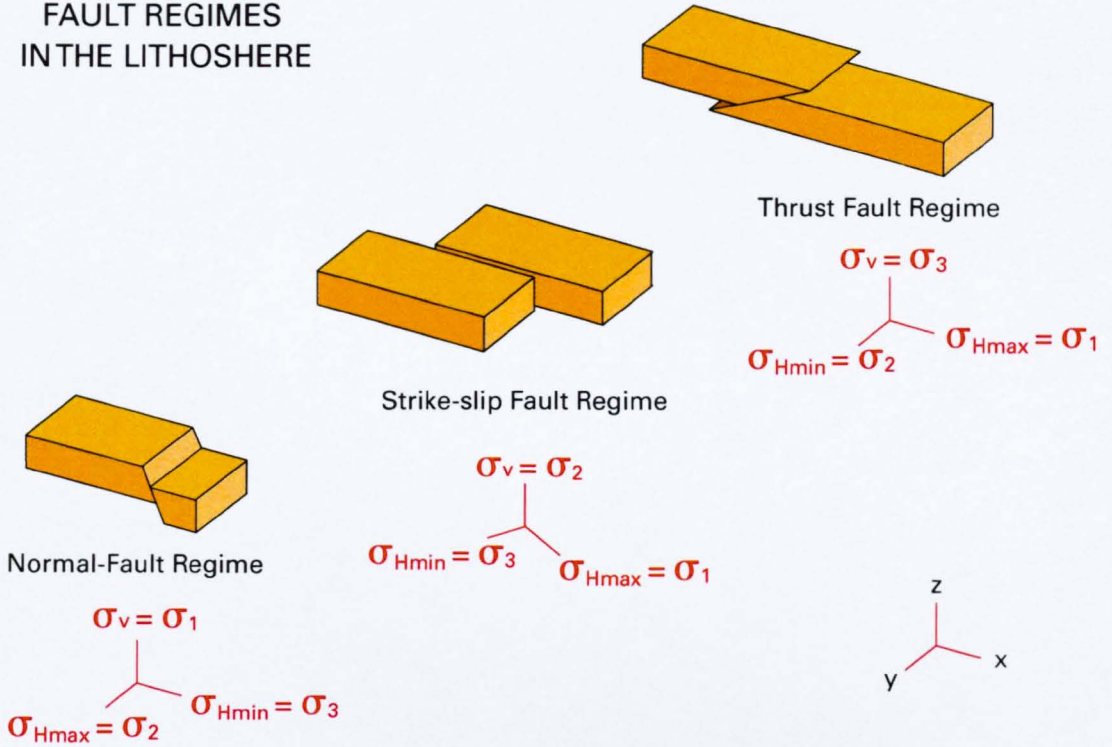


Figure 2.2 - The three states of stress, known as the Andersonian stress states, encountered within the Earth (Engelder, 1993).

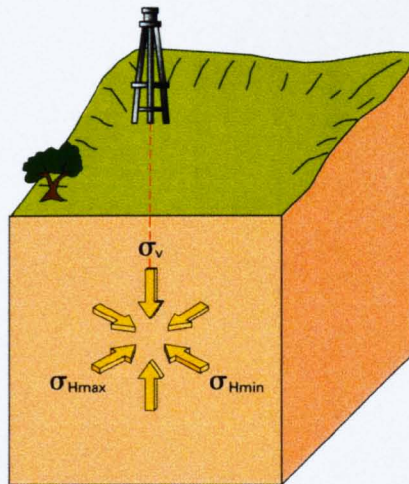


Figure 2.3 - Stress tensor described in terms of the magnitude and orientation of three orthogonal principal stresses in a rock mass (adapted from Bell, 1996).

2.2.3.1 Indirect Methods

Geological Indicators

The earliest methods for determining stress orientations and relative magnitudes come from geological features that can be observed at the surface, including small neo-tectonic faults (Bell, 1996), volcanic vents (Zoback, 1992) and quarry stress-relief structures (Hoek and Brown, 1980b). Faults, folds, intrusions and slickensides, have long been used to interpret paleostress fields, but such features may not represent the modern day stress. Such geological information represents the patterns established over geological time and are a result of the continual interaction between the varying amplitudes and directions of tectonic stress and the typically heterogeneous, anisotropic rocks present in the earth's crust.

Earthquake Focal Mechanisms

Earthquake focal mechanisms (FM) solutions form the majority of stress orientation and relative magnitude data in the World Stress Map (WSM) database (section 2.3.2). FM solutions are derived from examining the first motion of an earthquake recorded on a suitably distributed seismic network (Zoback, 1992). These first motions give information on the orientation of the principal stresses (σ_1 , σ_2 & σ_3). Stereographic plots of these first motions, give the fault plane mechanism solution for strike-slip or dip-slip faults by assessing whether compressional or dilatational motion has occurred first and in what direction.

2.2.3.2 Direct Methods

Flat Jack

This simple and reliable stress technique measures both the stress magnitude and orientation. The technique can only be used at the surface or at a shallow mine face.

A series of regular slots are cut, at orthogonal azimuths between measuring pins securely fixed into the rock, using a diamond saw. As the slots are cut, the previously secured pins record the stress release in the form of strain. Hydraulic flat jacks are then cemented into the slots. These jacks are then pressurized to recover the initial strain recorded by the pins. From this the *in situ* stress orientation and magnitude can be deduced by using the elastic properties of the rock.

Overcoring

Overcoring provides a simple and reliable technique, allowing the measurement of both the stress orientation and magnitude. It relies on the same principle as the flat jack method, i.e. strain recovery upon release of the *in situ* stress field (Engelder, 1993). A borehole is drilled into the rock mass under investigation, and a second narrow hole is then drilled beyond the base of the first hole. The narrower, second hole then has a deformation meter, comprising of an array of strain gauges, cemented into it. The surrounding volume of rock is then overcored, and as this happens the strain relief is measured by the strain gauges as the *in situ* stresses are removed from the volume of rock. By then using the elastic properties of the rock a determination of the *in situ* stress magnitudes and orientation can be made.

Anelastic Strain Recovery

Anelastic strain recovery yields stress magnitudes and orientation. This method involves the collection of stress data from orientated core, usually at depths greater than 300 m. The core, upon recovery, is placed into a strain cell consisting of three mutually perpendicular measuring transducers. These transducers measure the time dependant strain recovery of the core as it 'relaxes' from its *in situ* stress conditions to effectively zero stress (Teufel, 1983).

2.2.3.3 Borehole Methods

Stress in a borehole

When a borehole is drilled into a rock mass, the presence of the borehole disturbs the pre-existing stress regime. As a borehole is drilled, the rock mass surrounding the hole must carry the force previously carried by the removed rock. This can be described as the conservation of energy, since mass has been removed whilst energy (stress) have not (Cuss, 1998). This results in a stress concentration around the edge of the borehole, which if it becomes greater than the rock strength results in compressional or extensional failure in and behind the borehole wall (Cuss, 1998). The compressive stress is concentrated in the σ_{Hmin} direction and the tensile stress is a concentrated in the σ_{Hmax} direction when a borehole is vertical. For boreholes that are deviated from the vertical, or are drilled in an area with significant topographic relief, stress concentrations are related in a complex way to the relative magnitudes of all three principal stresses and their orientations relative to that of the borehole (Mastin, 1988). This problem also complicates the computation of the three principal stresses (σ_v , σ_{Hmax} and σ_{Hmin}) in deviated boreholes.

The stress concentrations around a borehole can be studied by considering the stress concentrations caused by a circular hole in a homogeneous, isotropic, infinite elastic plate, subjected to external uniaxial far field stress (Timoshenko and Goddier, 1970). The solutions for the stress concentrations in such a plate were defined by Kirsch, 1898 (Jaeger and Cook, 1984). The Kirsch solution is easily modified to consider biaxial loading and the effect of pore pressure (Jaeger and Cook, 1984), conditions that represent those typically found in a borehole. The modified Kirsch model (Figure 2.4) shows a hole of radius r loaded by maximum and minimum stresses σ_{Hmax} and σ_{Hmin} respectively at infinity (or at distance $\gg r$). The pore-fluid pressure (P_p) acts within the hole opposing the far-field stresses superimposing additional borehole-periphery stresses (Cuss, 1998).

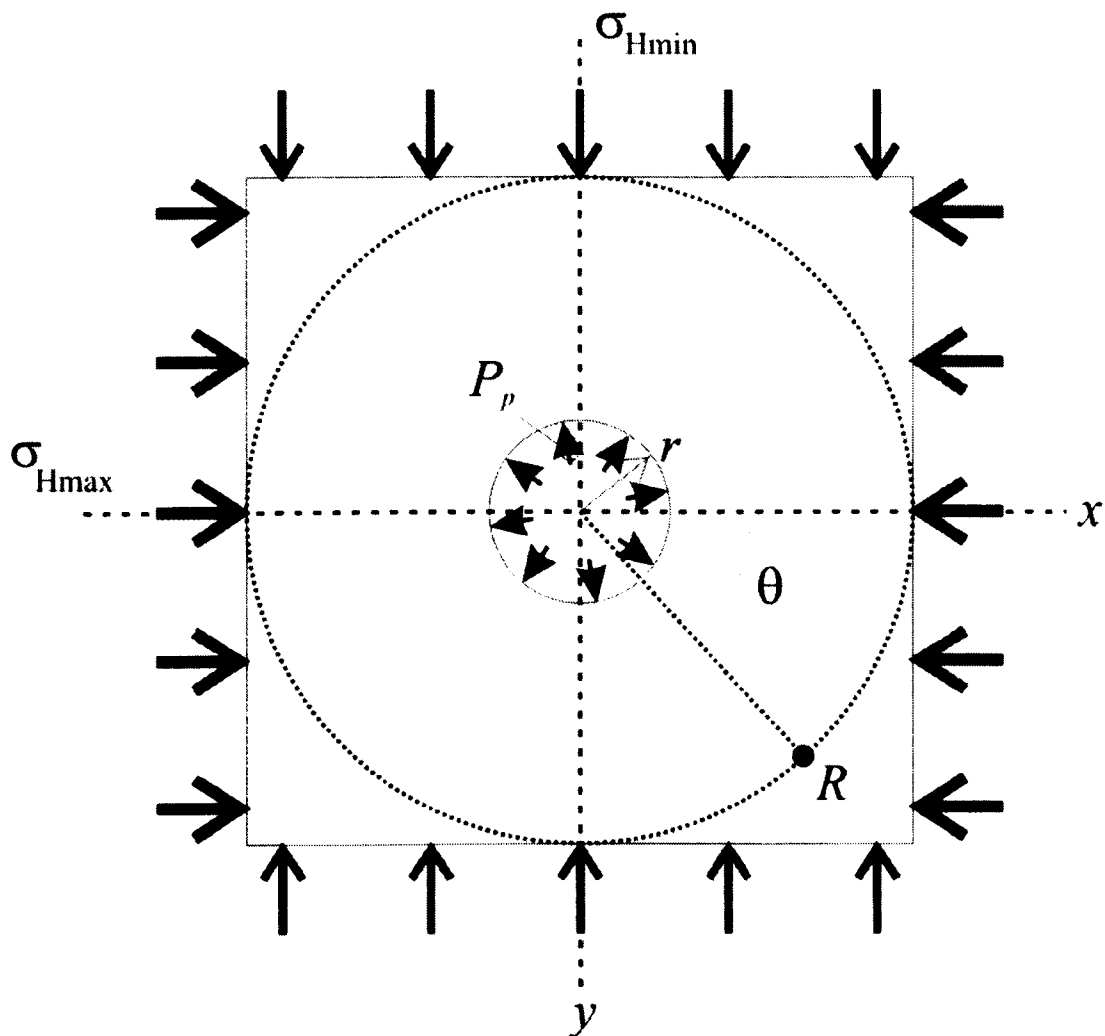


Figure 2.4 – Model used in the calculation of the modified Kirsch solution for the stress concentration at point R created by a hole of radius r with internal pressure P_p in a plate loaded at infinity by biaxial *in situ* stresses σ_{Hmax} and σ_{Hmin} where R makes an angle of θ with σ_{Hmax} (from Cuss, 1998).

$$\begin{aligned}
 \sigma_r &= \frac{\sigma_{H\max} + \sigma_{H\min}}{2} \left(1 - \frac{r^2}{R^2}\right) + \frac{P_p \cdot r^2}{R^2} + \frac{\sigma_{H\max} - \sigma_{H\min}}{2} \left(1 - \frac{4r^2}{R^2} - \frac{3r^4}{R^4}\right) \cos 2\theta \\
 \sigma_\theta &= \frac{\sigma_{H\max} + \sigma_{H\min}}{2} \left(1 + \frac{r^2}{R^2}\right) - \frac{P_p \cdot r^2}{R^2} - \frac{\sigma_{H\max} - \sigma_{H\min}}{2} \left(1 + \frac{3r^4}{R^4}\right) \cos 2\theta \\
 \tau_{r\theta} &= \frac{\sigma_{H\max} - \sigma_{H\min}}{2} \left(1 + \frac{2r^2}{R^2} + \frac{3r^4}{R^4}\right) \sin 2\theta
 \end{aligned} \quad \text{Eq.2.1}$$

where; σ_r is the radial stress, σ_θ is circumferential or hoop stress, $\tau_{r\theta}$ is shear stress, σ_v is the vertical stress, R is distance from center of bore to point where stress are being calculated, θ is the angle made between R and $\sigma_{H\max}$. Note: polar co-ordinate frame.

Figure 2.5 shows the stress trajectory pattern and stress component magnitude for both hydrostatic and nonhydrostatic situations, assuming no P_p . Stress modification under hydrostatic conditions is simple (Figure 2.5a) with a concentric stress increase towards the borehole wall. Circumferential stress (σ_θ) shows a concentric pattern, with radial stress (σ_r) normal to σ_θ at all times. Circumferential and radial stress concentrations reduce rapidly away from the borehole and approximate the far-field stress (S), by $R=10r$. Radial stress is zero at the bore-wall with circumferential stress equal to $2S$. Shear stress is created within the system locally around the bore as $\sigma_r \neq \sigma_\theta$. Damage will be localized, with significant damage occurring only within 2-3 bore radii of the borehole wall. The non-hydrostatic case is more complex, with heterogeneous stress distribution around the bore (Figure 2.5b). Tensile regions are highlighted in the $\sigma_{H\max}$ direction where the mean stress is positive (in the example of Figure 2.5b, tensile stress is not created as $3\sigma_{H\min} > \sigma_{H\max}$ and P_p is zero). In the $\sigma_{H\max}$ direction, radial stress (σ_r) shows an initial rise from $3\sigma_{H\min} - \sigma_{H\max}$ to $0.7\sigma_{H\max}$ within $0.4r$ of the borehole wall ($R=1.4r$), then decays to $\sigma_{H\min}$ by $R=10r$. Circumferential stress (σ_θ) is zero at the borehole wall and increases to $0.9\sigma_{H\max}$ by $R=3.3r$ and approximates $S_{H\max}$ by $R=10r$. In the $\sigma_{H\min}$ direction, σ_r is zero at the borehole wall and rapidly increases to $0.9\sigma_{H\min}$ by $R=1.5r$.

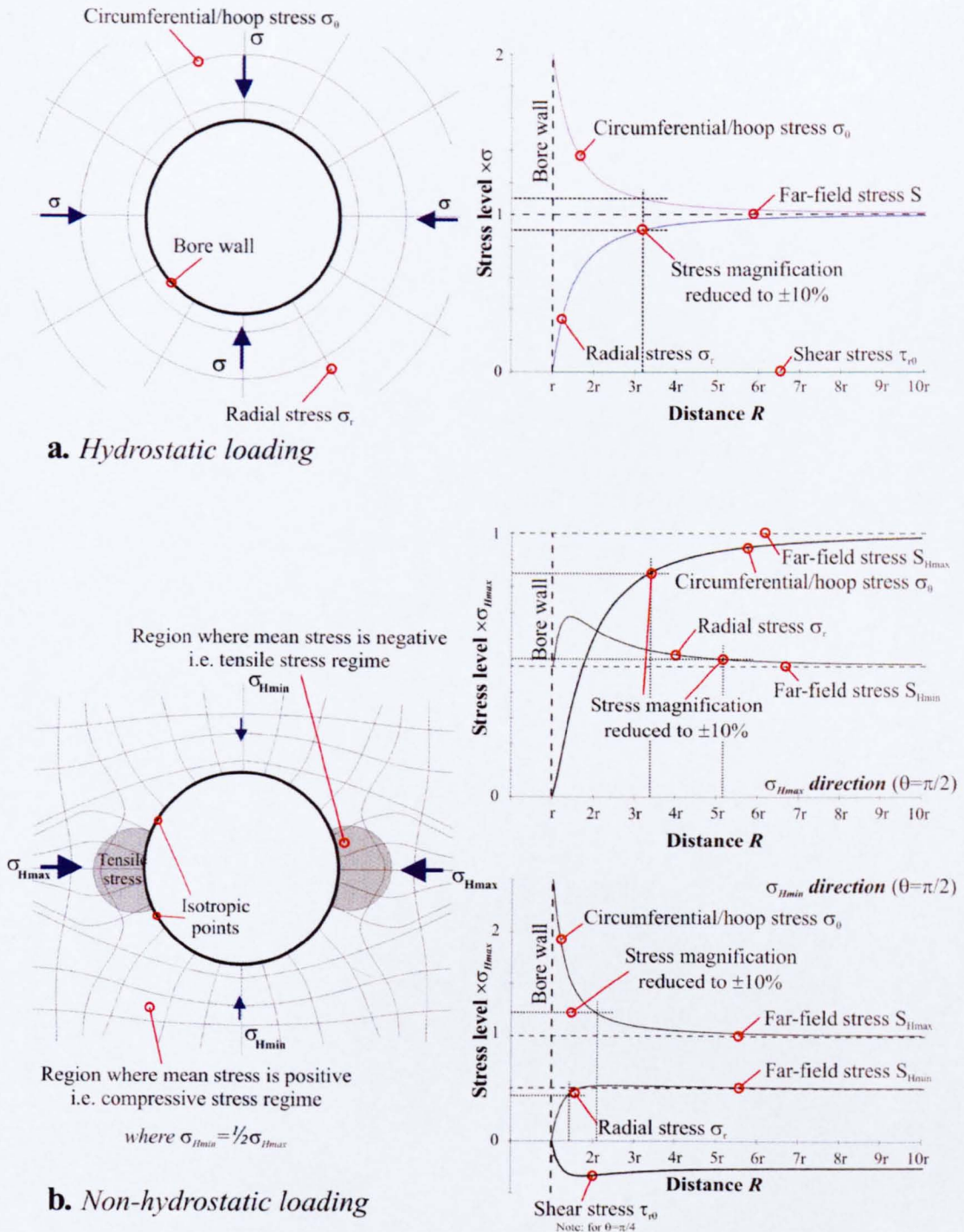


Figure 2.5 – Graphical representation of stress intensification around (a) hydrostatically (where $\sigma_{Hmin}=\sigma_{Hmax}$) and (b) nonhydrostatically (where $\sigma_{Hmin}=1/2\sigma_{Hmax}$) loaded boreholes predicted from the modified Kirsch solution. The deviation from a uniform stress field is seen by a changing stress trajectory. The graphs show changes in radial stress (σ_r), circumferential/hoop stress (σ_θ) and shear stress ($\tau_{r\theta}$), with distance away from the borehole center. Stress can be seen to be greatest at the borehole periphery, and generally, the stress concentrations become insignificant within 3-4r distance (from Cuss, 1998).

At the borehole wall, $\sigma_\theta = \sigma_{Hmax} - \sigma_{Hmin}$, and rapidly reduces to $1.1\sigma_{Hmax}$ by $R=2.2r$ and approximates S_{Hmax} by $R=10r$. In the direction of the far-field stresses (S_{Hmin} and S_{Hmax}), shear stress ($\tau_{r\theta}$) is zero. Figure 2.5b shows the maximum shear stress which occurs in the direction of $\theta=\pi/4$. At the borehole wall, $\tau_{r\theta}$ is zero and rapidly rises to $\pm\frac{1}{2}(\sigma_{Hmax}-\sigma_{Hmin})$ within $2r$. As described, a complex stress field is created in all directions with stress concentrating around the bore periphery. Magnified stress levels decay rapidly, approximating far-field stresses S_{Hmin} and S_{Hmax} within 1 to 4 bore radii ($1-4r$) of the borehole wall.

Therefore, at the borehole wall the σ_r and $\tau_{r\theta}$ are zero and the stress field is defined by the σ_θ (in terms of principal horizontal stresses σ_{Hmax} & σ_{Hmin}):

$$\sigma_\theta = \sigma_{Hmax} + \sigma_{Hmin} - 2(\sigma_{Hmax} + \sigma_{Hmin}) \cos 2\theta - P_p \cdot r^2/R^2 \quad Eq.2.2$$

Circumferential stress is maximized at the azimuth of σ_{Hmin} . Where the maximum circumferential stress exceeds the compressive strength of the rock forming the borehole wall, compressional shear failure may occur (Hillis and Reynolds, 2000). Failure of intersecting, conjugate shear planes may cause borehole breakout (Figure 2.6 – discussed in more detail below). Circumferential stress is minimized at the azimuth of σ_{Hmax} . Tensile fractures form where the circumferential stress is less than the tensile strength of the rock forming the borehole wall, and are orientated at right angles to breakout (Figure 2.6 - discussed in more detail below as hydrofractures).

Hydraulic Fracturing

Hydraulic fracturing (hydro-fracing) was pioneered in the late 1950's in the petroleum industry to enhance the permeability of reservoir rocks by the propagation of tensile fractures (Hubbert and Willis, 1957). Haimson (1978) was the first to realize the true potential of this technique to obtain deep (5000m) measurements of the stress field. By 1980, hydro-fracing was used on a regular basis for the determination of the *in situ* stress field.

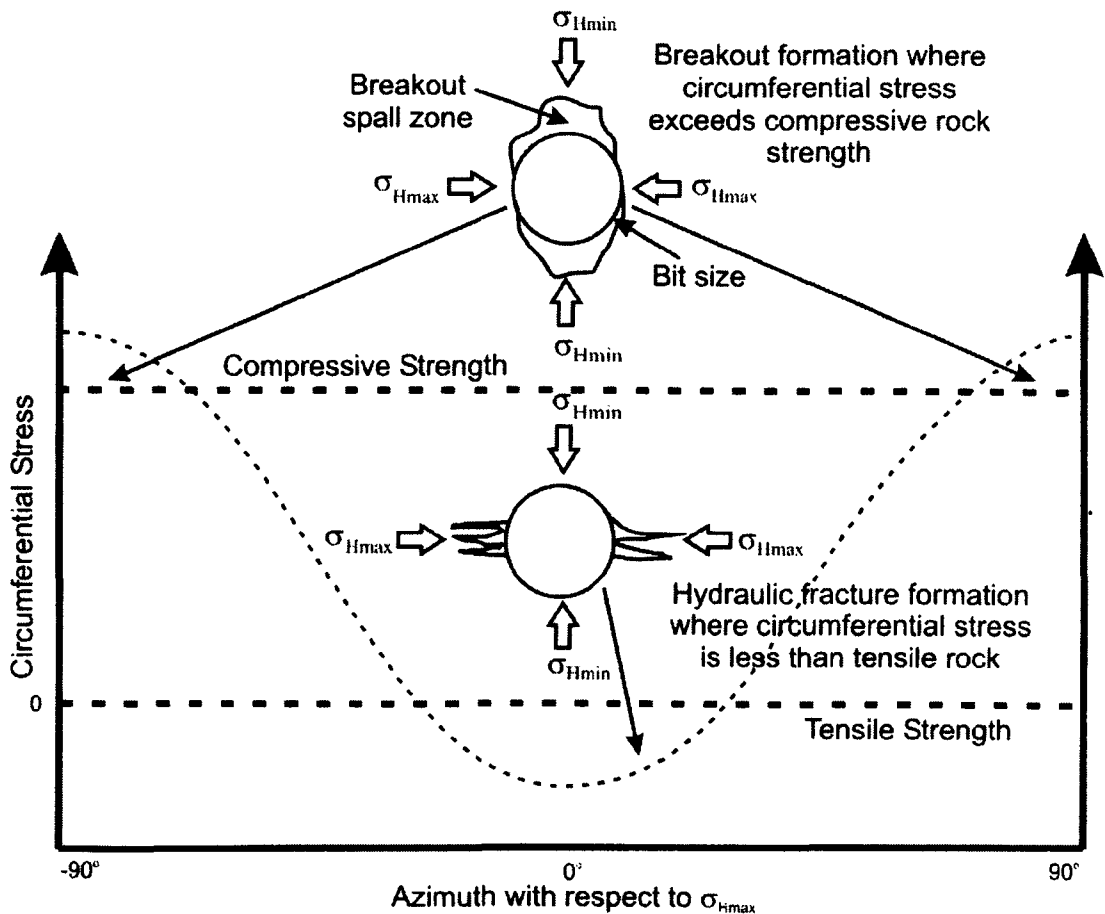


Figure 2.6 – Variation of circumferential stress (σ_θ) acting at the borehole wall with azimuth around the borehole. Schematic cross-sections of borehole shape associated with breakout and drilling induced tensile fracturing also shown. σ_H denotes the maximum horizontal stress and σ_h denotes the minimum horizontal stress (from Hillis and Reynolds, 2000).

A hydrofrac test involves sealing-off a small section (0.5 to 2 meters) of a borehole using two inflatable rubber packers (Cowgill, 1994). Ideally, the lithology should be uniform throughout the sealed-off interval and free from natural fractures. The borehole is then pressurized by pumping drilling fluid (water or drilling mud) into the sealed-off section. The sealed-off area is then pressurized until the critical fluid pressure for rupture and tensile failure of the borehole wall occurs producing the initial discontinuity. Pumping then ceases and the interval is 'shut-in'. The discontinuity continues to propagate until the drilling fluid pressure falls below the normal stress across the discontinuity. The pressure is then increased once more until the previously induced discontinuity re-opens at the 're-opening' pressure. The 're-opening' or 'shut-in' pressure is considered equal to σ_3 , or σ_{Hmin} . The tensile hydro-fractures theoretically open normal to the σ_{Hmin} and propagate in the direction of σ_{Hmax} . The magnitudes of the horizontal stress ratio can then be calculated from a number of simple equations, which are reviewed in Engelder (1993).

Drilling-induced tensile fractures form by the same critical 'breakdown' of the rock mass as happens in a hydro-fracture test. They develop from drilling in a highly stressed environment or because the drilling mud has 'over-pressured' the borehole. Drilling-induced tensile fractures form when the conditions in the borehole cause tensile failure of the borehole wall to occur without sealing the borehole. Further detailed accounts of drilling-induced tensile fractures is presented in Peska and Zoback (1995); Wiprut *et al.* (1997) & Aadnoy and Bell (1998).

Borehole Breakout

Breakout are elliptical elongations (eccentricity) of the borehole cross-sections that occur where an anisotropic stress field exists (Bell, 1990). The concentration of horizontal stresses around a vertical or near-vertical borehole can cause failure and spalling of the borehole in the direction of σ_{Hmin} . The specific failure mechanism may vary with rock strength, depth, or state of stress (Plumb, 1989).

These features have long been observed from measurements made by the four-arm dipmeter-tool. This tool has four orthogonal opposing spring-loaded arms with pads that contact the borehole wall directly, measuring the borehole diameter in two directions and the resistivity of the rock. As a four-arm dipmeter-tool is pulled up from the bottom of a borehole, cable torque causes the tool to rotate, when a borehole elongation is encountered, the tool ceases to rotate and the arms can become aligned by an enlargement of the borehole (Figure 2.7 & Table 2.1).

It was Leman (1964) who first identified elliptical elongations in a dipmeter caliper log. He deduced that these features were caused by fracturing. Cox (1970) in a study in Alberta, Canada, noted a preferential elongation of borehole enlargements independent of geological age and the magnitude of dip. Babcock (1978) extended Cox's observations and described them as breakout outlining the chief diagnostic criteria (Table 2.1). Babcock described breakout as zones that were associated with a slowing or cessation of the dipmeter-tool rotation, since the calipers lock into a preferred azimuth. Babcock (1978) and some subsequent authors suggested that the elongation of the borehole was caused by the borehole failing at the intersection with steeply dipping fractures (Babcock, 1978; Schafer, 1980). In an alternative explanation, Bell and Gough (1979) suggested that the Western Canadian Basin was anisotropically stressed, that the holes themselves could concentrate and amplify the stress, and that the breakout long axes were parallel to σ_{Hmin} .

Subsequent authors also noted a similar alignment with σ_{Hmin} (Hottman *et al.*, 1979; Zoback and Zoback, 1980; Hickman *et al.*, 1985; Zoback *et al.*, 1985). Breakouts now are generally accepted to form due to the influence of the *in situ* stress field surrounding the borehole.

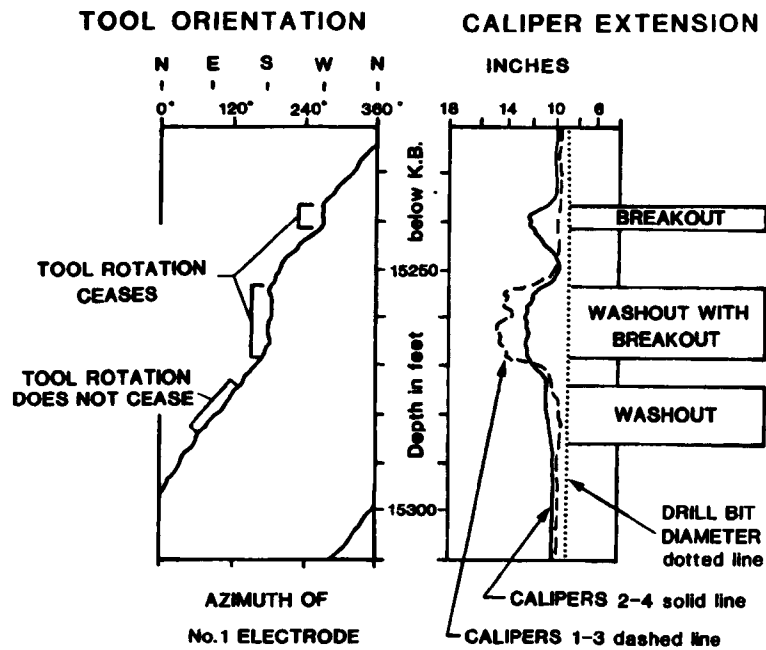


Figure 2.7 – Representation of a four-arm dipmeter caliper log showing how borehole breakouts are identified by coincident cessation of tool rotation and differential caliper extension (from Bell, 1990).

-
1. The tool must stop rotating
 2. Significant changes in conductivity should be recorded by all four pads.
 3. There should be no conductivity anomaly recorded by one or two pads.
 4. The large caliper curve should exceed hole gauge. The smaller should not be less than hole gauge and in trace should be straight.
 5. The larger diameter of hole elongation should not coincide with azimuth of hole deviation.
 6. The direction of the hole elongation should not coincide with azimuth of hole deviation.
-

Table 2.1 – Criteria for recognizing breakout on four-arm dipmeter logs
(adapted from Bell, 1990).

Besides the dipmeter (discussed above), several other downhole devices can be used for examining borehole breakout. These include: acoustic (BHTV/UBI) and electrical (FMS/FMI) borehole-imaging devices (Newmark *et al.*, 1984, Paillet and Kim, 1987, Hickman *et al.*, 1985; Plumb and Hickman, 1985, Zoback *et al.*, 1985, Barton, 1988, Barton *et al.*, 1988, Shamir *et al.*, 1988, Pezard and Luthi, 1988; Barton *et al.*, 1997).

Borehole televiewers (BHTV/UBI) are ultrasonic geophysical logging tools that were originally designed and developed by Mobil (Zemanek *et al.*, 1969 & Zemanek *et al.*, 1970). They provide a high-resolution detailed 360° record about borehole elongation and the distribution of natural discontinuities. The tool uses a rapidly rotating (~three revolutions per second) pulsed sound source, a piezoelectric transducer, which also has a fluxgate magnetometer, attached to help orientate the tool and the subsequent images (Rider, 1996, Prenskey, 1999). The BHTV/UBI transducer sends and receives the sound signal measuring both the amplitude of the reflected signal waveform (AMWF) and the two-way travel time waveform (TTWF) between the tool and the borehole wall at a resolution of 0.83 cm (Rider, 1996). These responses are processed by static normalisation into a colour or gray scale 'unwrapped' image log of the borehole. The cylindrical borehole surface image is unzipped at the north azimuth of the borehole and is rolled out into a flat strip (Figure 2.8). The BHTV/UBI records provide spectacular detailed records of breakouts. Breakouts cause distortion to the waveforms, due to an increase in the amount of discontinuities encountered around a breakout (Paillet and Kim, 1987).

Breakout is visible in the AMWF and TTWF image logs as vertical strips where poor reflectivity, long travel time or a loss of signal is encountered. The elongation of the borehole is identified best by the AMWF image log. The BHTV/UBI tools are more sensitive to borehole geometry than the electrical devices and can be processed to show borehole shape (Plumb and Hickman, 1985 & Newmark *et al.*, 1984; Figure 2.8). It is essential to ensure that the

tool is centered throughout its log run; otherwise, the waveforms generated can be distorted and attenuated, causing incorrect images of the borehole wall to be generated. Paillet *et al.* (1990), Rider (1996) and Prenskey (1999) give good in depth accounts and evaluations of the acoustic BHTV/UBI imaging tool.

The electrical imaging tools, the Formation MicroScanner (FMS) and the Fullbore Formation MicroImager (FMI), use an array of electrodes on orientated pads and flaps to produce an electrical image of the borehole wall that can be interpreted as either conductive or resistive features (Standen, 1991). The raw data (traces) acquired by the imaging tool must be corrected for variations of EMEX (Emitter Exciter) focusing current and the curves have to be equalized to compensate for variations in tool speed during logging (Harker *et al.*, 1990). This restored data is then individually assigned to one of 17 grey-levels or one of 256 colour shades (light = resistive; dark = conductive). The image created is then enhanced by either (Harker *et al.*, 1990):

- Static normalization – normalization of grey-scales over a large interval (400-500 ft). Shows gross resistivity variations.
- Dynamic normalization – normalization of grey-scale within a short (1-3 ft) sliding window. Enhances small resistivity variations.

An 'unwrapped' image log of the borehole is then produced (Figure 2.9). Breakout form long vertical strips showing areas of decreased resistivity, due to the increase in the discontinuities encountered within the borehole around a breakout (Figure 2.9). The FMS tool combines elements of both the four-arm dipmeter and BHTV/UBI tools (Ekstrom *et al.*, 1987; Bourke, 1989; Paillet *et al.*, 1990). The FMS consists of four orthogonal pads, which are pressed against the borehole surface (Rider, 1996). As with the BHTV/UBI a fluxgate magnetometer is employed to orientate the tool. This tool does not cover the whole diameter of the borehole (Table 2.2), the electrical response from the four orthogonal pads is processed to produce four narrow vertical 'strips' and has a vertical and horizontal resolution of 0.5 cm

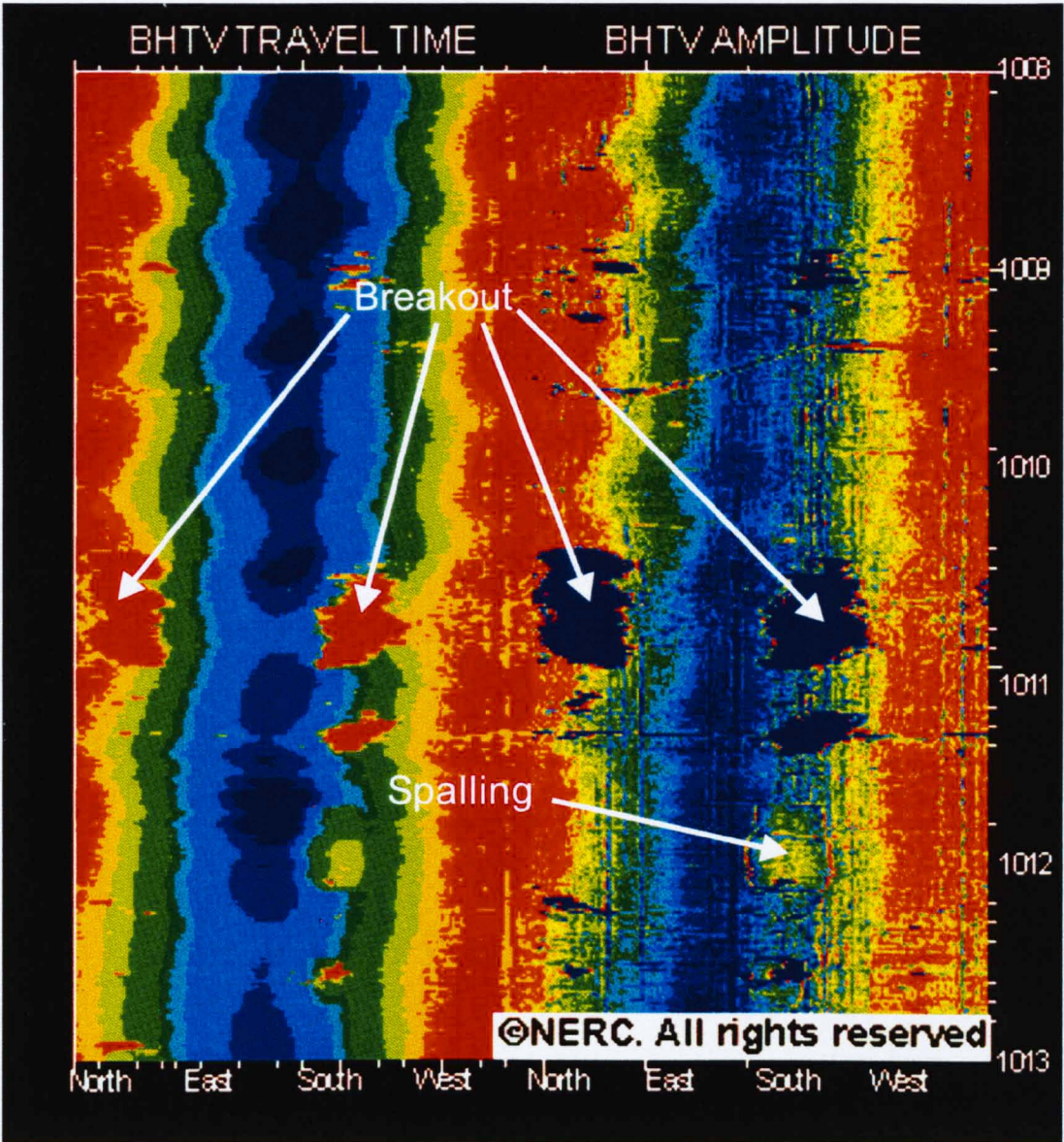


Figure 2.8 – a) Image of the borehole televiwer amplitude of the reflected signal waveform (AMWF) and the two-way travel time waveform (TTWF).

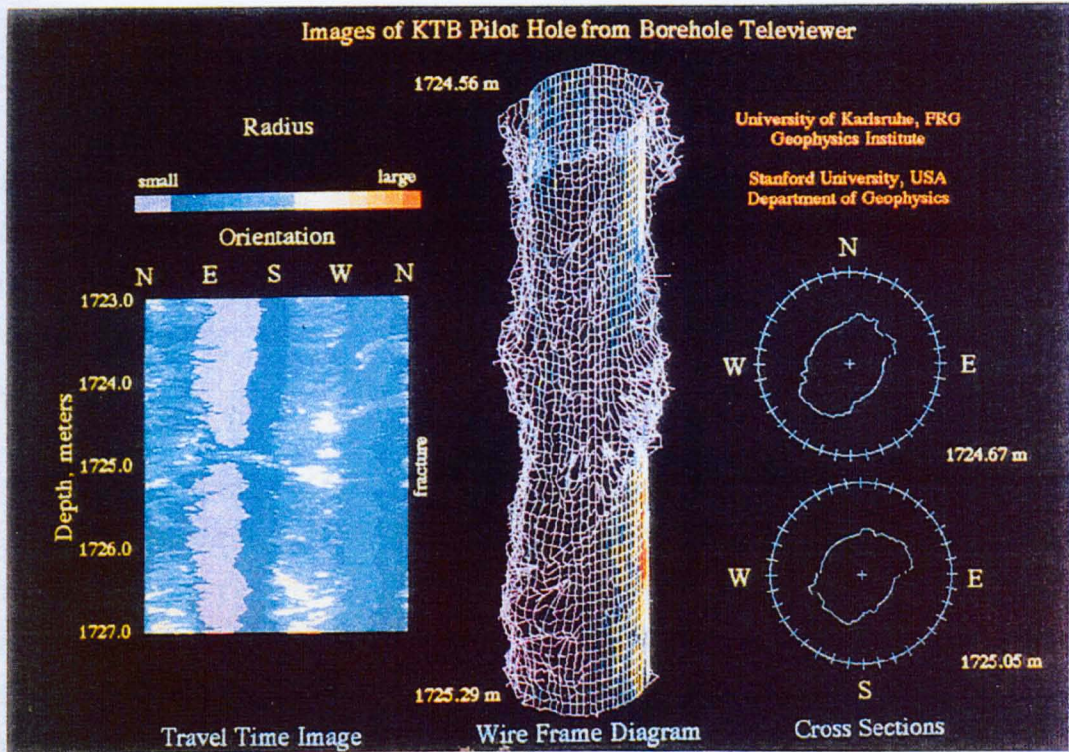


Figure 2.8 – b) Presentation of the borehole televiwer data showing the geometry of part of the KTB pilot borehole. Left: Travel time log of borehole section. Middle: Three-dimensional wire mesh diagram showing the borehole geometry. Colours on the wire frame indicate the amplitude of the reflected pulse (warmer colours indicate higher amplitude). Right: Cross-sectional shapes of the borehole at two depths (from Mastin *et al.*, 1989).

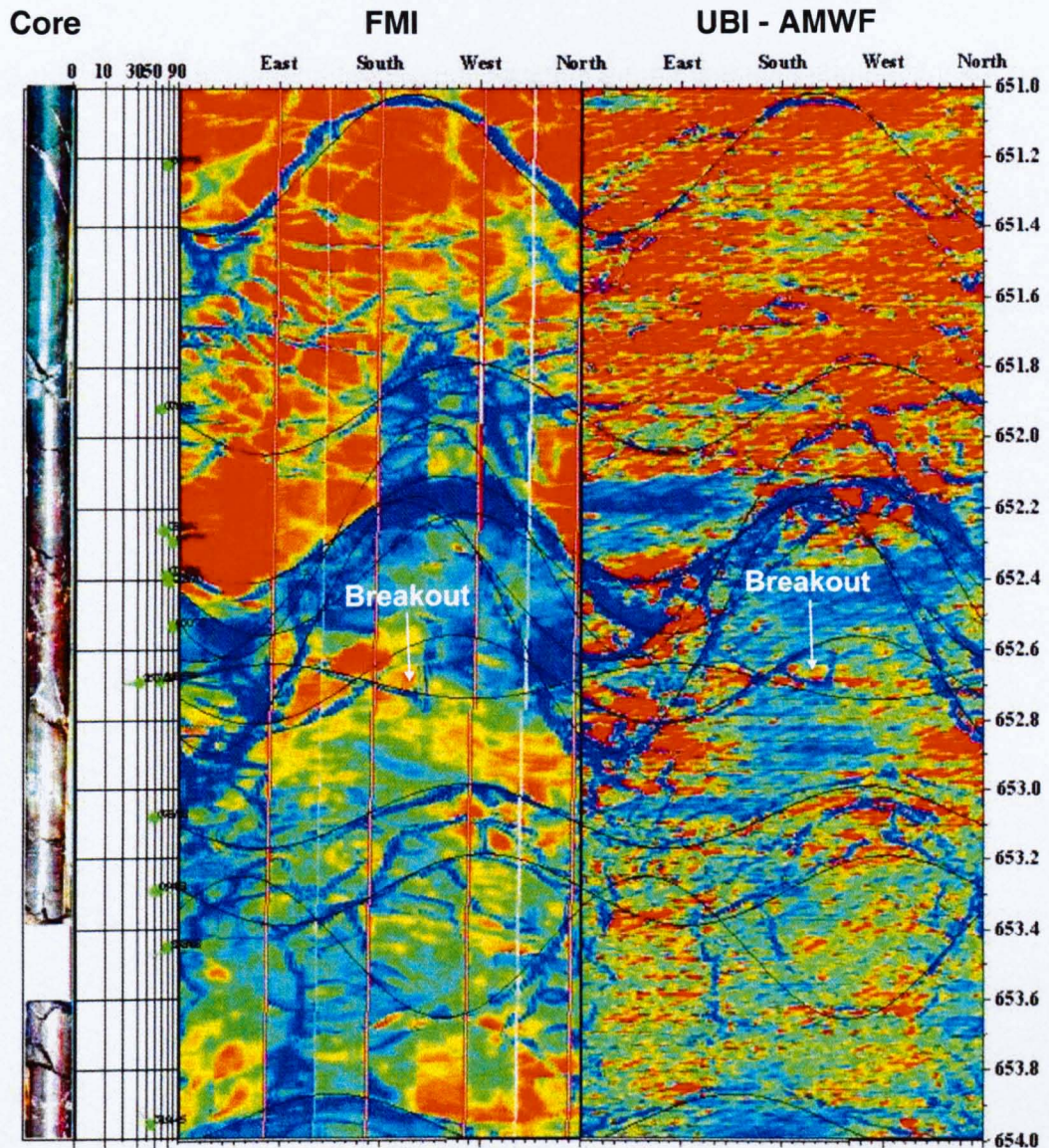


Figure 2.9 – A section of core, FMI and UBI imagery demonstrating breakout features seen within the BVG in Sellafield borehole RCF3 (651-654 mbRT).

The FMI tool has much better coverage of the borehole (Figure 2.9) than the FMS (Table 2.2), the electrical response produces four wide vertical 'strips' and a vertical and horizontal resolution of 0.25 cm. The FMI tool consist of four orthogonal pads each having a hinged flap, so as to extend the area of electrical contact against the borehole surface (Schlumberger, 1992; Rider, 1996). Paillet *et al.* (1990), Schlumberger (1992); Rider (1996) and Prenskey (1999) give a good account and evaluation of the electrical imaging tools.

The generation of breakout is based on the Kirsch equation (*Eq. 2.1*, section 2.2.3.3). Plumb and Hickman (1985) recognised four common borehole geometries, during interpretation of a dipmeter caliper log (Figure 2.10). An *in gauge* hole is dimensionally equal to the drill-bit, implying that failure has not occurred. A *washout* shows dimensions that increase in all orientations within the hole, resulting in cross-sectional enlargement. *Key seats* occur when the four-arm dipmeter is not centered in the borehole or the hole is pear shaped due to drill-pipe wear so that one caliper reading is less than the dip size. *Breakout* are the most common form of borehole failure geometry causing a one-diameter elongation of the borehole. Lofts and Bourke (1999) provide a detailed description of the various artifacts identified in acoustic (BHTV/UBI) and electrical, mirco-resistivity (FMS/FMI) image logs.

A number of researchers (Gough and Bell, 1982, Zoback *et al.*, 1985, Plumb and Luthi, 1989 & Zheng *et al.*, 1989) have looked into how to predict and model the shape, formation, development and eventual stabilization of borehole breakout. With the development of the acoustic (BHTV/UBI) image log, the problem of viewing the shape and form of the breakout was solved. Even though a variety of models have been proposed, a single unifying model has yet to be proposed. Controversy still exists as to the exact mode of failure that causes breakouts to form. A good discussion of these controversies can be found in Engelder (1993), Cowgill (1994) & Cuss (1998). Many modes of failure occur including tensile and shear failure at the azimuth of σ_{Hmin} occurring both at and behind the borehole wall.

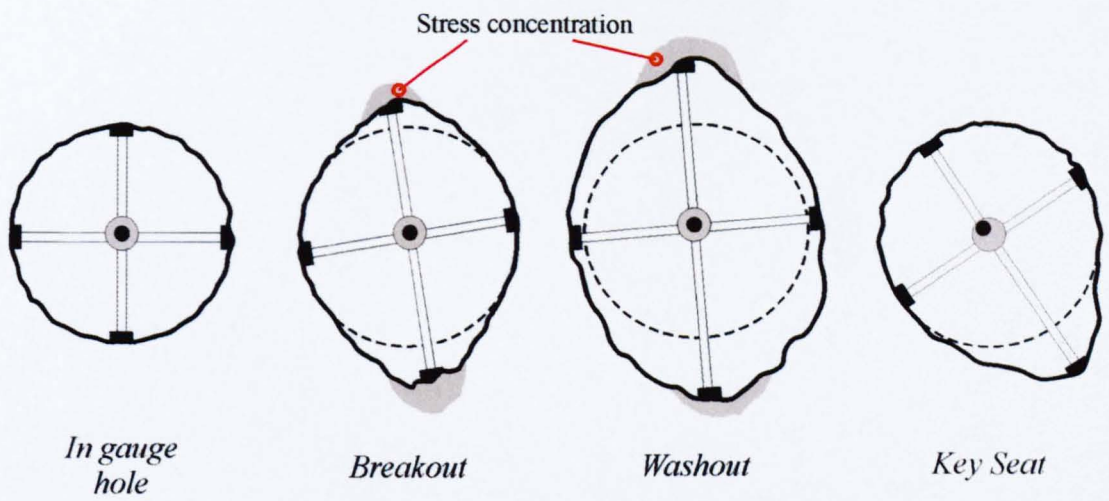


Figure 2.10 – The four common geometries of a borehole measured using a dipmeter caliper-logging tool (from Plumb and Hickman, 1985).

Tool	No of electrodes	Logging speed(m/h)	Hole diameter		
			6"	8.5"	12.25"
FMI 4 pad + flaps	192	550	90%	80%	50%
FMI 4 pad	96	1100	50%	40%	25%
FMS 4 pad	64	500	50%	40%	25%
FMS 2 pad	54	500	25%	20%	12%

Table 2.2 – Borehole circumference coverage of Schlumberger's electrical imaging tool, approximate percentages (adapted from Rider, 1996).

2.3 Regional Stress Map

2.3.1 Introduction

One area of research that has helped to advance an understanding of *in situ* stress globally has been the funding of large-scale stress map projects. In particular the World Stress Map (WSM), the European Stress Map (ESM) and to a lesser extent the UK Stress Map projects. All these investigations are described in more detail below.

2.3.2 World Stress Map

The World Stress Map (WSM) project is a global cooperative effort to compile and interpret data on the orientation and relative magnitudes of the contemporary *in situ* tectonic stress regime in the Earth's lithosphere (Zoback, 1992). The focus of this research was to try and characterize the state of stress within plates around the world (Figure 2.11).

Mary Lou Zoback initiated this project in 1986 as part of the International Lithosphere Program. Over 30 scientists from 18 countries around the world have been directly responsible for the collating this information (Zoback, 1992). As of 2000, the WSM had over 10920 *in situ* stress readings compiled into a digital WSM database (Mueller *et al.*, 2000). Since 1995, the WSM Project has been based at the Heidelberg Academy of Sciences and Humanities, with the WSM research group located at the Karlsruhe University within the Institute of Geophysics (Mueller *et al.*, 2000).

The stress data comes from four types of geological and geophysical sources to infer the tectonic stresses: earthquake focal mechanisms (63%); borehole breakout and drilling induced fractures (23%); *in situ* stress measurements - hydraulic fracturing and overcoring (9%); and young geological data - fault slip and volcanic alignment (5%) (Mueller *et al.*, 2000 - Figure 2.11). The quality ranking scheme developed by Zoback and Zoback (1989) has been applied to WSM data.

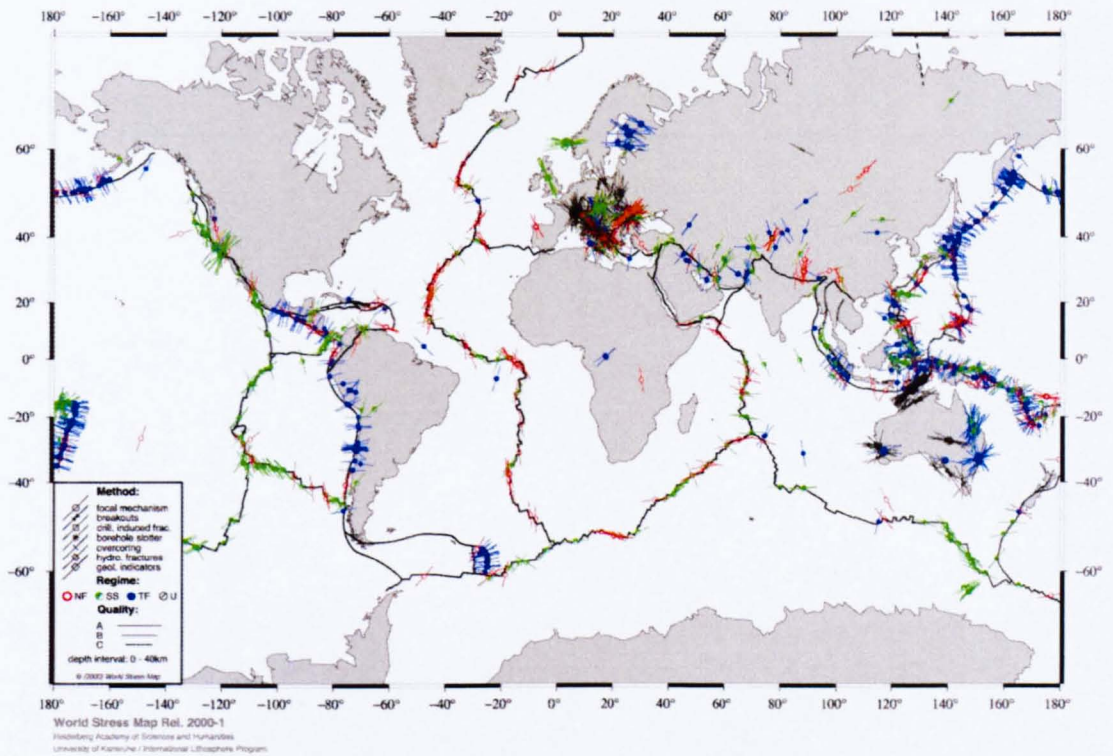


Figure 2.11 - The World Stress Map displaying the orientations of the maximum horizontal stress (σ_{Hmax}). The length of the stress symbols represents the data quality, with A as the best quality category. A-quality data are believed to record the orientation of the horizontal tectonic stress field to within 10° - 15° , B-quality data to within 15° - 20° and C-quality data to within 25° . D-quality data are considered to yield questionable tectonic stress orientations. The tectonic regimes are: NF for normal faulting, SS for strike-slip faulting, TF for thrust faulting & U for unknown regime (from Mueller *et al.*, 2000).

From the WSM, rotation of the stress field in various locations around the world was observed, due to tectonic forces acting on the plates (Zoback *et al.*, 1989). Smaller scale rotations of stress fields have also been observed around relatively large and small-scale faults and fractures. Structurally controlled local stress rotations were first suggested by data presented by Springer (1987). Rotation of the horizontal stress field in the vicinity of the San Andreas fault is particularly well documented by Zoback *et al.* (1989). Bell (1989) also identified rotations relative to faults in the Scotian Shelf. Shamir and Zoback (1989) noted gradual and fractured changes in the breakout orientation observed in the Cajon Pass research borehole in California. They interpreted these local perturbations of the stress field, as areas where the borehole intersected fractured zones. Rawnsley *et al.* (1992) discovered a similar association when investigating discontinuity development in perturbed stress fields. They concluded that joint patterns were perturbed near faults. A comprehensive study by Barton and Zoback (1994) investigated stress perturbations associated with active faults and concluded these perturbations were associated due to slip on active faults.

2.3.3 European Stress Map

Before 1986, European measurements of rock stress were very scarce (Brereton and Mueller, 1991). The development of borehole breakout (section 2.2.3.3) has assisted in the dramatic increase in the geographical distribution of rock stress orientations. A number of collaborative projects between the British Geological Survey (BGS), the Geophysikalisches Institut of the University of Karlsruhe (GIK) and the Institut de Physique du Globe de Paris (IPG) have been undertaken to help aid in the determination, prediction and interpretation in situ rock stress within Europe (Brereton *et al.*, 1993). From this collaboration, a European Stress Map (ESM) and database were produced (Figure 2.12). This research has been closely related to the WSM project. As you can see from Figure 2.12 much of north-western Europe has a broadly consistent NW-SE ($135/315^\circ$) maximum compressive stress orientation from the Alps to the north of the UK.

The correlation of stress orientations with the stress trajectories of plate motion suggest that the stress field is caused by forces associated with the east to southeasterly separation of Europe from North America and the north to northeasterly movement between the African plate and Europe (Brereton *et al.*, 1993). Although the current data coverage for other areas in Europe is good (Figure 2.12), the tectonic stress regime is still relatively unknown and therefore further detailed interpretation is difficult to undertake.

2.3.4 UK Stress Map

Until comparatively recently, very few stress measurements had been made in the UK and knowledge of the state of stress in UK was limited. Klein and Brown (1983) produced the first UK stress map. They only had six sets of measurements, which were generally poor quality (Evans, 1987).

Until recently the only high quality, horizontal stress direction and magnitude determinations had come from the Camborne School of Mines Hot Dry rock programme at the Rosemanowes Quarry in the Carnmenellis Granite, Cornwall (Pine *et al.*, 1983a; Batchelor and Pine, 1986). Here sixteen hydraulic fracture tests were carried out from the near surface to a maximum depth of 2550 metres. A series of overcoring tests were also undertaken at the South Crofty Mine on the edge of the Carnmenellis Granite at a depth of 790 metres (Pine *et al.*, 1983b). At roughly the same time, an unrelated project was investigating the stress field at a quarry at Carwynnen (Cooling and Hudson, 1986). All these tests suggest a regional NW-SE (135/315°) maximum stress orientation.

Evans (1987) compiled a report into the crustal stress in the UK, as part of the Geothermal Resources Program at the British Geological Survey (BGS). He reviewed all stress measurements taken in the UK and documented the results from some new breakout analysis and hydraulic fracture tests carried out by the BGS. Evans (1987) produced the first comprehensive UK stress map (Figure 2.13) and confirmed a compressive NW-SE (135/315°) regional trend for the maximum stress orientation.

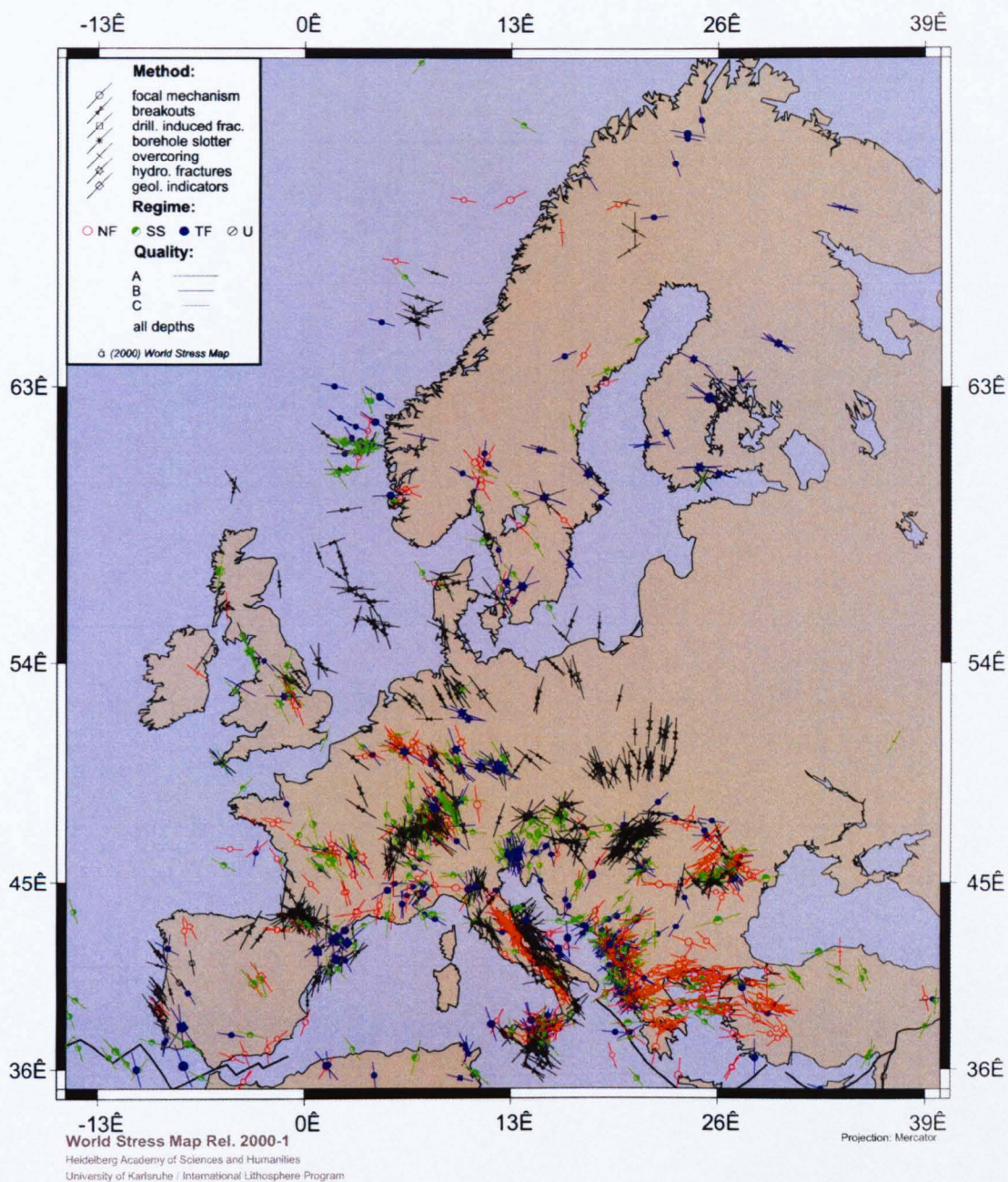


Figure 2.12 – The European Stress Map displaying the orientations of the maximum horizontal stress (σ_{Hmax}). The length of the stress symbols represents the data quality, with A as the best quality category. A-quality data are believed to record the orientation of the horizontal tectonic stress field to within 10° - 15° , B-quality data to within 15° - 20° and C-quality data to within 25° . D-quality data are considered to yield questionable tectonic stress orientations. The tectonic regimes are: NF for normal faulting, SS for strike-slip faulting, TF for thrust faulting & U for an unknown regime (from Mueller *et al.*, 2000).

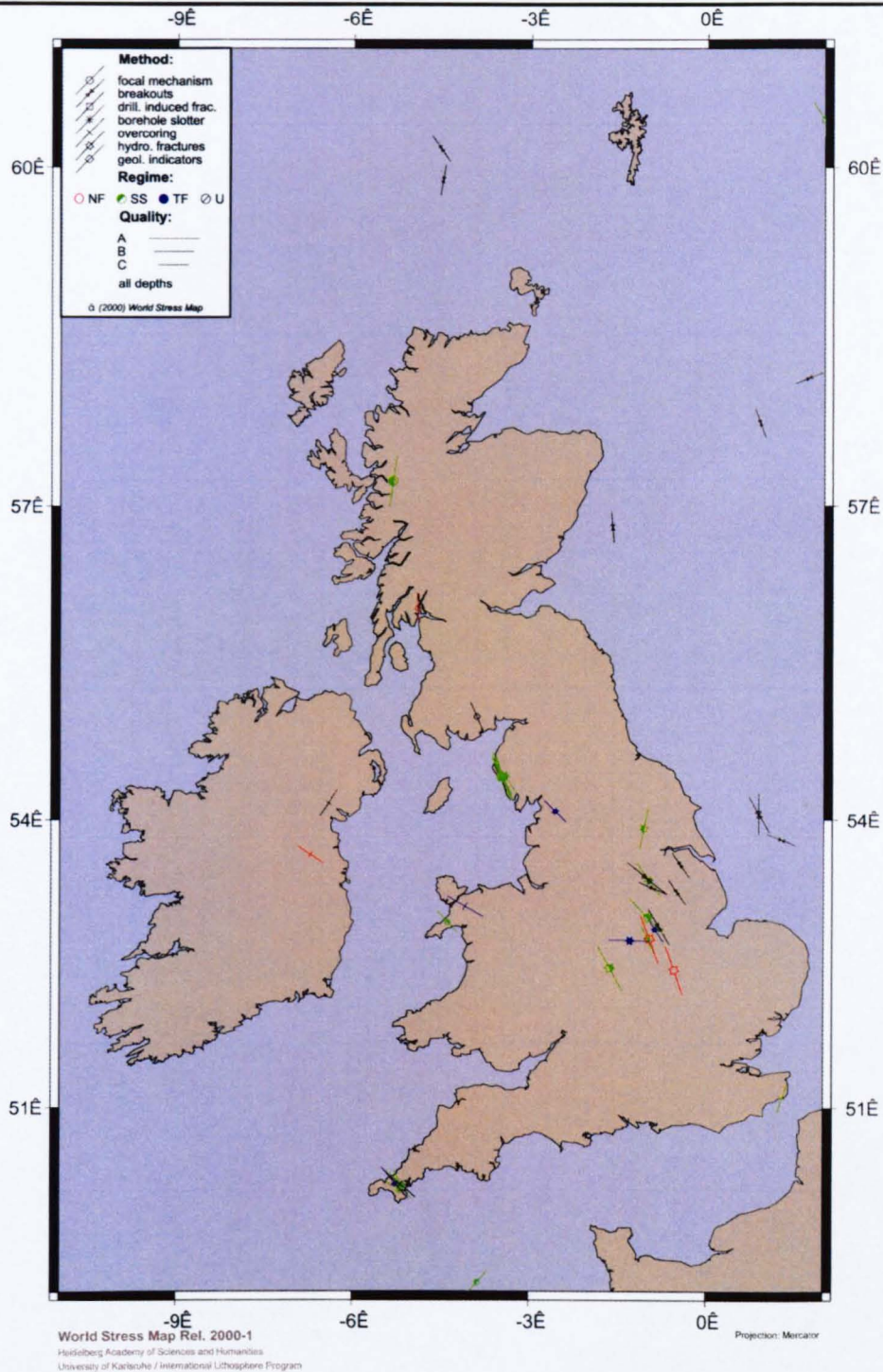


Figure 2.13 – The UK Stress Map displaying the orientations of the maximum horizontal stress (σ_{Hmax}). The length of the stress symbols represents the data quality, with A as the best quality category. A-quality data are believed to record the orientation of the horizontal tectonic stress field to within 10° - 15° , B-quality data to within 15° - 20° and C-quality data to within 25° . D-quality data are considered to yield questionable tectonic stress orientations. The tectonic regimes are: NF for normal faulting, SS for strike-slip faulting, TF for thrust faulting & U for an unknown regime (from Mueller *et al.*, 2000).

Evans also noted bimodal variations (NW-SE and W-E) from the regional trend, and concluded that these originated from multiple tectonic events that occurred in the geological past. Also identified was a possible decoupling effect (Figure 2.14) in the regional stress field with depth, at approximately 760 metres below ground level. Evans concluded that this was due to the minimum stress changing from vertical to horizontal. There is insufficient evidence to infer any directional change in the horizontal stress field at this decoupling level, but a sudden change in the magnitude of the stress with depth has been shown by Haimson (1982) to coincide with a change in the direction of the principal stresses. Evans also noted that large deviatoric stress was created by the orders of magnitude difference between the maximum and minimum horizontal principal stresses. Shear stresses in the UK are therefore sufficiently high to require only the pore pressure to be hydrostatic for critical differential stress to develop below 2km. At this point, faulting could occur on favorably orientated pre-existing faults, i.e. strike-slip faulting (Evans, 1987). It is therefore not surprising that two of the fault plane mechanism solutions displayed on the UK stress map (Figure 2.13) demonstrate strike-slip motion within the middle-upper crust (0-20 km).

The UK stress map has now been incorporated into the European and World stress map databases. Recent oil and gas exploration in the North Sea (Cowgill, 1994) has greatly expanded the information available and helped to develop and expand the UK stress map.

2.4 Characterisation of Discontinuities

Discontinuities are significant mechanical breaks (brittle deformation features) in rock masses. They originate from strains that arise from stress concentrations around flaws, heterogeneities and physical discontinuities (Anon, 1996). They form in response to lithostatic, tectonic and thermal stresses, together with high fluid pressures. Stress heterogeneities control the initiation and propagation of individual discontinuities and the localization and clustering of discontinuity systems/networks.

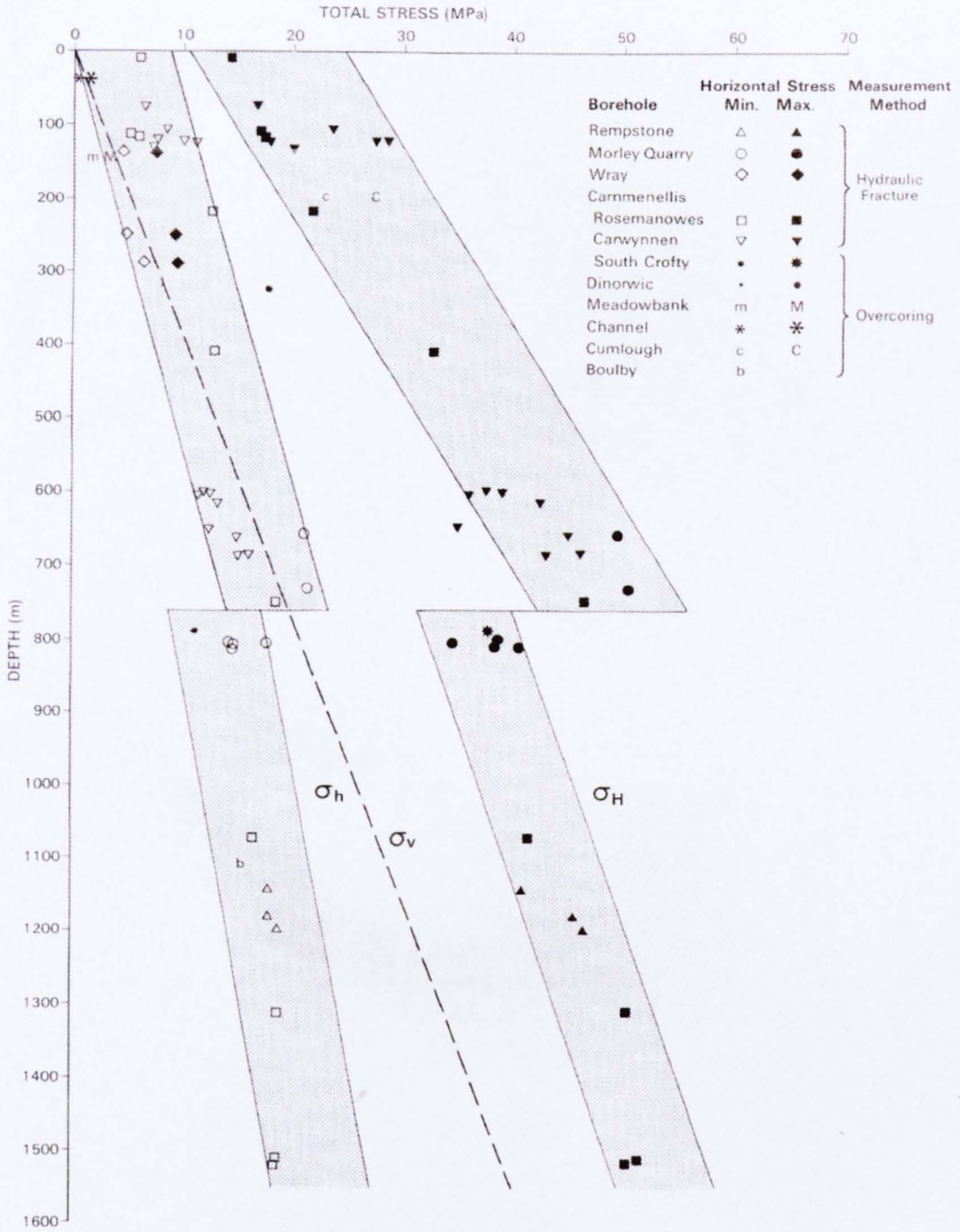


Figure 2.14 – Summary of the *in situ* stress measurements in the UK (from Evans, 1987).

Rock properties play an important role in the formation of discontinuities and in the structure of discontinuity zones. Discontinuities occur on a variety of scales, from microscopic to continental (Anon, 1996). The term discontinuity makes no distinction concerning the age, geometry or mode of origin of the feature (Priest, 1993). Throughout this thesis, mechanical breaks identified in the rock mass are called discontinuities. In many cases it is helpful to distinguish between natural discontinuities, which are geological or geomorphological in origin, and artificial discontinuities, which are created by activities such as drilling (section 2.2.3.3). Natural discontinuities can be divided into four basic groups (Figure 2.15):

1. dilating discontinuities (mode I);
2. shearing discontinuities (shearing mode II);
3. closing discontinuities (shearing mode III);
4. natural geological formation break (e.g. bedding plane) shown by a change in grain size, grain orientation, mineralogy or chemistry (Priest, 1993).

Dilating discontinuities can be idealized as two rough surfaces with tensile displacement. Surfaces have moved away from each other in a direction perpendicular to the surface, in plane shear (Anon, 1996). Shear discontinuities, which are also referred to as faults, are shear displacements that occur predominately parallel to the discontinuity surfaces. This relative movement is either perpendicular (mode II) or parallel (mode III) to the discontinuity front. Discontinuities can form with a combination of these modes (mix-mode discontinuities). Rock masses with complex deformation histories have discontinuities produced by two or more of these modes in a sequential manner (Anon, 1996).

Discontinuities initiate and propagate when the stresses becomes equal to the strength of the rock. Essential to understanding how a discontinuity begins and propagates are the concepts of stress concentration (section 2.2.3.3), amplification and energy balance (Anon, 1996).

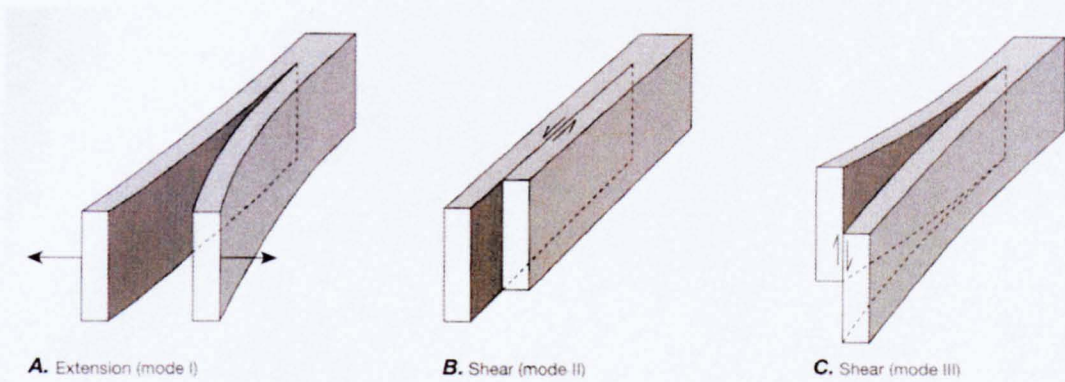


Figure 2.15 – The distinctions between the major types of natural discontinuities. A) Dilating, or mode I. The relative displacement is perpendicular to the discontinuity. B) Shear, mode II. Relative displacement is a sliding parallel to the discontinuity and perpendicular to the edge of the discontinuity. C) Closing, mode III. Relative displacement is sliding parallel to the discontinuity and to the edge of the discontinuity. D) Natural geological formation break, bedding plane (from Twiss and Moores, 1992).

Griffith (1921) showed experimentally how glass fractured at an applied stress level, much lower than the predicted theoretical strengths. Griffith (1921) attributed this to the amplification of stress around flaws in the glass, which are known as stress concentration (section 2.2.3.3). Regional stress fields are generally insufficient to initiate discontinuities. As a result, heterogeneous stress concentrations are generally necessary for discontinuity propagation (Anon, 1996). Such concentrations are abundant in the Earth's crust. Hence, the heterogeneity and textures in rocks often cause pervasive heterogeneity in the stress field. Once initiated the discontinuities significantly alter the stress field in the adjacent rock.

The first step to understanding and predicting the behavior of discontinuities involves the identification and location of discontinuities. Discontinuities can be detected remotely by various means, ranging from simple extrapolation of surface observations to more sophisticated geophysical seismic and electromagnetic soundings (Anon, 1996). Discontinuity detection can be divided up into three distinct scales:

1. large-scale associated with surface geophysical surveys,
2. intermediate-scale associated with surface-to-borehole and borehole-borehole soundings, and
3. small-scale associated with measurements made on rocks immediately adjacent to a borehole or tunnel.

Table 2.4 provides a general list of the methods available for fracture detection. Further detailed descriptions of geophysical and non-geophysical discontinuity detection is given in Anon (1996) and more detail on the geophysical techniques is also laid out in Schlumberger (1989).

Only the single borehole methods are applicable to this research, in particular acoustic (BHTV/UBI) and electrical (FMS/FMI) geophysical imaging tools. Both these methods provide a direct and effective method for detecting discontinuities in boreholes.

Methods	Length Scale of Investigation & [Resolution]	Location technique used at
Elastic methods: seismic band (10-100 Hz)	100-5000 m	
P-wave reflection (2D)	[1-2 (velocity)] [1/4 (amplitude)]	Surface
P-wave reflection (3D)	[1-2 (velocity)] [1/8 (amplitude)]	Surface
S-wave reflection (2D)	[1-2 (velocity)] [1/4 (amplitude)]	Surface
P-wave vertical seismic profiling (VSP) (including offset, reverse)	<1 (velocity)]	Borehole-Borehole/ Borehole-Surface
S-wave vertical seismic profiling (VSP) (including offset, reverse)	<1 (velocity)]	Borehole-Borehole/ Borehole-Surface
P-wave tomography	10-100 m [1/2 (velocity)]	Borehole-Borehole/ Borehole-Surface
Cross-hole reflections	10-100 m [1/2 (velocity)]	Borehole-Borehole/ Borehole-Surface
Coupled methods	10-5000 m [1/2 (velocity)]	Borehole-Borehole/ Borehole-Surface
Elastic methods: sonic band (2-20 Hz)	0.1-10 m	
P-wave transmission (acoustic Log, ID)	[1-2 (velocity)] [1/2 (amplitude)]	Borehole-Borehole/ Borehole-Surface
Acoustic waveform Log P and S	[1-2 (velocity)] [1/2 (amplitude)]	Single Borehole
Acoustic emissions	10-100 m {1-10 m}	Borehole-Borehole/ Borehole-Surface
Elastic methods: ultrasonic band (200-2000 kHz)	0.1-5 m	
Borehole televiewer (BHTV/UBI)	10-30 cm [0.3-5 cm]	Single Borehole
Electrical methods	10-300 m	
Electric sounding	[1-10 m]	Surface
Electric profiling	[1-10 m]	Surface
Electric resistivity tomography	[1-10 m]	Borehole-Borehole/ Borehole-Surface
Electrical borehole imaging device (FMS/FMI)	[0.1-3 cm]	Single Borehole
Electromagnetic methods	[10-300 m]	
Electromagnetic sounding	[3-10 m]	Surface
Electromagnetic profiling	[3-10 m]	Surface
Electromagnetic tomography	[3-10 m]	Borehole-Borehole/ Borehole-Surface
Radar methods	[3-100 m]	
Ground-penetrating radar (reflection)	[0.1-5 m]	Surface
Borehole radar (reflection)	[1-5 m]	Borehole-Borehole/ Borehole-Surface
Radar tomography (transmission)	[2-10 m]	Borehole-Borehole/ Borehole-Surface
Conventional well logs	0.1-10 m	
Neutron log	[0.1 m]	Single Borehole
Resistivity log	[0.1 m]	Single Borehole
Density log	[0.1 m]	Single Borehole
Gamma log	[0.1 m]	Single Borehole
Caliper log	[0.01 m]	Single Borehole
Temperature log	[0.01 m]	Single Borehole
Fluid conductivity log	[0.01 m]	Single Borehole
Fluid replacement log	1-100 m [1-10 m]	Single Borehole
Geological observations	0.1-500 km	
Satellite airborne imaging	1-500 km [1-100 m]	Surface
Core inspection	[0.1-10 cm]	Single Borehole
Optical imaging	[0.1-10 cm]	Surface
Tiltmeter methods	100-2000 m	Borehole-Borehole/ Borehole-Surface
Flowmeters	1-100 m	
Heat-pulse flowmeter	[1-10 m]	Single Borehole
Electromagnetic flowmeter	[1-10 m]	Single Borehole
Acoustic doppler flowmeter	[1-10 m]	Single Borehole

**Table 2.3 - Geophysical techniques available for fracture detection
(from Anon, 1996).**

The BHTV/UBI tool enables an acoustic image of the borehole wall to be logged; section 2.2.3.3 describes how the BHTV/UBI tool works to produce an image of the borehole wall. The intersection of a discontinuity within the borehole wall scatters acoustic energy, producing dark sinusoidal features on the image log (Figure 2.16b). When the image log is viewed, these sinusoidal features can be identified (Figure 2.16b). By using sine wave fitting routines and simple trigonometry, the azimuth and dip of the discontinuity can be deduced (Figure 2.17c). Software has been developed by a number of companies (British Geological Survey – FMSBHTV, Reeves Wireline – PC ImagePro, Baker Atlas - VISION), to allow the ‘picking’ of image sine waves through a whole image log, enabling the dip and azimuth to be automatically generated by the specialist software (Torres *et al.*, 1990; Prosser *et al.*, 1999). Most of the modern BHTV/UBI tools have enabled the true orientation of the discontinuity to be deduced by correcting the calculated discontinuity orientation from the orientation of the borehole and for the deviation between local magnetic field and true north (Anon, 1996). The fluxgate magnetometer is employed on the BHTV/UBI tool to orientate the tool/borehole. The benefit of the acoustic method for discontinuity analysis over other electrical imaging tools is that the acoustic tool gives a full 360° coverage. This is essential when studying discontinuities, which are often irregular, branching and non-planar features (Laubach *et al.*, 1988). The BHTV/UBI detects discontinuities down to a resolution of 0.05 cm to 0.10 cm, while two discontinuities must be separated by about 0.80 cm to be recognised (Dudley, 1993). In core to image comparisons, the logs are seen to detect perhaps only 25% of all discontinuities although possibly 50% of the larger, more important ones with apertures above 0.05 cm are recognised (Dudley, 1993). The apparent thickness of the sinusoidal feature identified on the BHTV/UBI image log may be taken as a qualitative indicator of discontinuity ‘size’ or aperture. This thickness depends on the discontinuity aperture, the beam width of the image tool and represents the discontinuity where it has been affected by the effects of drilling (spalling, chipping and erosion of the discontinuity).

For these reasons, the interpretation of fractures using BHTV/UBI image logs is at best semi-quantitative (Anon, 1996). Due to the effects of drilling, it is important to also identify the type of discontinuity. As more image logs become available, it is clear that drilling induced discontinuities are far more common than was originally thought (Lincecum *et al.*, 1993). Table 2.3 identifies different types of artifacts that can occur on BHTV/UBI image logs. One aspect that can help to identify those naturally occurring discontinuities is whether the feature has opened or closed or is mineralized. Comparison between the amplitude of the reflected signal (AMWF) and the two-way travel time (TTWF) images can suggest whether a discontinuity is open or mineralized: open discontinuities have an image on both logs, mineralized discontinuities on only the AMWF image (Taylor, 1991). Discontinuities that are mineralized and in filled with weak materials (e.g. chlorite, feldspars) can be heavily effected an eroded away by the drilling of the borehole. This can therefore cause the identification of open or mineralized discontinuities to be ambiguous. Interpretation of BHTV/UBI image logs in massive crystalline rocks (Figure 2.16b) provide a uniformly reflective borehole wall, making an ideal background for discontinuity identification (Paillet *et al.*, 1985). Discontinuity interpretation in sedimentary rocks is much more difficult due to the sediments having less acoustic reflectivity, a more variable background reflectivity (especially in bedded sedimentary rocks) and generally more extensive drilling damage due to the rocks being friable (Paillet *et al.*, 1985).

The FMS/FMI tool gives an electrical image of the borehole wall (Figure 2.16a); section 2.2.3.3 describes how the tool works to produce an image. This tool is designed to focus small beams of electrical current into the borehole wall (Ekstrom *et al.*, 1987). It measures the ease with which this electrical current enters the borehole walls. Sharp electrical contrasts occur in the borehole image where either pore fluids act as good conductivity/flow paths or where discontinuities are open and filled with drilling fluid, cemented or have associated displacement or show some geometrical relationship such as high dip in a sequence with low structural dip (Rider, 1996).

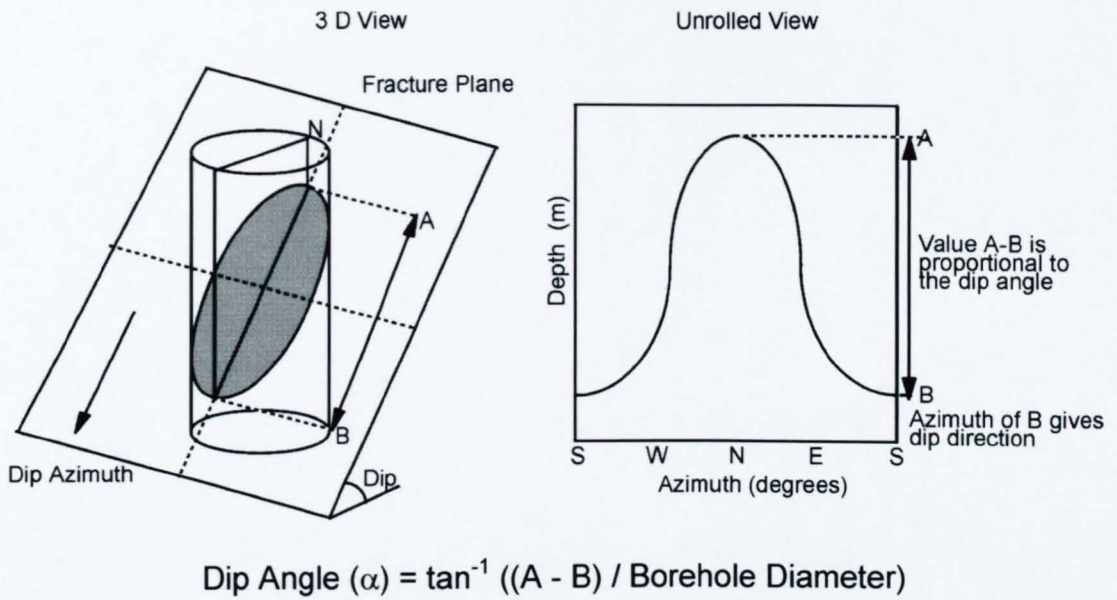


Figure 2.16c – Schematic illustration of how a discontinuity’s orientation is calculate from the sine wave viewed on a BHTV/UBI or FMS/FMI image log (Figure 2.16a/b) of the borehole.

If Chlorite or other alteration minerals are encountered, minerals that have adhered water in their chemical bonds, within a discontinuity will have a low resistivity (high conductivity) image recorded. This can therefore cause ambiguous identification of opened and filled mineralized discontinuities. By using sine wave fitting routines and specialist image log software (discussed above – Figure 2.16c), the dips and azimuths of picked discontinuities can be generated. Care needs to be taken when analysing discontinuities using either the FMS or FMI image tools, as they do not produce a complete image of the borehole (Table 2.2) like the BHTV/UBI image tool. The FMS tool has vertical and lateral resolution in the order of 0.50 cm (Paillet *et al.*, 1990). As with the BHTV/UBI discontinuities, apertures have also been modeled, quantitatively using the FMS image tool (Plumb *et al.*, 1985; Luthi and Souhaite, 1990; Hornby *et al.*, 1992). Plumb *et al.* (1985) concluded from their study that discontinuities with apertures of less than 0.10 cm could be detected. This compares to Laubach *et al.* (1988) who concluded from their investigation of the Travis Park Formation, East Texas, that discontinuities with apertures less than 0.03 cm could be detected by the FMS tool. Luthi and Souhaite (1990) successfully traced discontinuities apertures in the Moodus basement, Connecticut. Apertures as small as 10 μ m were detected and discontinuities as little as 1cm apart were resolved. As discussed above for the BHTV/UBI image log, the discontinuity aperture can be enhanced by the effects of drilling (spalling, chipping and erosion of the discontinuity). For these reasons, the interpretation of a discontinuities aperture using the FMS/FMI image log is at best semi-quantitative. 'Artifacts' formed due to the effects of drilling need to be identified. Lofts and Bourke (1999) identified different types of 'artifacts' that can occur in FMS/FMI image logs. The FMS/FMI tool was originally developed by Schlumberger for use in sedimentary sequences. Numerous authors (Dennis *et al.*, 1987; Ekstrom *et al.*, 1987; Laubach *et al.*, 1988; Bourke, 1989; Heliot *et al.*, 1989; Plumb and Luthi, 1989; Lehne, 1990; Standen, 1991) have used these tools to image sedimentary formations.

Other authors (Pezard and Luthi, 1988; Luthi and Souhaite, 1990; Hornby and Luthi, 1992; Hornby *et al.*, 1992; Pezard *et al.*, 1992; Gentier and Hopkins, 1997; Lovell *et al.*, 1997) have also used this tool successfully in igneous formations.

2.4.1 Biased Sampling of Discontinuities

Methods that probe deeply into the subsurface have a poor ability to spatially resolve the locations of all discontinuities and generally form biased data sets influenced by the orientation in which the sampling of the discontinuities was undertaken (Priest, 1993). One of the first to analyse this bias was Terzaghi (1965), who advocated the application of a geometrical correction factor based on the observed angle of between the sampling line (borehole) and the normal to a particular discontinuity. The key to characterizing a fractured rock mass, which is sampled by a borehole, is to ensure that a sufficient number of boreholes are drilled at varying orientations (Terzaghi, 1965). This ensures that no discontinuity is under sampled. This effect must always be considered when collecting discontinuity data for analysis and interpretation of a rock mass. Terzaghi (1965); Baecher (1983) and Priest (1985) provide a good summary of the techniques used to counteract sampling bias.

2.5 Hydrogeological Characterisation

Hydrogeological investigations of fractured rock masses hinge upon trying to understand a complex flow system within a poorly defined volume. A fundamental step to understanding and predicting the behavior of discontinuities involves the identification of hydraulically significant discontinuities within the rock mass. Such discontinuities are the main conduits for the flow of fluids and can be connected to other hydraulically conductive discontinuities to form systems or networks. Conductive discontinuity networks may include a large number of interconnected hydraulically active features or may be limited to a very small proportion of the total discontinuity population.

One way that the hydraulic properties of fractured rock masses can be assessed is by using geophysical logging techniques. One of the earliest reports on these applications, Keys and MacCary (1971), is still a standard reference for groundwater investigations (now republished in Keys, 1988 & Keys, 1990). With the recent increased interest in groundwater contamination (actual or potential) and the use of groundwater as water source, considerable advancement has been made in groundwater geophysical logging, with logging of both fluid (fluid resistivity/conductivity, temperature, flow and geochemistry) and formation properties (natural gamma, density and porosity). A British Standard guide for "Geophysical Logging of Boreholes for Hydrogeological Purposes" was produced in 1988 (Anon, 1989). There has also been a Working Party Report produced by the Engineering Group of the Geological Society of London (Anon, 1988). Both these reports give a good outline of the techniques required for hydrogeological analysis in rock masses. Table 2.4 sets out a good summary of the suggested methods required when undertaking a geophysical hydrogeological investigation and discusses their uses.

Rider (1996) provides further detailed information on the various logging methods discussed above. Specialist hydrogeological testing was undertaken at Sellafield (section 1.2.1), and some of the data sets from these studies have been used in this thesis. The techniques used to derive the data and the data sets themselves are discussed in more detail in section 5.2.

2.6 Stress, Fractures & Flow

Discontinuities have long been recognized as playing an important role in controlling hydraulic properties of rock masses by providing permeable conduits for fluids (Finkbeiner *et al.*, 1997). Analysis of drill core or borehole imagery logs may reveal the presence of hundreds or even thousands of discontinuities.

Targets: Porosity, permeability, groundwater quality, fracturing, geological correlation

Constraints: Deep investigations have to be mud drilled with oilfield techniques. Old boreholes often cased with limited slotted or perforated sections.

Natural Gamma	Universal applications for geological correlation and fault determination in or between bedded strata. Clay content of strata and variation in sandstone matrices.
Resistivity	Most widely used technique for determining potential production zones.
Guard Resistivity or Laterolog	Originally developed to operate in highly saline environments. The focused measurement is indicative of formation resistivity.
Acoustic Borehole Imager	Orientation and location of discontinuities. Useful with hydrogeological logs for identifying flowing discontinuities.
Induction	As with resistivity above. Can only operate in dry hole and oil based muds.
Neutron/Neutron	Rock mass assessment and porosity indicator in known lithologies.

Table 2.4 – Summary of suggested geophysical methods used in hydrogeological investigations.

However production logging and experience demonstrates that only a relatively small proportion of these discontinuities contribute to fluid flow in the borehole (Long *et al.*, 1991). Heffer and Lean (1993) demonstrated a strong empirical relationship between the flow of fluid (flooding directionality) within a fractured rock masses and the prevailing stress field. Experimental work by Wilbur and Amedei (1990) suggest that the transmissivity of a discontinuity varies with the normal stress acting on it. This suggests that discontinuities orientated normal to σ_{Hmin} are most conductive (Jolly *et al.*, 2000), as they experience the lowest normal stress (Figure 2.17).

An alternative theory suggests that these discontinuities that are actively undergoing shear are most conductive (Barton *et al.*, 1995). Subsequent authors have applied and tested this theory (Barton *et al.*, 1997; Finkbeiner *et al.*, 1997; Hickman *et al.*, 1997; Ito and Zoback, 2000; Rogers, 2000; Talbot and Sirat, 2001; Rogers and Evans, in press). In their research, Barton *et al.* (1995) examined the relationship between discontinuity permeability, discontinuity orientation and the state of *in situ* stress. They evaluated the resultant shear (τ) to effective normal (σ_n) stresses acting on a discontinuity plane and represented these results on a σ_v normalized Mohr circle of the current stress regime (Jaeger, 1969 - Figure 2.18). Barton *et al.* (1995) assumed that if a discontinuity plane was optimally orientated to the stress field (Figure 2.18) and had a coefficient of friction (μ) $\mu \geq 0.6$, frictional failure of the discontinuity could occur. The Coulomb failure criterion for frictional sliding (Jaeger, 1969) was applied. From this analysis Barton *et al.* (1995) showed that the permeability of discontinuities that were 'critically' stressed for frictional failure had much higher permeability's than discontinuities not 'critically' stressed in the current stress field (Figure 2.18). They concluded that discontinuities close to localised shear failure were acting as potentially active faults. The Coulomb frictional failure criterion is represented as

$$\tau = \mu(\sigma_n - P_p).$$

Eq.2.3

Where μ is the coefficient of friction and P_p is the hydrostatic pore pressure (Jaeger, 1969). Frictional sliding will occur on a discontinuity plane with a ratio of shear to effective normal stress of $\geq \mu$. Generally, μ is thought to be in a range of 0.6 to 1.0 (Byerlee, 1978). Byerlee (1978) compiled a wealth of shear test data containing a wide range of rocks and discontinuity types. He concluded that discontinuities experiencing a normal stress greater than 200 MPa (i.e. 5 - 6 km depth) are well constrained during shear failure by using a coefficient of friction of between 0.6 to 1.0.

The shear (τ) and normal (σ_n) stresses acting on a plane of a discontinuity (Figure 2.18) are given as a function of the three principal stresses ($\sigma_1, \sigma_2, \sigma_3$):

$$\tau = \beta_{11}\beta_{21}\sigma_1 + \beta_{12}\beta_{22}\sigma_2 + \beta_{13}\beta_{23}\sigma_3 \quad \text{Eq.2.4}$$

$$\sigma_n = \beta_{11}^2\sigma_1 + \beta_{12}^2\sigma_2 + \beta_{13}^2\sigma_3$$

(see Jaeger and Cook, 1984 or Priest, 1993 for full derivation), where β_{ij} are the direction cosines between the normal to the discontinuity plane and the axes of σ_1, σ_2 and σ_3 (Figure 2.18). This 'critical stress' analysis assumes an isotropic and homogeneous rock mass.

When a discontinuity undergoes localised shear failure, if the magnitude of the normal stress, the roughness of the discontinuity and the strength of the discontinuity wall and infilling material is sufficient, the asperities will ride up and over each other resulting in dilation (Figure 2.19, section 2.4), causing an increase in permeability (Heffer and Koutsabeloulis, 1995 & Yeo *et al.*, 1998). This deformation can arise from a change in fluid pressure or a perturbation of the stress field in the rock mass. The degree to which the discontinuity deformation is elastic is important in determining the degree to which fluid flow properties are independent of stress. If deformation is totally elastic, the fluid flow properties of fractures will be totally dependant on the current stress regime (Anon, 1996). There are two elements that are not considered in this concept, the effect of frictional sliding of the asperities or asperity breakage.

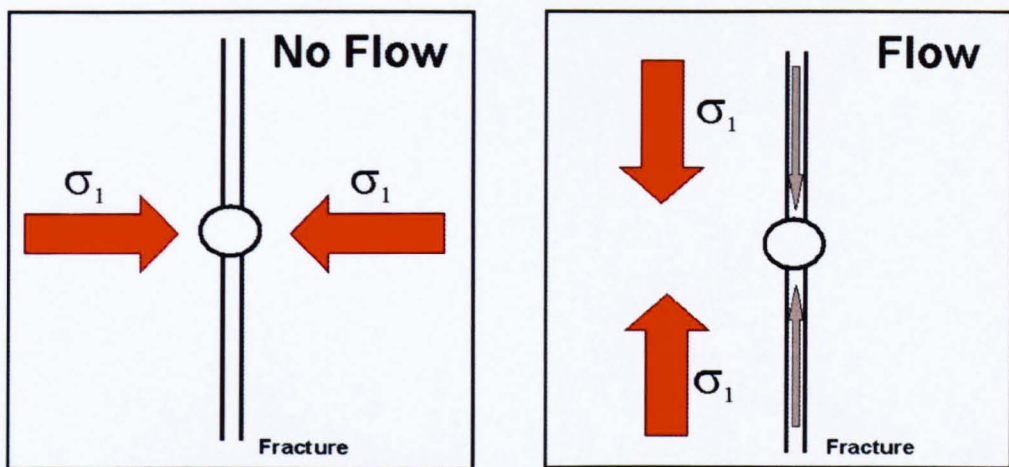


Figure 2.17 – Assumed relationship between permeability and stress regime (from Rogers, 2000).

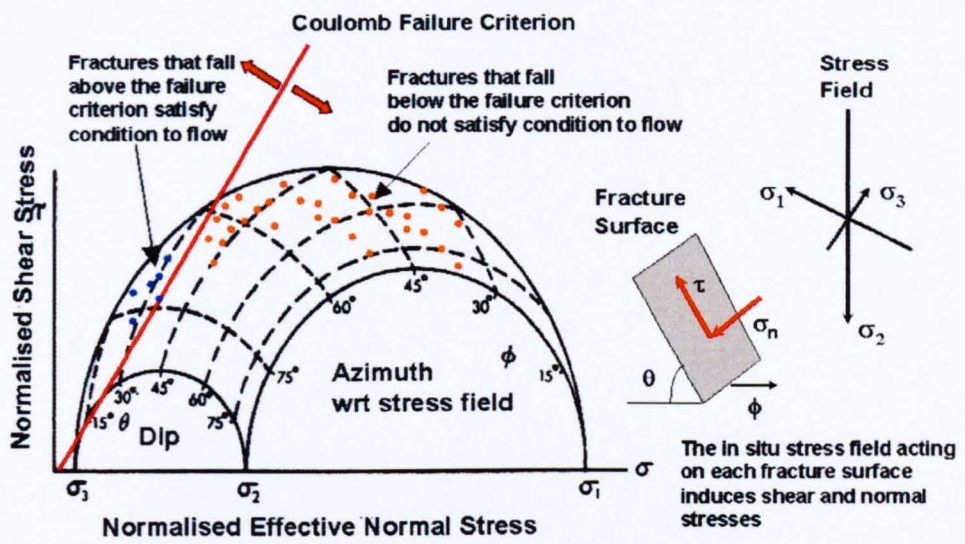
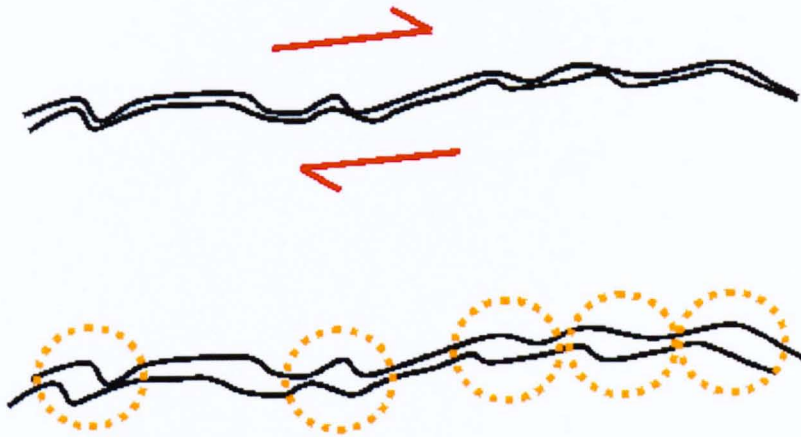


Figure 2.18 – Three-dimensional sketch of a cubic stress element on an inclined discontinuity plane (from Rogers, 2000).

This analysis should enable the identification of discontinuities (section 2.4) that are capable of allowing the flow of fluids (section 2.5) within a rock mass, due to their orientation within the present stress regime (section 2.2 & 2.3).



**Permeability increases
perpendicular to the
direction of shearing**

Figure 2.19 – Dilation of a discontinuity when sheared (from Rogers, 2000).

3. - Geological & Hydrogeological Characterisation

3.1 Geology - Introduction

It is not the purpose of this chapter to give a detailed interpretation of the geology of the Sellafield region, district and site, but to provide the background geological setting for these areas. For more detailed information the reader is referred to McL. Michie and Bowden (1994), NIREX (1995b), Chaplow (1996), McL. Michie (1996), BGS (1997), and NIREX (1997c).

3.1.1 Regional/District Geology

The Sellafield region is situated in the transitional structural zone between the western margin of the Lower Palaeozoic Caledonian basement high (Lake District massif) and the adjacent, mainly offshore area of the younger, East Irish Sea Sedimentary Basin (McL. Michie, 1996). These main geological elements can be observed in the satellite images (Plates 3.1a/b) and regional geological maps of the Sellafield region and district (Figures 3.1 a/b). A central upland area can be seen to form the main *basement inlier* of igneous and metamorphic Lower Palaeozoic rocks (Lake District massif), which are surrounded by an uncomfortably overlying *cover sequence* of Carboniferous and Permo-Trias rocks that dip away from the inlier (Plates 3.1a/b & Figures 3.1 a/b).

These two distinctive geological terrains also markedly influence the major structural architecture. Within the basement of the Lake District Massif, a dominant east-north-easterly trending tectonically folded, sub-green-schist facies, metamorphic fabric can be recognized from regional geophysical analysis and remote sensing (BGS, 1997). This fabric probably relates to the Acadian orogeny, which caused the deformation and reactivation of earlier structures and influences both the later sedimentary evolution and emplacement of igneous intrusions (McL. Michie, 1996). Vertical displacements along faults show a considerable range, from less than one metre to several thousand of metres (Figure 3.2).



Plate 3.1a – Satellite Landsat image of the Sellafield region. Landsat 5 Thematic Mapper scene 204-022 of the Sellafield Region, from an altitude of 700km – this winter image is an enhanced false-colour composite of three reflected infrared bands (water appears black, vegetation appears red and bare rock, soil and buildings appear green) (from McL. Michie, 1996).

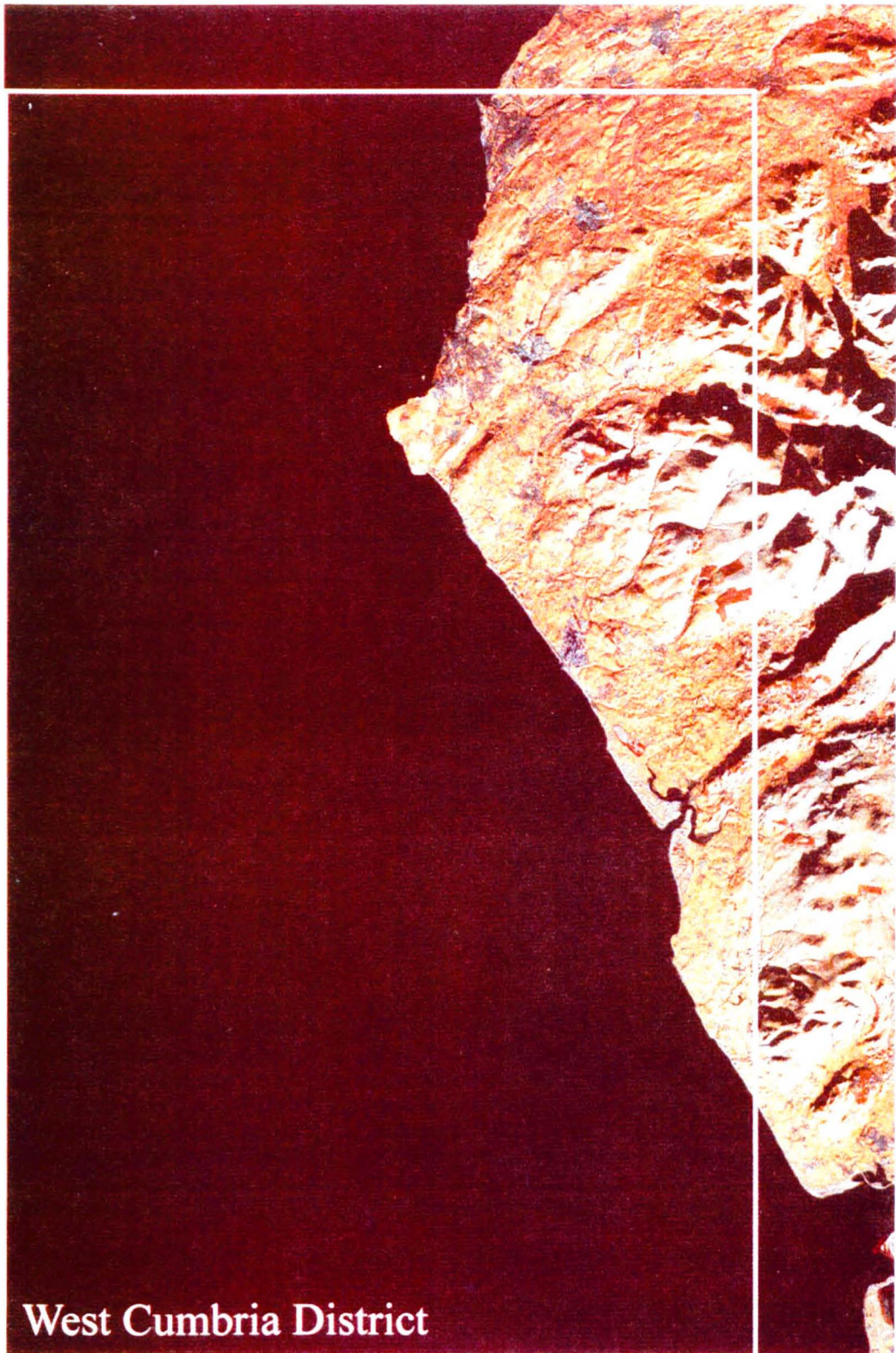


Plate 3.1b – Satellite Landsat image of the Sellafield district. Processed by the BGS, Keyworth. Bands 4, 5 and 7, edged enhanced, geometrically corrected to British National Grid (from BGS, 1997).

A)

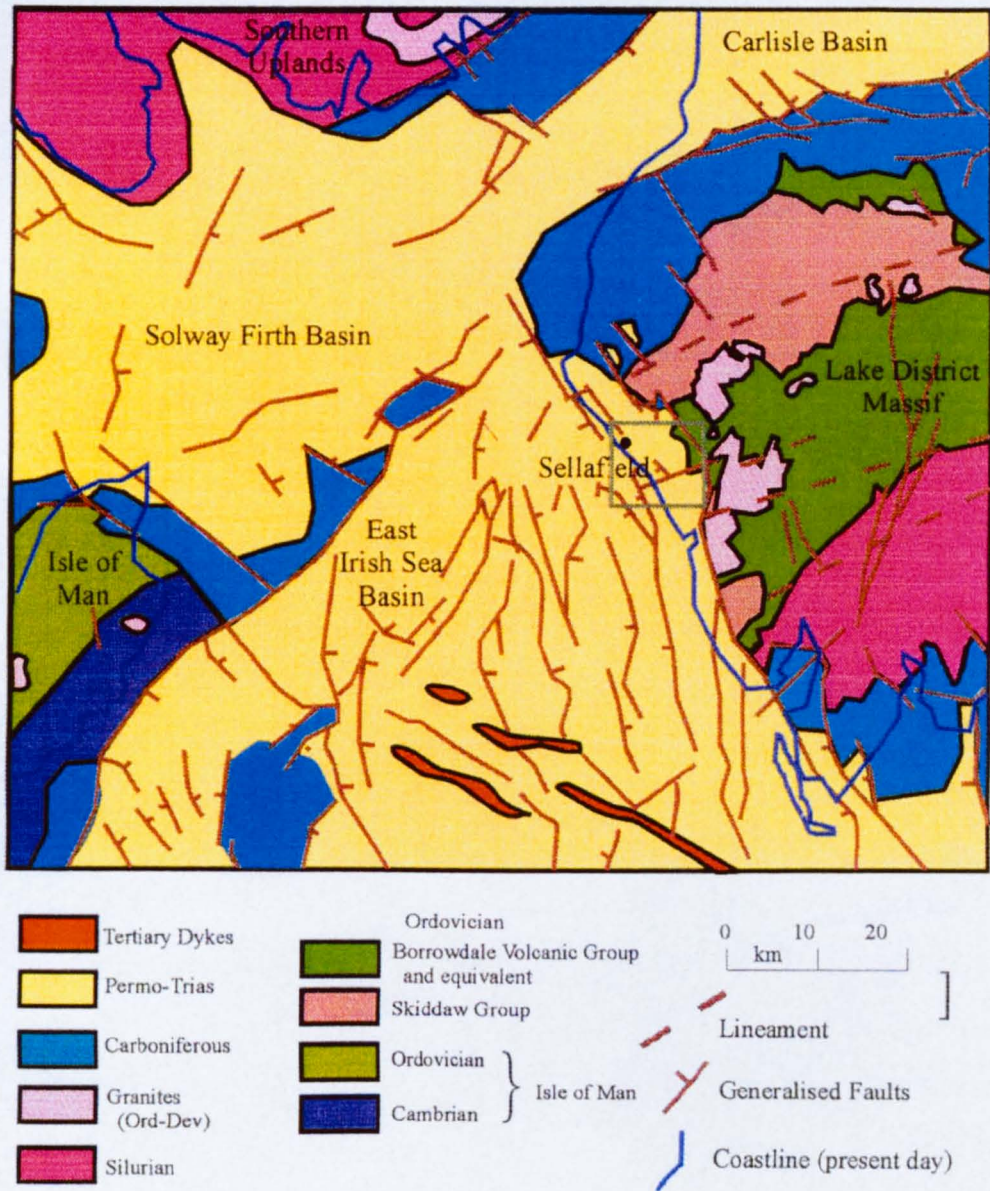


Figure 3.1a/b – Map showing the (a) regional and (b) district (Appendix 1B – Oversized Figures) geological and structural setting of Sellafield (from (a) NIREX, 1997j & (b) NIREX, 1995f).

Many faults in the Lower Palaeozoic volcanic rocks probably originated as volcano-tectonic structures. Faults initiated or reactivated during the late development of the Lake District Massif (Permian-Triassic) show a dominant northwest or north preferred orientation (McL. Michie, 1996 - (Figure 3.2)). The fault pattern within the younger Carboniferous and Permo-Trias sedimentary cover is characterized by curved or sinuous anastomosing faults, trending north to northwest linked by broadly east to northeast trending faults (McL. Michie, 1996). Faults usually dip steeply and have dominantly normal net displacements. Within the Carboniferous, consistently larger displacements are observed compared to the Permo-Trias suggesting reactivation of earlier structures. There is also some reverse faulting, identified from seismic profiling, within the Carboniferous. These Carboniferous reverse faults may have originally been normal faults, which have subsequently been affected by tilting and minor folding (McL. Michie, 1996).

Table 3.1 - Summarizes the geological history and events of the Sellafield region. Section 3.1.2 describes some of the lithostratigraphic units in more detail.

3.1.2 – Site Geology

The Sellafield site, as defined in Figure 1.2, has been subjected to a more detailed investigation than the surrounding Region and District. At the Sellafield site, a number of geological periods and formations are encountered (Table 3.1). Due to tectonic events, mainly uplift and erosion, occurring throughout Sellafield's geological history a number of geological periods and formations are consequently omitted at Sellafield. The geology of the site area can be seen in the Geological map (Figure 3.3 a, Appendix 1B) and cross-sections (Figure 3.3 b/c, Appendix 1B). Table 3.2 shows the generalised Pre-Quaternary stratigraphy and lithostratigraphy for the Sellafield Site. Each stratigraphic unit, including the Quaternary, is described in more detail below.

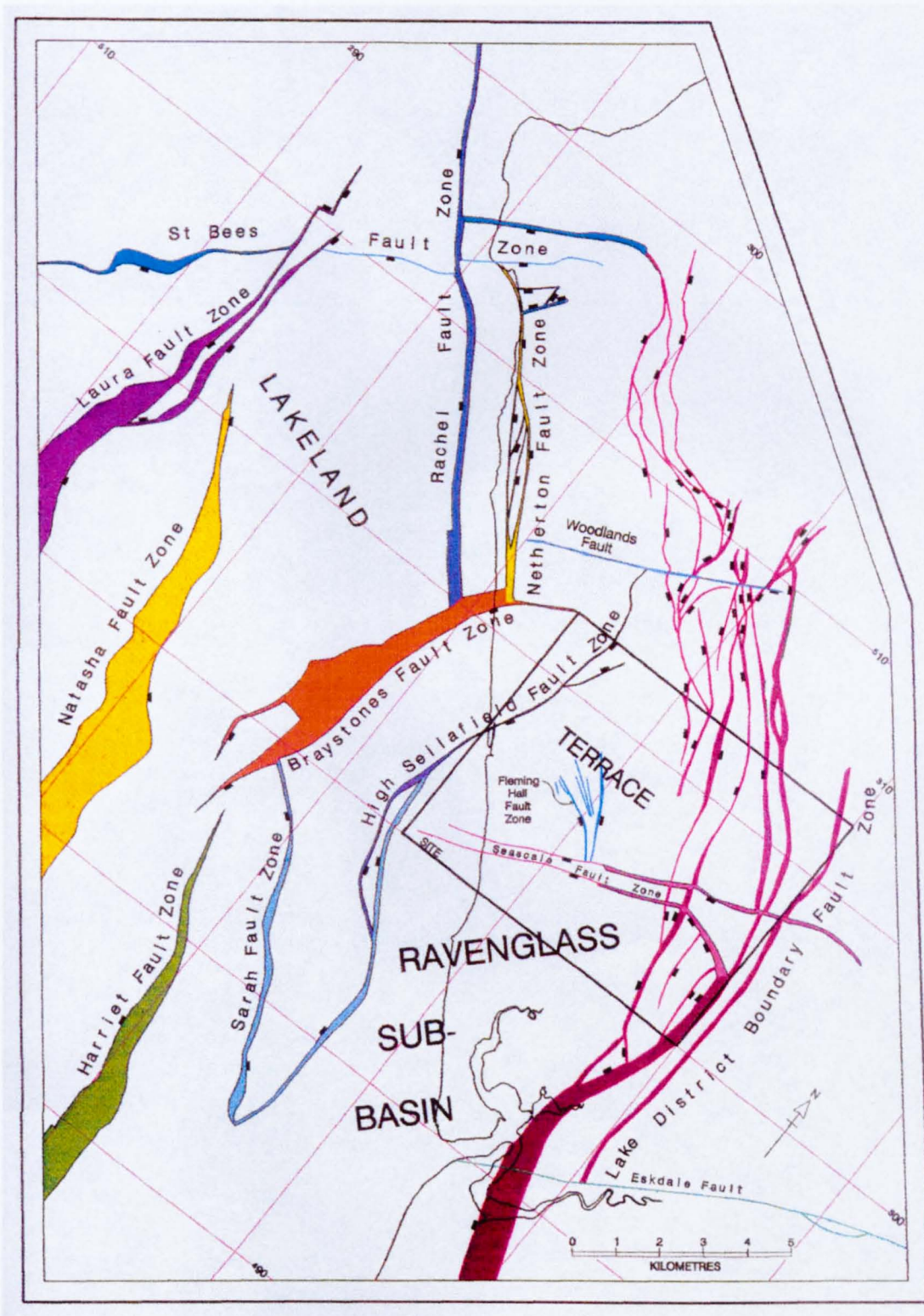


Figure 3.2 – Named structural features in the District at the top of the BVG (NIREX, 1993a).

Geological Period	Group/Formation	Rock Type	Thickness (m)	Geological Events
Recent/Holocene/ Flandrian				Post glacial deposits & marine transgression Isostatic uplift
Upper Pleistocene Devensian/ Weichselian				Last glaciation
Ipswichian/Eemian				Last inter-glacial deposit
Middle Pleistocene Pre-Ipswichian				Older glacial deposits (Thornsgill Till)
Lower Pleistocene				Eroded
Pliocene	-	-		Uplift & tilting
Miocene	-	-		? Minor basin inversion
Oligocene	-	-		Uplift & tilting
Eocene	-	-		Uplift
Palaeocene	-	-		Regional thermal uplift (emplacement Fleetwood dykes); superimposed minor basin inversion; oblique reversal of basin margin faults
Upper Cretaceous	-	-		?Minor basin inversion Post-extensional shelf subsidence
Middle Cretaceous	-	-		Regional (?N-S), widespread thermal uplift and erosion
Lower Cretaceous	-	-		
	UNCONFORMITY			Development of Late-Cimmerian unconformity
Late Jurassic	-	-		Regional (?N-S) extension superimposed on shelf subsidence
	-	-		Post-extensional shelf subsidence
Early Jurassic	-	-		Regional (?E-W) extension superimposed upon thermal (shelf) subsidence
Triassic	Lias Group	Mudstone	not known	
	Penarth Group	Mudstone	not known	
	Mercia Mudstone Group	Mudstone with halite, dolomite & anhydrite	about 3000	Deposition over Lake District Block
	Sherwood Sandstone Group			Subsidence
	Ormskirk Sandstone	Medium-grained aeolian sandstone	150-250	
	Calder Sandstone	Aeolian or fluvial sandstone	500-1000	
	St Bees Sandstone	Sandstone with thin mudstone beds common at the base	<1000	Overlap onto Lake District Block
				Extensional fault movement
Permian	Cumbrian Coast Group			
	St Bees Shale	Siltstone, sandstone, claystone & breccia with gypsum	<200	
	St Bees Evaporite	Limestone, dolomite, anhydrite, sandstone, siltstone & mudstone	50-200	Extensional fault movement
	Appleby Group			
	Colly Hurst Sandstone	Sandstone	not known	
	Brockram	Breccio-conglomerate	20-150	Uplift and erosion
	UNCONFORMITY			Variscan deformation. ? Minor reverse faulting
Carboniferous	Whitehaven Sandstone	Red sandstone, siltstone, mudstone & limestone	300	
	Coal Measures	Sandstone, mudstone, siltstone, seatearth & coal	370-440	
	Hensingham Group	Sandstone, siltstone, argillaceous limestone & coal	50-110	Gradual, minor subsidence of Lake District Block
	Chief Limestone Group			Extensional fault movement
	Urswick Limestone	Limestone, peloid grainstones with numerous palaeokarst surfaces	at least 42	
	Frizington Limestone	Limestone & sandy limestone with thin shale interbeds	up to 100	
	Martin Limestone	Limestone, sandy limestone & sandstone	37231	
	UNCONFORMITY			Uplift erosion

Table 3.1 – Geological history of the Sellafield Region (Adapted from BGS, 1997 & McL. Michie, 1996).

Table 3.1 (continued) – Geological History of the Sellafield Region (Adapted from BGS, 1997 & McL. Michie, 1996).

Geological Period	Group/Formation	Rock Type	Thickness (m)	Geological Events
Devonian	-	-	-	Caledonian (Acadian) Orogeny, metamorphism & batholith intrusion
Silurian	-	-	-	Subsidence
Ordovician	Borrowdale Volcanic Group			Igneous activity and related volcano-tectonic faulting
	<i>Succession in Calder Hall area</i>			
	Yottenlews	Rheomorphic welded rhyolitic tuff	190	
	Newton Manor	Volcaniclastic sandstone, siltstone & tuffs	240	
	<i>Succession west of the Thistleton Fault</i>			
	Blendale	Parataxitic rhyolitic tuff & tuff-breccia	about 250	
	Lowcray	haematised and silicified parataxitic tuff & lapilli-tuff	about 650	
	Fleming Hall	Rheomorphic andesitic tuff, lapilli-tuff & tuff-breccia	400-800	
	Brown Bank	Dacitic & rhyolitic lithic-rich lapilli-tuff, & pyroclastic-breccia	50-370	
	Bleawath	Andesitic to rhyodacitic coarse pumice lapilli-tuff	<416	
	Broom Farm	Volcaniclastic sandstone & siltstone	<15	
	Moorside Farm	Andesitic to rhyolitic lapilli-tuff & coarse pyroclastic breccia	>120	
	<i>Succession east of the Thistleton Fault</i>			
	Birker Fell	Andesite sheets with basalt, dacite & volcaniclastic rocks	2600	
	Latterbarrow	Pebbly sandstone with interbeds of mudstone	0-400	
	UNCONFORMITY			Uplift & erosion
	Skiddaw Group			Subsidence
	Buttermere	Olistostrome of disrupted, sheared & folded mudstone & sandstone	at least 1500	
	Kirk Stile	Siltstone & mudstone interpreted as low-density turbidites	1500-250	
	Loweswater	Sandstone & mudstone in a coarsening-& fining-upwards sequence	about 300	
	Watch Hill	Predominantly sandstone, commonly with mudstone intraclasts	<100	
	Bitter Beck	Mudstone with thin sandstone beds	up to 500	

	Mercia Mudstone Group		
Triassic	Sherwood Sandstone Group	Ormskirk Sandstone Formation	
		Calder Sandstone Formation	
		St Bees Sandstone Formation	
		----- North Head Member	
Permian	Cumbrian Coast Group	St Bees Shale Formation	Moss Side Member
		St Bees Evaporite Formation	-----
	Appleby Group	Brockram	
Carboniferous (Dinantian)	Chief Limestone Group	Urswick Limestone	
		Frizington Limestone	
		Martin Limestone	

Potential Repository Zone Area Borrowdale Volcanic Group

Ordovician	Borrowdale Volcanic Group	Fleming Hall Formation	Longlands Farm Member
			----- Sides Farm Member
		Brown Bank Formation	Town End Farm Member
			----- Seascale Hall Member
		Bleawath Formation	
		Broom Farm Formation	
		Moorside Farm Formation	

Table 3.2 – Stratigraphic succession for the Sellafield site area (from NIREX, 1997)).

3.1.2.1. – Ordovician (Lower Palaeozoic basement)

The Ordovician rocks encountered at the Sellafield site comprises solely of the late Ordovician (Caradocian) pyroclastic volcanic rocks known as the Borrowdale Volcanic Group (BVG). The BVG originated from a subaerial, subduction related, calc-alkaline volcanic field that formed due to the closure of the Iapetus Ocean (Millward *et al.*, 1994 and references therein). The early Ordovician Skiddaw Group, which can be seen in other areas of west Cumbria to predate the BVG, were uplifted and completely eroded away following injection of large volumes of magma due to the closure of the Iapetus Ocean. The volcanoclastic BVG, outcrops in the top northeast corner of the site (Figure 3.3 a/b) and is encountered in the Sellafield boreholes (2, 3, 4, 5, 7A, 8A/B, 9A, 10A, 11A, 12A, 13A, 14A, RCF1/2/3, RCM1/2/3, PRZ2/3, Holmrook 13 & Boonwood). The stratigraphy for the Sellafield site BVG was defined by Millward *et al.* (1994) and is summarised in Figure 3.4a. Millward *et al.* (1994) defined, from the cored Sellafield boreholes, three distinct successions at the Sellafield site (Figure 3.4a) seen in, respectively the Longlands area (mainly covers the PRZ area of Sellafield), the Calder Hall area and the Seascale area. In the Longlands area, five formations are identified from the PRZ boreholes (2, 4, 5, 10A, 12A, RCF1/2/3, RCM 1/2/3, PRZ 1/2/3, Holmrook 13 & Boonwood) and borehole 11. These are the Moorside Farm, Broom Farm, Bleawath, Brown Bank and Fleming Hall formations (Figure 3.4b), which collectively form a sequence that is about 1140 m thick (BGS, 1997). These formations comprise mainly of volcanoclastic rocks (tuffs, lithic breccias, volcanoclastic sandstones), with some intrusive basalt and andesite sills and dykes (Millward *et al.*, 1994). In the Calder Hall area the Newton Manor and the Yottenfews formation are encountered in boreholes 7A and 14A. These consist of mainly volcanoclastic rocks (welded tuffs, tuffs, volcanoclastic sandstones, sandstones) with some andesite and dacite sills and dykes (Figure 3.4c). The Seascale area does not have any formal stratigraphy identified from boreholes 3 and 13A, because it is not possible to correlate the sequence here with other established sequences known to exist within the BVG.

Four welded tuffs are intercalated with tuff, lapilli tuff, volcanoclastic breccia, sandstone and siltstone. Millward *et al.* (1994) suggesting that this sequence must be a part of the pyroclastic lithostratigraphy of the Sellafield area, though the available data do not indicate a correlation with either the Longlands area or the Seascale area.

3.1.2.2 - Carboniferous

The preserved Carboniferous rocks within the Sellafield site are not found outcropping at the surface, but are encountered within a number of the Sellafield boreholes (3, 7A, 10A, 12A, 13A, 14A). The stratigraphy for the Sellafield Carboniferous was defined by Barclay *et al.* (1994) and is depicted in Figure 3.5. It consists of mainly limestones from the Chief Limestone Group of which the Urswick Limestone Formation, Frizington Limestone Formation, Martin Limestone Formation and Basal Beds Formation occur. These formations consist mainly of limestones with minor interbedded shale and sandstone, of Dinantian age (Figure 3.5). These Carboniferous rocks were deposited in equatorial shallow, tropical seas over the eroded Lower Palaeozoic basement, following the Caledonian Orogeny (Table 3.1). At Sellafield, a reduced thickness of Carboniferous strata occurs, possibly due to uplift and erosion, related to the Variscan Orogeny, prior to deposition of the Permian strata (BGS, 1997). The preserved thickness of the strata decreases from 150m in the west to an erosional cut-off in the central and eastern parts of the site (Barclay *et al.*, 1994). In the northwest of the site stratigraphic evidence indicates, up to 5km of Carboniferous was eroded away (BGS, 1997) leaving only the older Dinantian Carboniferous. This means therefore, that the upper and lower bounding surfaces of the Carboniferous are unconformities. Seismic reflection data suggest that much of the sub-Permian unconformity is generally subparallel with, or at a low angle to, the dip of the underlying Carboniferous strata (BGS, 1997).

This unconformity also has locally sub-Permian reddening of the underlying strata, which developed during the long period of non-deposition associated with the Variscan Orogeny (BGS, 1997).

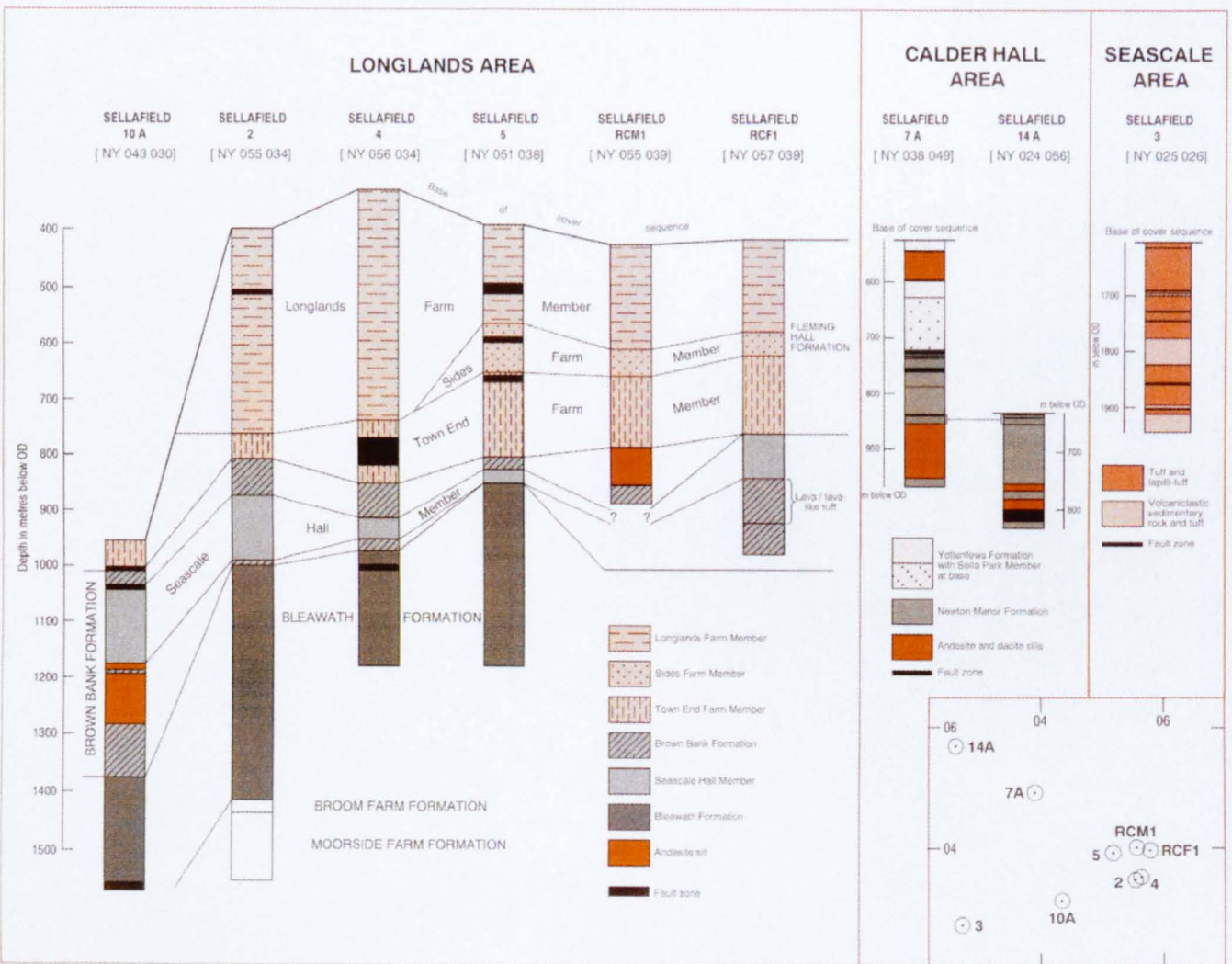


Figure 3.4a – Lithostratigraphy of the BVG in the Sellafield site (from BGS, 1997).

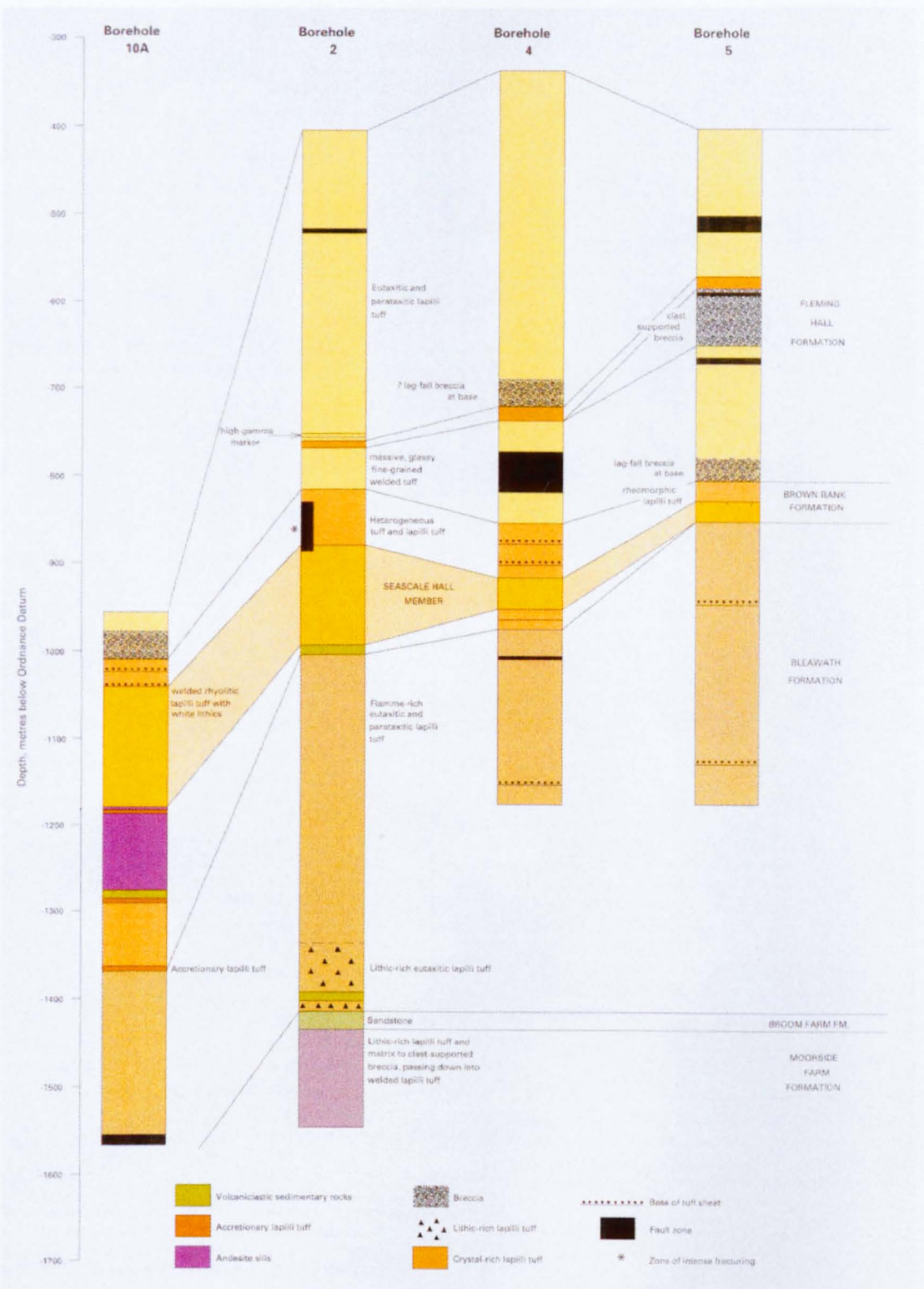


Figure 3.4b – Lithostratigraphy of the BVG the PRZ area (from Millward *et al.*, 1994).

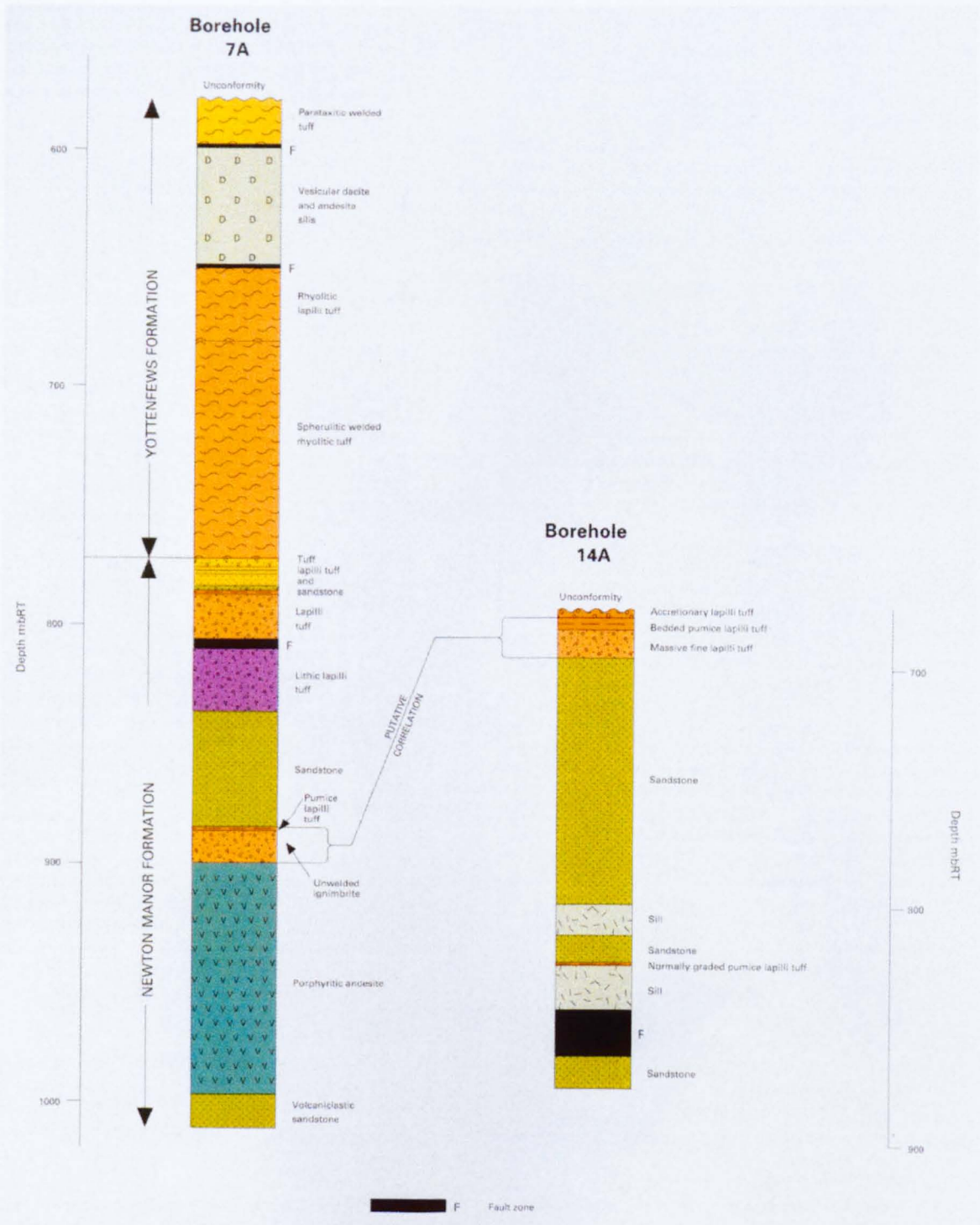


Figure 3.4c – Lithostratigraphy of the BVG the Calder Hall area (from Millward *et al.*, 1994).

The Dinantian Limestones are commonly dolomitised close to the unconformity, and the Lower Palaeozoic rocks are locally altered and reddened (BGS, 1997).

3.1.2.3 – Permian & Triassic

The Permian and Triassic outcrops across most of the Site (Figure 3.3a) and in the Sellafield boreholes (1/1A, 2, 3, 4, 5, 7A/B, 8A/B, 10A/B, 11A, 12A, 13A/B, 14A, RCF1/2/3, RCM1/2/3, PRZ 1/2/3, Holmrook 13 & Boonwood). The stratigraphy of the Permian and Triassic at the Sellafield site is described by Barnes *et al.* (1994). Exposures of the Permian at outcrop are solely encountered in the northeast corner of the site (Figure 3.3a, Appendix 1B). They are patchy exposures preserving less than 50m of sedimentary succession, which thickens towards the southwest in the subsurface to a maximum thickness of 340m in borehole 3 (NIREX, 1997c). In borehole 3 the full sequence of Permian strata can be observed (Figure 3.6a/b), comprising of the Appleby Group in which the Brockram formation (matrix or clay supported breccias) occurs at the base and the Cumbrian Coast Group in which the St Bees Evaporite (varied sequence of limestone, dolomitic limestone, dolomite and anhydrite) and the St Bees Shale formations (interlaminated siltstone, very fine grained sandstone, with subordinate claystone and fine to medium grained sandstone) occur.

The Triassic strata forms rockhead over much of the Sellafield site (NIREX, 1997c). It is mainly made up of a thick sandstone succession, known as the Sherwood Sandstone Group, which comprises the St Bees Sandstone, Calder Sandstone and Ormskirk Sandstone Formations (Table 3.2 & Figure 3.7). The Mercia Mudstone Group forms the top of the Triassic. It is not encountered onshore, within the Sellafield site, or within any of the Sellafield boreholes but outcrops just offshore to the southwest of the site and (Figure 3.7). The Mercia Mudstone Group comprises of mudstone facies that is dominantly reddish brown in colour, commonly with beds of halite and minor amounts of dolomite, dolomitic mudstone and anhydrite (BGS, 1997).

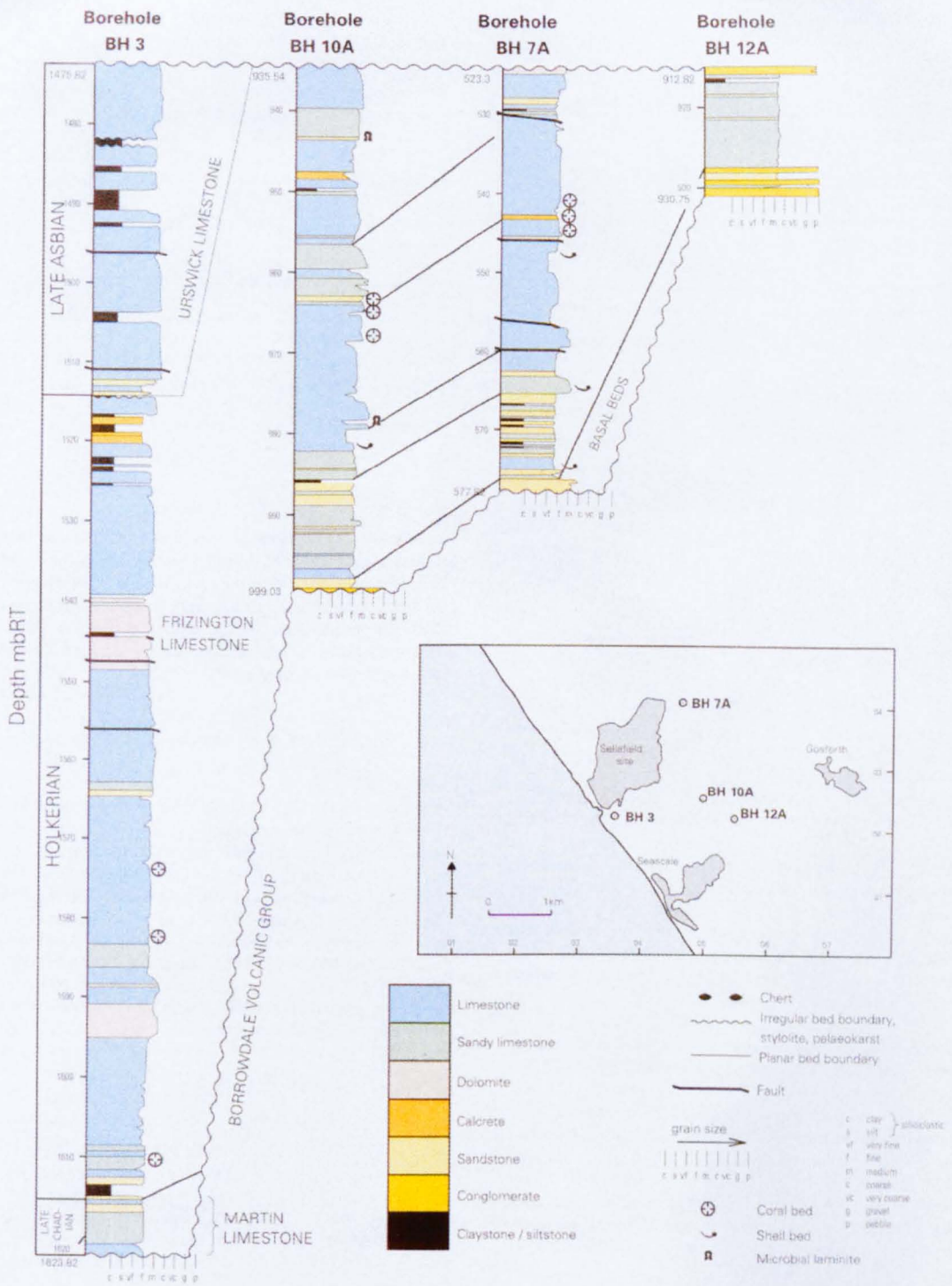


Figure 3.5 – Lithostratigraphy of the Carboniferous in the Sellafield site (from Barclay *et al.*, 1994).

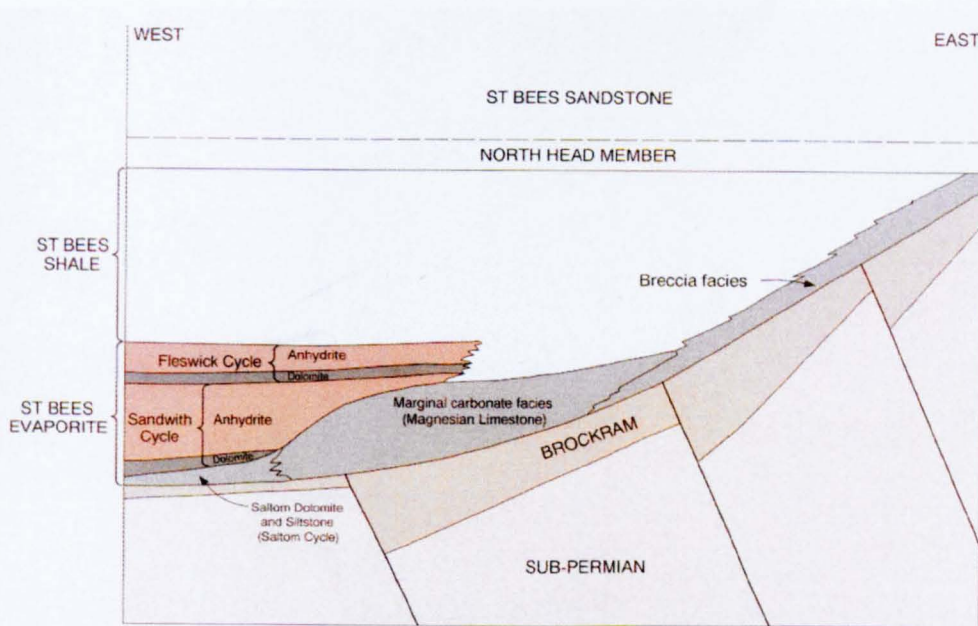


Figure 3.6a - Lithostratigraphy of the Permian in the Sellafield site. Borehole correlation of Permian lithostratigraphy (from BGS, 1997).

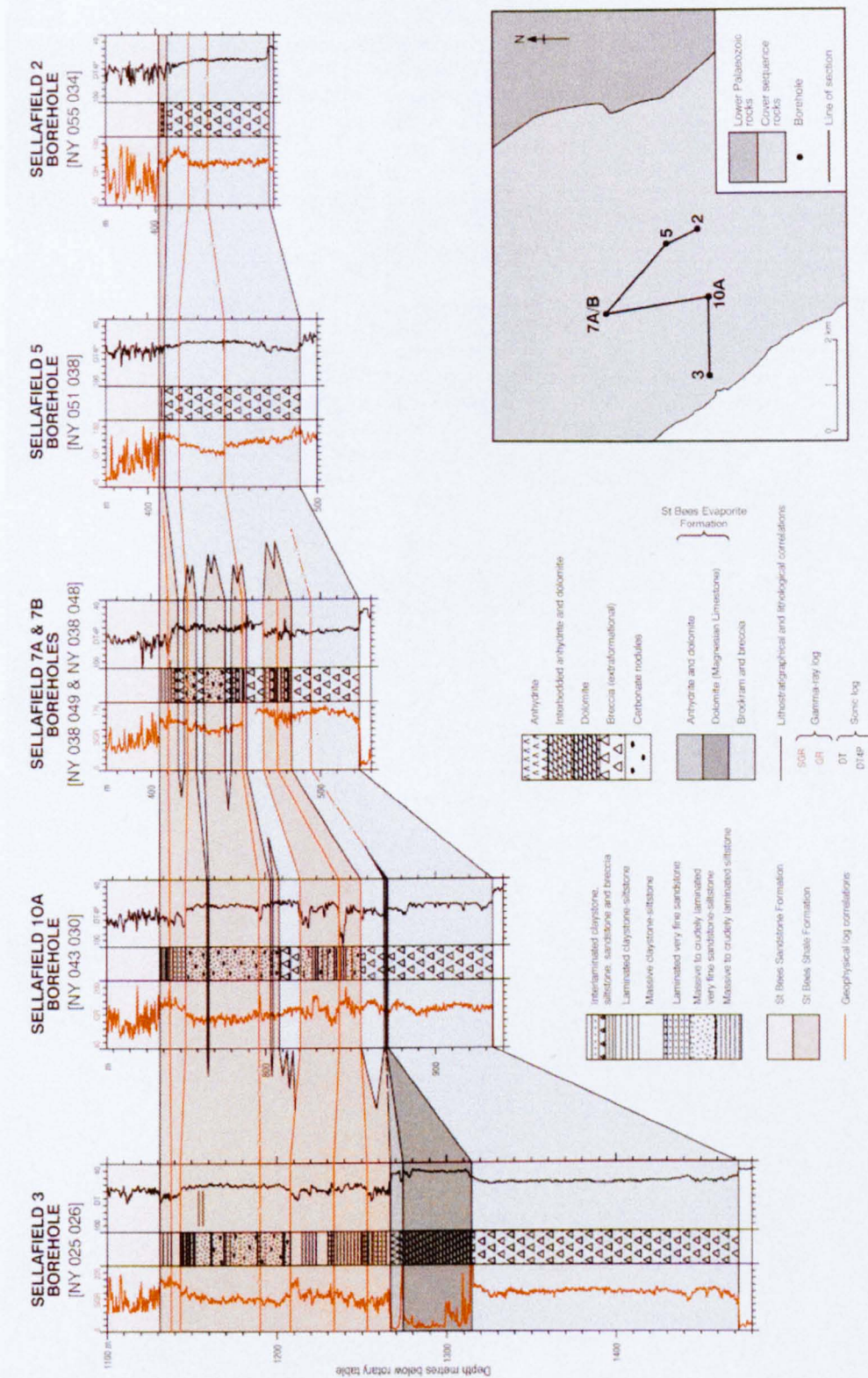


Figure 3.6b - Lithostratigraphy of the Permian in the Sellafield site. Schematic cross-section (west to east) of stratigraphic relationships in the Permian (from BGS, 1997).

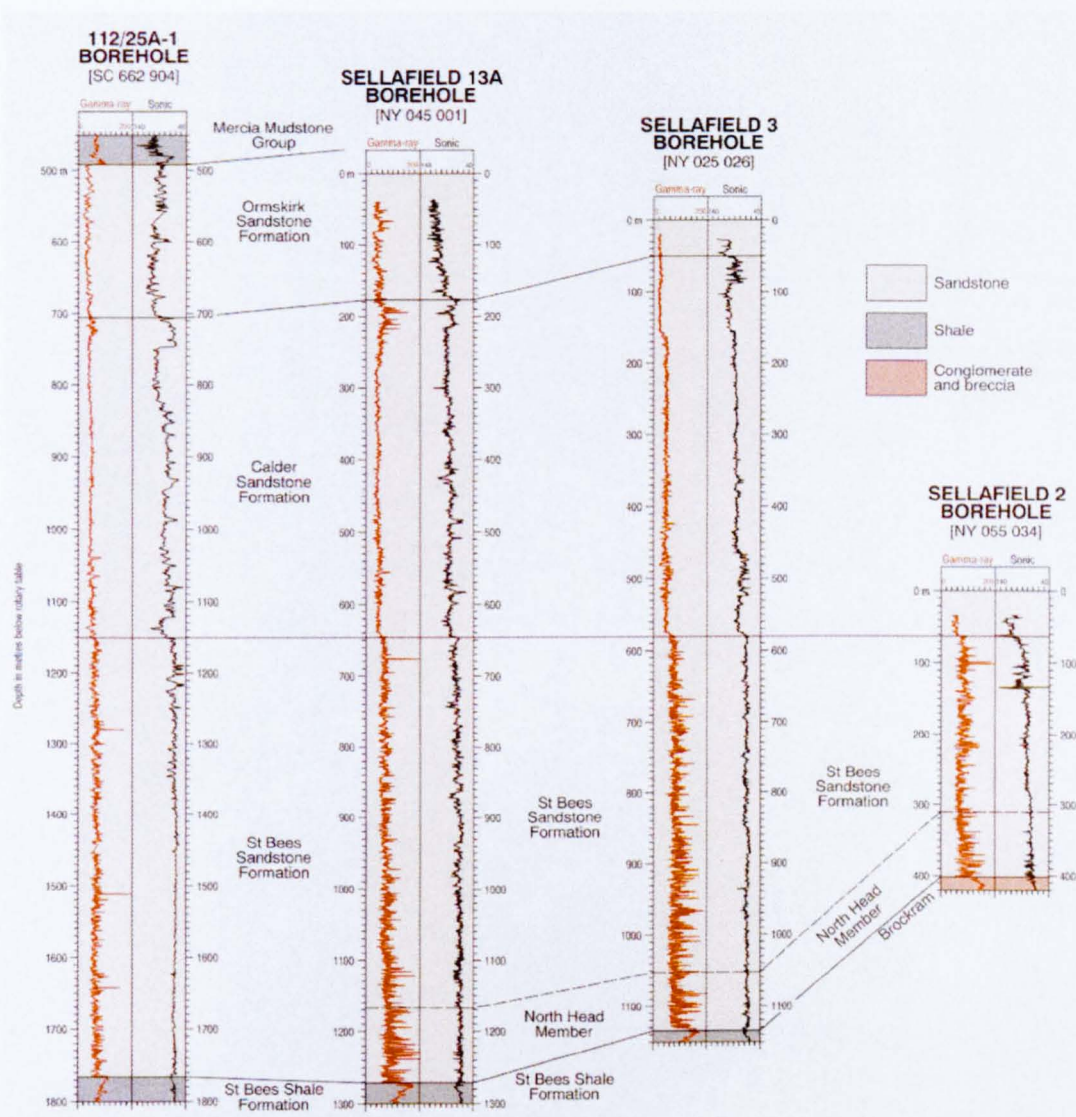


Figure 3.7 – Borehole correlation of the Triassic strata in the Sellafeld site (from BGS, 1997).

These Permian and Triassic rocks were deposited in what is known as the East Irish Sea Basin, which is the largest and deepest of a series of linked Permo-Triassic extensional basins on the western side of Britain (BGS, 1997). The East Irish Basin was initiated by extensional fault-controlled subsidence (rifting), locally associated with alkali basalt volcanism, which began during the early Permian, and continued periodically throughout the Triassic into Jurassic times (BGS, 1997). Many of the northwest trending fault structures, across the site area, are interpreted as minor syn-depositional normal faults (NIREX, 1997c). Considerable syn-depositional faulting can be observed occurring across the southwest dipping Fleming Hall Fault zone, locally across the western end of the Seascale Fault Zone and at faults 1,2 and 10 (Figures 3.2). The Permo-Triassic rocks have undergone diagenetic modification from the time of their deposition to the present day. Changes in temperature, pressure and groundwater chemistry during progressive burial and later uplift (Table 3.1) have caused dissolution, mineralogical alteration and replacement of the primary components of the Permo-Triassic rocks. In addition the precipitation and dissolution of interstitial authigenic cements has occurred (BGS, 1997). Table 3.3 describes the eleven diagenetic episodes (DE1-11).

3.1.2.4 – Quaternary

Quaternary sediments are encountered onshore and offshore in the Sellafield Site. Onshore, the Quaternary record is fragmented (Figure 3.8a/b), although sequences up to 90 meters thick are present locally (NIREX, 1993b). The sediments comprise mainly glacial deposits laid down during Upper Pleistocene (Late Devensian) glaciation and its associated ice readvances together with sediments deposited during deglaciation and Holocene times (Figure 3.8a/b); locally pockets of Middle Pleistocene (pre-Late Devensian) can also be found (BGS, 1997). Seismic profiles indicate the presence of extensive mid-late Quaternary sediments in offshore areas, which generally have thicknesses of less than 50m, but can be found in places up to 100m thick when glacial channels have been incised into rockhead (BGS, 1997).

Diagenetic episode	Principal mineralogical characteristics	Equivalent mineralisation episode	Diagenetic stage	Age
DE1	Shallow, near surface 'red bed' diagenesis with development of infiltrated clay coatings, haematite grain coatings, haematite + anatase replacement of detrital ferromagnesian minerals, micromolar non-ferroan calcite and dolomite cement (calcrete, dolocrete, constones), anhydrite cements, interstitial precipitation of gypsum and anhydrite in sabkhas etc.	No corresponding fracture mineralisation events	EODIAGENESIS Synsedimentary near surface processes	PERMIAN- EARLY TRIASSIC Diachronous
DE2	Early diagenetic precipitation of smectite grain coatings + minor K-feldspar overgrowths			
DE3	Neomorphism of early carbonate cements and precipitation of idiomorphic non-ferroan dolomite and calcite overgrowth cements. Precipitation of ferroan dolomite and calcite as late-stage overgrowths. Conversion of gypsum to anhydrite, some dissolution of anhydrite	ME4	EARLY MESODIAGENESIS Shallow burial	
DE4	Precipitation of quartz, K-feldspar and albite overgrowths			
DE5	Precipitation of minor haematite, dissolution of earlier calcite and dolomite			
DE6	Precipitation of major pore-filling evaporite cement (anhydrite) prior to major compaction	ME5	MIDDLE MESODIAGENESIS Moderate burial	EARLY-MID- TRIASSIC BURIAL
DE7	Dissolution of earlier carbonate and evaporite cements, precipitation of kaolinite, illitisation of kaolinite, illite precipitation (evident only in Brockram)			
DE8a	Precipitation of ferromanganous calcite and major collomorphic haematite (in Brockram only, preserved as relicts)	ME6a	LATE MESODIAGENESIS Deep burial	
DE8b	Corrosion of calcite, precipitation of non-ferroan dolomite, becoming ferroan in later stages (all formations). Precipitation of anhydrite	ME6b		
DE8c	Corrosion of dolomite, precipitation of ankerite (all formations)			
DE8d	Corrosion and dissolution of earlier carbonates and anhydrite, precipitation of barite (all formations)			
DE8e	Precipitation of traces of fluorite, sulphides and selenides (fluorite only seen in Brockram)	ME6c		
DE8f	Precipitation in two stages of ferromanganous calcite, traces of pyrite (all formations)			
DE9	Extensive dissolution of evaporite cements particularly in the Sherwood Sandstone Group, and some dissolution of feldspar grains, precipitation of fibrous and platey illite in secondary rejuvenated porosity	ME7		POST-MID- TRIASSIC
DE10	Late-stage oxidative dissolution of carbonate cements, hydration and dissolution of anhydrite, associated precipitation of iron and manganese oxides and oxyhydroxide alteration products. In part contemporaneous with present-day groundwater alteration	ME8	TEI ODIAGENESIS	PALAE- OCENE- RECENT
DE11	Late-stage precipitation of euhedral calcite (all formations), locally also gypsum or anhydrite, in secondary porosity in Brockram and dissolution cavities after anhydrite nodules in St Bees Shale; hydration of anhydrite to gypsum and dissolution of gypsum (St Bees Evaporite and Shales)	ME9	Uplift and tectonic invasion	

Table 3.3 – Summary of the Diagenetic Episodes encountered at Sellafield (BGS, 1997).

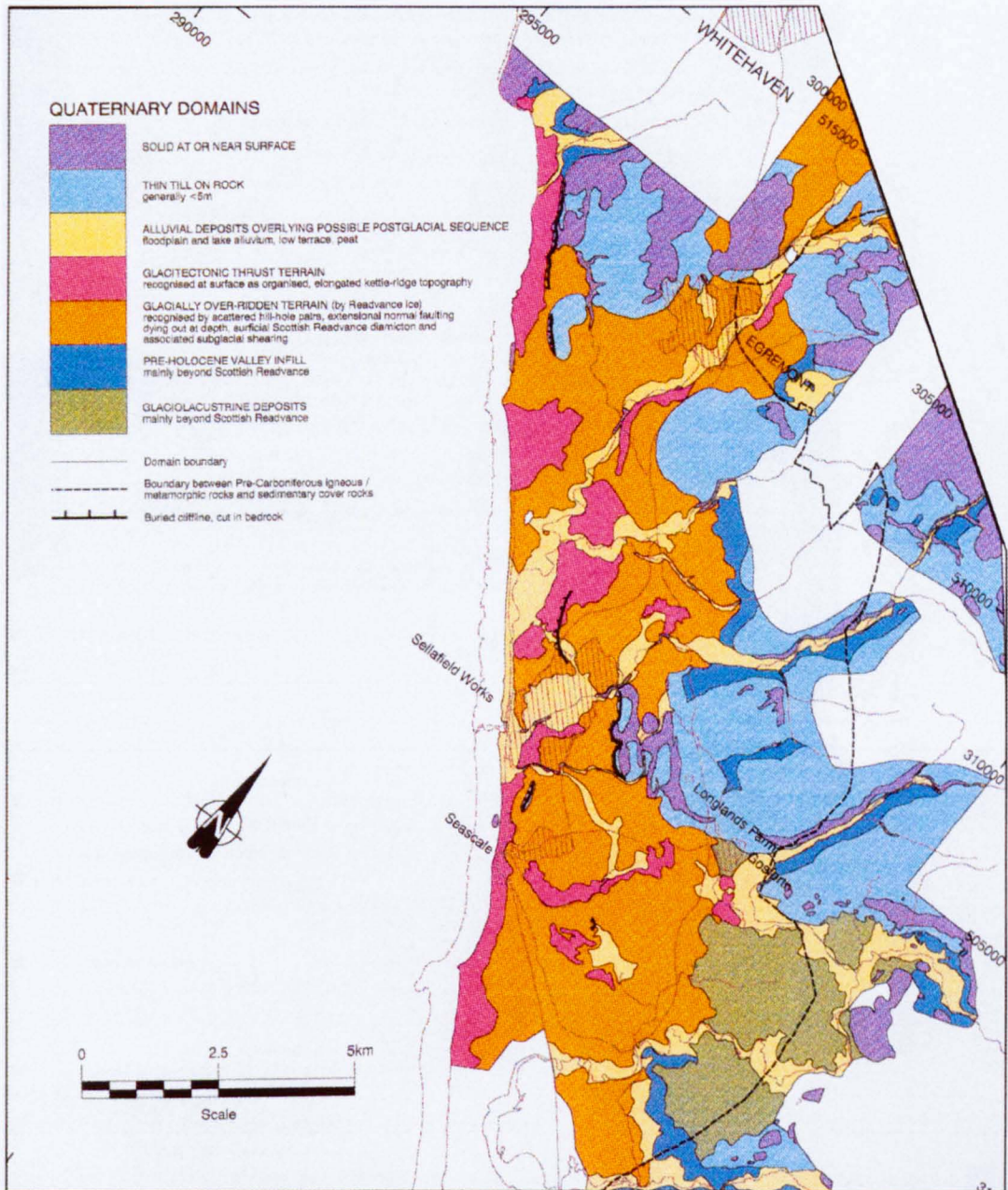


Figure 3.8a – Onshore a) District and b) Site (Appendix 1A) Quaternary domains map of Sellafeld (NIREX, 1995f; NIREX, 1997h).

Glacigenic sediments and substantial accumulations of glaciomarine and marine sediments comprise the bulk of the offshore record. Unconformities and glacio-tectonic effects occur within the sediments indicating changes in sea level due to eustatic and isostatic events, as well as variations in glacial environment, climate and sediment input (BGS, 1997).

3.1.3 PRZ Geology

A number of specialist geological studies within the Sellafield boreholes were undertaken as part of Nirex's investigations into Sellafield as a potential radioactive waste repository (section 1.2). Many of these geological studies have centred on the analysis of the boreholes and their core material, and in particular the measurement and analysis of discontinuities within the core. All the data obtained from these investigations have been presented in composite logs (NIREX, 1995f) and summary charts (NIREX, 1996e) for each of the PRZ boreholes (Appendix 11, Volume III).

3.2 – Hydrogeology

It is not the purpose of this thesis to provide a detailed interpretation of the hydrogeology of the Sellafield region, district and site. However, a brief summary is outlined within the following sections to provide background information to the present study. For more detailed information the reader is referred to NIREX (1993b), NIREX (1994), McL. Michie and Bowden (1994), NIREX (1995b), Chaplow (1996), McL. Michie (1996), NIREX (1996d), NIREX (1997e) and NIREX (1997d).

3.2.1 – Regional/District Hydrogeology

The hydrogeological conceptual model developed for the Sellafield region/district by Black and Brightman (1996), divides the groundwater up into three distinct groundwater regimes (Figure 3.9):

- ***The Coastal Plain*** – predominantly fresh groundwater driven by gravity through the sedimentary units, which overly the Ordovician Basement.

The groundwater regime is recharged in the east, from the topographically high Lake District massif, with discharge into streams, river and the Irish Sea to the west. The top boundary of this regime is defined by the water table (NIREX, 1997e);

- ***The Hills and Basement Regime*** – predominantly saline groundwater moving slowly through the fractures within the Ordovician Basement. Groundwater is a mixture of evaporite-derived brine (originating from the dissolution of halite and evaporates from Permian and Triassic rocks of the East Irish Sea Basin) and meteoric water. Groundwater has also been modified by water/rock chemical interactions (NIREX, 1997e); and
- ***The Irish Sea Basin Regime*** – evaporite-derived brines and highly saline groundwater (dissolution of halite and evaporates from Permian and Triassic rocks of the East Irish Sea Basin), in a relatively stagnant basinal environment. Processes such as the dewatering of sediments, thermal effects and fluid density influence groundwater movement in this regime (NIREX, 1997e).

3.2.2 – Site Hydrogeology

Within the conceptual hydrogeological model (Black and Brightman, 1996), hydrogeological units have been identified and provide a greater definition to the nature of groundwater flow through Sellafield. Each hydrogeological unit is defined as a discrete subdivision of the rock mass within which the hydrogeological characteristics are essentially similar (NIREX, 1997e). The hydrogeological variability within the Sellafield site is generally the result of the varying geological structure and properties within the rock mass (McL. Michie, 1996). The geological stratigraphy of the site greatly influences the divisions of the hydrogeological units. Table 3.4 lists hydraulic conductivity values for some of the hydrogeological units determined in the Sellafield boreholes as a guide to the hydrogeological parameters (McL. Michie, 1996). Each hydrogeological unit is described below in more detail.

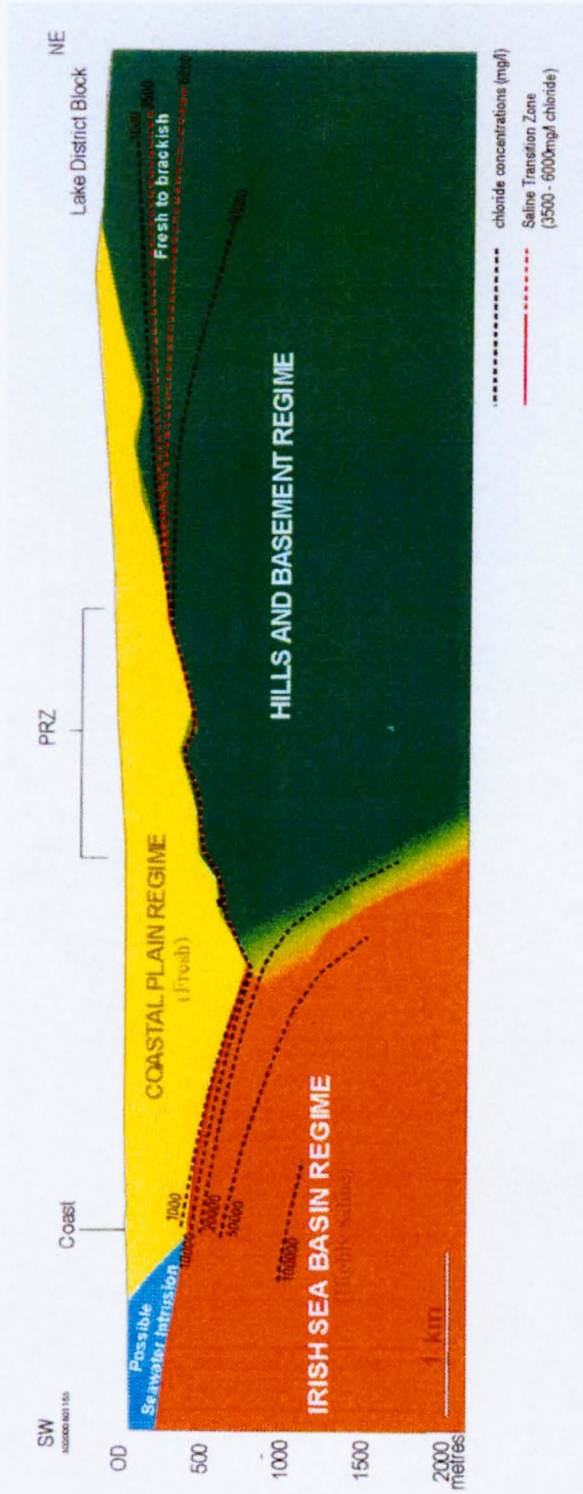


Figure 3.9 – Cross-section of Sellafield site showing groundwater regimes and corresponding salinity (from NIREX, 1997e).

	Number of EPM	Minimum (ms ⁻¹)	Medium (ms ⁻¹)	Maximum (ms ⁻¹)
Triassic (Sherwood Sandstone Group)				
Calder Sandstone	9	3.2 x 10 ⁻⁸	1.0 x 10 ⁻⁷	1.6 x 10 ⁻⁵
St Bees Sandstone	66	7.9 x 10 ⁻¹¹	2.5 x 10 ⁻⁸	1.0 x 10 ⁻⁵
Permian				
(St Bees Shale, St Bees Evaporite, Brockram)	18	4.0 x 10 ⁻¹³	6.3 x 10 ⁻¹⁰	1.0 x 10 ⁻⁵
Carboniferous Limestone	6	2.5 x 10 ⁻⁹	5.0 x 10 ⁻⁸	7.9 x 10 ⁻⁶
Ordovician (Borrowdale Volcanic Group)	84	7.9 x 10 ⁻¹⁴	1.0 x 10 ⁻¹⁰	1.0 x 10 ⁻⁶

Table 3.4 – Borehole hydraulic conductivity determinations from specialist hydrogeological testing, known Environmental Pressure Measurements (EMP) over 50m length (adapted from McL. Michie, 1996).

3.2.2.1 – Ordovician Borrowdale Volcanic Group

Groundwater flow in the BVG is primarily through a complex network of discontinuities; therefore, the matrix permeability in the BVG is very low. The BVG also has a low hydraulic conductivity (Table 3.4). Detailed discontinuity studies have determined that discontinuity flow within the BVG primarily occurs through a subset of the total discontinuity system (NIREX, 1997e). This subset has been identified as a possible conduit for groundwater flow and have therefore been termed flowing features. Many of these flowing features have also been identified in the subsurface, through the interpretation of wireline hydrogeological production test logs (section 5.2). These features have been termed flow zones (FZ). A FZ refers to a point at which, or an interval within which, groundwater flow into a borehole has been identified through production test logs (NIREX, 1997k). Subsequent mineralogical and/or petrographical examination and analysis of the discontinuities found in the borehole core around these FZ have produced evidence for the correlation between discontinuities containing particular types of mineral infills and flow zones intersecting the boreholes (NIREX, 1995c). These discontinuities or discrete horizons in the rock mass are considered, based on mineralogical and/or petrographical characteristics alone, to be capable of conducting groundwater flow within the present-day hydrogeological system. These features are called Potentially Flowing Features (PFF). PFF's have been characterised by the identification of late-stage calcite mineralisation, known as ME9 mineralisation, within a discontinuity combined with open porosity (NIREX, 1997e). Nine mineralisation episodes have been identified at Sellafield, termed ME1 to ME9. Table 3.5 describes these differing mineral episodes in more detail and provides an in-sight into the fluid evolution of the area over geological time (Table 2.4). ME9 mineralisation is inferred to be close to chemical equilibrium with the present-day groundwaters and may be actively precipitating and/or undergoing recrystallisation, at least in parts of the present-day groundwater system (NIREX, 1997e). Thus, the frequency, character and disposition of the PFF can be used to provide insights into the nature of the flowing

features within the BVG (NIREX, 1997e). NIREX, 1997e states that there is no single association of PFF or clusters of PFF with the geological structure of the BVG, although there appears to be a partial correlation with fault damage zones. Figure 3.10 illustrates a conceptual flow model that was developed by Nirex to represent the flow of discontinuities within the BVG.

3.2.2.2 – Carboniferous Limestone

In the Carboniferous Limestone, the groundwater flow is dominantly along joints and there is evidence of dissolution having created channelled openings (McL. Michie, 1996). Bedding plane fractures also remain open and there is abundant evidence from the development of stylolites (McL. Michie, 1996). The effective permeability of the Carboniferous is assumed to be much higher than that of the hydrogeological units above (Brockram) and below (BVG), and it therefore is thought to act as a preferential pathway for groundwater movement at depth (NIREX, 1997e). Groundwater flow through the Carboniferous is also significantly influenced both by faulting that wholly or partly disrupts the continuity of the unit (McL. Michie, 1996) and by the effects of over a century of sub-surface iron ore exploration, extraction and associated mine dewatering to the northwest of the Sellafield site (NIREX, 1997e).

3.2.2.3 – Permian Brockram

The hydrogeological properties of the Brockram are very variable (McL. Michie, 1996). It is essentially a low permeability unit but where faulting has modified the unit and caused a small number of discrete discontinuities to form, it can become quite transmissive (NIREX, 1997e). This modified Brockram becomes more susceptible to the leaching of mineral cements (mainly anhydrite) from its matrix, due to the increased rate of groundwater flow through the unit (NIREX, 1997e). Consequently, this causes flow connectivity to be increased between individual discontinuities and a secondary porosity increases the permeability of the unit (McL. Michie, 1996).

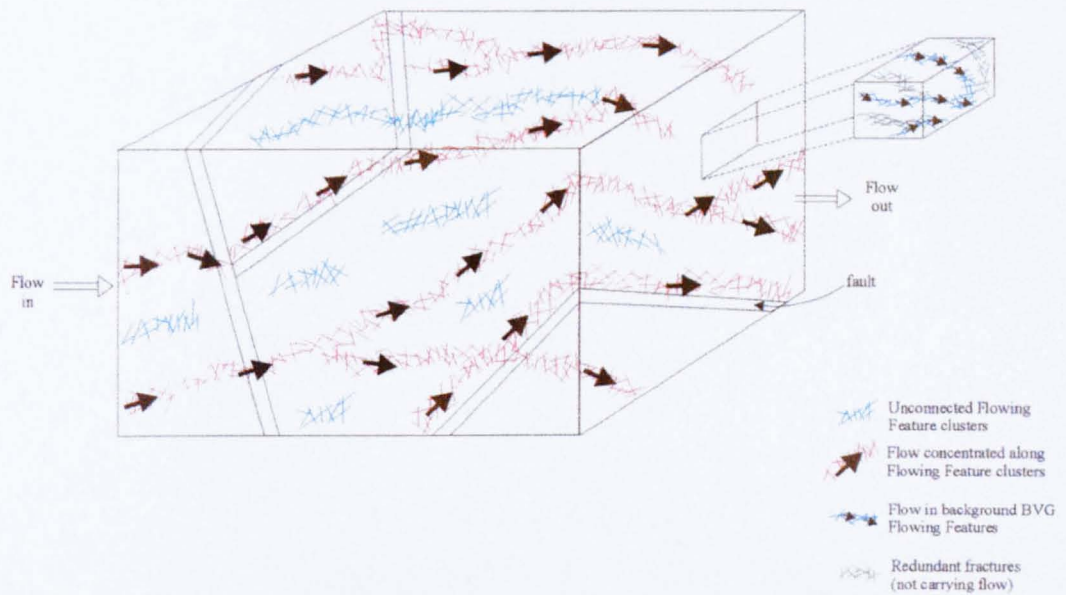


Figure 3.10 – Illustration of a possible conceptual flow model developed by Nirex to represent the flow of discontinuities within the BVG (NIREX, 1997e).

Mineralising Episode	Principal Associated Minerals	Dominant Type of Mineralisation
ME1	K-feldspar/adularia \pm quartz, \pm chlorite, \pm albite, \pm hematite	Silicate
ME2	<u>Quartz</u> \pm epidote, \pm calcite, \pm chlorite, \pm apatite, \pm K-feldspar, \pm albite, \pm sericite, \pm hematite	Silicate (and carbonate)
ME3	<u>Pyrite</u> \pm traces of chalcopyrite, arsenopyrite, marcasite, galena, sphalerite, Bi-Se sulphosalts and quartz	Sulphide (and possibly silicate)
ME4	<u>Anhydrite</u> \pm barite, \pm fluorite, \pm hematite, \pm quartz, \pm siderite (possibly), \pm K-feldspar	Sulphate
ME5	Albite, K-feldspar, <u>kaolinite</u> , <u>illite</u> , \pm hematite	Silicate
a	<i>Early ME6a: ferroan/manganous carbonate now replaced completely by specular hematite and <u>calcite</u> with abundant inclusions of Fe- and Mn-oxides. Late ME6a: <u>calcite</u> and hematite</i>	Carbonate
ME6 b	Dolomite, <u>ferroan dolomite</u> , ankerite, \pm siderite, \pm quartz, \pm anhydrite, \pm ferroan calcite	\pm sulphate
c	<u>Calcite</u> (usually ferroan) \pm barite, \pm fluorite, \pm hematite, \pm pyrite, \pm sphalerite, \pm galena	\pm sulphide
ME7	<u>Illitic clay</u> and <u>hematite</u>	Silicate and oxide
ME8	<u>Mn- and Fe-oxides/oxyhydroxides</u>	Oxide
ME9	<u>Calcite</u> \pm pyrite, \pm anhydrite, \pm gypsum	Carbonate \pm sulphate \pm sulphide

Table 3.5 – Mineralisation Episodes encountered at Sellafield (NIREX, 1997e).

3.2.2.4 – Permian St Bees Shale & St Bees Evaporite Group

These formations generally have a very low permeability and the existence of anhydrite and other soluble units indicate a very limited flow of groundwater through them (McL. Michie, 1996). Dissolution of the anhydrite and other soluble units could increase transmissivity in certain zones and cause localized increases in permeability (McL. Michie, 1996). Only a few flowing features (section 2.3.2.1) have been identified in the St Bees Shale and Evaporite Group. NIREX (1997e) suggest that these formations may form a partial barrier to vertical flow, at least locally.

2.3.2.5 – Triassic Sherwood Sandstone Group

The Sherwood Sandstone Group forms a coastal aquifer that is anisotropic, with horizontal hydraulic conductivity up to twenty times greater than the vertical conductivity. Groundwater flow through the Sherwood Sandstone is governed by their sedimentary architecture together with their subsequent burial and decompaction history, including diagenesis (NIREX, 1997e). The sandstones have a component of matrix permeability (flow) developed as a result of the influence of mineralisation and dissolution events superimposed on the on the basic sedimentary fabric causing a interconnected secondary porosity to have been developed (NIREX, 1997e). In places, there is also a component of discrete fracture permeability (flow), which occurs mainly through bedding-plane features, although at depths greater than 200 m, joints perpendicular to bedding are prominent and enhance flow (NIREX, 1997e). Because of the varying hydrogeological characteristics found within the Sherwood Sandstone Group, five distinct hydrogeological units have been identified. Table 3.6 describes each of these hydrogeological units in more detail.

Geological Unit		Major Hydrogeological Unit	Comments
Sherwood Sandstone Group	Ormskirk Sandstone Formation & Calder Sandstone Formation	Near-Surface Calder Sandstone	Unit variable thickness (to ca 200m), thins to the east. Open bedding plane features play important role in groundwater flow, together with a component of matrix flow. The open bedding plane features have a finite extent and are not extensively connected. Matrix flow plays an important role in determining regional scale groundwater flow.
		Undifferentiated Calder Sandstone	Unit at depths greater than 200m below ground level. Groundwater flow is predominantly through matrix flow and fracture flow is not considered to be significant.
	St Bees Sandstone Formation	Near-Surface St Bees Sandstone	Unit variable thickness (to ca 200m), thins to the east. Open bedding plane features play important role in groundwater flow, together with a component of matrix flow.
		Undifferentiated St Bees Sandstone	Unit at depths greater than 200m below ground level. Groundwater flow is predominantly through matrix flow and fracture flow is not considered to be significant.
		Basal part of the North Head Member	Unit defined as bottom 30m of the St Bees Sandstone Formation. Groundwater flow is predominantly through matrix flow and fracture flow is not considered to be significant.

Table 3.6 – Hydrogeological units in the Sherwood Sandstone Group (NIREX, 1997e).

3.2.2.6 – Triassic Mercia Mudstone Group

There is little direct information on the hydrogeological properties of the Mercia Mudstone Group, as it does not outcrop onshore at the Sellafield site or in any of the Sellafield boreholes. It is expected to have poor permeability, as does the Mercia Mudstone encountered in hydrocarbon reservoirs in the East Irish Sea Basin (McL. Michie, 1996). Offshore there is evidence, from seismic reflection surveys, that indicates disrupted and in places, dissolved salt horizons within the Mercia Mudstone Group (McL. Michie, 1996). Strong *et al.* (1994) and Bath *et al.* (1996) have both suggested that this indicates evidence of dissolution which could be the possible source of the groundwater salinity within the Hills and Basement, and Irish Sea Basin groundwater regimes.

3.2.2.7 – Quaternary

Within the heterogeneous Quaternary deposits at Sellafield distinct areas of hydrogeological character have been recognised. These are termed Hydrogeological Domains, and have been identified based on features governing run-off, limited recharge and discharge, and controlling the lateral and vertical flow within the unconsolidated sediments (NIREX, 1997e). Onshore around the Sellafield site, seven hydrogeological domains have been identified (Table 3.7 & Figure 3.11). These domains are described in more detail in Table 3.7 and located on Figure 3.11.

3.2.3 – PRZ Hydrogeology

A number of specialist hydrogeological studies within the PRZ boreholes were undertaken as part of Nirex's investigations into Sellafield as a potential radioactive waste repository (section 1.2). The results of these studies have been summarised in composite logs for each of the PRZ boreholes and are presented in Appendix 11, Volume III.

Description of Quaternary Hydrogeological Domains

Bedrock Domain	This comprises weathered rock outcrop, with locally thin layer of Drift. Recharge in such areas is largely governed by the permeability of the underlying bedrock, which may be less than that of the Drift. Some interflow may occur along the top of the bedrock, but is likely to be minor.
Thin Till Domain	Recharge and interflow are largely determined by the properties of the underlying solid rock, with interflow possibly occurring at the base of the Drift. Fracturing and fissuring in the till is important in conveying water through what otherwise might be a low permeability material.
Till & clay Domain	Although the upper part is fractured, recharge through this sequence is expected to be small, with a significant contribution to interflow.
Till-sand-till Domain	The upper till is fissured and is likely to permit water movement into the sand. Additional recharge is possible through windows in the upper till. The sand is permeable and carries water. The lower till may confine the underlying Sherwood Sandstone Group locally, restricting but not preventing interchange within the sands. The extent of this behaviour cannot be quantified with available data.
Lacustrine Domains (Single till, Double till or Multi till)	Interlayered sequences of tills (of medium to low permeability), silts (of low permeability) and lacustrine sands (of medium permeability). The uppermost part of the succession may be a thin till, restricting recharge and leading to localised development of peat bogs or perched aquifers isolated from the main Sherwood Sandstone Group aquifer. These sequences are expected largely to prevent recharge/discharge from the Sherwood Sandstone Group, although the limited existing data does not quantify the extent of this process.
Buried Channel Domain	Infilled channels with sequences of gravels, sands and interbedded tills. The gravels and sands are permeable, locally high so, and probably from a hydrogeologically continuous unit of appreciable extent. The till appears to delay and divert recharge rather than prevent it. The unit is, at least locally, in hydraulic continuity with the Sherwood Sandstone Group and probably forms a single aquifer with it.
Alluvial Domain (Alluvial Floodplain & Estuarine Deposits)	Alluvium associated with the floodplains of the modern valleys is generally coarse grained and permeable. In a number of places, the alluvium has cut down through low permeability surface deposits, to connect underlying sands with the surface.

Table 3.7 – Descriptions of Quaternary hydrogeological domains
(from Nirex, 1997h).

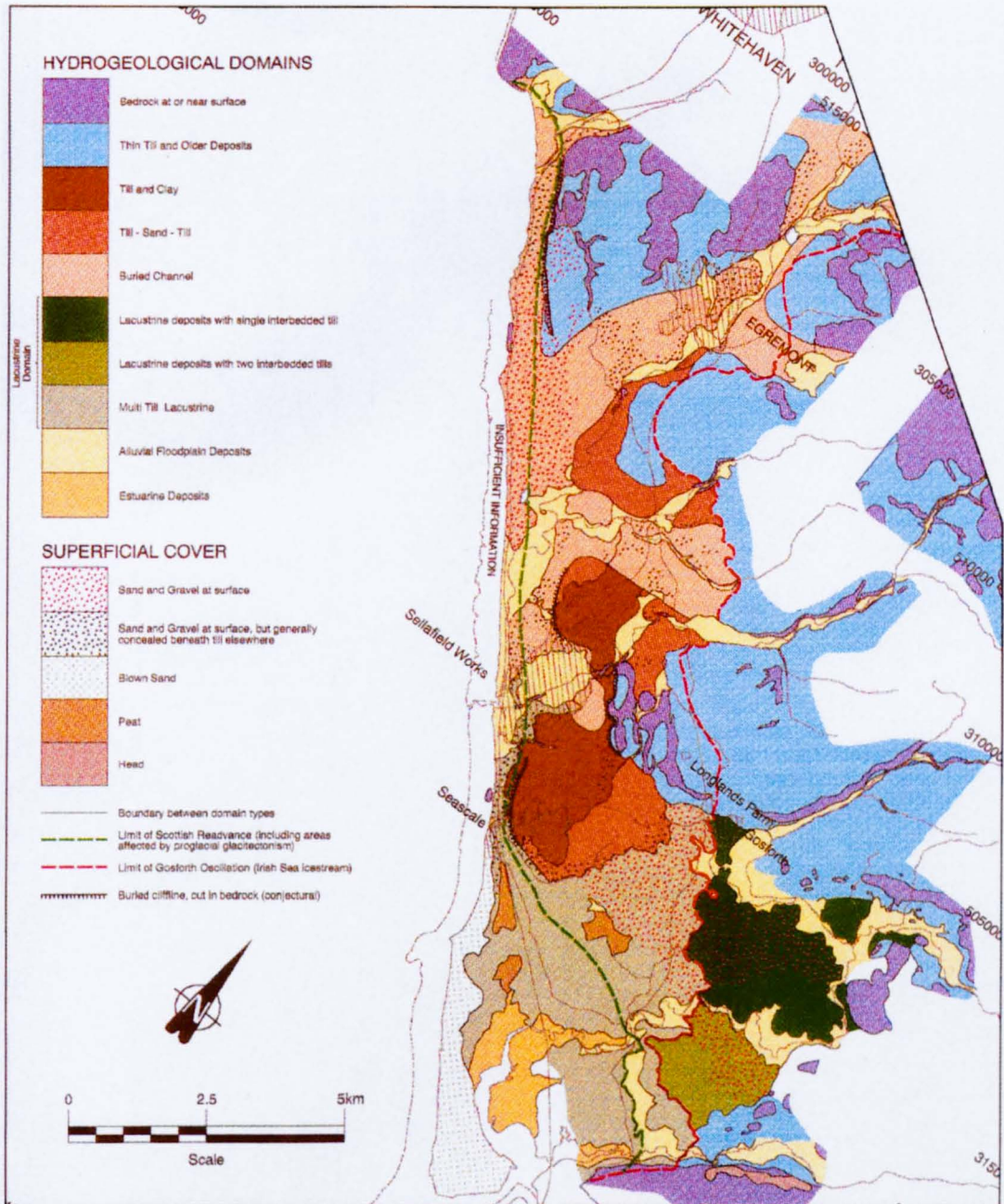


Figure 3.11 – Quaternary Hydrogeological Domains Map (from NIREX, 1997h).



4. - Regional Stress Map

4.1 Introduction

Brereton *et al.* (1997) produced a number of regional stress maps looking at breakouts encountered within the Borrowdale Volcanic Group (BVG) and the Permian-Triassic rocks at Sellafield as part of the Joule II, European Commission Research Project into reservoir anisotropy (section 2.3.4). Brereton *et al.* (1997) identified distinct similarities, particularly in the top one hundred meters of the BVG at Sellafield, between breakout orientations (σ_{Hmin}) and discontinuity dip azimuth orientations. They concluded that further detailed work was needed to understand the nature of the relationship between the stress field and discontinuities. The work discussed in this chapter investigates whether it is possible to eliminate the effects of discontinuities during *in situ* stress analysis and goes some way to aid the understanding of the relationship between stress fields and discontinuities. Also investigated and discussed here is the ability to detect breakout from the various geophysical downhole imaging tools used at Sellafield. In addition, an investigation into the occurrence of possible stress field rotations, with depth was undertaken.

4.2 Acquisition of *In Situ* Stress Data

In situ stress orientation data at Sellafield was obtained by analysing the elongation of the borehole cross-section, through the identification of borehole breakout (section 2.2.3.2). A comparison between the results obtained by Brereton *et al.* (1997) and this research could be undertaken in the top hundred meters of the BVG in the Sellafield boreholes (Table 4.1). This depth criterion allowed a large number of the Sellafield boreholes to be analysed, giving good coverage of the stress field in the area. It must be noted, however that within this depth range various lithostratigraphical units of the BVG are encountered (Table 4.1). Ideally, similar lithostratigraphical units are required for the *in situ* stress analysis of each borehole, but due to variability of the BVG, it is impossible to do so.

Breakout analysis was undertaken in Sellafield boreholes 2, 3, 5, 7A, 8A, 9A, 9B, 10A, 11A, 12A, 13A, 14A, RCF1, RCF2, RCF3, RCM1, RCM2, RCM3, PRZ2 and PRZ3 (Table 4.1). Unix-based software routines, developed by Dr. Chris Evans of the British Geological Survey (BGS), were used to identify borehole breakout from geophysical downhole image logs (BHTV/UBI and FMS/FMI). The BGS software routines divide into two separate programs, *Breaking* and *Breaknrb*.

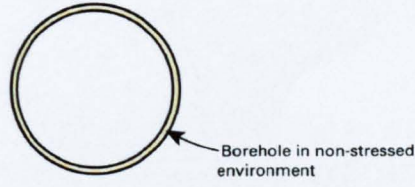
Breaking is the first element of the *in situ* stress analysis. BHTV/UBI (AMWF – amplitude of reflected signal waveform and TTWF – two-way travel time waveform) and FMS/FMI (conductance) logs from the Sellafield boreholes were statistically analysed to identify possible breakout orientations induced by the refraction and concentration of the stress tensors near the free surface of the borehole wall (section 2.2.3.3). This statistical approach recognises that non-breakout features will also be encompassed within the processing procedure, but by carrying out the analysis over a sufficiently large sample range (i.e. depth range) then the orientations of the breakout features will become orientationally randomised while the breakout features will become orientationally highlighted (Brereton, 1992). *Breaking* carries out this analysis by using either the amplitude, time or conductivity readings, from the relevant image tool, to measure the elongation or eccentricity (ECC) of the borehole (section 2.2.3.3 – Figure 4.1a/b/c). When using the BHTV/UBI tool for breakout analysis, the tools transducer measures both the AMWF and the TTWF between the tool and the borehole wall (section 2.2.3.3). Breakouts cause distortions to the waveforms, due to an increase in the amount of discontinuities encountered around a breakout (Paillet and Kim, 1987). Breakouts are reflected in the AMWF and TTWF image logs as vertical strips where poor reflectivity, long travel time or a loss of signal is encountered. The FMS/FMI tool use an array of electrodes on orientated pads and flaps to produce an electrical image of the borehole wall that can be interpreted as either conductive or resistive features (Figure 4.1c). Breakouts form long vertical strips showing areas of increased conductivity, due to the increase in the discontinuities encountered within the borehole around a breakout.

Borehole	Depth Range for the top 100m of the BVG (mbRT)	Trajectory of Borehole	Geology for for the top 100m of the BVG (Formation/Member)
BH2	468 - 568	Vertical	Fleming Hall/Longlands Farm
BH3	1621 - 1721	Vertical	Not named
BH5	490 - 590	Vertical	Fleming Hall/Longlands Farm
BH7A	578 - 678	Vertical	Yottenfew Formation
BH8A	203.1 - 303.1	Vertical	Not named
BH9A	29 - 129	Vertical	Not named
BH9B	24.7 - 124.7	Vertical	Not named
BH10A	999.03 - 1099.03	Vertical	Fleming Hall/ Town End Farm & Brown Bank/Seascale Hall
BH11A	964 - 1064	Vertical	Fleming Hall Formation
BH12A	930.75 - 1030.75	Vertical	Fleming Hall/Longlands Farm
BH13A	1620 - 1720	Vertical	Not named
BH14A	672 - 772	Vertical	Newton Manor Formation
RCF1	540 - 640	Deviated (~60m East)	Fleming Hall/Longlands Farm
RCF2	533 - 633	Deviated (~100m North)	Fleming Hall/Longlands Farm
RCF3	525 - 630	Vertical	Fleming Hall/Longlands Farm
RCM1	525 - 625	Vertical	Fleming Hall/Longlands Farm
RCM2	530 - 630	Vertical	Fleming Hall/Longlands Farm
RCM3	555 - 655	Deviated (~100m North)	Fleming Hall/Longlands Farm
PRZ2	459.71 - 559.71	Inclined (~175m East)	Fleming Hall/Longlands Farm
PRZ3	588.5 - 688.5	Inclined (~225m East)	Fleming Hall/Longlands Farm

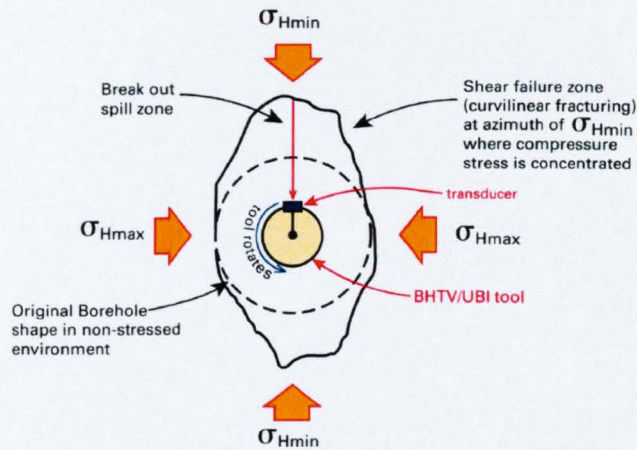
Table 4.1 – The depths, deviation and geology of the top one hundred meters of the BVG in the Sellafield boreholes (adapted from NIREX, 1995f & NIREX, 1996e).

The technique used to measure the eccentricity of the borehole depends on the type of image tool used (Figure 4.1b/c). BHTV/UBI AMWF and TTWF logs enable the actual shape of the borehole wall to be determined, by analyzing the values derived from the amplitude of the reflected waveform (AMWF log) and the two-way travel time (TTWF log). The amplitude of the reflected waveform (AMWF log) and the two-way travel time (TTWF log) are analysed at each depth, the amplitude or two-way travel time reading and there opposing reading are identified and then added together, so an average can be calculated (Figure 4.1b). This average then enables the maximum borehole diameter (D_{max}) and the minimum borehole diameter (D_{min}), with their associated azimuthal orientations to be determined. This averaging helps to ensure that if the BHTV/UBI image tool is not properly centered in the borehole then the breakout analysis is not affect (Figure 4.1b). The eccentricity (ECC) of the borehole can then be determined by calculating the difference between D_{max} and D_{min} . For the BHTV/UBI AMWF log it is the minimum amplitude that is correlated to an elongation of the borehole occurring. This is due to the AMWF log being a reflected waveform. For the BHTV/UBI TTWF log it is the maximum time traveled that is correlated to an elongation of the borehole occurring. The FMS/FMI log uses the information obtained from the orthogonal resistivity pads (section 2.2.3.3) and adds these values together so an average can be determine (Figure 4.1c). This average forms the D_{max} and D_{min} values. The eccentricity (ECC) of the borehole is then determined by calculating the difference between D_{max} and D_{min} . It is the eccentricity value that is then correlated to determine whether an elongation of the borehole has occurred. This elongation occurs due to a breakout being caused by a concentration of the stress tensor near the borehole wall (section 2.2.3.3). This causes an increase in the amount of discontinuities found around the borehole wall due to shear fracturing, which in turn causes an increased conductivity reading to be measured compared to the background rock signal (Figure 4.1c).

A) Non stressed Environment



B) Stressed Environment BHTV/UBI



C) Stressed Environment FMS/FMI

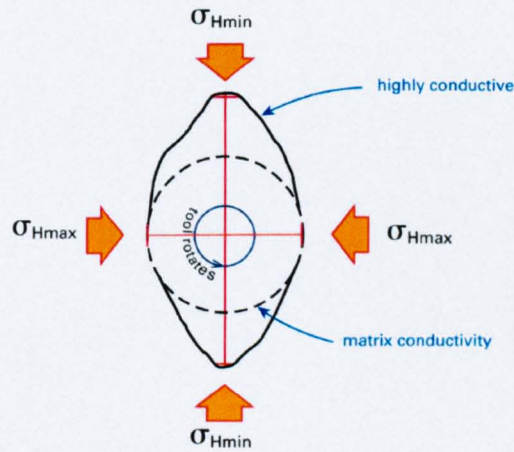


Figure 4.1 - A schematic cross-sectional view of a vertical borehole in the a) non-stressed environment & the deviatoric stressed environment (breakout) logged by the b) BHTV/UBI image tool and c) the FMS/FMI image tool.

One main principle that underpins the rationale behind the *Breaking* software is that *Breaking* is biased to breakout. The software tries to illuminate things that could be misinterpreted as breakout (i.e. image logging tool not centered; malfunctioning button on image tool – section 2.2.3.2). It applies the classical approach to breakout analysis, where the minimum amplitude, maximum time or maximum conductivity reading are assumed to represent the orientation in the borehole of σ_{Hmin} (breakout azimuth) and then assumes that at right angles to the σ_{Hmin} would be the σ_{Hmax} (Figure 4.1).

When the BHTV/UBI or FMS/FMI log data is loaded into *Breaking* it is processed and then vertically filtered. The filter is supposed to eliminate any noise in the image log data due to the effect of discontinuities, which are represented as short wavelengths (high frequencies) in the logs. The filtered data is then analysed by *Breaking* to identify breakout. A step-by-step guide of how to use *Breaking* is detailed in Appendix 2, section 2.1. The results from the *Breaking* analysis create an ASCII text output data file of the breakout results, an example of which is shown in Table 4.2.

After the image log data has been analysed for breakout, in *Breaking*, a second routine called *Breaknrb* is used to visualize the results from the breakout analysis. *Breaknrb* enables the breakout data to be visually represented as rose diagrams, histograms or cross plots for a specific depth range. A systematic guide of how to use *Breaknrb* to visualise the *Breaking* output data files is outlined in Appendix 2, section 2.2.

4.2.1 Preliminary Acquisition of *In Situ* Stress Data

Before the main *in situ* stress data were acquired, two preliminary studies were undertaken to investigate: -

- The capability of the geophysical imaging tools to detect the occurrence of breakouts in a borehole; and
- The best vertical filter to use on the geophysical imaging logs to eliminate the effects of discontinuities during *Breaking* analysis.

DEPTH	ECC	DMAX	DMIN	AMAX	AMIN
525.0434	-32.0863	32.0863	55.1881	51.84	139.68
525.0434	22.649	32.5093	55.527	51.84	141.12
525.0688	22.6417	32.8853	55.1726	51.84	139.68
525.0688	21.7248	33.2238	54.8693	51.84	139.68
525.0942	20.716	33.712	54.9788	51.84	178.56
525.0942	20.6693	33.8093	55.1236	50.4	178.56
525.1196	20.5504	33.5729	54.3218	50.4	178.56
525.1196	20.2791	33.3563	53.5867	50.4	178.56
525.145	19.4661	33.722	53.4467	50.4	141.12

Table 4.2 - Sample of Output Data File Created from *Breaking*.

When downhole geophysical imaging tools are used in boreholes for site characterisation and exploration studies, both onshore and offshore, it is the norm that only one type and generation of tool is used mainly due to cost. In the Sellafield boreholes, a number of differing types and generations of Schlumberger imaging tools (FMS/FMI and BHTV/UBI) were used. This provides a unique opportunity to assess the various imaging tools capabilities; in particular their ability to detect breakout. A small investigation into the comparison between the FMI (conductivity) and UBI (AMWF – amplitude waveform and TTWF – time traveled waveform) imaging tools abilities to detect breakout was undertaken. In addition, the effect of varying the length of the vertical filter was assessed for each tool. The objective here was to obtain an idea of the optimum filter length required to eliminate the effects of discontinuities without distorting the breakout.

For this analysis the top hundred meters of the BVG (525–630 mbRT) in Sellafield borehole RCF3 was used. The methods discussed in section 4.2.1 and the systematic guides of how to use *Breaking* and *Breaknr* in Appendix 2, section 2.1 and 2.2, were followed to obtain the results for this study. The default settings outlined in Appendix 2 were both used in *Breaking* and *Breaknr*, apart from applying a varying vertical filter in *Breaking* and using the rose diagram method to represent the breakout orientation in *Breaknr*. The image data was analysed in *Breaking* using no vertical filter, the default vertical filter (101 - FMI = 10 inch & UBI = 33 inch) and a one and two inch vertical filter (FMI = 33/71 and UBI = 11/21).

4.2.2 Main Acquisition of *In Situ* Stress Data

After the preliminary studies had been completed, the main *in situ* stress study was embarked upon. Recommendations from the preliminary study (Section 4.4.1) were applied to the main investigation. A systematic guide of how *Breaknr* and *Breaking* was used to produce the breakout analysis in the top hundred meters of the BVG (Table 4.1), in Sellafield boreholes 2, 3, 5, 7A, 8A, 9A, 9B, 10A, 11A, 12A, 13A, 14A, RCF1, RCF2, RCF3, RCM1,

RCM2, RCM3, PRZ2 and PRZ3, was developed and the routines are outlined in Appendix 3, sections 3.1 and 3.2.

To be able to assess whether discontinuities influence the breakout result even after vertically filtering, discontinuity data from the top hundred meters of the BVG (Table 4.1) in Sellafield boreholes 2, 3, 5, 7A, 8A, 9A, 9B, 10A, 11A, 12A, 13A, 14A, RCF1, RCF2, RCF3, RCM1, RCM2, RCM3, PRZ2 and PRZ3, were analysed. The discontinuity data were obtained by the identification of discontinuities from downhole geophysical image logs (FMS/FMI and BHTV/UBI). The methods used to acquire this discontinuity data are explained and discussed further in Chapter 5, section 5.4.

4.3 Presentation of Data

4.3.1 Presentation of Preliminary *In Situ* Stress Data

The results from the preliminary investigation's *in situ* stress analysis are presented in Table 4.3 and the rose plots associated with the results are in Appendix 4 (Figures App 4.1-4.12). Discussion of these results are presented in section 4.4.1.

4.3.2 Presentation of Main *In Situ* Stress Data

All the breakout orientations (σ_{Hmin}) from the top one hundred meters of the BVG are presented in the form of rose diagrams (Figure App 5.1-5.20, Appendix 5) to ease the comparison of results. The results from these diagrams are summarized in Table 4.4. To help aid the spatial visualisation of the breakout results with respect to the geological structure of the BVG, the breakout roses were mapped out onto the top of the BVG (basement) structure contours maps (Figure 4.2 a/b, Appendix 1B) from NIREX (1995) (Drawing No. 010053 & 010054) and onto an Ordnance Survey (OS) 1:50 000 base map (sheets 89 & 96). The breakout roses represented on Figure 4.3 a/b (Appendix 1B) show the assumed σ_{Hmax} direction (+90° from σ_{Hmin} , breakout orientation), to help with the visualisation of the stress field and its relationship to the geological structure at Sellafield.

Type of Image Tool	Filter Length (inches)	σ_{Hmin} Orientation (Degrees)	σ_{Hmax} Orientation (Degrees)	Confidence (+/-)	No. Data Points	Max Rose Value	Data File Used to Produce Results	Figure (Appendix 4)
BHTV (AMWF)	0	67.3	157.3	24.0	8266	0.09	rcf3_amwf_hjrbrkdef_525_630.dat	App 4.1
BHTV (AMWF)	33 (default)	70.6	160.6	21.3	8266	0.16	rcf3_amwf_ddef_525_630.dat	App 4.2
BHTV (AMWF)	1	70.9	160.9	22.0	8266	0.13	rcf3_amwf_varf33_525_630.dat	App 4.3
BHTV (AMWF)	2	70.9	160.9	22.0	8266	0.14	rcf3_amwf_varf71_525_630.dat	App 4.4
BHTV (TTWF)	0	24.4	114.4	24.8	8266	0.07	rcf3_ttwf_hjrbrkdef_525_630.dat	App 4.5
BHTV (TTWF)	33 (default)	37.8	127.8	24.1	8266	0.08	rcf3_ttwf_ddef_525_630.dat	App 4.6
BHTV (TTWF)	1	22.9	112.9	25.0	8266	0.07	rcf3_ttwf_varf33_525_630.dat	App 4.7
BHTV (TTWF)	2	169.3	259.3	25.0	8266	0.08	rcf3_ttwf_varf71_525_630.dat	App 4.8
FMI	0	135.2	225.2	25.8	8267	0.07	rcf3_fmi_hjrbrkdef_525_630.dat	App 4.9
FMI	10 (default)	31.8	121.8	26.3	8267	0.08	rcf3_fmi_ddef_525_630.dat	App 4.10
FMI	1	173.1	263.1	25.5	8267	0.07	rcf3_fmi_varf11_525_630.dat	App 4.11
FMI	2	174.3	264.3	25.7	8267	0.07	rcf3_fmi_varf21_525_630.dat	App 4.12

Table 4.3 - Results from the preliminary *in situ* stress investigation of the top one hundred meters of the BVG.

Borehole ID	Depth (mbRT)	σ_{Hmin} Orientation (Degrees)	σ_{Hmax} Orientation (Degrees)	Confidence (+/-)	No. Data Points	Max Rose Value	Data File Used to Produce Results	Figure (Appendix 5)
BH2	487 - 587	34.8	124.8	22.5	9842	0.10	sell2_amwf_hjrbrk_487_587.dat	App 5.1
BH3	1621 - 1721	15.3	105.3	27.2	9842	0.09	s3_amwf_hjrbrk_1621_1721.dat	App 5.2
BH5	490 - 590	83.5	173.5	25.4	9842	0.09	sell5_amwf_hjrbrk_490_590.dat	App 5.3
BH7A	578 - 678	75.1	165.1	22.9	9842	0.12	s7a_amwf_hjrbrk_578_678.dat	App 5.4
BH8A	203.1 - 303.1	152.8	242.8	21.6	9842	0.12	s8a_amwf_hjrbrk_203_303.dat	App 5.5
BH9A	29 - 119	58.7	148.7	21.8	8858	0.12	s9a_amwf_hjrbrk_29_119.dat	App 5.6
BH9B	24.7 - 124.7	71.6	161.6	23.7	9842	0.08	s9b_amwf_hjrbrk_24_124.dat	App 5.7
BH10A	1052.02 - 1152.02	68.6	158.6	20.6	9842	0.16	s10a_amwf_hjrbrk_1052_1152.dat	App 5.8
BH11A	1024 - 1124	167.9	257.9	24.3	9842	0.10	s11a_amwf_hjrbrk_1024_1124.dat	App 5.9
BH12A	930.75 - 980.75	85.1	175.1	24.1	9842	0.10	s12a_amwf_hjrbrk_930_980.dat	App 5.10
BH13A	1620 - 1720	101.9	191.9	24.9	9840	0.08	s13a_amwf_hjrbrk_1620_1720.dat	App 5.11
BH14A	721 - 821	88.6	178.6	20.1	9842	0.20	s14a_amwf_hjrbrk_721_821.dat	App 5.12
RCF1	565 - 640	119.3	209.3	19.4	7302	0.20	rcf1_amwf_hjrbrk_565_665.dat	App 5.13
RCF2	533 - 633	29.2	119.2	20.5	9842	0.17	rcf2_amwf_hjrbrk_533_633.dat	App 5.14
RCF3	525 - 630	70.9	160.9	22	8266	0.13	rcf3_amwf_hjrbrk_525_630.dat	App 5.15
RCM1	525 - 625	77.8	167.8	20.4	9842	0.16	rcm1_amwf_hjrbrk_525_625.dat	App 5.16
RCM2	530 - 630	73.3	163.3	18.8	9842	0.21	rcm2_amwf_hjrbrk_530_630.dat	App 5.17
RCM3	555 - 655	74.1	164.1	13	9842	0.27	rcm3_amwf_hjrbrk_555_655.dat	App 5.18
PRZ2	459.49 - 539.49	50.6	140.6	18.9	7874	0.18	prz2_amwf_hjrbrk_459_539.dat	App 5.19
PRZ3	588.5 - 688.5	171.7	261.7	20.8	9842	0.15	prz3_amwf_hjrbrk_588_688.dat	App 5.20

Table 4.4 - Results from the main *in situ* stress investigation of the top one hundred meters of the BVG.

The discontinuity dip azimuth orientation data were analysed so a comparison could be made against the breakout orientation. The discontinuity dip azimuth orientation rose plots are summarized in Table 4.5 and presented in Appendix 5 (Figures App5.21-5.40). The spatial relationship between the discontinuity results and the geological structure of the BVG, were mapped out onto the top of the BVG (basement) structure contours maps (NIREX, 1995 - Figure 4.4 a/b, Appendix 1B) and onto an Ordnance Survey (OS) 1:50 000 base map (sheets 89 & 96). This discontinuity data was visualised using a software routine, developed by Dr. Chris Evans (BGS), called Vector. It was used to assess and present the discontinuity data in the form of orientation roses. A systematic guide of how to use Vector, to produce orientation rose plots, is outlined in Appendix 2, section 3.0.

4.4 Analysis & Assessment of Results

4.4.1 Analysis & Assessment of Preliminary Results

The objective of the preliminary investigations were to assess how well the FMI image tool was able to detect borehole breakout compared to the UBI tool and how applying varying vertical filters to the borehole image log data affected *in situ* stress analysis. Breakout orientations were obtained for the top one hundred meters of the BVG (525 – 630 mbRT) in Sellafield borehole RCF3, using both the FMI and UBI image log data (Table 4.3). The UBI, amplitude (AMWF) and time traveled (TTWF) waveform data, generated breakout orientations (σ_{Hmin}) that were consistently orientated in a NE-SW direction (Figures App4.1 & 4.5, Appendix 5). The AMWF data generated a well-defined uniaxial breakout rose (Figure App 4.1, Appendix 5), orientated $067.3^\circ \pm 24.0^\circ$. The TTWF data generated a more circular shaped, less well defined breakout rose (Figure App4.5, Appendix 5), orientated in a direction of $024.4^\circ \pm 24.8^\circ$. The FMI conductivity data produced a breakout rose that was almost circular in shape (Figure 4.9, Appendix 5), with a breakout orientated in a NW-SE direction ($135.2^\circ \pm 25.8^\circ$).

Borehole ID	Depth (mbRT)	Mean Orientation (Degrees)	Confidence (+/-)	No. Data Points	Data File Used to Produce Results	Figure (Appendix 5)
BH2	487 - 587	150.3	16.3	7803	s2_BGS.spck	App 5.21
BH3	1621 - 1721	150.4	17.6	7174	s3_BGS.spck	App 5.22
BH5	490 - 590	76.7	23.8	6122	s5_BGS.spck	App 5.23
BH7A	578 - 678	136.3	20.7	2573	s7a_BGS.spck	App 5.24
BH8A	203.1 - 303.1	92.7	25.5	7144	s8a_BGS.spck	App 5.25
BH9A	29 - 119	85.2	22.3	3067	s9a_BGS.spck	App 5.26
BH9B	24.7 - 124.7	71.7	24.9	1476	s9b_BGS.spck	App 5.27
BH10A	1052.02 - 1152.02	69.7	21.8	6611	s10a_BGS.spck	App 5.28
BH11A	1024 - 1124	143.8	22.8	5213	s11a_BGS.spck	App 5.29
BH12A	930.75 - 980.75	148.5	18.6	5221	s12a_BGS.spck	App 5.30
BH13A	1620 - 1720	40.8	19.7	3947	s13a_BGS.spck	App 5.31
BH14A	721 - 821	15.8	11	4554	s14a_BGS.spck	App 5.32
RCF1	565 - 640	155.6	15.5	3768	rcf1_BGS.spck	App 5.33
RCF2	533 - 633	132.6	24.4	3041	rcf2_BGS.spck	App 5.34
RCF3	525 - 630	123.9	24.6	3712	rcf3_BGS.spck	App 5.35
RCM1	525 - 625	88.3	25.4	7126	rcm1_BGS.spck	App 5.36
RCM2	530 - 630	155.9	15.5	4820	rcm2_BGS.spck	App 5.37
RCM3	555 - 655	105.4	25.7	5889	rcm3_BGS.spck	App 5.38
PRZ2	459.49 - 539.49	85.3	24.9	2268	prz2_BGS.spck	App 5.39
PRZ3	588.5 - 688.5	139.5	22.8	3429	prz3_BGS.spck	App 5.40

Table 4.5 - Results from the discontinuity analysis of the top one hundred meters of the BVG.

A series of hydrofrac tests (section 2.2.3.2), carried out by Nirex in ten of the Sellafield boreholes, concluded that the mean orientation of σ_{Hmax} was 159/339°, within a range of results from 118/298° to 190/010° NIREX (1996a). The orientation of σ_{Hmin} is therefore interpreted as being at 90° to the σ_{Hmax} orientation giving a mean σ_{Hmin} orientation of 069/249°, within a range of 028/208° to 100/280°. This is in broad agreement with the UBI results, particularly the AMWF results. The FMI results are markedly anomalous compared to these hydrofrac results. From these observations, it is possible to conclude that the UBI, AMWF image log seems to be detecting the true stress field in the Sellafield region. The results and Nirex's hydrofrac test results are consistent with the UK regional stress (σ_{Hmax} orientation of NW-SE (135/315°) and σ_{Hmin} orientation of NE-SW (045/225°)) field that has been determined by Evans (1987).

When analysing the varying vertical filter, breakout orientations were also obtained for the same borehole (RCF3) and depth range (525 – 630 mbRT) as above (Table 4.3). The UBI image data again produced the most consistently orientated breakout orientation, with the AMWF breakout roses being well defined and uniaxially orientated in a NE direction (Figures App 4.1 - 4.4, Appendix 5). The TTWF breakout roses were more circular in shape and had a less well-defined orientation in a NNW-NE direction (Figures App 4.5 – 4.8, Appendix 5). By increasing the length of the vertical filter being applied to the UBI AMWF data, from no vertical filter up to a 33-inch (default setting - 101) vertical filter, the breakout rose became sharper and better defined (Figures App 4.1 – 4.4, Appendix 5). The overall mean breakout orientation of the UBI AMWF data did not change, within +/- 4° of each other (Table 4.3). The UBI TTWF data generally showed little improvement in the shape of the breakout rose, when applying the varying vertical filters (Figures App 4.5 – 4.8, Appendix 5). Only when the large 33 inch (default filter - 101) filter was used did the overall shape of the breakout rose change for the worse, becoming more biaxial in shape compared to the more circular uniaxial shape produced when using no vertical filter, a 1 inch

or 2 inch vertical filter. The overall mean breakout orientation of the UBI TTWF data did not change much, within +/- 15° of each other, apart from an anomalous orientation (169.3°) produced when a 2-inch vertical filter was applied to image log data (Table 4.3). The FMI breakout analysis produced a more variably oriented breakout rose, with the breakout direction rotating from an approximate NW-N direction, with no vertical filter, a 1 inch and 2 inch vertical filter, to a NE direction for a 10 inch (default filter - 101) vertical filter. The breakout rose was always very poorly defined, with a nearly circular shape to the breakout rose.

From the investigation it can be concluded that the best image tool to use for *in situ* stress breakout analysis, within the BVG is the UBI tool, in particular the AMWF log. Of the two tools analysed this image log was the most sensitive, for detecting borehole breakouts within the BVG at Sellafield. This log is therefore used for the *in situ* stress analysis within the main investigation in this chapter (section 4.2.2) and in any further breakout analysis carried out in this thesis. These results are consistent with the views of Newmark *et al.* (1984); Plumb *et al.* (1985); Rider (1996) and Prenskey (1999), who state that the AMWF, BHTV/UBI image log is the best for detecting the geometry of the borehole and detecting borehole breakout.

From the results of *in situ* stress analysis, it could be concluded that the FMI tool may not be functioning correctly. For example in the Amax (section 4.2) depth log, in Figure App 4.10 (Appendix 4), an oscillating, zigzagging effect can be observed. Usually the Amax depth log forms a consistent constant straight line. At 600.0m, there is a rapid change in gradient in both the Amax and Dmax depth logs (Figure App 4.10, Appendix 4), this is possibly caused due to breakouts occurring. By looking at the FMI and AMWF imagery logs for these depths, this is confirmed. Breakouts can be observed between 600.5–603.5 mbRT on the AMWF imagery log (Figure 4.5, Appendix 1B). The southerly direction for these observable breakouts is hidden within the analysed depth range due to the FMI tool not correctly imaging the borehole and therefore masking the true breakout results. The zigzagging effect seen

on the Amax depth log, in Figure App 4.10 (Appendix 4), is most likely the effect of the tool rotating around the borehole. As the FMI tool is pulled up the borehole, during the logging of the hole, a torque is introduced onto the drilling cable, which causes the tool to rotate. Usually you have a large amount of noise on the Amax signal from the four orthogonal pads (section 2.2.3.3) and the tool rotation cannot be observed. There are two possible reasons why the tool is not functioning correctly, a 'dead button' on the image tool or a problem with the pads not having good contact with the borehole wall. To be able to identify the problem accurately, the FMI image log for this section of borehole (Sellafield RCF3, 525-630mbRT) needs to be studied. Artefacts can then be identified within the log to help indicate which, if any of the problems above can explain why the tool seems not to be functioning correctly (artefacts are discussed in more detail in section 2.2.3.3). In this case the analysis of the image log suggests that all the buttons were working correctly, but there is a problem with one of the pads on the image tool. It is most likely that one of the arms on the tool is not pushing correctly against the borehole wall and is therefore hampering the contact of the pad with the borehole wall, although there are no obvious artefacts to indicate this problem. All that can be concluded is that the image tool was functioning within specification, but by trying to use this tool to image a crystalline rock mass, it is actually being applied beyond the remit of the tools specifications. The FMI tool was designed by Schlumberger for use in sedimentary hydrocarbon reservoirs that contained pore space (Schlumberger, 1992) and not for high resistivity crystalline rocks with limited pore space. The FMI image tool will not be used in any further stress analysis within this thesis.

When analysing the *in situ* stress results obtained whilst a varying vertical filter was applied to the image log data, it is apparent that some noise in the image log attributed to discontinuities has been eliminated (Table 4.3 and Figures App 4.1 – 4.12, Appendix 5). The use of the vertical filter has sharpened up the breakout roses. Using the data from the UBI AMWF image log, Figure 4.6 demonstrates how the discontinuity orientation rose (Figure App 5.35, Appendix5), for the top 100 meters of the BVG in borehole RCF3,

compares to the various breakout roses created when altering the vertical filter (Figures App 4.1–4.4, Appendix 5). This clearly shows how by increasing the length of the vertical filter the breakout rose becomes more uniaxial and orientationally better defined as the effect of the discontinuities noise on the image log is eliminated. It is also apparent however, that as the length of the vertical filter increases, the orientation range of the breakout result decreases. In effect, with the longer vertical filters (33 and 2 inch), the breakout results become desensitised. The image data is being heavily sub-sampled and causes the results to be smoothed out and therefore altered. It is vital that the vertical filter used in the *in situ* stress analysis reduces the effect of discontinuity noise with out greatly altering the breakout result produced. The only filter that meets both requirements is where the UBI AMWF image log has a 1-inch vertical filter. This is used in the *in situ* stress analyse within the main investigation and throughout this thesis.

4.4.2 Analysis & Assessment of Main Results

The main objective of this analysis was to produce breakout roses, applying the vertical filter, for the top one hundred meters of the BVG. These results (Figure 4.2 a/b & 4.3 a/b, Appendix 1B) can then be compared to those of Brereton *et al.* (1997) which are an unfiltered breakout analysis (Figure 4.7) of the same boreholes. Breakout orientations were obtained during the present study for the top one hundred meters of the BGV (Table 4.1) in Sellafield boreholes 2, 3, 5, 7A, 8A, 9A, 9B, 10A, 11A, 12A, 13A, 14A, RCF1, RCF2, RCF3, RCM1, RCM2, RCM3, PRZ2 and PRZ3 (Table 4.4 and Figures App 5.1-5.20, Appendix 5). In Sellafield boreholes 2, 9A, 10A, 11A, 12A, 14A, RCF1 and PRZ2, it was not possible to analyse the top 100 meters of the BVG, since in these boreholes the image log run ended and started within this depth range. Various solutions to this problem were found. In borehole 2, the depth range was moved slightly down the borehole, by 19 meters, to 487-587mbRT. In boreholes 10A, 11A, 12A, 14A and RCF1 the image logs were analysed on both sides of the log run break, as well as the closest one hundred meters in the BVG after the break in the log run.

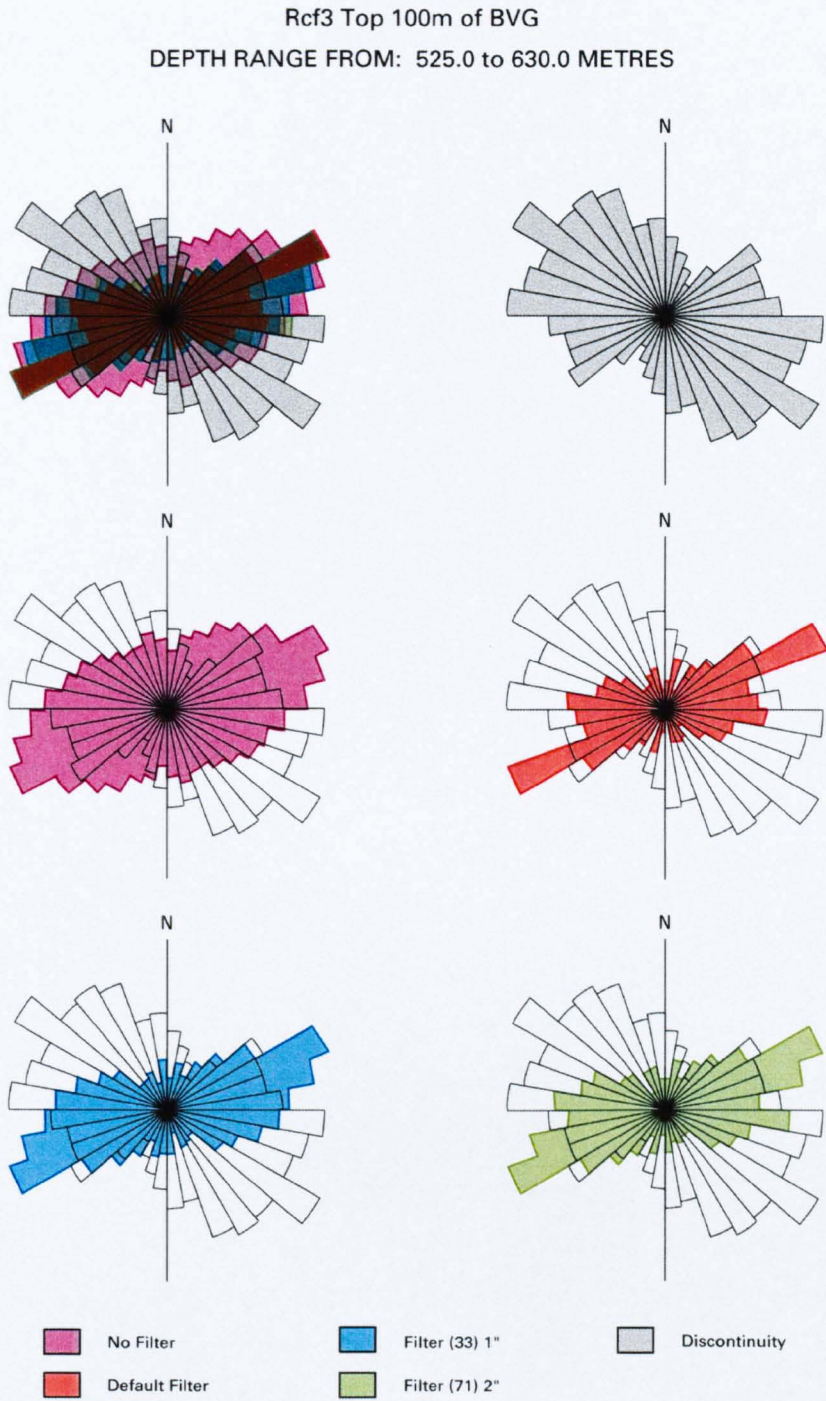


Figure 4.6 – Summary figure of all the UBI (AMWF) filtered and unfiltered breakout roses for the top one hundred meters of the BVG in RCF3, compared to the discontinuity dip azimuth orientation rose.

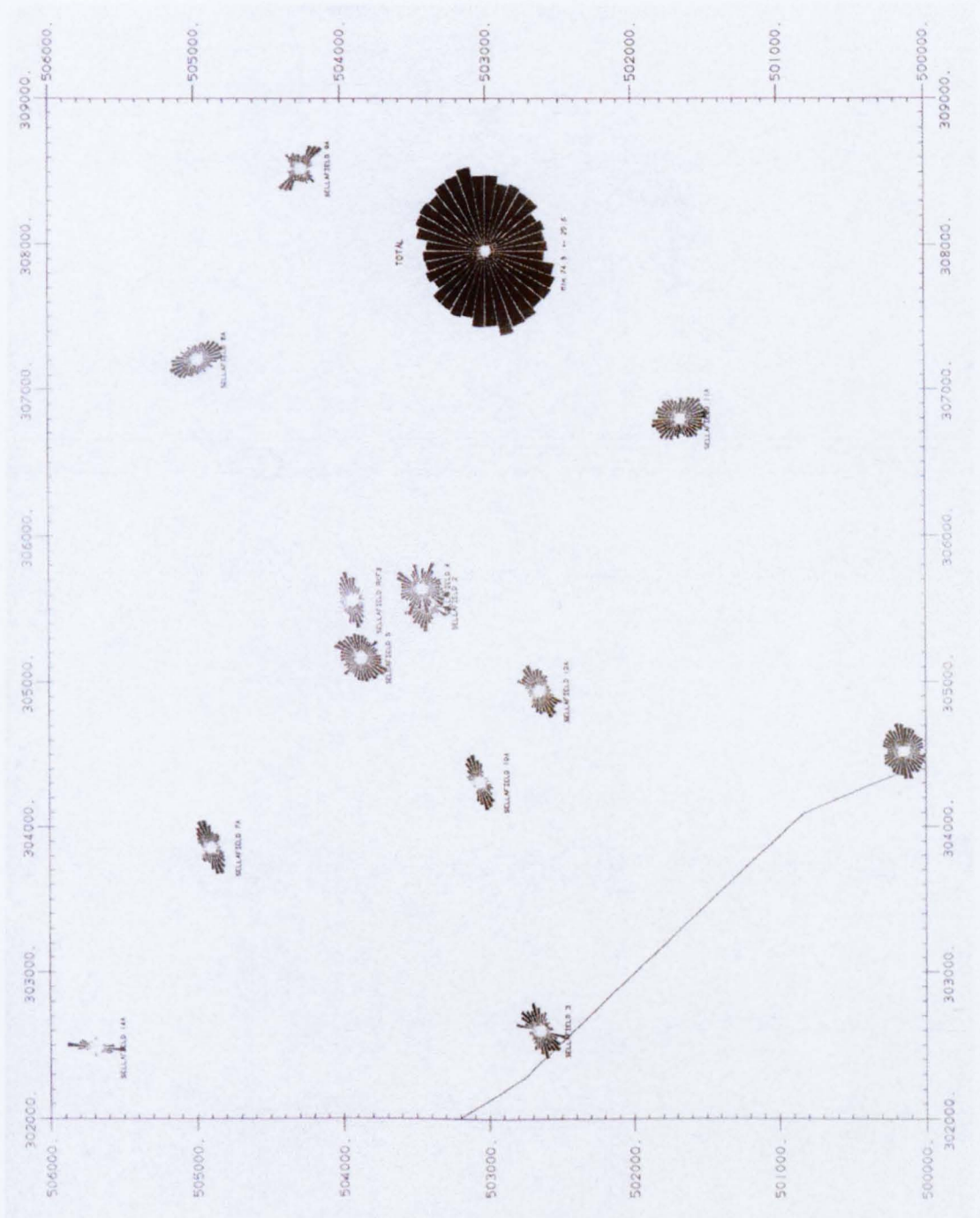


Figure 4.7 - Brereton *et al.*, 1997 breakout rose diagram for the top one hundred meters of the BVG at Sellafield using BHTV AMWF logs.

The most representative breakout result was then used in the analysis of the top one hundred meters of the BVG. Table 4.6 summarizes these results and highlights the results used in the top one hundred meters of the BVG *in situ* stress analysis in Table 4.4 (Figure 4.2 a/b & 4.3 a/b, Appendix 1B). In boreholes 9A and PRZ2 the depth ranges analysed were slightly decreased.

When the breakout roses from this *in situ* stress analysis (Figures App 5.1-5.20, Appendix 5 and Figure 4.2 a/b, Appendix 1B) were compared to the breakout roses created by Brereton *et al.* (1997) in Figure 4.7, it was apparent that this analysis created breakout roses that were generally better defined and uniaxial in shape. There were a few exceptions. Borehole 3 did not show any improvement in the shape of the breakout rose (Figure 4.2 a/b, Appendix 1B). In fact, the breakout rose was more dispersed and circular compared to that of Brereton *et al.* (1997), Figure 4.7. Borehole 2 had a sharper breakout rose, but was still biaxial in shape (Figure 4.2 a/b, Appendix 1B). Boreholes 5, 7A, 10A & 12A showed only slight improvement in breakout shape (Figure 4.2 a/b, Appendix 1B). In addition, boreholes 9B, RCF1, RCF2, RCM1, RCM2, RCM3, PRZ2 and PRZ3 could not be compared since Brereton *et al.* (1997), did not analyse these in their study because the boreholes were deviated (Table 4.1). Deviated boreholes can complicate the computation of the principal stress (section 2.2.3.3). They were analysed here to see how the results differed from the results of the surrounding boreholes, which were not deviated. As can be seen from Figure App 5.18 and 5.19 (Appendix 5) and Table 4.4, boreholes RCM3 (σ_{Hmin} 74.1°) and PRZ2 (σ_{Hmin} 50.6°) produced breakout (σ_{Hmin}) results that were consistent with results in the surrounding non-deviated boreholes (Figure 4.2 a/b). Borehole RCF1 (σ_{Hmin} 119.3°) produced a breakout rose (Figure App 5.13, Appendix 5, & Table 4.4) that was slightly rotated (~-45°) from the surrounding non-deviated boreholes (Figure 4.2 a/b, Appendix 1B). Borehole RCF2 (σ_{Hmin} 29.2°) produced a breakout rose (Figure App 5.14, Appendix 5, & Table 4.4) that was slightly rotated (~+45°) from the surrounding non-deviated boreholes (Figure 4.2 a/b, Appendix 1B).

Borehole ID	Depth (mbRT)	σ_{Hmin} Orientation (Degrees)	σ_{Hmax} Orientation (Degrees)	Confidence (+/-)	No. Data Points	Max Rose Value	Data File Used to Produce Results	Figure (Appendix 5)
BH10A	999 - 1051	64	154	18.6	6824	0.19	s10a_amwf_hjrbrk_999_1051.dat	App 5.8b
BH10A	1052.02 - 1099	72.3	162.3	21.3	9248	0.15	s10a_amwf_hjrbrk_1052_1099.dat	App 5.8c
BH10A	1052.02 - 1152.02	68.6	158.6	20.6	9842	0.16	s10a_amwf_hjrbrk_1052_1152.dat	App 5.8a
BH11A	964 - 1024	175.2	265.2	24.9	7874	0.07	s11a_amwf_hjrbrk_964_1024.dat	App 5.9b
BH11A	1024 - 1064	162.9	252.9	24.8	3936	0.08	s11a_amwf_hjrbrk_1024_1124.dat	App 5.9c
BH11A	1024 - 1124	167.9	257.9	24.3	9842	0.1	s11a_amwf_hjrbrk_1024_1124.dat	App 5.9a
BH12A	930.75 - 980.75	85.1	175.1	24.1	9842	0.1	s12a_amwf_hjrbrk_930_980.dat	App 5.10b
BH12A	980.75 - 1030.75	72.2	162.2	25.5	4920	0.09	s12a_amwf_hjrbrk_980_1080.dat	App 5.10c
BH12A	980.75 - 1080.75	72.6	162.6	24.7	9842	0.09	s12a_amwf_hjrbrk_980_1080.dat	App 5.10a
BH14A	672 - 723	4.5	94.5	22.3	6692	0.14	s14a_amwf_hjrbrk_672_723.dat	App 5.12b
BH14A	721 - 772	90.8	180.8	18.4	5020	0.17	s14a_amwf_hjrbrk_721_821.dat	App 5.12c
BH14A	721 - 821	88.6	178.6	20.1	9842	0.2	s14a_amwf_hjrbrk_721_821.dat	App 5.12a
RCF1	540 - 570	109.6	199.6	21.7	5904	0.14	rcf1_amwf_hjrbrk_540_570.dat	App 5.13b
RCF1	565 - 640	119.3	209.3	19.4	7302	0.2	rcf1_amwf_hjrbrk_565_665.dat	App 5.13a
RCF1	565 - 665	117.3	207.3	20.6	9842	0.16	rcf1_amwf_hjrbrk_565_665.dat	App 5.13c

Table 4.6 – Summary of the representative results for boreholes 10A, 11A, 12A, 14A and RCF1, which had problems analysing the top 100m of BVG due to log runs start/stopping (Highlighted results are used in the top one hundred meters of the BVG stress map).

Both Borehole RCF1 and RCF2 produced breakout roses (Figure 4.2 a/b, Appendix 1B) that were in broad agreement with the mean orientation of σ_{Hmax} 159/339 (σ_{Hmin} 069/249° - section 4.4.1), within a range of σ_{Hmax} 028/208 (σ_{Hmin} 118/298°) to σ_{Hmax} 100/280° (σ_{Hmin} 190/010°), derived from hydrofrac analysis (section 2.2.3.3) carried out by Nirex (NIREX, 1996a). Borehole PRZ3 (σ_{Hmin} 171.7°) produced a breakout result (Figure 4.2 a/b, Appendix 1B, Figure App 5.40, Appendix 5, & Table 4.4) that was rotated (~ +100°) from the surrounding non-deviated boreholes, and did not tally with the mean orientation of σ_{Hmax} from Nirex's hydrofrac analysis. By comparing the amount of deviation (Table 4.1) of the boreholes (RCF1, RCF2, RCM3, PRZ2 & PRZ3) and the breakout results (Table 4.4 & Figure 4.2 a/b, Appendix 1B) it seems that there is an approximate correlation between the amount a borehole's trajectory is deviated and the divergence of the breakout result produced, but by how much and in what direction is difficult to assess. Further investigation is needed to quantify this relationship, but is beyond the scope of this thesis. The breakout results recorded for the deviated boreholes are therefore concluded to be unrepresentative of the true stress regime encountered within the borehole and therefore the results will be disregarded from further analysis here.

When looking at the breakout roses created in this investigation (Figures App 5.1-5.20, Appendix 5 and Figure 4.2 a/b, Appendix 1B) and comparing them to the discontinuity dip azimuth orientation roses (Figures App 5.21-5.40, Appendix 5 and Figure 4.4 a/b, Appendix 1B) in the majority of cases any effect likely to have attributed to background discontinuity noise has been reduced. When compared to Brereton *et al.* (1997) results (Figure 4.7). Table 4.7 and Figure 4.8 summarizes the orientation results from the breakout and discontinuity roses, and compares the two data sets. It is apparent that most of the boreholes still show some signs of the effects of discontinuities in the breakout roses, but the shape of the breakout roses are sharper, indicating that the vertical filter has improved the clarity of the breakout results produced (Figure 4.2 a/b Appendix 1B, Figure 4.7 & Figure 4.8).

Borehole ID	Depth (mbRT)	Reeves Breakout σ_{break} Orientation (Degrees)	Comment on breakout rose produced	Brereton et al 1997 breakout σ_{break} Orientation (Degrees)	Discontinuity Mean Orientation (Degrees)	Comment on discontinuity rose produced	Comment on comparison of breakout rose to discontinuity rose
BH2	487 - 587	34.8	Biaxial - axis NE-SW & NW-SE	87.0	150.3	Biaxial - axis NNW-SSE & ENE-WSW	Effects of discontinuities still observed in breakout results. Breakout rotated (+90°) in comparison the Brereton et al (1997).
BH3	1621 - 1721	15.3	Circular biaxial - axis NNE-SSW & WNW-ESE	73.0	150.4	Biaxial - axis N-S & E-W	Effects of discontinuities still observed in breakout results. Effects increased in comparison the Brereton et al (1997).
BH5	490 - 590	83.5	Circular biaxial - axis E-W & NE-SW	28.0	76.7	Circular uniaxial - E-W	Effects of discontinuities still observed in breakout results. Effects slightly reduced and breakout rotated (+45°) in comparison the Brereton et al (1997).
BH7A	578 - 678	75.1	Biaxial - axis ENE-WSW & NW-SE	65.0	79.2	Circular biaxial - axis ENE-WSW & NNW-SSE	Effects of discontinuities still observed in breakout results. Effects reduced in comparison the Brereton et al (1997).
BH8A	203.1 - 303.1	152.8	Uniaxial - NNW-SSE, with small biaxial component (NE-SW)	157.0	92.7	Circular biaxial - axis ENE-WSW & NNW-SSE	Small effects of discontinuities still observed in breakout results. Effects reduced in comparison the Brereton et al (1997).
BH9A	29 - 119	58.7	Uniaxial - NE-SW, with small biaxial component (N-S)	136.0	85.2	Biaxial - axis ENE-WSW & N-S	Effects of discontinuities still observed in breakout results. Breakout rotated (+90°) in comparison the Brereton et al (1997).
BH9B	24.7 - 124.7	71.6	Uniaxial - NE-SW, with small biaxial component (NNW-SSE)	Not Analysed	71.7	Biaxial - axis NE-SW & NNW-SSE	Effects of discontinuities still observed in breakout results. Not able to compare to Brereton et al (1997) as they did not analyse.
BH10A	1052.02 - 1152.02	68.6	Uniaxial - ENE-WSW	74.0	69.7	Biaxial - axis ENE-WSW & NNW-SSE	Small effects of discontinuities still observed in breakout results. Effects slightly reduced in comparison the Brereton et al (1997).
BH11A	1024 - 1124	167.9	Circular uniaxial - NNE-SSW	169.0	143.8	Biaxial - axis NNW-SSE & NE-SW	Effects of discontinuities still observed in breakout results. Effects reduced in comparison the Brereton et al (1997).
BH12A	930.75 - 980.75	85.1	Uniaxial - E-W, with small biaxial component (N-S)	64.0	148.5	Biaxial - axis NNW-SSE & ENE-WSW	Small effects of discontinuities still observed in breakout results. Effects slightly reduced and breakout rotated (+45°) in comparison the Brereton et al (1997).
BH13A	1620 - 1720	101.9	Circular biaxial - axis ENE-WSW & NE-SW	76.0	40.8	Circular uniaxial - NE-SW	Effects of discontinuities still observed in breakout results. Effects reduced in comparison the Brereton et al (1997).
BH14A	721 - 821	88.6	Uniaxial - W-E, with small biaxial component (N-S)	8.0	15.8	Biaxial - axis N-S & NW-SE	Effects of discontinuities still observed in breakout results. Breakout rotated (+90°) in comparison the Brereton et al (1997).
RCF3	525 - 630	70.9	Circular uniaxial - NE-SW	74.0	123.9	Circular uniaxial - NW-SE	Small effects of discontinuities still observed in breakout results. Effects reduced in comparison the Brereton et al (1997).
RCM1	525 - 625	77.8	Uniaxial - ENE-WSW, with small biaxial component (NNE-SSW)	Not Analysed	88.3	Circular biaxial - axis NW-SE & NE-SW	Small effects of discontinuities still observed in breakout results. Not able to compare to Brereton et al (1997) as they did not analyse.
RCM2	530 - 630	73.3	Uniaxial - ENE-WSW	Not Analysed	155.9	Circular biaxial - axis NNW-SSE & ENE-WSW	Small if any effects of discontinuities still observed in breakout results. Not able to compare to Brereton et al (1997) as they did not analyse.

Table 4.7 – Comparison of the mean breakout and discontinuity orientation results for the top 100m of the BVG.

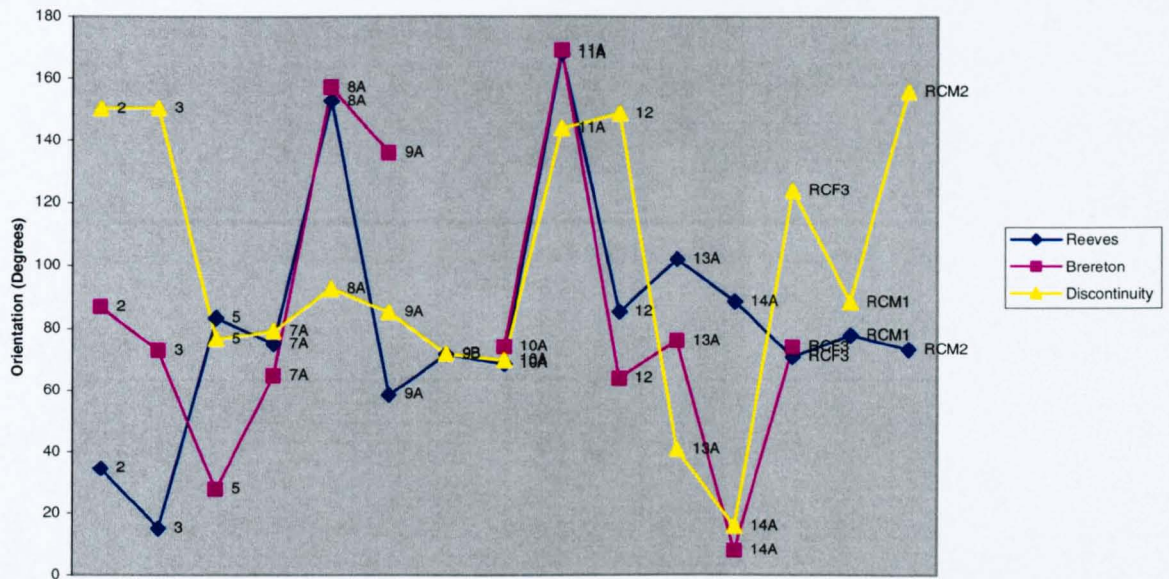


Figure 4.8 – Figure representing the mean orientation of Reeves' breakout (σ_{Hmin}) results, Brereton et al (1997) breakout (σ_{Hmin}) results & Reeves' discontinuity results for the top 100m of the BVG in the Sellafield Boreholes.

To check if there is any correlation between the mean breakout orientation (σ_{Hmin}) and the mean discontinuity dip azimuth orientation, a cross plot of the two results was produced (Figure 4.9a). The random scatter of data suggests no obvious linear correlation between the results. It is difficult to place a linear trend line (Figure 4.9b) through the data points that produces a good value for the coefficient of determination (R-squared). R-squared gives an indication of how closely the estimated values for the trend line correspond to the data, by using a range in values from zero to one. A trend line is most reliable when its R-squared value is at or near one. The linear trend line (Figure 4.9b) produces an R-squared value of 0.0002, it can therefore be concluded that the trend line does not correspond very well to the breakout orientation (σ_{Hmin}) versus the mean discontinuity dip azimuth orientation data. This suggests that the vertical filter has worked effectively.

One observation that can be concluded from Figure 4.9a is that the breakout orientation results show two distinct patterns:-

- A primary clustering of breakout orientations around σ_{Hmin} (derived from Nirex's hydrofrac test results (NIREX, 1996a - section 4.4.1)),
- A secondary clustering of breakout orientations around σ_{Hmax} (derived from Nirex's hydrofrac test results (NIREX, 1996a - section 4.4.1)).

The clustering of breakout orientations around σ_{Hmin} shows a greater degree of scatter, when the orientations of discontinuities fall close to σ_{Hmax} . This effect suggests that the breakout results have been defocused by discontinuities interacting with stress field (σ_{Hmax}) causing drilling induced tensile discontinuities (section 2.2.3.3) to form. The clustering of breakout orientations around σ_{Hmax} also indicates hydrofrac style, drilling induced tensile discontinuities are forming within some of the Sellafield boreholes and are causing the breakout direction to be misinterpreted. It can therefore be concluded that in areas where discontinuities are orientated closed to σ_{Hmax} , interaction with the stress field can cause drilling induced tensile discontinuities to form resulting in anomalous breakout orientations to be measured.

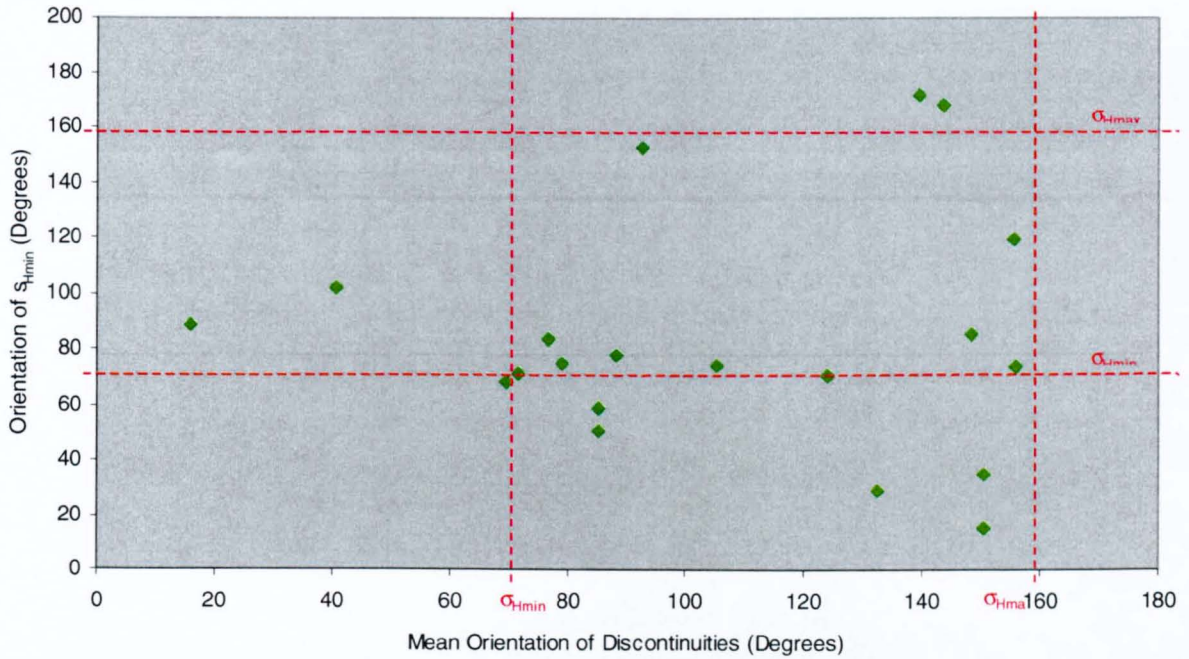


Figure 4.9a – Cross Plot of mean discontinuity orientation against mean σ_{Hmin} direction. σ_{Hmin} and σ_{Hmax} orientation lines are derived from Nirex's hydrofrac test results (NIREX, 1996a), which concluded that the mean orientation of σ_{Hmax} was $159/339^\circ$, within a range of results from $118/298^\circ$ to $190/010^\circ$ and the mean σ_{Hmin} orientation was $069/249^\circ$, within a range of $028/208^\circ$ to $100/280^\circ$.

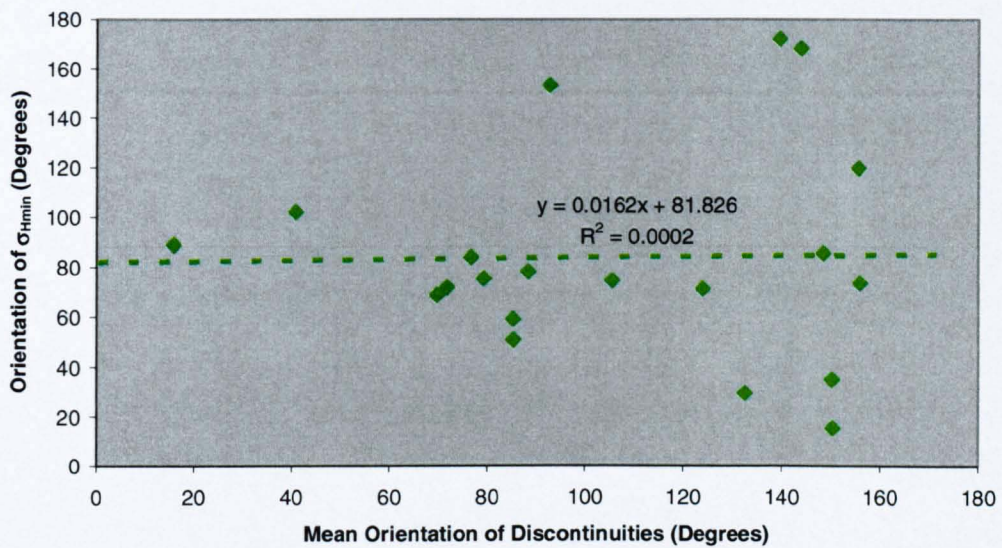


Figure 4.9b – Cross Plot of mean discontinuity orientation against mean σ_{Hmin} direction with linear trend line. σ_{Hmin} and σ_{Hmax} orientation lines are derived from Nirex's hydrofrac test results (NIREX, 1996a), which concluded that the mean orientation of σ_{Hmax} was $159/339^\circ$, within a range of results from $118/298^\circ$ to $190/010^\circ$ and the mean σ_{Hmin} orientation was $069/249^\circ$, within a range of $028/208^\circ$ to $100/280^\circ$.

The mean breakout orientation (σ_{Hmin}) for most of the results produced in this analysis (Figures 4.2 a/b, Appendix 1B) have very similar directions to the breakouts produced by Brereton *et al.* (1997) in Figure 4.7. Figure 4.8 demonstrates this observation and highlights that boreholes 2, 3, 5, 9A, 12A, 13A and 14A show rotations of the mean breakout orientation (σ_{Hmin}) compared to those calculated by Brereton *et al.* (1997). In boreholes 5, 9A & 14A rotations have caused the breakout orientations (σ_{Hmin}) to be in closer agreement to the mean orientation of σ_{Hmax} of $159/339^\circ$ (σ_{Hmin} $069/249^\circ$ - section 4.4.1), derived from hydrofrac analysis carried out by Nirex (NIREX, 1996a), compared to the breakout analysis by Brereton *et al.* (1997). Whether the use of the vertical filter has caused these rotations is difficult to assess. For borehole 14A, the use of the vertical filter has removed the effects of discontinuities noise from the breakout rose and has caused a $\sim +90^\circ$ rotation of the breakout rose away from the mean orientation of the discontinuity rose. In boreholes 5 and 9A it is more difficult to come to any definite conclusions as the breakout rose and discontinuity rose are orientated in the same direction. With boreholes 2, 3, 12A & 13A the breakout orientation has not improved, in fact the breakout orientation has moved away from the Nirex derived hydrofrac (NIREX, 1996a) interpreted result of σ_{Hmin} (section 4.4.1). In the case of boreholes 2 & 3 they have moved closer to the mean discontinuity orientation.

The σ_{Hmax} orientated breakout results obtained from most boreholes shown on Figure 4.3 a/b (Appendix 1B) and Figure 4.8, agree well with the mean σ_{Hmax} orientation of $159/339^\circ$ (section 4.4.1), within a range of $118/298^\circ$ to $190/010^\circ$, derived from hydrofrac analysis carried out by Nirex (NIREX, 1996a). Boreholes 3, 8A and 11A did not follow this trend. Large faults lie close to these boreholes (Figure 4.3 a, Appendix 1B) and it is possible that stress perturbations and/or rotation of the stress field (section 2.3.2) could have occurred here as has been previously suggested in other settings by a number of authors (Springer, 1987, Bell, 1989 & Zoback *et al.*, 1989; Barton and Zoback, 1994). Due to the nature of the BVG (highly fractured and

faulted rock mass – section 3.1.2), local perturbations of the stress field (section 2.3.2) could occur within the borehole due to the intersection with faults and fractures (Shamir and Zoback, 1989; Rawnsley *et al.*, 1992; Barton and Zoback, 1994). This might explain the anomalous mean orientations of σ_{Hmax} observed in Figure 4.3a, Appendix 1B. A small investigation to examine these possible stress perturbation/rotations was undertaken using *Breaknrb*. *Breaknrb* was used to visualise the original breakout results, generated by *Breaking*, as a stress profile. The top one hundred meters of the BVG in all the vertical boreholes analysed (Table 4.1) for the main investigation (section 4.2.2), boreholes 2, 3, 5, 7A, 8A, 9A, 9B, 10A, 11A, 12A, 13A, 14A, RCF3, RCM1 & RCM2 were examined. The methodology used to create these stress profiles is described in Appendix 3, Section 3.0. The results of the stress profiles are presented in Appendix 5, Figures App 5.41-5.55 and are summarised in Table 4.8, Appendix 1A. The location of all faults encountered within each of the stress profiles analysed were added to each stress profile. The locations of all these faults were obtained from the Nirex Digital Geoscience Database (NDGD – NIREX, 1996c). This fault data is presented in Appendix 5, Table App 5.1.

From this analysis it can be concluded that three types of stress profiles were identified in the Sellafield boreholes (Table 4.8, Appendix 1A): -

- Profiles that demonstrate a consistent σ_{Hmin} (breakout - A_{min}), orientation across the depth range analysed (Figure 4.10a, Appendix 1B), with no more than a 30° orientation range for σ_{Hmin} (e.g. borehole 12A),
- Profiles that have a rapid change in gradient in the σ_{Hmin} orientation across the depth range analysed (Figure 4.10b, Appendix 1B), but otherwise demonstrate a consistent orientation (e.g. boreholes 7A, 8A, 9A, 9B, 10A, 14A, RCF3, RCM1 & RCM2),
- Profiles that display a variable σ_{Hmin} orientation (Figure 4.10c, Appendix 1B) across the depth range analysed (e.g. boreholes 2, 3, 5, 11A & 13A).

Boreholes 5, 7A, 10A and 14A (Figure 4.11, Appendix 1B) are the only boreholes where the location of faults and rotations of the stress field are observed to occur simultaneously across the stress profile (Figure App 5.43, 5.44, 5.48 & 5.52, Appendix 5). However, within all these boreholes, there is no direct correlation found between the types of stress profile produced or the number of faults present (Table 4.8, Appendix 1A) that might help to identify boreholes where stress rotations would be expected to occur. Boreholes 5, 7A, 10A and 14A only demonstrate very small stress perturbations (Figure 4.11, Appendix 1B), which still approximately fall within the range for the hydrofrac results mean σ_{Hmax} orientation of 159/339° (σ_{Hmin} 069/249° - section 4.4.1), and fall within the range of 118/298° (σ_{Hmin} 028/208°) to 190/010° (σ_{Hmin} 100/280 °), derived by Nirex (NIREX, 1996a). Whether it is therefore correct or not to call these interpretations stress perturbations is uncertain. In the rest of the boreholes analysed (2, 3, 8A, 9A, 9B, 11A, 12A, 13A, RCF2, RCF3, RCM1 & RCM2), faults can, in some cases, be found to sometimes affect the stress profile and cause the σ_{Hmin} orientation to alter and rotate. In other examples, they don't alter the σ_{Hmin} orientation at all. There does not appear therefore to be any correlation, within the stress profiles analysed, to indicate any common relationship between stress perturbations/rotations and locations of faults. More detailed and extensive studies are needed to investigate this relationship further at various depths within the BVG. This is beyond the scope of the present thesis.

Boreholes, that showed a possible rotation of the σ_{Hmin} orientation (3, 8A & 11A) in Figure 4.2a and 4.8, did not show obvious correlations between the location of faults down the stress profile and observed rotations of the stress field (Table 4.8, Appendix 1A & Figure 4.12, Appendix 1B). There was also no consistent correlation to the type of stress profile produced or the number of faults encountered down the stress profile (Table 4.8, Appendix 1A). These boreholes have stress profiles that have an average breakout orientation (σ_{Hmin}) of 100/280° to 180/360° (Table 4.8, Appendix 1A). This

hydrofrac analysis carried out by Nirex (section 4.4.2 describes Nirex's hydrofrac result in more detail). It is concluded from these observations that the breakouts are not the main stress effect being observed in these boreholes. Instead, hydrofrac style, drilling induced tensile failure and dilation along pre-existing discontinuities (section 2.2.3.3 – Figure 2.6), are being identified. Tensile failure along pre-existing discontinuities is expected to form in the direction of σ_{Hmax} within the borehole (Hillis and Reynolds, 2000). Boreholes 3, 8A & 11A produce results that are consistent with the mean σ_{Hmax} orientation of 159/339°, and fall within the range of 118/298° to 190/010°, derived from hydrofrac analysis carried out by Nirex (NIREX, 1996a). Borehole 2 also displays this characteristic profile and is the only borehole that displays a true biaxial shape, whose axes are orientated 90° to each other (NE-SW and NW-SE). This is most likely due to both breakout (σ_{Hmin}) and induced tensile failure occurring along discontinuities in the σ_{Hmax} direction within this borehole. This is perhaps not surprising since the BVG is an anisotropic highly fractured and faulted crystalline rock mass (section 3.1.2.1). Drilling into the BVG could easily cause the borehole wall to become oval in shape, instead of circular, due to the tensile failure and dilation occurring along pre-existing discontinuities (section 2.4).

The production of the new filtered stress map for the top one hundred meters of the BVG has successfully identified the overall stress field within the Sellafield site (Figure 4.2 a, Appendix 1B) and PRZ (Figure 4.2 b, Appendix 1B) area. The breakout analysis carried out on the Sellafield boreholes has produced a σ_{Hmin} , and consequently σ_{Hmax} ($\sigma_{Hmin} + 90^\circ$), stress orientations that are generally consistent with both hydrofrac analysis carried out by Nirex (NIREX, 1996a, section 4.4.1) and the UK regional stress field (section 2.3.4), which has a NW-SE σ_{Hmax} orientation (Evans, 1987). The effect of noise, due to discontinuities, in the breakout results has been reduced (Figure 4.2 a/b, Appendix 1B) compared to the original unfiltered breakout analysis carried out by Brereton *et al.*, 1997 (Figure 4.7). Investigations into possible rotations of the stress field around faults, within the top one hundred

analysis carried out by Brereton *et al.* (1997) (Figure 4.7). Investigations into possible rotations of the stress field around faults, within the top one hundred meters of the BVG (boreholes 2, 3, 8A & 11A), have found that they are not stress rotations at all. Instead, the apparent breakouts are most probably the result of tensile failure and dilation along pre-existing discontinuities (section 2.4) in the borehole. This places some doubt as to the effectiveness of the breakout analysis and certainly suggests that this method of stress analysis needs to be carefully scrutinised and compared to the results of other methods, such as overcoring. Particularly care is needed when breakout analysis is applied to a fractured crystalline rock mass that has had a complex geological and structural history (section 3.1), as has occurred at Sellafield. This result also places some doubt over Nirex's hydrofrac test results (NIREX, 1996a). The hydrofrac tests (section 2.2.3.3) at Sellafield were carried out in a fractured rock mass. It could be perceived that pre-existing discontinuities will be reactivated instead of new hydrofractures being generated.

The major reactivating Permo-Triassic sedimentary basin will have undoubtedly affected the stress field measured within BVG. Certainly the crystalline BVG would be expected to be able to hold and support stress much better than the highly consolidated, highly permeable Permo-Triassic basin rocks. The massive difference in the surface topography across the Sellafield site (section 3.1.1) could also have affected the regional stress regime seen within the BVG. These ideas certainly place some question marks over the data and results collected in this analysis. Further detailed studies are required to investigate the above points.

5. - Characterisation of Flow, *In Situ* Stress & Discontinuities

5.1 Introduction

This chapter starts by introducing the detailed information obtained by UK Nirex, during its scientific investigations at Sellafield (section 1.2 & 1.2.1) on flowing and non-flowing features. This information is used to identify flowing and non-flowing zones. Techniques are then used to collect data on the state of *in situ* stress and discontinuities' attributes within these zones from downhole geophysical imagery. This information has been obtained in order to investigate the relationship between the flow of fluid through a fractured rock mass and the prevailing stress field, suggested by Barton *et al.* (1995) (section 2.1), within the Permo-Triassic and the Borrowdale Volcanic Group (BVG) rocks at Sellafield (Chapter 6). This chapter solely presents the methods used to collect the information and the data needed to be able to investigate this relationship.

5.2 Flow Zone Data

As part of Nirex's scientific investigations at Sellafield, a number of hydrogeological tests were undertaken within the deep boreholes (section 1.2.1). Full Sector Tests (FSTs), also known as production tests, were generally run prior to the completion of the borehole and were carried out over large depth intervals (10's of meters) within the borehole usually over a period of one or two days (NIREX, 1997f). During this period, fluid flow was induced in the borehole by reduction of the hydrostatic head, which imposed a drawdown of the borehole fluids (NIREX, 1997f). These production tests allowed a measurable profile of the borehole's fluid conductivity, pressure, temperature and velocity to be logged. Where sufficient inflow of fluid occurred in the borehole, measurable changes to the logged fluid conductivity and temperature profiles were identified. These areas were termed by Nirex as 'Flow Zones' (NIREX, 1997f). Nirex did not attempt to assess the hydraulic properties of the flow zones (FZ), but where available

fullbore spinner logging data was used to confirm the location of the larger FZ and to provide some means of attempting to quantify the flow (NIREX, 1997f). The purpose of the production logging was to identify points of groundwater inflow to allow discrete testing (Environmental Pressure Measurement (EPM)) and fluid sampling (Discrete Extraction Tests - DET). These were not designed to comprehensively identify all inflows, but were meant to identify a sufficient number of inflows to satisfy testing and sampling requirements (NIREX, 1997f). The FZ results therefore should not be considered as a complete listing (NIREX, 1997f). The results from Nirex's FZ analysis are presented in Table App 6.1 (Appendix 6).

The only detailed (meter-scale) investigation into the hydrogeological properties of the FZ detected within the Sellafield boreholes was undertaken within Sellafield borehole RCF3. One hundred contiguous pulse tests and six constant rate abstraction tests were undertaken between 634 – 790 meters below rotary table (mbRT), within the BVG (Armitage *et al.*, 1996). Schlumberger's Modular Dynamic Tester (MDT) tool was used for this investigation (Armitage *et al.*, 1996). The tool was configured with a Dual Packer (Figure 5.1), having a test interval length of 1.56m (Armitage *et al.*, 1996). A detailed description of how the Short Interval Test (SIT) was performed is presented in Armitage *et al.* (1996). From the SIT investigation flow rates (transmissivities) of the pulse test intervals were calculated. The results from the SIT pulse tests are presented in Table App 6.2 (Appendix 6).

From the SIT zone investigation (Table App 6.2, Appendix 6), eight areas of increased transmissivity were identified (Figure 5.2 & Table 5.1) from the pulse tests, within the interval tested (Armitage *et al.*, 1996). These areas had transmissivities from $10^{-11} \text{ m}^2\text{s}^{-1}$ to greater than $10^{-9} \text{ m}^2\text{s}^{-1}$ and are seen as areas of increased flow (Figure 5.2).

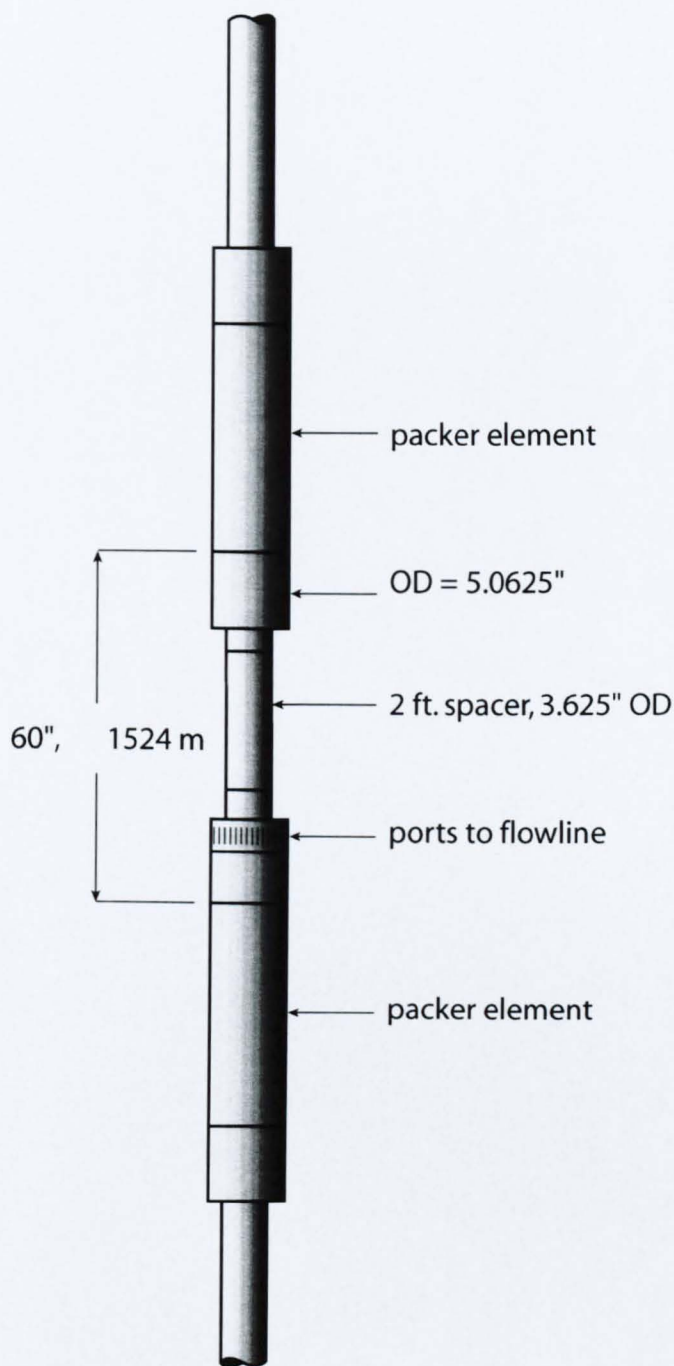
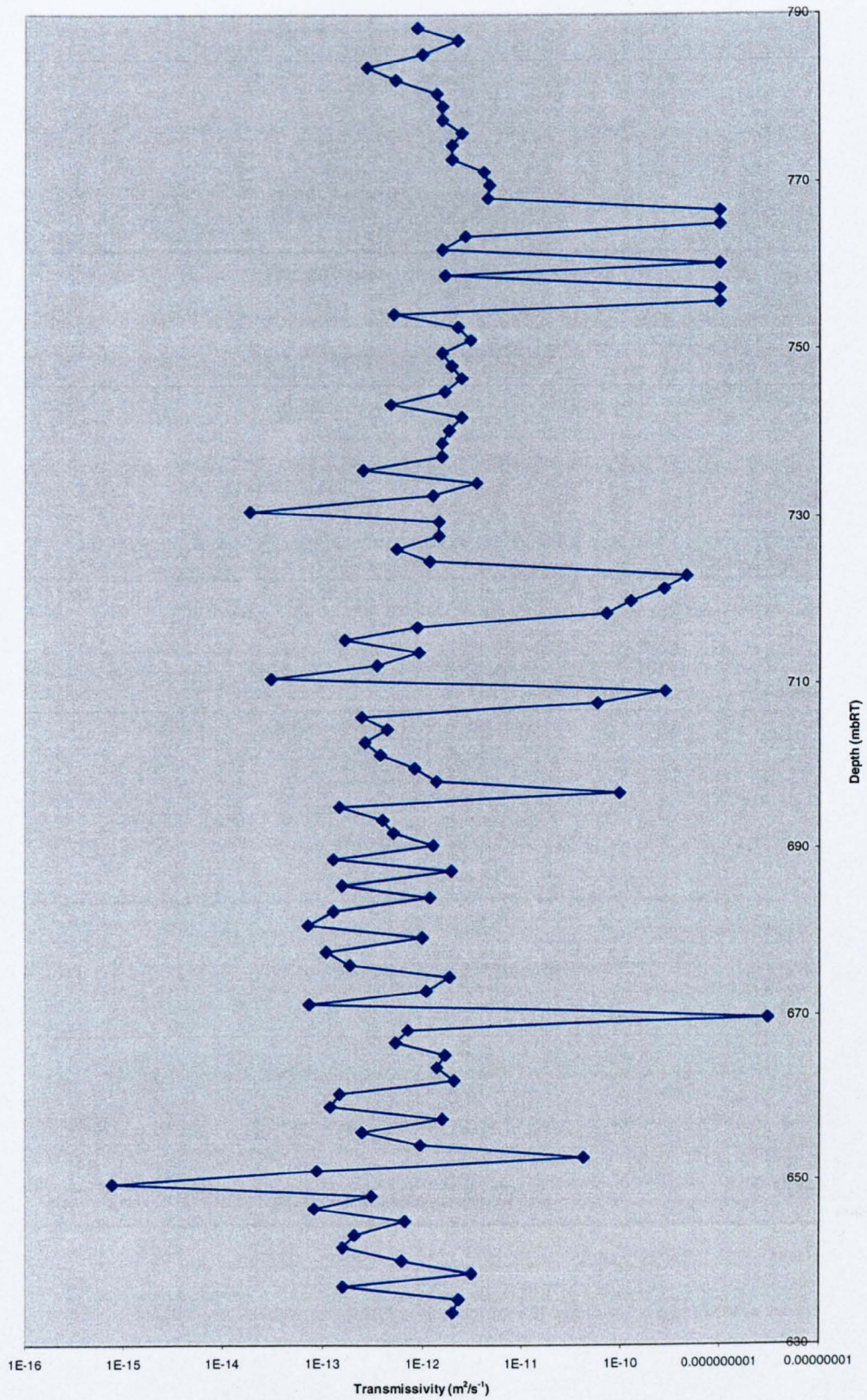


Figure 5.1 - Schlumberger's Modular Dynamic Tester
(from Armitage *et al.*, 1996).

Figure 5.2 – Transmissivity profile from the SIT zone (634 - 790 mbRT), calculated from pulse test data (adapted from Armitage et al., 1996).



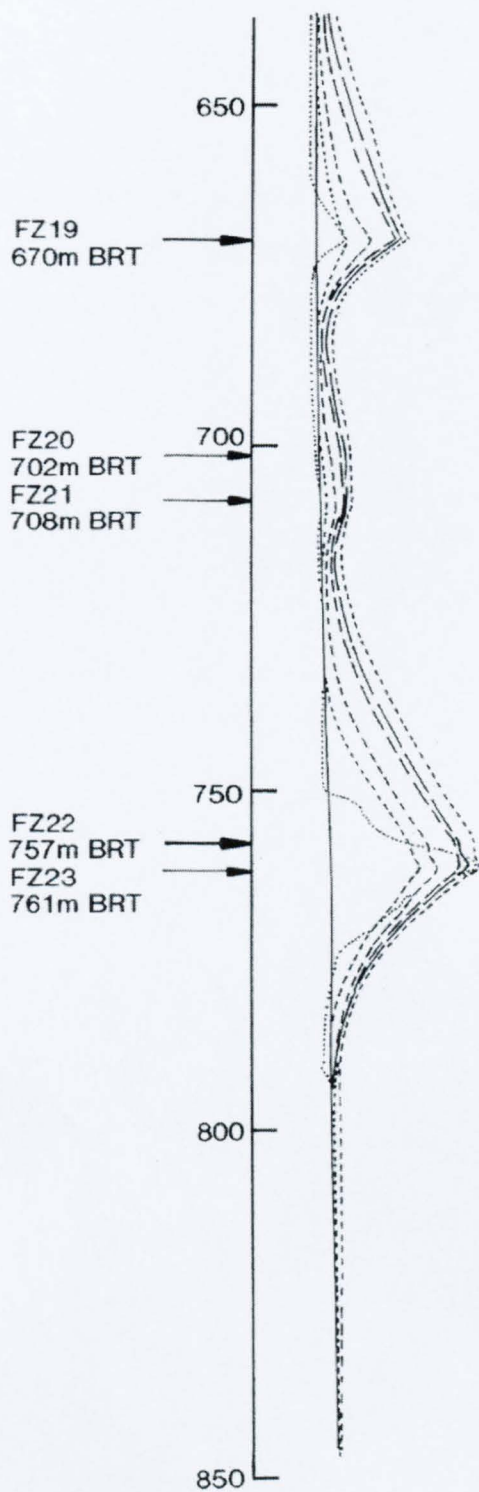


Figure 5.3 – Production log for Sellafeld borehole RCF3 (635–850 mbRT) (from Armitage *et al.*, 1996).

SIT Flowing Areas	Test Number	Top of Interval (mbRT)	Bottom of Interval (mbRT)	Best Transmissivity (m ² s ⁻¹)	Correlation to Production Log Flow Zones	Geological Sequence	Geological Formation	Geological Member
A	88	651.89	653.45	3.00E-09	1(No19)	BVG	Fleming Hall	Longlands Farm
B	77	668.98	670.54	3.00E-09	1(No19)	BVG	Fleming Hall	Longlands Farm
C	60	695.64	697.2	1.00E-10	0	BVG	Fleming Hall	Longlands Farm
D	53	706.61	708.17	6.00E-11	1(No y)	BVG	Fleming Hall	Longlands Farm
D	52	708.14	709.7	2.90E-10	0	BVG	Fleming Hall	Longlands Farm
E	46	717.5	719.06	7.40E-11	0	BVG	Fleming Hall	Longlands Farm
E	45	719.02	720.58	1.30E-10	0	BVG	Fleming Hall	Longlands Farm
E	44	720.6	722.16	2.80E-10	0	BVG	Fleming Hall	Longlands Farm
E	43	722.15	723.71	4.70E-10	0	BVG	Fleming Hall	Longlands Farm
F	22	754.91	756.47	1.00E-09	0	BVG	Fleming Hall	Sides Farm
F	21	756.44	758	1.00E-09	1(No 20)	BVG	Fleming Hall	Sides Farm
G	19	759.54	761.1	1.00E-09	1(No 21)	BVG	Fleming Hall	Sides Farm
H	16	764.26	765.82	1.00E-09	0	BVG	Fleming Hall	Sides Farm
H	15	765.83	767.39	1.00E-09	0	BVG	Fleming Hall	Sides Farm

Table 5.1 – Eight areas that demonstrated an increase in transmissivity within the SIT zone.

5.3 *In Situ* Stress Data

5.3.1 Flow Zones

Using the locations of Nirex's identified FZ (Table App 6.1, Appendix 6) as a guide to areas where discontinuity flow could occur, analysis of the *in situ* stress regime within these zones was performed within the BVG and Permian-Triassic units. Only the Sellafield boreholes that had vertical trajectories (section 4.4.2 - Table 4.1), hence not deviated or inclined, and were within or within close proximity to the PRZ area at Sellafield (Figure 1.3) were analysed in this study (i.e. boreholes 2, 5, 8A, 11A, RCF3, RCM1 & RCM2). Sellafield boreholes 4 and 7A could not be analysed as no digital imagery data could be obtained for this borehole at the time of this study. Sellafield boreholes 10A and 12A did not contain many FZ within the BVG (Table App 6.1, Appendix 6) and were therefore disregarded.

5.3.1.1 Flow Zones - Acquisition of *In Situ* Stress Data

In this *in situ* stress analysis the BGS's *Breaking* and *Breaknrb* software (section 4.2) was again used to analyse the stress regime encountered around each of the FZ, identified within Sellafield boreholes 2, 5, 8A, 11A, RCF3, RCM1 & RCM2. The theories and assumptions used to generate the stress data are the same as discussed in Chapter 4. A specific methodology concerning the use of *Breaking* and *Breaknrb* to generate the *in situ* stress analysis for the FZ has been written, and is presented in Appendix 7 sections 7.1 and 7.2. Before the *in situ* stress analysis was undertaken, the imagery logs (FMS/FMI & BHTV/UBI AMWF) for each borehole were viewed using the BGS's *Welllog FMS/BHTV* software module (section 5.4). The study was carried out +/- 5 m around each FZ, to see if there were any sinusoidal outlines of discontinuities around the identified FZ. If there were, then a mean orientation of σ_{Hmin} for each FZ was obtained. If no sinusoidal outlines of discontinuities were identified around the FZ then it was disregarded from the study, because there was no discontinuity observed, which could cause the flow of fluid into the borehole.

From the previous hydrogeological characterization by Nirex of the BVG and the Permian-Triassic rocks, at Sellafield, it was found that discrete fracture permeability was an important element in the hydrogeological regime of the area (section 3.2). The methods used to acquire this discontinuity data are explained and discussed further in section 5.4.

5.3.1.2 Flow Zones - *In Situ* Stress Data

The breakout roses produced for all the FZ analysed, within Sellafield boreholes 2, 5, 8A, 11A, RCF3, RCM1 & RCM2 are presented in Table 5.2, Appendix 1A. The individual breakout roses are laid out in Appendix 8, Figures App 8.1 – 8.132. For each of the FZ where an *in situ* stress analysis was carried out, the image log derived discontinuity data (section 5.4) for the same depth interval was visualised using a software routine, developed by Dr. Chris Evans (BGS), called *Vector*. It was used to assess and present the discontinuity data in the form of orientation roses and enable mean discontinuity orientations to be determined for each FZ. A systematic guide of how to use *Vector* is outlined in Appendix 2, section 2.3. The results of this visualisation exercise are displayed in Table 5.2 Appendix 1A, and the orientation rose plots are presented Appendix 8, Figures App 8.133 – 8.264.

5.3.1.3 Flow Zones - Assessment of *In Situ* Stress Data

Mean breakout orientations and mean discontinuity orientations were obtained for FZ within the BVG and Permian-Triassic (Table 5.2, Appendix 1A). A represented selection of the breakout and discontinuity roses for the FZ within the BVG and Permian-Triassic are presented in Figures 5.4 and 5.5 (Appendix 1B). As a check to make sure that the effects of discontinuities were being effectively filtered out from the breakout results, a cross plot showing the comparison of the discontinuity orientation data and breakout orientation data (σ_{Hmin}) was produced (Figure 5.6). From Figure 5.6 it is apparent that the data is randomly scattered across the cross plot, which suggests no obvious linear correlation between the results.

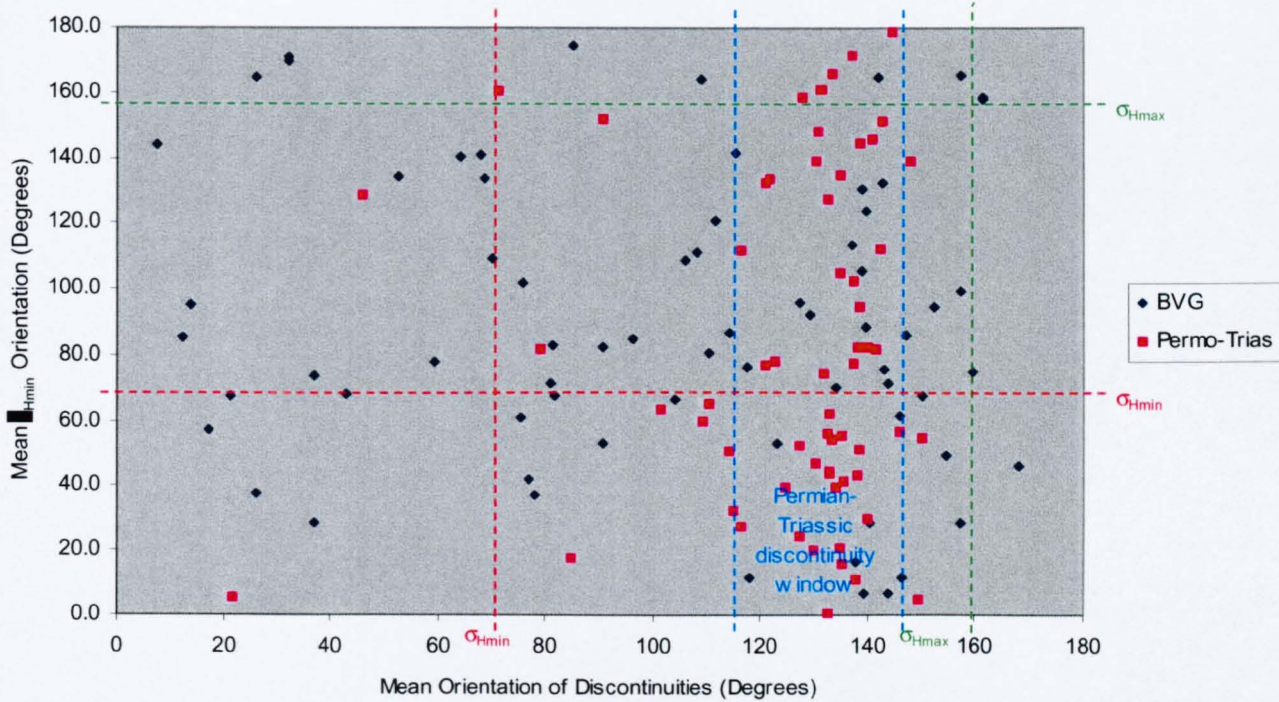


Figure 5.6 – Cross plot showing the comparison of the mean discontinuity orientation data and mean breakout orientation data for the Flow Zone stress analysis. σ_{Hmin} and σ_{Hmax} orientation lines are derived from Nirex's hydrofrac test results (NIREX, 1996a), which concluded that the mean orientation of σ_{Hmax} was 159/339°, within a range of results from 118/298° to 190/010° and the mean σ_{Hmin} orientation was 069/249°, within a range of 028/208° to 100/280°.

This gives a good indication that the vertical filter applied to the imagery data during breakout analysis has worked, as there is little correlation between the mean breakout orientations and the mean discontinuity dip azimuth.

Figure 5.6 also indicates the FZ discontinuities encountered within the Permian-Triassic rocks have a mean orientation of 115° - 145° , $\sim +15$ - 45° of σ_{Hmax} ($159/339^{\circ}$) direction derived by Nirex during a series of hydrofrac test (NIREX, 1996 – section 4.4.1). This mean orientation (115° - 145°) is consistent to the dominant Permian-Triassic discontinuity dip azimuth (NIREX, 1996e - Appendix 11) and the northwest-trending fault structures that are associated with opening up of the East Irish Sea Basin during the Permian-Triassic (Section 3.1.2.3). The BVG data in contrast is more randomly orientated (Figure 5.6). These two observations are consistent with the contrasts in discontinuity patterns observed by Nirex and reported in NIREX (1995) and NIREX (1996e) (Appendix 11).

When looking at the breakout orientation results displayed in Figure 5.6, there are two distinct patterns that can be observed:-

- A clustering of breakout orientations around σ_{Hmin} (derived from Nirex's hydrofrac test results (NIREX, 1996a - section 4.4.1)),
- A clustering of breakout orientations around σ_{Hmax} (derived from Nirex's hydrofrac test results (NIREX, 1996a - section 4.4.1)).

The clustering of breakout orientations around σ_{Hmin} shows a greater degree of scatter, when the orientations of discontinuities fall close to σ_{Hmax} . This effect suggests that the breakout results have been defocused by discontinuities interacting with stress field (σ_{Hmax}) causing drilling induced tensile discontinuities (section 2.2.3.3) to form. The clustering of breakout orientations around σ_{Hmax} also indicates that drilling induced tensile discontinuities are forming within some of the Sellafield boreholes and are causing the breakout direction to be misinterpreted. It can therefore be concluded that in flow zones where discontinuities are orientated close to σ_{Hmax} , interaction with the stress field can cause drilling induced tensile

discontinuities to form resulting in anomalous breakout orientations to be measured.

The results from this analysis are used, applied and discussed further in Chapter 6, section 6.2.

5.3.2 Short Interval Test (SIT) Zone

The detailed SIT (Table App 6.2, Appendix 6) carried out in Sellafield borehole RCF3, enabled an accurate (metre scale) guide to flow within the test zone (634–790 mbRT) and was therefore an ideal area to test the relationship between the flow of fluid through a fractured rock mass and the prevailing stress field (Chapter 6), suggested by Barton *et al.* (1995). To enable this relationship to be tested, an analysis of the *in situ* stress regime within this test zone was required.

5.3.2.1 SIT Zone - Acquisition of *In Situ* Stress Data

In the SIT zone, two differing *in situ* stress analyses were undertaken. Firstly an investigation into the eight (A - H) flowing areas (Table 5.1 & section 5.2) and the nine corresponding (NA - NI) non-flowing areas (in between each flowing area) that were identified during the SIT test. Secondly, a detailed *in situ* stress analysis down the full length of the SIT zone was undertaken. For both these analyses, the BGS's Breakimg and Breaknrb software (section 4.2) were again used to analyse the stress field. A specific method of how Breakimg and Breaknrb was used to generate the *in situ* stress data for the SIT zones flowing areas and detailed stress analysis is presented in Appendix 7 sections 7.3 - 7.4.

Discontinuity data for each of the flowing and non-flowing areas (Table 5.1) were collected and analysed. The discontinuity data were obtained by the identification of discontinuities from downhole geophysical image logs (FMS/FMI and BHTV/UBI). The methods used to acquire this discontinuity data are explained and discussed further in section 5.4.

5.3.2.2 SIT Zone - Presentation of Data

The breakout roses produced for the flowing and non-flowing areas analysed are presented in Appendix 8, Figure App 8.265 – Figure App 8.281. The results of the breakout roses produced for the flowing and non-flowing areas analysis are summarised in Table 5.3. The breakout roses produced for the SIT zone detailed *in situ* stress analysis are presented in Table 5.4. For each analysis of the flowing and non-flowing areas image log derived discontinuity data (section 5.4) for the same depth intervals were visualised using Vector. It was used to assess and present the discontinuity data in the form of orientation roses and enable a mean discontinuities orientation for the to be concluded. A systematic guide of how to use Vector, to produce orientation rose plots, is outlined in Appendix 2, section 2.3. The individual discontinuity roses are present in Appendix 8, Figures App 8.282 – 8.298. The results of this visualisation exercise are displayed in Table 5.3. To allow the discontinuity orientation azimuth data, for the flowing and non-flowing areas, to be separately visualised graphically, two data sets were generated collating all the discontinuities that were found in the flowing and non-flowing areas within the SIT.

5.3.2.3 SIT Zone - Assessment of Data

Mean Breakout orientations were obtained for the SIT zones flowing and non-flowing areas (Table 5.3). These results were presented on a frequency plot (Figure 5.7). From Figure 5.7 it can be concluded that the breakout results (σ_{Hmin}) for the SIT zones flowing and non-flowing areas produce breakout results that are consistent ($\sim \pm 5-30^\circ$) with the σ_{Hmin} direction derived from Nirex's hydrofrac test results (NIREX, 1996a), which concluded that the mean orientation of σ_{Hmax} was $159/339^\circ$, within a range of results from $118/298^\circ$ to $190/010^\circ$ and the mean σ_{Hmin} orientation was $069/249^\circ$, within a range of $028/208^\circ$ to $100/280^\circ$. A represented selection of the breakout and discontinuity roses for the SIT zones flowing and non-flowing areas are presented in Figures 5.8 (Appendix 1B).

SIT Non-Flowing & Flowing Areas	Top of Interval (mbRT)	Bottom of Interval (mbRT)	σ_{Hmin} (Degrees)	σ_{Hmax} (Degrees)	Stress Confidence (+/-)	No. Data Points	Max Stress Rose Value	Stress Figure (Appendix 8)	Mean Fracture Orientation (Degrees)	Mean Fracture Confidence (+/-)	Discontinuity Figure (Appendix 8)
NA	630.00	651.89	72.3	162.3	16.9	1720	0.21	App 8.265	105.7	23.5	App 8.282
A	651.89	653.45	79.2	169.2	18.7	124	0.24	App 8.266	154.9	11.2	App 8.283
NB	653.45	668.98	60.4	150.4	22	122	0.18	App 8.267	56.5	16.5	App 8.284
B	668.98	670.54	26.6	116.6	22.2	124	0.31	App 8.268	172.2	4.1	App 8.285
NC	670.54	695.64	48.8	138.8	20.5	1976	0.15	App 8.269	47.9	22.8	App 8.286
C	695.64	697.20	40.1	130.1	16.9	122	0.25	App 8.270	37.6	19.6	App 8.287
ND	697.20	706.61	52.2	142.2	18.8	742	0.18	App 8.271	90.5	17.9	App 8.288
D	706.61	709.70	21.6	111.6	25.8	242	0.19	App 8.272	16.9	14.5	App 8.289
NE	709.70	717.50	71.7	161.7	19.6	616	0.19	App 8.273	52.8	21.5	App 8.290
E	717.50	723.71	60.8	150.8	24.6	488	0.17	App 8.274	103.6	22.1	App 8.291
NF	723.71	754.91	84.8	174.8	14.1	1802	0.36	App 8.275	76.9	25.1	App 8.292
F	754.91	758.00	82.3	172.3	11.1	244	0.31	App 8.276	43.1	13	App 8.293
NG	758.00	759.54	58.7	148.7	12.1	122	0.43	App 8.277	121.5	8.8	App 8.294
G	759.54	761.10	51.9	141.9	10.9	122	0.39	App 8.278	139.3	17	App 8.295
NH	761.10	764.26	62	152	12.9	248	0.34	App 8.279	40.6	3.6	App 8.296
H	764.26	767.39	55.6	145.6	16.4	248	0.27	App 8.280	109.4	16.5	App 8.297
NI	767.39	790.00	81	171	12.9	1780	0.34	App 8.281	36	20.3	App 8.298

Table 5.3 – Results from stress analysis for flowing and non-flowing areas identified from SIT.

Depth Breakout orientaion calculated over (mbRT)	σ_{Hmin} (Degrees)	σ_{Hmax} (Degrees)	Stress Confidence (+/-)	No. Data Points	Max Stress Rose Value	Data File Used to Produce Results
630.0 - 646.0	73.3	163.3	15.3	1258	0.28	rcf3_amwf_hjrbrk_630_735.dat
646.0 - 646.1	169.7	259.7	5.9	6	0.83	rcf3_amwf_hjrbrk_630_735.dat
646.1 - 646.3	0.5	90.5	5.1	14	0.86	rcf3_amwf_hjrbrk_630_735.dat
646.3 - 646.8	144.5	234.5	13.7	40	0.45	rcf3_amwf_hjrbrk_630_735.dat
646.8 - 646.9	63.4	153.4	0.8	8	0.75	rcf3_amwf_hjrbrk_630_735.dat
646.9 - 648.5	35.8	125.8	11.1	126	0.36	rcf3_amwf_hjrbrk_630_735.dat
648.5 - 648.85	164.2	254.2	12.4	28	0.36	rcf3_amwf_hjrbrk_630_735.dat
648.85 - 649.4	66.3	156.3	18.8	42	0.38	rcf3_amwf_hjrbrk_630_735.dat
649.4 - 651.0	139.6	229.6	11.3	126	0.47	rcf3_amwf_hjrbrk_630_735.dat
651.0 - 652.9	89	179	18.6	150	0.31	rcf3_amwf_hjrbrk_630_735.dat
652.9 - 653.1	132.6	222.6	7.5	16	0.94	rcf3_amwf_hjrbrk_630_735.dat
653.1 - 659.8	89.9	179.9	15.2	528	0.2	rcf3_amwf_hjrbrk_630_735.dat
659.8 - 660.6	159	249	15.9	62	0.42	rcf3_amwf_hjrbrk_630_735.dat
660.6 - 661.7	50.5	140.5	26.2	88	0.26	rcf3_amwf_hjrbrk_630_735.dat
661.7 - 662.45	116.9	206.9	9.4	58	0.69	rcf3_amwf_hjrbrk_630_735.dat
662.45 - 662.9	42.5	132.5	15.1	36	0.39	rcf3_amwf_hjrbrk_630_735.dat
662.9 - 663.3	112.3	202.3	0.8	32	0.87	rcf3_amwf_hjrbrk_630_735.dat
663.3 - 665.75	53.6	143.6	12.6	35	0.35	rcf3_amwf_hjrbrk_630_735.dat
665.75 - 665.95	141.5	231.5	1.4	16	0.94	rcf3_amwf_hjrbrk_630_735.dat
665.95 - 666.8	22	112	18.5	66	0.39	rcf3_amwf_hjrbrk_630_735.dat
666.8 - 666.9	149.6	239.6	0.8	8	0.88	rcf3_amwf_hjrbrk_630_735.dat
666.9 - 668.55	44.2	134.2	14.5	130	0.45	rcf3_amwf_hjrbrk_630_735.dat
668.55 - 668.65	161.3	251.3	0.8	8	0.75	rcf3_amwf_hjrbrk_630_735.dat
668.65 - 669.18	27.1	117.1	11.2	42	0.76	rcf3_amwf_hjrbrk_630_735.dat
669.18 - 669.29	157.3	247.3	21.6	10	0.4	rcf3_amwf_hjrbrk_630_735.dat
669.29 - 670.35	32.9	122.9	20	84	0.38	rcf3_amwf_hjrbrk_630_735.dat
670.35 - 670.9	171.3	261.3	14	44	0.48	rcf3_amwf_hjrbrk_630_735.dat
670.9 - 671.0	32.6	122.6	0.8	8	1	rcf3_amwf_hjrbrk_630_735.dat
671.0 - 671.3	81.7	171.7	19.6	24	0.42	rcf3_amwf_hjrbrk_630_735.dat
671.3 - 671.8	18.3	108.3	12.3	38	0.61	rcf3_amwf_hjrbrk_630_735.dat
671.8 - 671.9	180	270	0.8	8	1	rcf3_amwf_hjrbrk_630_735.dat
671.9 - 672.8	22.2	112.2	14.8	72	0.39	rcf3_amwf_hjrbrk_630_735.dat
672.8 - 672.85	164.2	254.2	0.8	4	1	rcf3_amwf_hjrbrk_630_735.dat
672.85 - 672.95	16	106	15.9	8	0.63	rcf3_amwf_hjrbrk_630_735.dat
672.95 - 673.04	159.4	249.4	0.8	6	1	rcf3_amwf_hjrbrk_630_735.dat
673.04 - 673.06	12	102	0.8	2	1	rcf3_amwf_hjrbrk_630_735.dat
673.06 - 674.6	50.7	140.7	19.8	122	0.23	rcf3_amwf_hjrbrk_630_735.dat
674.6 - 674.8	149.8	239.8	12.3	14	0.71	rcf3_amwf_hjrbrk_630_735.dat
674.8 - 675.3	52.2	142.2	13.6	4	0.3	rcf3_amwf_hjrbrk_630_735.dat
675.3 - 675.4	155.1	245.1	0.8	8	0.88	rcf3_amwf_hjrbrk_630_735.dat
675.4 - 676.3	21.5	111.5	6.5	70	0.34	rcf3_amwf_hjrbrk_630_735.dat
676.3 - 677.3	137.4	227.4	20.5	80	0.33	rcf3_amwf_hjrbrk_630_735.dat
677.3 - 677.7	53.6	143.6	8.5	32	0.53	rcf3_amwf_hjrbrk_630_735.dat
677.7 - 677.8	146.9	236.9	0.8	8	0.75	rcf3_amwf_hjrbrk_630_735.dat
677.8 - 678.3	57.4	147.4	13.8	38	0.45	rcf3_amwf_hjrbrk_630_735.dat
678.3 - 678.4	41.1	131.1	7.1	8	0.38	rcf3_amwf_hjrbrk_630_735.dat
678.4 - 678.5	24.1	114.1	0.8	8	1	rcf3_amwf_hjrbrk_630_735.dat
678.5 - 678.75	177.1	267.1	6.9	20	0.9	rcf3_amwf_hjrbrk_630_735.dat
678.75 - 679.2	35.1	125.1	5.2	36	0.83	rcf3_amwf_hjrbrk_630_735.dat
679.2 - 679.3	170	260	0.8	8	0.63	rcf3_amwf_hjrbrk_630_735.dat
679.3 - 679.45	36	126	0.8	12	0.92	rcf3_amwf_hjrbrk_630_735.dat
679.45 - 679.8	115.9	205.9	17.9	28	0.54	rcf3_amwf_hjrbrk_630_735.dat
679.8 - 681.2	55.8	145.8	12.1	110	0.61	rcf3_amwf_hjrbrk_630_735.dat
681.2 - 682.3	59.7	149.7	12.3	88	0.62	rcf3_amwf_hjrbrk_630_735.dat
682.3 - 683.2	149.4	239.4	9.9	70	0.4	rcf3_amwf_hjrbrk_630_735.dat

Table 5.4 – Results from detail stress analysis over the SIT zone.

Table 5.4 (continued) – Results from detail stress analysis over the SIT zone.

Depth Breakout orientation calculated over (mbRT)	σ_{Hmin} (Degrees)	σ_{Hmax} (Degrees)	Stress Confidence (+/-)	No. Data Points	Max Stress Rose Value	Data File Used to Produce Results
683.2 - 686.7	84.9	174.9	12.9	276	0.23	rcf3_amwf_hjrbrk_630_735.dat
686.7 - 686.9	129.9	219.9	1.5	16	0.37	rcf3_amwf_hjrbrk_630_735.dat
686.9 - 690.2	48.9	138.9	16.2	260	0.27	rcf3_amwf_hjrbrk_630_735.dat
690.2 - 690.35	162.4	252.4	0.8	12	1	rcf3_amwf_hjrbrk_630_735.dat
690.35 - 693.25	53.2	143.2	16.4	228	0.31	rcf3_amwf_hjrbrk_630_735.dat
693.25 - 693.5	165.7	255.7	6.2	20	0.95	rcf3_amwf_hjrbrk_630_735.dat
693.5 - 694.8	65.4	155.4	18.7	102	0.27	rcf3_amwf_hjrbrk_630_735.dat
694.8 - 695.0	138.2	228.2	0.8	16	0.69	rcf3_amwf_hjrbrk_630_735.dat
695.0 - 696.55	45.6	135.6	15.5	122	0.29	rcf3_amwf_hjrbrk_630_735.dat
696.55 - 696.85	157.8	247.8	8.2	24	0.71	rcf3_amwf_hjrbrk_630_735.dat
696.85 - 697.4	22.4	112.4	11.7	42	0.29	rcf3_amwf_hjrbrk_630_735.dat
697.4 - 697.75	91	181	12.3	28	0.32	rcf3_amwf_hjrbrk_630_735.dat
697.75 - 700.1	43	133	14.7	184	0.38	rcf3_amwf_hjrbrk_630_735.dat
700.1 - 700.5	179.9	269.9	5.5	32	0.94	rcf3_amwf_hjrbrk_630_735.dat
700.5 - 706.7	53	143	17.2	488	0.21	rcf3_amwf_hjrbrk_630_735.dat
706.7 - 706.95	116.9	206.9	11.3	20	0.4	rcf3_amwf_hjrbrk_630_735.dat
706.95 - 707.4	37.9	127.9	8.8	36	0.5	rcf3_amwf_hjrbrk_630_735.dat
707.4 - 707.95	161.8	251.8	12.8	44	0.48	rcf3_amwf_hjrbrk_630_735.dat
707.95 - 710.0	78.8	168.8	16	160	0.23	rcf3_amwf_hjrbrk_630_735.dat
710.0 - 714.0	103.8	193.8	22.6	316	0.2	rcf3_amwf_hjrbrk_630_735.dat
714.0 - 722.0	75.1	165.1	18.5	630	0.19	rcf3_amwf_hjrbrk_630_735.dat
722.0 - 722.3	160	250	20.9	24	0.38	rcf3_amwf_hjrbrk_630_735.dat
722.3 - 722.4	23	113	0.8	6	1	rcf3_amwf_hjrbrk_630_735.dat
722.4 - 722.55	113.5	203.5	3.8	12	0.83	rcf3_amwf_hjrbrk_630_735.dat
722.55 - 725.1	40.7	130.7	18.2	202	0.21	rcf3_amwf_hjrbrk_630_735.dat
725.1 - 725.25	161.6	251.6	0.8	12	0.83	rcf3_amwf_hjrbrk_630_735.dat
725.25 - 726.6	45.6	135.6	16.2	106	0.39	rcf3_amwf_hjrbrk_630_735.dat
726.6 - 726.7	172.8	262.8	0.8	8	1	rcf3_amwf_hjrbrk_630_735.dat
726.7 - 726.85	25.2	115.2	9.7	12	0.75	rcf3_amwf_hjrbrk_630_735.dat
726.85 - 727	177.1	267.1	7.5	12	0.83	rcf3_amwf_hjrbrk_630_735.dat
727.0 - 728.1	21.7	111.7	13.9	86	0.67	rcf3_amwf_hjrbrk_630_735.dat
728.1 - 728.75	123.1	213.1	11.8	50	0.32	rcf3_amwf_hjrbrk_630_735.dat
728.75 - 729.0	30.4	120.4	5.1	20	0.8	rcf3_amwf_hjrbrk_630_735.dat
729.0 - 729.65	134.9	224.9	7.7	52	0.46	rcf3_amwf_hjrbrk_630_735.dat
729.65 - 730.0	29.4	119.4	5	18	0.5	rcf3_amwf_hjrbrk_630_735.dat
730.0 - 730.2	122	212	11.5	16	0.62	rcf3_amwf_hjrbrk_630_735.dat
730.2 - 730.6	41.7	131.7	9	30	0.4	rcf3_amwf_hjrbrk_630_735.dat
730.6 - 731.1	110.2	200.2	19.3	40	0.3	rcf3_amwf_hjrbrk_630_735.dat
731.1 - 731.65	0.8	90.8	17.1	44	0.32	rcf3_amwf_hjrbrk_630_735.dat
731.65 - 732.25	148.7	238.7	11.8	46	0.03	rcf3_amwf_hjrbrk_630_735.dat
732.25 - 732.35	55.5	145.5	7.4	8	0.63	rcf3_amwf_hjrbrk_630_735.dat
732.35 - 732.40	170	260	0.8	4	1	rcf3_amwf_hjrbrk_630_735.dat
732.40 - 733.6	117.6	207.6	15.8	94	0.29	rcf3_amwf_hjrbrk_630_735.dat
733.6 - 734.4	101.2	191.2	22.9	64	0.2	rcf3_amwf_hjrbrk_630_735.dat
734.05 - 757.5	84	174	12.8	1946	0.36	rcf3_amwf_hjrbrk_732_837.dat
757.5 - 757.7	28.3	118.3	6.9	16	0.5	rcf3_amwf_hjrbrk_732_837.dat
757.7 - 764.7	56.6	146.6	14.7	552	0.33	rcf3_amwf_hjrbrk_732_837.dat
764.7 - 764.95	157	247	5.5	20	0.8	rcf3_amwf_hjrbrk_732_837.dat
764.95 - 768.6	86.8	176.8	13.7	286	0.33	rcf3_amwf_hjrbrk_732_837.dat
768.6 - 768.7	158.4	248.4	3.2	8	0.75	rcf3_amwf_hjrbrk_732_837.dat
768.7 - 809	74.5	164.5	16.9	3174	0.28	rcf3_amwf_hjrbrk_732_837.dat
809 - 809.2	174.4	264.4	10.4	16	0.75	rcf3_amwf_hjrbrk_732_837.dat
809.2 - 815.5	69.3	159.3	14.8	496	0.32	rcf3_amwf_hjrbrk_732_837.dat
815.5 - 815.8	17.9	107.9	1.8	24	0.92	rcf3_amwf_hjrbrk_732_837.dat
815.8 - 837	69.6	159.6	0.33	1668	0.33	rcf3_amwf_hjrbrk_732_837.dat

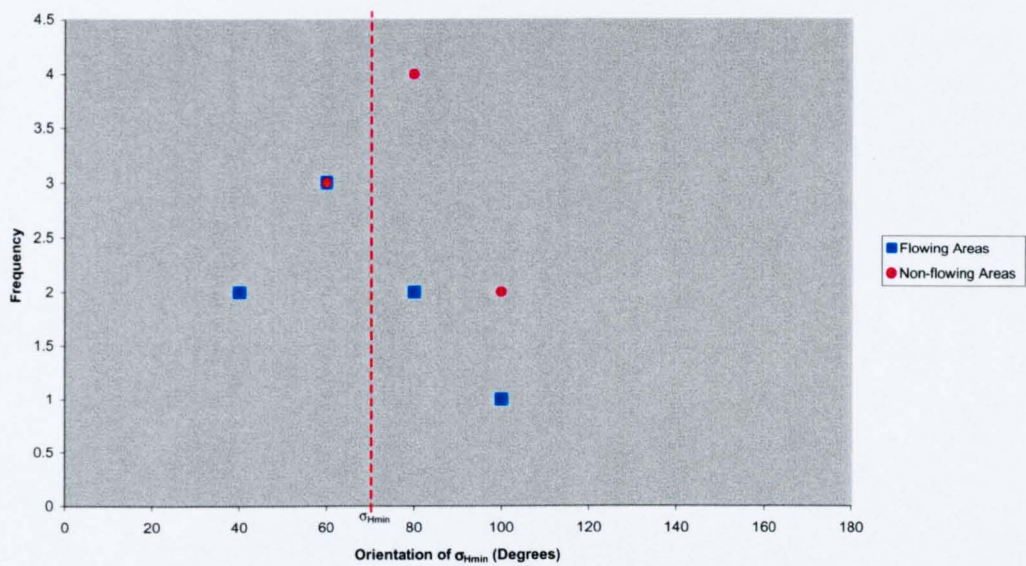


Figure 5.7 – Frequency plot showing the σ_{Hmin} orientation for all the flowing and non-flowing areas analysed within the SIT zone in Sellafield Borehole RCF3.

The detailed *in situ* stress analysis (Table 5.4) was performed so the variations in the stress field down the SIT zone could be identified. From this data, it is now possible to create a synthetic stress log. This log is used, applied and discussed further in Chapter 6, section 6.3.

Mean discontinuity orientations were obtained for the SIT zone flowing and non-flowing areas (Figure 5.9a). From Figure 5.9a it is possible to conclude that the orientation azimuths for flowing and non-flowing areas within the SIT zone show different orientation patterns. Due to the differences in the size of the discontinuity data sets (flowing 113 & non-flowing 638 discontinuities), it is difficult to compare the results. A random filtering technique was completed on the non-flowing discontinuity data set. A sixth of the data was sub-sampled to make a comparable data set to the flowing areas (Figure 5.9b). This subsampled data set will be known as the non-flowing subset discontinuity data set. From Figure 5.9b flowing discontinuities are clustered at $\sim 020^\circ$ and $\sim 120^\circ$, and non-flowing discontinuities cluster at $\sim 160^\circ$ (σ_{Hmax}). From Figure 5.9b it can be observed that the discontinuities contained within the flowing areas are orientated at $\sim 40-45^\circ$ to σ_{Hmax} and σ_{Hmin} . The region $\sim 45^\circ$ to σ_{Hmax} and σ_{Hmin} is the orientation where shear failure would be expected to occur within a rock mass placed under triaxial laboratory conditions. To aid in the visualisation of this observation a frequency orientation plot showing the difference between the number of flowing to non-flowing discontinuities at certain orientations was created (Figure 5.10). Figure 5.10 clearly shows that an increase in the number of flowing discontinuities, compared to non-flowing discontinuities occurs $\sim 45^\circ$ to σ_{Hmax} and σ_{Hmin} . An increase in the number of non-flowing discontinuities compared to flowing discontinuities occurs at $\sim 160^\circ$ (σ_{Hmax}). This observation suggests that shear failure does seem to relate to the flow of fluid within discontinuities at Sellafield.

The results from this investigation are used, applied and discussed further in Chapter 6, section 6.2 and 6.3.

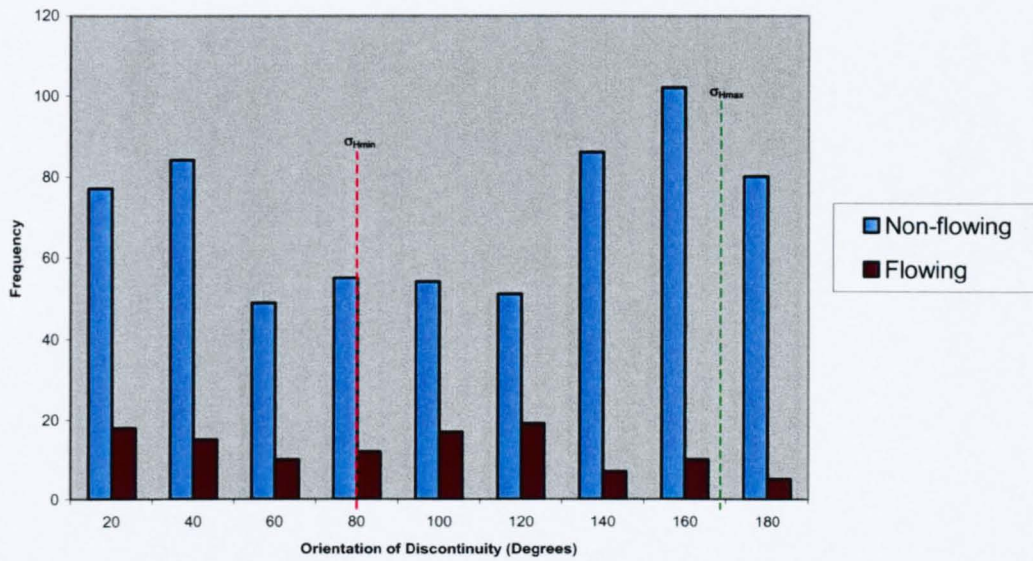


Figure 5.9a – Frequency plot of the orientation of discontinuities encountered within the flowing and non-flowing areas analysed in the SIT zone in Sellafield borehole RCF3. σ_{Hmin} and σ_{Hmax} orientation lines are derived from Nirex’s hydrofrac test results (NIREX, 1996a), which concluded that the mean orientation of σ_{Hmax} was 159/339°, within a range of results from 118/298° to 190/010° and the mean σ_{Hmin} orientation was 069/249°, within a range of 028/208° to 100/280°.

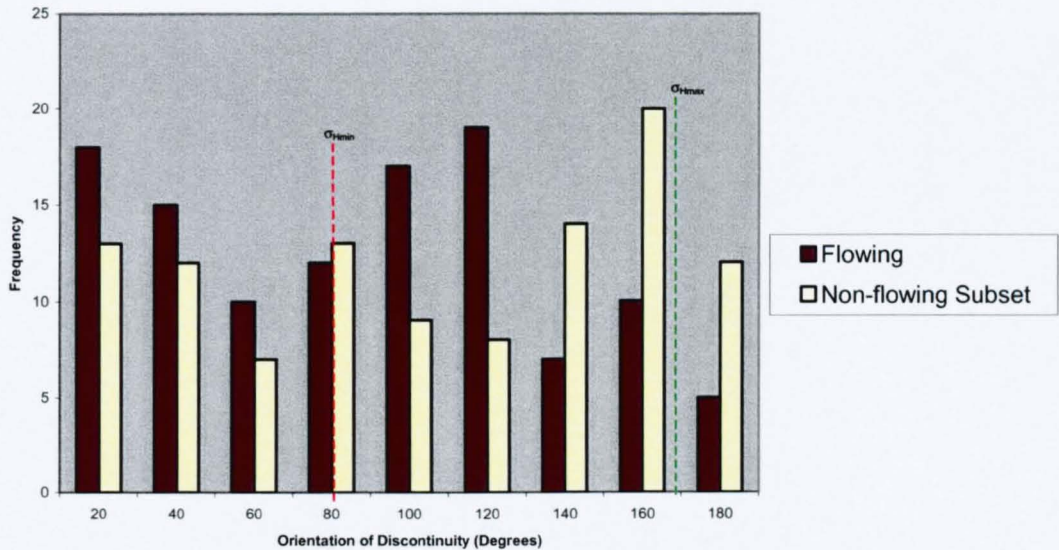


Figure 5.9b – Frequency plot of the orientation of discontinuities encountered within the flowing and non-flowing subset areas analysed in the SIT zone in Sellafield borehole RCF3. σ_{Hmin} and σ_{Hmax} orientation lines are derived from Nirex’s hydrofrac test results (NIREX, 1996a), which concluded that the mean orientation of σ_{Hmax} was 159/339°, within a range of results from 118/298° to 190/010° and the mean σ_{Hmin} orientation was 069/249°, within a range of 028/208° to 100/280°.

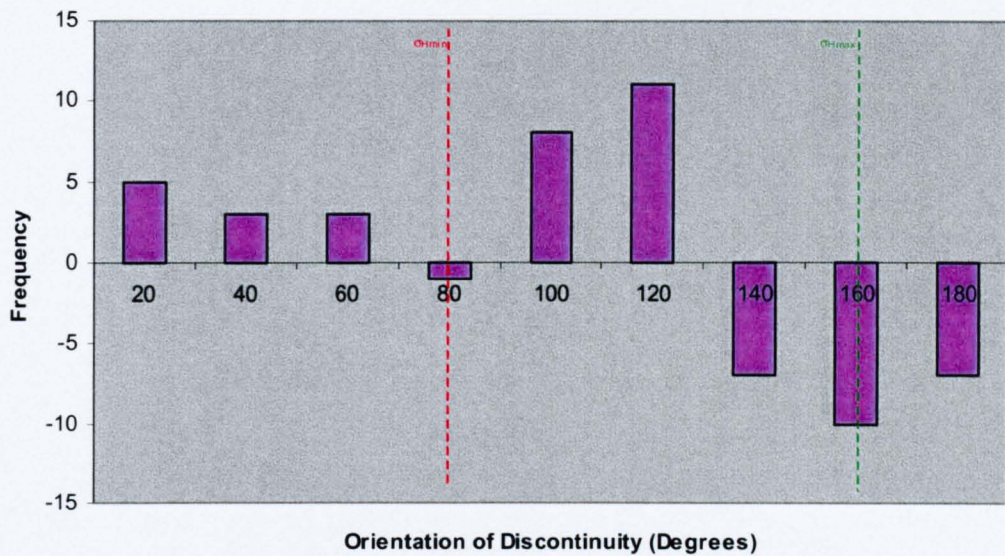


Figure 5.10 – Orientation frequency plot of the difference between the discontinuities encountered within the flowing to non-flowing areas analysed in the SIT zone in Sellafield borehole RCF3. σ_{Hmin} and σ_{Hmax} orientation lines are derived from Nirex's hydrofrac test results (NIREX, 1996a), which concluded that the mean orientation of σ_{Hmax} was 159/339°, within a range of results from 118/298° to 190/010° and the mean σ_{Hmin} orientation was 069/249°, within a range of 028/208° to 100/280°.

5.4 Discontinuity Orientation Data

At Sellafield, a mixture of borehole core and downhole geophysical image logs from the FMS/FMI and BHTV/UBI tools (section 2.4) were used by Nirex within the Sellafield boreholes to identify, orientate and characterise discontinuities (Chaplow, 1996). The logging tools provided orientated images of the borehole wall from which discontinuity attributes were identified by the British Geological Survey (BGS) and used solely to aid in the orientation of the borehole core (NIREX, 1995d). This was the main rationale set when discontinuities were identified by the BGS for Nirex. It was not the intention of Nirex to generate a second discontinuity data set, in addition to the main core-derived discontinuity data set. At the time of this study, it was not possible to obtain a digital format of Nirex's main core-derived discontinuity data set. Only the image-derived discontinuity data could be obtained. It was therefore necessary that before being able to use the BGS's image derived discontinuity data sets, a small investigation to validate the discontinuity information was preformed.

5.4.1 Validation of Discontinuity Data – Acquisition of Data

For this validation exercise, the BVG in Sellafield borehole RCF3, 630 – 790mbRT, was analysed using downhole geophysical imagery data from the FMI and UBI (AMWF – amplitude waveform and TTWF – time travelled waveform) image tools. Discontinuities were identified and characterised using the BGS's *Welllog*, *FMS/BHTV* interpretation module, developed by Andy Lee. This software enable the image logs to be viewed. Planar discontinuities appeared on the images of the borehole wall as 'unwrapped' sinusoidal features. From these features, the orientation (dip angle and dip azimuth) of the planar discontinuities was derived (section 2.4 - Figure 2.17). *FMS/BHTV* allowed the interactive 'picking' of these sinusoidal features on the downhole geophysical image log. *FMS/BHTV* then calculates the best-fit sine wave through the sinusoidal feature. This procedure was repeated for all the features identified on the image logs between 630 – 790mbRT.

Depth (mbRT)	Dip (Degrees)	Dip Azimuth (Degrees)	Type of Picked Discontinuity	Caliper (ins)	Date Picked	Time Picked	FMS/FMI (F) or BHTV/UBI (B) tool Picked from	Depth Shift (m)	Pick Number
618.93	57.64	219.09	6	6.35	16-Dec-99	17:04:34	F	0	1
619.09	76.32	172.96	6	6.35	11-Jan-00	13:46:12	B	0	2
619.32	51.98	179.78	6	6.42	11-Jan-00	13:46:38	B	0	3
619.46	39.28	154.88	6	6.42	16-Dec-99	17:04:41	F	0	4
619.98	79.08	284.56	6	6.57	16-Dec-99	17:04:50	F	0	5
620.90	57.59	359.94	6	6.68	16-Dec-99	17:13:06	F	0	6
621.62	75.53	90.05	6	6.52	16-Dec-99	17:13:28	F	0	7
621.78	63.75	115.07	6	6.53	11-Jan-00	13:51:17	B	0	8
621.83	49.44	82.72	6	6.52	11-Jan-00	13:51:04	B	0	9
622.41	46.36	20.08	6	6.62	16-Dec-99	17:13:36	F	0	10
624.11	66.82	12.04	6	6.52	16-Dec-99	17:15:22	F	0	11
624.81	47.83	48.15	6	6.52	16-Dec-99	17:15:30	F	0	12
624.95	46.66	50.06	6	6.62	16-Dec-99	17:15:52	F	0	13
625.48	55.68	42.84	6	6.54	16-Dec-99	17:15:46	F	0	14
625.76	63.16	50.49	6	6.47	16-Dec-99	17:16:00	F	0	15

Table 5.5 – Example of database generated from the picking of discontinuities in Wellog.

Classifications Type	Amount discontinuity covers image log
1	100%
2	100% - 75%
3	75% - 50%
4	50% - 25%
5	25% or less

Table 5.6 – Discontinuity type classification with respect to the discontinuities coverage across the downhole geophysical image log.

HJR's picked discontinuities

Type of Image Tool	Depth (mbRT)	Mean Orientation (Degrees)	Confidence (+/-)	Class	No. Data Points	Data File Used to Produce Results	Figure (Appendix 6)
UBI (AMWF)	630.74 - 789.94	126.70	24.10	3	390	rcf3_amwf.spck	App 9.1 & 9.2
UBI (TTWF)	630.57 - 790.95	21.70	15.50	1	425	rcf3_ttwf.spck	App 9.3 & 9.4
FMI	630.60 - 789.89	67.00	24.30	3	838	rcf3_fmi.spck	App 9.5 & 9.6

Nirex's picked discontinuities

Type of Image Tool	Depth (mbRT)	Mean Orientation (Degrees)	Confidence (+/-)	Class	No. Data Points	Data File Used to Produce Results	Figure (Appendix 6)
FMI/UBI	630.00 - 790.00	55.6	24.2	3	751	rcf3_BGS.spck	App 9.7 & 9.8

Table 5.7 – The results of the dip azimuth orientation rose plots produced from the 'picked' discontinuity data generated from the FMI and UBI (AMWF & TTWF) imagery data of Sellafeld borehole RCF3.

The dip and dip azimuths are calculated (section 2.4 - Figure 2.17) by the software and are saved as an ASCII text output data file, together with the depth of the feature, an identifier (pick type) as to the type of discontinuity seen and a unique pick number. Table 5.5 shows an example of the type of database generated from the 'picking' of discontinuities in *FMS/BHTV*. For the purpose of this analysis, discontinuities were not classified by the type of discontinuity encountered, as it is generally very difficult to determine and classify a discontinuity encountered on a downhole geophysical image log. Instead, discontinuities were classified by the amount of coverage they displayed across the image log (Table 5.6). The method used for the 'picking' of discontinuities in *Wellog* is set out in a systematic guide of how to use *Wellog's FMS/BHTV* interpretation module and can be found in Appendix 2, section 2.4.

5.4.2 Validation of Discontinuity Data - Presentation of Data

The discontinuity data derived and 'picked' from the image logs (Tables App 9.1 – 9.4, Appendix 9) were visualised using *Vector* (Appendix 2, section 2.3). It was used to assess and present the discontinuity data obtained from *FMS/BHTV* in the form of dip azimuth orientation roses and lower hemisphere equal area (Schmidt net) density stereographic projections. The orientation rose plots and lower hemisphere equal area (Schmidt net) density stereographic projections are presented in Figure 5.11 (Appendix 1B) and Appendix 9 (Figures App 9.1 – 9.6). Table 5.7 summarises these results.

5.4.3 Validation of Discontinuity Data - Assessment of Data

The main objective of this validation exercise was to carry out a small discontinuity picking exercise to see how the various image tools data sets compare to the original discontinuity data set generated by the BGS for Nirex.

The UBI generated discontinuity data from the AMWF and TTWF image logs, did not correlate very well with the original BGS data (Table 5.7 & Figure 5.11, Appendix 1B). The discontinuity dip azimuth orientation roses produced from the UBI tools were almost circular in shape. The AMWF image log produced a circular triaxial shaped rose, with a mean direction of $126.7 \pm 24.1^\circ$ (Figure 5.11, Appendix 1B) and the TTWF image log gave a circular biaxial shaped rose, with a mean direction of $21.7 \pm 15.5^\circ$ (Figure 5.11, Appendix 1B). The BGS's discontinuity dip azimuth orientation rose produced a biaxial shaped rose, with a mean direction of $55.6 \pm 24.2^\circ$ (Figure 5.11, Appendix 1B). Similarities within the UBI's discontinuities data sets and the original BGS discontinuity data sets equal area density stereographic projections can be observed (Figure 5.11, Appendix 1B). Both the UBI and the BGS's stereographic projections (Figure 5.11, Appendix 1B) exhibit a clustering of discontinuities poles to plane in the SW and W corners of the stereonets. However, in the UBI data a significant cluster of discontinuities is missing in the center of the NW quadrant of the stereonets, which are evident in the BGS's data.

The FMI-generated discontinuity data shows a good correlation with the original BGS generated data (Table 5.7 & Figure 5.11, Appendix 1B). The discontinuity dip azimuth orientation roses produced from the FMI tool display a biaxial shaped rose with a mean direction of $60.7 \pm 24.3^\circ$ (Figure 5.11, Appendix 1B), which compare closely to the BGS's discontinuity dip azimuth orientation rose that is biaxial in shape with a mean direction of $55.6 \pm 24.2^\circ$ (Figure 5.11, Appendix 1B). The biaxial element in the FMI discontinuity data is more pronounced than the BGS's data. The FMI and the original BGS's discontinuity data sets equal area density stereographic projections are almost identical (Figure 5.11, Appendix 1B). Both equal area density stereographic projections display a clustering of discontinuities poles to plane in the SW and W quadrant and in the center of the NW quadrant of the stereographic projections. The intensity of the clustering does vary between the two data sets.

During the picking of discontinuities on the FMI and UBI (AMWF and TTWF) image logs, discontinuities were assigned a classification. The classification of a discontinuity was determined by the amount of coverage a discontinuity displayed across the image log (section 5.4.1 & Table 5.6). These classifications have been used to partly analyse and assess the FMI and UBI image tools ability to detect and image a discontinuity (Table 5.8 & Figure 5.12). The original picked discontinuity data files (Tables App 9.1 - 9.3, Appendix 9) contain all the information on the varying classification results.

Overall, it can be concluded that the FMI image tool was more sensitive (detected more discontinuities) and resolved finer scale features than the UBI tool in the BVG. Within the BVG there are a large number of hairline, minute discontinuities and therefore the imaging capabilities of the FMI tool are advantageous. This is due to the FMI tool's ability to probe a small volume of rock beyond the borehole wall, whilst the UBI only 'sees' the intersection of the discontinuity within the borehole wall. This principle can be seen in the data analysed: the UBI AMWF tool detected 390 discontinuities; the UBI TTWF tool detected 425 and the FMI tool detected 839 discontinuities (Table 5.8). This is due to the resistivity imaging (FMS/FMI) tools being more sensitive, primarily to resistivity contrasts (fluid contrasts) in the rock and ability to resolve finer scale features than acoustic devices (Prensky, 1999). The resistivity imaging tool scans and probes the electrical conductivity of a rock mass that is a function of the porosity, pore fluid, pore geometry, cementation and mineral infilling conductivity. This compares to the acoustic tools that probes the acoustic impedance of the rock mass, which is a function of the seismic velocity and density of the rock.

The BHTV/UBI AMWF image log was able to discriminate the sinusoidal length of the discontinuities better than the FMI image log. The AMWF image had 69% of the picked discontinuities displaying over 50% coverage across the image log (Table 5.8 & Figure 5.12). This compares to the FMI image that detected 60%, and the TTWF image, which detected 43% of the picked discontinuities displaying over 50% coverage of the image log (Figure 5.12).

This result is not surprising, due to the UBI tool's ability to image the full borehole wall (100% coverage) compared to the FMI that gives between ~ 50 – 90% coverage (Table 2.2) depending on the diameter of the borehole (Rider, 1996). These conclusions are consistent with what has been previously stated by Paillet *et al.* (1990) and Prensky (1999).

Due to the similarities between the FMI and BGS discontinuity data sets (majority of discontinuities picked by the BGS identified using the FMS/FMI imagery logs), and the conclusion that the FMI image tool is more sensitive (detected more discontinuities) and resolved finer scale features than the UBI tool in the BVG, it seems reasonable, to conclude that the BGS's picked discontinuity data is a good representation of the discontinuities encountered in the imagery logs and therefore within the borehole and the surrounding area. There are limitations encountered when using image logs to create discontinuity data sets (i.e. under-sampling of the discontinuities due to the resolution of the imagery tools and sub-sampling discontinuity data due to the orientation of the borehole - section 2.4 & 2.4.1). Thus the data set created can never be considered as a definitive and correct discontinuity data set for the rock mass.

From the results of this validation exercise it has been assumed that the discontinuity data collected by the BGS, in the rest of the Sellafield boreholes, will also display a true representation of the discontinuities encountered. The BGS's discontinuity data, derived from image logs of the Sellafield boreholes, will therefore be used in any further investigations in this thesis and are derived from the Nirex Digital Geoscience Database (NDGD) (NIREX, 1996c).

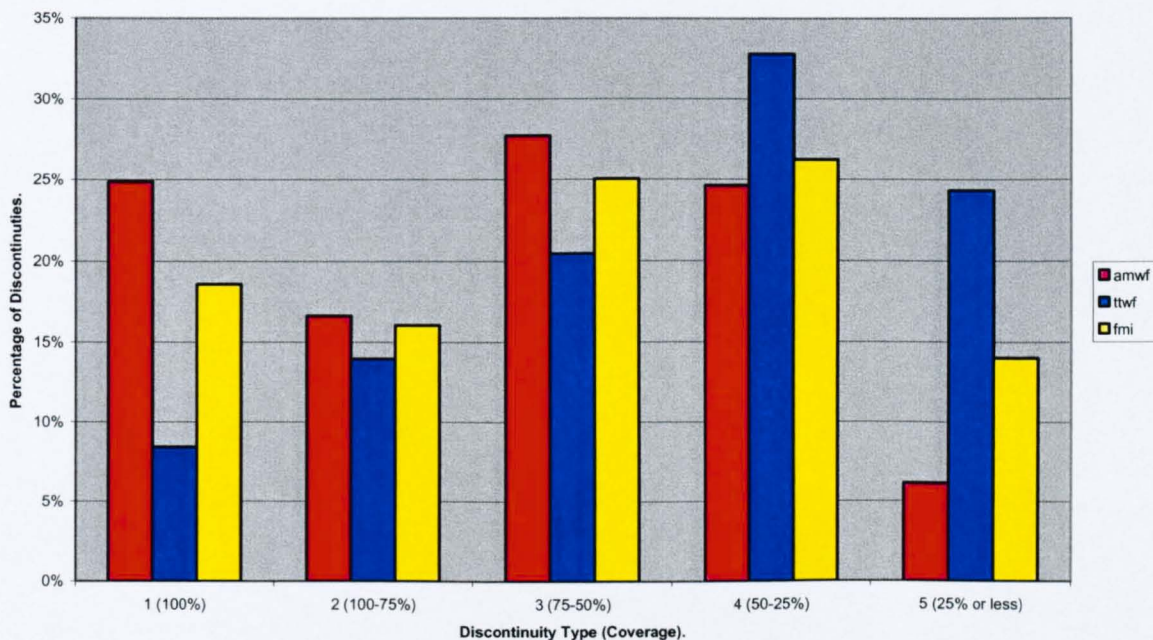


Figure 5.12 – Graph showing the percentage of discontinuities encountered by each imagery tool with respect to the discontinuity type (Table 5.6).

Classification of Discontinuity (coverage)	Downhole geophysical image Tool used					
	amwf		ttwf		fmi	
1 (100%)	97	25%	35	8%	154	19%
2 (100-75%)	65	17%	58	14%	133	16%
3 (75-50%)	108	28%	85	20%	207	25%
4 (50-25%)	96	25%	136	33%	217	26%
5 (25% or less)	24	6%	101	24%	116	14%

Table 5.8 – Results of the percentage of discontinuities encountered by each imagery tool with respect to the discontinuity type (Table 5.6).

6. - *In Situ* Stress, Fracture Systems and Groundwater Flow Pathways

6.1 Introduction

Discontinuities have long been identified as playing an important role in controlling hydraulic properties of rock masses by providing permeable conduits for fluids (Finkbeiner *et al.*, 1997). Analysis of drill core or borehole imagery logs may reveal the presence of hundreds or even thousands of discontinuities (section 2.4 for detailed discussion on discontinuities). However production logging and experience demonstrates that only a relatively small proportion of these discontinuities will contribute to flow in the borehole (Long *et al.*, 1991).

Recent research by Barton *et al.* (1995) indicates that stress plays an important role in controlling the flow of fluid within a fractured rock mass (section 2.6). These authors calculated the shear (τ) to normal (σ_n) stress ratio acting on the plane of a discontinuity (Figure 2.19),

$$\tau = \beta_{11}\beta_{21}\sigma_1 + \beta_{12}\beta_{22}\sigma_2 + \beta_{13}\beta_{23}\sigma_3 \quad \text{Eq.6.1}$$

$$\sigma_n = \beta_{11}^2\sigma_1 + \beta_{12}^2\sigma_2 + \beta_{13}^2\sigma_3$$

(Jaeger and Cook, 1984), where β_{ij} are the direction cosines between the fracture plane and the components of the stress tensor (section 2.2.2). From this analysis Barton *et al.* (1995) were able to determine whether each discontinuity was in a state of stress close to localised shear failure and therefore acting as a potentially active fault ('critically stressed'). The ratio of the induced shear to effective normal stress indicates how close a discontinuity is to failure. In this analysis Barton *et al.* (1995) used the Coulomb failure criterion (assuming effective stress)

$$\tau = \mu(\sigma_n - P_p). \quad \text{Eq.6.2}$$

Where P_p is the hydrostatic pore pressure and μ is the coefficient of friction. Barton *et al.* (1995) assumed that if a discontinuity plane was optimally

orientated to the stress field (Figure 2.18) and had a $\mu \geq 0.6$, frictional sliding of the discontinuity could occur. These discontinuities were classed as being 'critically stressed'. Barton *et al.* (1995) assumed the $\mu \geq 0.6$ based on the work by Byerlee (1978) (section 2.6). When a discontinuity undergoes localised shear failure, if the strength of the discontinuity wall is sufficient, the asperities will ride up and over each other resulting in dilation (Figure 2.20) and causing an increase in permeability (Heffer and Koutsabeloulis, 1995 & Yeo *et al.*, 1998). If discontinuity permeability is stress dependant, because of discontinuity surfaces experiencing localised shear failure, then no longer will the stress field orientation alone be sufficient to define the most conductive pathways. Instead, the interplay between the discontinuity orientations and the full stress tensor needs to be considered.

The identification, orientation and distribution of discontinuities and their relationship to the current stress field are of great interest to the petroleum industry dealing with fractured reservoirs, the environmental sector looking at the migration of contaminants through fractured rocks and the water industry that deals with the abstraction of water from fractured aquifers. Hence, it is important to be able to identify hydraulically conductive (flowing) from hydraulically non-conductive (non-flowing) discontinuities. By using the hydrogeological (flow zone and Short Interval Test (SIT)), *in situ* stress and discontinuity data generated and presented in Chapter 5, the Barton *et al.* (1995) relationship between the flow of fluid through a fractured rock mass and the prevailing stress field can be investigated and the theory applied and tested within the Permian-Triassic and the Borrowdale Volcanic Group (BVG) rocks at Sellafield.

In addition, the geological, hydrogeological, *in situ* stress and discontinuity data from Sellafield are integrated here into composite borehole logs. These visual compilations should aid in the identification of hydraulically conductive (flowing) from hydraulically non-conductive (non-flowing) discontinuities using simple visual pattern analysis.

6.2 Integration of Discontinuity Data and *In Situ* Stress Data

6.2.1 Introduction

To be able to investigate the relationship between the flow of fluid through a fractured rock mass and the prevailing stress field, an understanding of how the regional stress tensor (section 2.2.2) alters with depth at Sellafield is required. As part of Nirex's scientific investigations, at Sellafield, hydrofracture stress measurements, breakout analysis, density log analysis and overcoring stress measurements were undertaken (NIREX, 1996a). From these analyses, it was possible to determine various *in situ* stress parameters (Table 6.1), the results of which are presented in Table 10.1, Appendix 10. From Nirex's *in situ* stress investigation (NIREX, 1996a) it was possible to determine the magnitude of the principal stresses (σ_1 , σ_2 , σ_3) within the Sellafield stress tensor (section 2.2.2). In NIREX, 1996a it was concluded that the maximum horizontal stress (σ_{Hmax}) was equivalent to σ_1 , the vertical stress (σ_v) was equivalent to σ_2 and the minimum horizontal stress (σ_{Hmin}) was equivalent to σ_3 . By using Nirex's hydrofracture stress measurements, density log analysis-derived principal stress (σ_{Hmax} , σ_{Hmin} , σ_v) and pore pressure (P_p) magnitudes were graphically presented (Figure 6.1) with respect to depth (meters below rotary table (mbRT)). The depth trends of the principal stress and pressure magnitudes were determined using linear regression analysis of best fit (Figure 6.1). Assumptions made during this analysis were as follows:-

1. There was no pore pressure (P_p) magnitude at the surface (0 mbRT) within the rock mass at Sellafield.
2. There was no vertical stress (σ_v) magnitude at the surface (0 mbRT) within the rock mass at Sellafield.
3. There is a maximum horizontal stress (σ_{Hmax}) magnitude at the surface (0 mbRT) within the rock mass at Sellafield.
4. There is a minimum horizontal stress (σ_{Hmin}) magnitude at the surface (0 mbRT) within the rock mass at Sellafield.

Therefore, both the pore pressure and vertical stress magnitudes have trend lines that intercept the origin of Figure 6.1 and the maximum horizontal and minimum horizontal stress magnitudes both cross the stress magnitude axis. These assumptions were based on the work undertaken by Blenkinsop *et al.* (1986) where horizontal *in situ* stresses measured by flatjack methods (section 2.2.3.3), and found to exist at the surface in quarries around the UK.

From Figure 6.1 it can be concluded that at Sellafield the regional stress regime suggests a dominant strike-slip tectonic setting where $\sigma_{Hmax} > \sigma_V > \sigma_{Hmin}$. This result is in agreement with observations made by Evans (1987) in his assessment of UK crustal stresses. By using the linear equations generated in Figure 6.1, for the depth trends of the principal stress (σ_{Hmax} , σ_{Hmin} , σ_V) and pressure (P_p) magnitudes, further detailed analyses (section 6.2.2) of individual discontinuity surfaces were undertaken.

6.2.2 Acquisition of Data

To investigate the possibility that localised shear failure is occurring on individual discontinuity planes, the stress and hydrogeological data presented, generated and discussed in Chapter 5 were used. The flow zones (section 5.3.1) in Sellafield boreholes 2, 5, 8A, 11A, RCF3, RCM1 and RCM2 and Sellafield borehole RCF3 SIT zone flowing and non-flowing areas (section 5.3.2) for the areas that have been investigated. To enable the analysis to be undertaken a specialist Unix-based software routine called *Stressit* was developed by Dr Chris Evans of the British Geological Survey (BGS). This software routine applies all the concepts and assumptions that Barton *et al.* (1995) used in their analysis (section 6.1). A systematic guide of how to use *Stressit* is presented in Appendix 2, section 2.5. *Stressit* firstly analyses the depth trends of the regional stress (σ_{Hmax} , σ_{Hmin} , σ_V) and pressure (P_p) magnitudes by using the linear equations generated from Figure 6.1.

In-Situ Stress Measurement Method	In-Situ Stress Parameters Determined		Comments
	Directly	By Computation	
Hydrofracture	σ_{Hmax} azimuth σ_{Hmin} magnitude	σ_{Hmax} magnitude σ_{Hmin} azimuth	May require Pp magnitude and mechanical properties of rock
Breakout Analysis	σ_{Hmin} azimuth	σ_{Hmax} azimuth	Also good indicator of orientation of principal stresses
Density Log Analysis	Trend of σ_v magnitudes with depth	N/A	Requires lithology versus depth data
Overcoring	Induced strains	σ_1 , σ_2 , & σ_3 magnitudes and orientations	Requires elastic properties of the overcore

Table 6.1 – Summary of stress parameters determined from the various stress analyses used at Sellafield (from NIREX, 1997a).

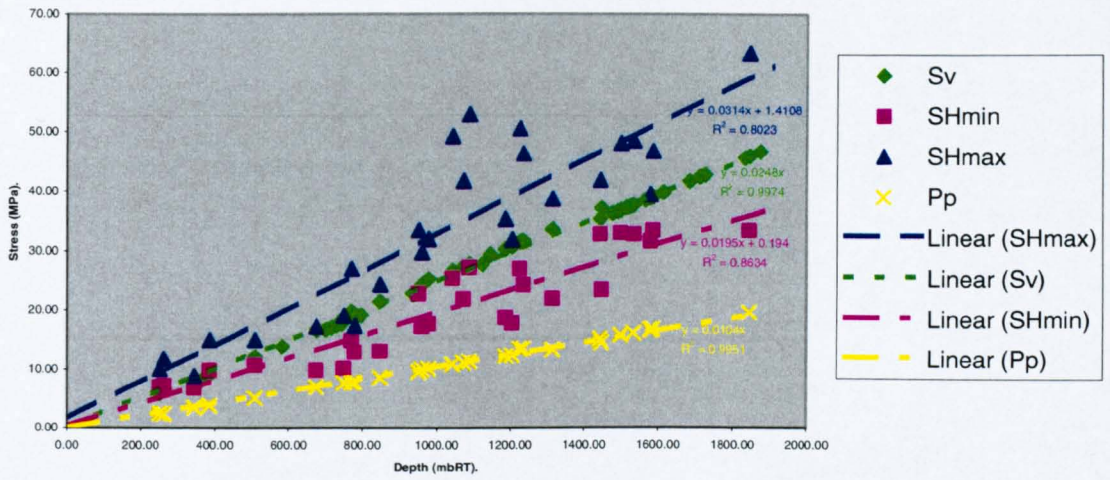


Figure 6.1 - Graphical presentation of the derived stress ($S_v = \sigma_v$, $S_{Hmin} = \sigma_{Hmax}$ & $S_{Hmax} = \sigma_{Hmin}$) and pressure (P_p) magnitudes versus depth (mbRT).

This information is then orientated for the appropriate local stress regime under investigation by applying the mean azimuth of σ_{Hmax} generated in section 5.3. From this information a Mohr diagram of stress, which represents the local stress regime, can be constructed (Figure 2.19). The ratio of shear to normal stresses acting on the plane of the discontinuity under investigation is then calculated (section 6.1). These results then enable the discontinuity planes to be located on the Mohr diagram, indicating the ratio of shear to normal stress acting upon them. Assessment of which discontinuities are in a state of stress close to localised shear failure, and therefore acting as a potentially active fault ('critically stressed') can then be performed by comparing the location of the fracture σ_n/τ point with the Coulomb failure criterion line.

6.2.3 Presentation of Data

6.2.3.1 Flow Zones

The Mohr diagram plots and the output files created from the *Stressit* analysis for the flow zones analysed in Sellafield boreholes 2, 5, 8A, 11A, RCF3, RCM1 & RCM2 are all presented in Appendix 10. A summary of the plots and the output files presented in this appendix are given in Tables 6.2 a/b/c/d/e/f/g (Appendix 1A – Oversized Tables).

6.2.3.2 SIT Zone

The Mohr diagram plots and the output files created from the *stressit* analysis carried out on flowing and non-flowing areas within the SIT zone in Sellafield borehole RCF3 are presented in Appendix 10. Table 6.3 provides a summary of the plots and the output files presented in Appendix 10.

SIT FZ ID	Top FZ Depth (mbRT)	Top FZ Depth (mbRT)	σ_{Hmax}	Stressit Output Data File	No. Data Points	Stressit Output Plot File
NA	630	651.89	162.3	rcf3_nfa_ssit_630_651.dat	115	Figure App 10.133
A	651.89	653.45	169.2	rcf3_fza_ssit_651_653.dat	7	Figure App 10.134
NB	653.45	668.98	150.4	rcf3_nfb_ssit_653_668.dat	87	Figure App 10.135
B	668.98	670.54	116.6	rcf3_fzb_ssit_668_670.dat	10	Figure App 10.136
NC	670.54	695.64	138.8	rcf3_nfc_ssit_670_695.dat	139	Figure App 10.137
C	695.64	697.2	130.1	rcf3_fzc_ssit_695_697.dat	5	Figure App 10.138
ND	697.2	706.61	142.2	rcf3_nfd_ssit_697_706.dat	41	Figure App 10.139
D	706.61	709.7	111.6	rcf3_fzd_ssit_706_709.dat	17	Figure App 10.140
NE	709.7	717.5	161.7	rcf3_nfe_ssit_709_717.dat	42	Figure App 10.141
E	717.5	723.71	150.8	rcf3_fze_ssit_717_723.dat	38	Figure App 10.142
NF	723.71	754.91	174.8	rcf3_nff_ssit_723_754.dat	103	Figure App 10.143
F	754.91	758	172.3	rcf3_fzf_ssit_754_758.dat	11	Figure App 10.144
NG	758	759.54	148.7	rcf3_nfg_ssit_758_759.dat	7	Figure App 10.145
G	759.54	761.1	141.9	rcf3_fzg_ssit_759_761.dat	7	Figure App 10.146
NH	761.1	764.26	152	rcf3_nfh_ssit_761_764.dat	12	Figure App 10.147
H	764.26	767.39	145.6	rcf3_fzh_ssit_764_767.dat	18	Figure App 10.148
NI	767.39	790	171	rcf3_nfi_ssit_767_790.dat	92	Figure App 10.149

Table 6.3 – Results of SIT Zone *Stressit* analysis for Sellafield borehole RCF3.

6.2.4 Assessment of Data

6.2.4.1 Flow Zones

The first observation arising from the flow zones *Stressit* analysis (Figures App 10.1 – 10.148, Appendix 10) was that between 0-120 mbRT differently oriented and shaped Mohr circles were generated (Figures App 10.77-10.80 & 10.104-10.106), even though the same linear stress and pressure magnitude equations (Figure 6.1) were used throughout the analysis. These Mohr circles (Figures App 10.77-10.80 & 10.104-10.106) show a change in the complete stress tensor. From Figure 6.1, it was apparent that the change in the complete stress tensor was due to the vertical stress (σ_v) rising from zero vertical stress at the surface until it equals the minimum horizontal (σ_{Hmin}) stress at approximately 120 mbRT, after which a switch in the principal stress orientations happens. As a result, the results for flow zones between 0-120 mbRT (Figure App 10.77-10.80 & 10.104-10.106) are not considered further and these results will be disregarded.

When looking at Figures App 10.1 – 10.148 (Appendix 10), it is apparent that there is a correlation between the type of geological unit (i.e. Permian-Triassic vs BVG) in which discontinuities occur and where they fall on a Mohr's diagram. Generally in the Permian-Triassic rocks, the discontinuities are closely placed together just above σ_2 (Figure 6.2a). In the BVG, discontinuities are randomly, scattered across the Mohr diagram (Figure 6.2b). This pattern probably reflects the consistency in the orientation of discontinuities within the Permian-Triassic rocks (strike \approx NW-SE, Dip \approx 30°SW) compared to the very varied orientation of the discontinuities in the BVG (NIREX, 1996e).

The main conclusion from the *Stressit* analysis is that none of the flow zones investigated (Tables 6.2a/b/c/d/e/f/g, Appendix 1A) indicates the presence of discontinuities that appear to be 'critically stressed' ($\mu \geq 0.6$) and are in frictional equilibrium with the *in situ* stress field. Each one of the flow zones analysed have been identified from production logs as locations where an

increase in groundwater flow occurs and where there is increased permeability (section 5.2). These observations are not apparently consistent with the predictions of Barton *et al.* (1995). On the Mohr diagrams for the flow zones at Sellafield (Figures App 10.1 – 10.148, Appendix 10), all discontinuities lie well away from the failure envelope. For these discontinuities to become 'critically stressed' ($\mu \geq 0.6$), a change in the principal stresses (σ_{Hmax} , σ_{Hmin} , σ_v) or pore pressure (Pp) within the rock mass needs to occur.

6.2.4.2 SIT Zone

The *Stressit* analysis suggests that the SIT zone, there also appears to be not 'critically stressed' ($\mu \geq 0.6$) discontinuities in frictional equilibrium with the *in situ* stress field (Figures App 10.133 – 10.149, Appendix 10). All the flowing areas here were identified using the specialist Schlumberger's Modular Dynamic Tester as being locations where an increase in groundwater flow (transmissivity) and increased permeability occurs (section 5.2). The result is not surprising, since exactly the same stress regime applies as in the study above (section 6.2.4.1).

In the results obtained between the flowing and non-flowing areas, (Figures App 10.133 – 10.149, Appendix 10), no clear relationship is established. The discontinuities in both non-flowing and flowing areas (Table 6.3) are randomly, scattered across the Mohr diagrams in a similar way (section 6.2.4.1 & Figure 6.2 b). The only exception to this rule is the non-flowing area NF, which shows a clustering of points to the far left of the Mohr diagram (Figure App 10.143, Appendix 10). In the flowing areas (Table 6.3), three trends were identified. In flowing areas B, C and D, all the discontinuities identified cluster to the right of the Mohr diagram (Figures App 10.136, 10.138 & 10.140, Appendix 10). In areas A, E, G and H, discontinuities were generally observed to cluster to the left of the Mohr diagram (Figures App 10.134, 10.142, 10.146 & 10.148, Appendix 10). In flowing area F, discontinuities were observed to be orientated more centrally within the Mohr circle (Figure

App 10.144, Appendix 10). These observations are thought to relate to the orientation of σ_{Hmax} , which was applied in the *Stressit* analysis. The flowing areas with values for σ_{Hmax} from 111 - 143° generally had discontinuities that were orientated to the right of the Mohr diagram. For flowing areas that have values for σ_{Hmax} from 145 - 170,° discontinuities were generally orientated to the left in the Mohr diagram (Table 6.3). Where σ_{Hmax} is greater than 170°, the discontinuities are orientated more centrally in the Mohr diagram (Table 6.3).

Adding all the flowing and non-flowing areas, discontinuity data together enabled a composite stressit analysis to be undertaken for the flowing and non-flowing areas. The procedure set out in section 6.2.2, above was followed (the σ_{Hmax} orientation of 159/339°, which was derived from Nirex's hydrofrac test results, was used (NIREX, 1996)). The results from this analysis are presented in Figure 6.3a/b. Again no discontinuities are identified as being 'critically stressed'. When Figure 6.3a is compared with Figure 6.3b, it is easy to see a definite distinction between the flowing and non-flowing data sets. The flowing discontinuities (Figure 6.3a) generally form a distinct subset in the upper portion of the Mohr diagram, compared to the non-flowing discontinuities (Figure 6.3b) that are more randomly orientated to the lower portions of the Mohr diagram. The non-flowing subset discontinuity data set, generated in section 5.3.1.3, was also analysed to enable a true comparison between the flowing and non-flowing discontinuity data, due to the data sets being similar in size. The results from this *stressit* analysis can be seen in Figure 6.3c. The same procedure that was applied to the flowing and non-flowing data above was again followed. The non-flowing subset discontinuity data (Figure 6.3c) again showed a randomly orientated distribution to the discontinuities in lower portion of the Mohr diagram. Although this result gives a more positive conclusion, it does not help to identify the precise discontinuities that are contributing to flow. Within the present stress regime one concludes that there would be no critical stress relate flow at Sellafield.

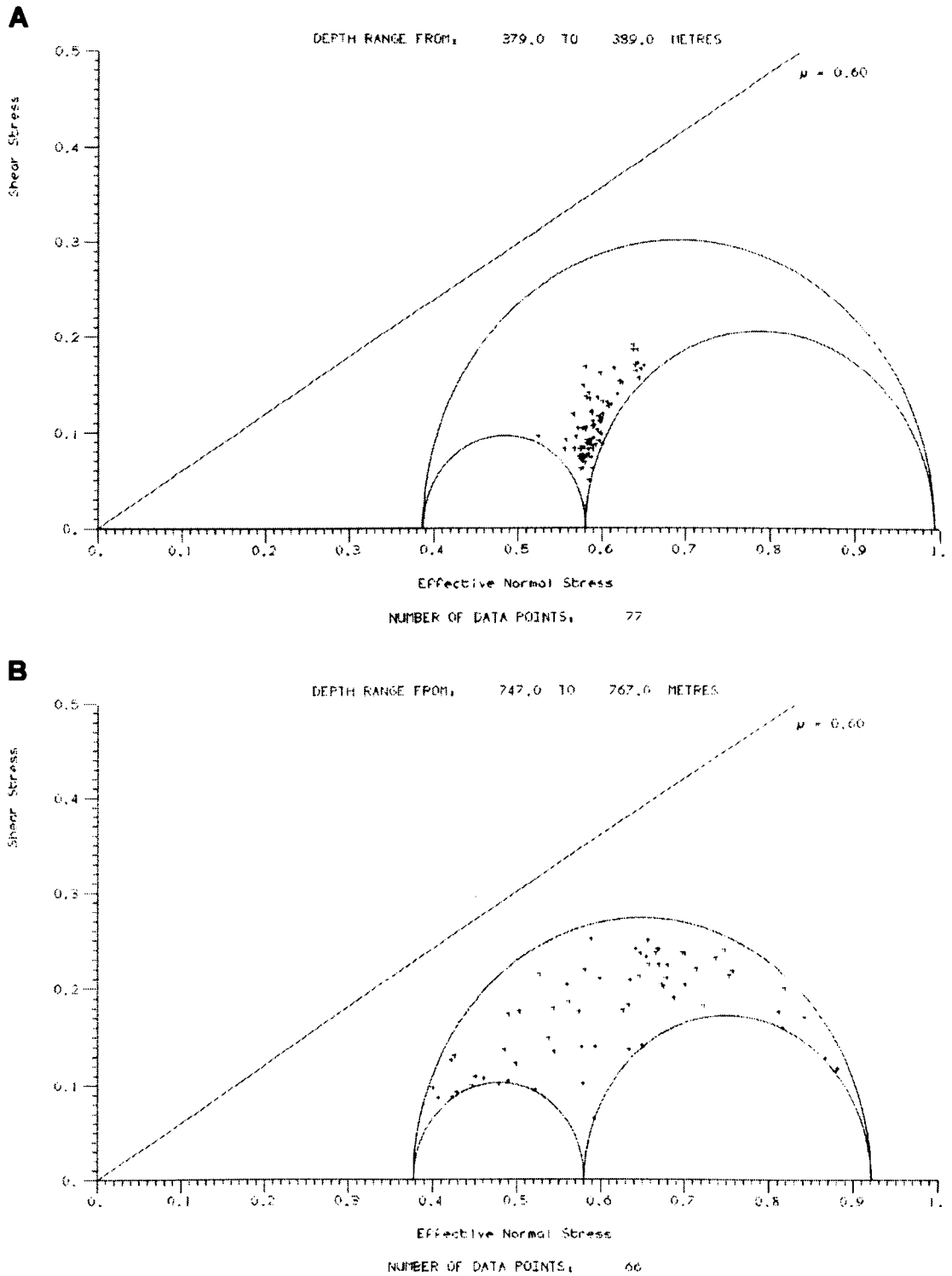
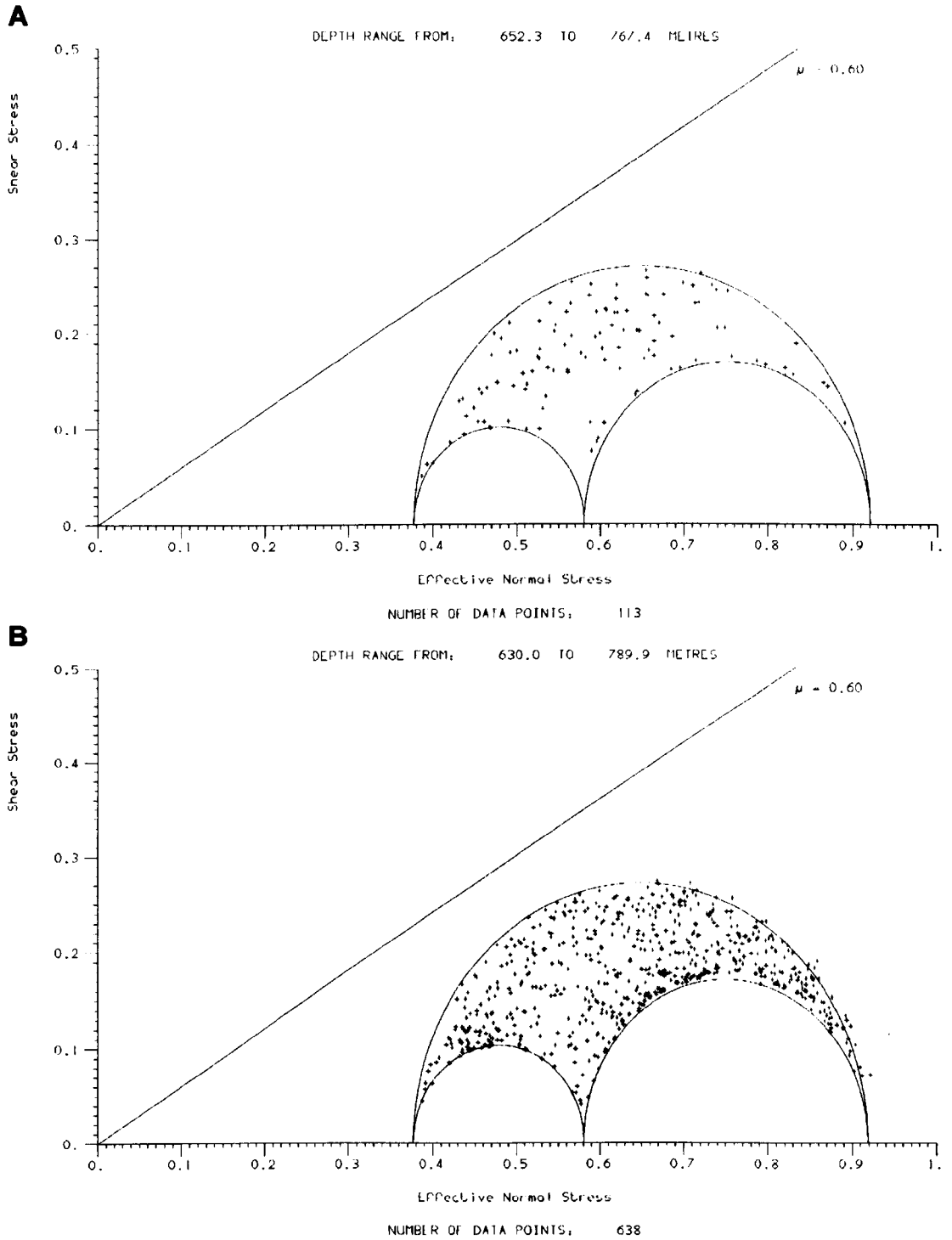
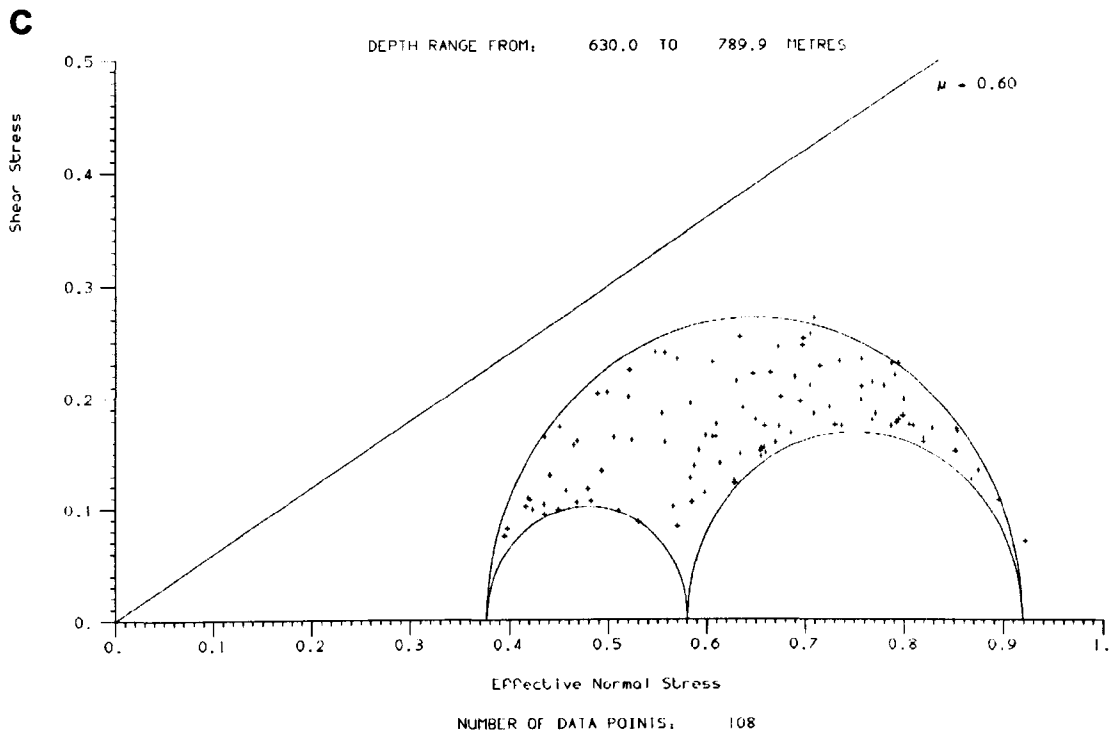


Figure 6.2a/b – Schematic diagram demonstrating the relationship between discontinuities found in the a) Permian-Triassic and the b) BVG with respect to their location on the Mohr's circle diagram of stress at Sellafield.



Figures 6.3a/b – Composite Mohr diagram for all the a) flowing and b) non-flowing areas in the SIT zone.



Figures 6.3c – Composite Mohr diagram for all non-flowing subset areas in the SIT zone.

From this investigation into the relationship between the flow of fluid through a fractured rock mass and the prevailing stress field, it has become apparent that, at least in the Sellafield region, there is no straightforward correlation between stress orientation and an increase in discontinuity permeability as predicted by Barton *et al.* (1995). 'Critically stressed' discontinuities (section 2.6) form from pre-existing flaws, because they are not in frictional equilibrium with the current stress field at Sellafield. A change in the magnitudes of the principal stresses (σ_{Hmax} , σ_{Hmin} , σ_V) or pore pressure (P_p) within the rock mass needs to occur for the discontinuities analysed to become 'critically stressed'. One way to improve the critical stress analysis undertaken would be to apply a differing failure criterion, such as modified Griffith-type (McLintock and Walsh, 1962) or the Hoek-Brown (Hoek and Brown, 1980a) model. At Sellafield the Barton *et al.* (1995) critical stress analysis merely identifies discontinuities that are more likely to have enhanced permeability and become 'critically stressed', if changes occur to the current stress fields stress magnitudes. It is therefore suggested that this technique is thought of as a characterisation tool that identifies discontinuities 'at risk' of becoming 'critically stressed', a technique that is indicative not prescriptive.

It seems likely that the assumptions and parameters which determine whether a discontinuity is counted as being 'critically stressed' or not are based on a simplified model of the rock mass (section 2.6). Assuming that the rock mass being analysed is isotropic and homogeneous is clearly overly simplistic. There are very few natural rocks that are anisotropic. Indeed the Permian-Triassic and the BVG at Sellafield are, quite clearly anisotropic and heterogeneous even within the same lithological units (section 3.1.2 & BGS, 1997 and Table 6.4). Many other elements that are known to exist in fractured rock masses are not considered in this analysis. For example, the effect of discontinuities having mineral coatings, clays or fault gouge infillings are not included. These would cause cohesion and greatly alter the coefficient of friction required for frictional failure to occur.

The critical stress analysis also encompasses a number of calculations that contain some degree of error. For example, if you consider the principal stress orientations that were generated in section 5.3, they have calculated errors varying from ± 3.3 to 27.1° (Table 5.2 & 5.3). The stress magnitudes are also statistically determined through linear regression analysis of best fit, a method that is open to error. Even small errors can have great effects on the very sensitive calculation used in *Stressit*. By altering only one of the stress or pressure magnitude gradients, this causes the Mohr circle to alter. For example, if you altered the pore pressure (P_p) magnitude gradient by ± 0.002 when using *Stressit* to analyse Sellafield borehole RCF3 SIT flowing area E (717.50 – 723.71 mbRT), it causes the Mohr circle to move either closer to the origin of the graph (Figures 6.4a) when the pore pressure (P_p) magnitude gradient is increased by 0.002, or to move away from the (Figures 6.4b) when the pore pressure (P_p) magnitude gradient is decreased by 0.002. This occurs because the changes in the pore pressure (P_p) magnitude gradient alter the values of σ_1 , σ_2 and σ_3 . It appears, therefore, that an in depth investigation into the size of errors that are generated from the critical stress analysis is required, so that its limitations are more fully appreciated. Such an analysis extends beyond the present thesis.

6.3 Integration of all Discontinuity Data, *In Situ* Stress Data, Flow Data, Geological Data and Geophysical Data

6.3.1 Introduction

One of the best ways to integrate and visualise borehole data, whether geological, geophysical or hydrogeological, is to produce a composite borehole log. Extensive literature exists dealing with the petrophysical characterisation and evaluation of rock mass properties from geophysical wireline logs and core samples, with a clear focus on examples from sedimentary hydrocarbon reservoir rocks (Hearst and Nelson, 1985; Doveton, 1986; Doveton and Prenskey, 1992).

Geological Period	Lithology	UCS (MPa)			Young's Modulus (GPa)			Poisson's Ratio		
		Maximum	Minimum	Mean	Maximum	Minimum	Mean	Maximum	Minimum	Mean
Permian-Triassic	Undifferentiated St Bees Sandstone	152.3	18.6	62.3	73.4	9.51	26.86	0.53	0.1	0.22
	North Head Member	189.6	55.6	99.6	45.9	21.8	31.05	0.25	0.08	0.18
	Brockram	69.4	7.2	36.4	37.9	34.2	36.12	0.32	0.16	0.22
BVG	Faulted Longlands Farm Member	157.8	104.2	128.4	/	/	60*	/	/	0.23*
	Altered Longlands Farm Member	41	38.1	39.6**	/	/	/	/	/	/
	Bulk Longlands Farm Member	308.8	29.1	157	97.5	73.8	84.6	0.25	0.22	0.24

* Only one sample use in analysis- Borehole RCF3

** Only two samples use in analysis

Table 6.4 – Rock mass characterisation data for some of the lithology encountered at Sellafield (adapted from NIREX, 1997b).

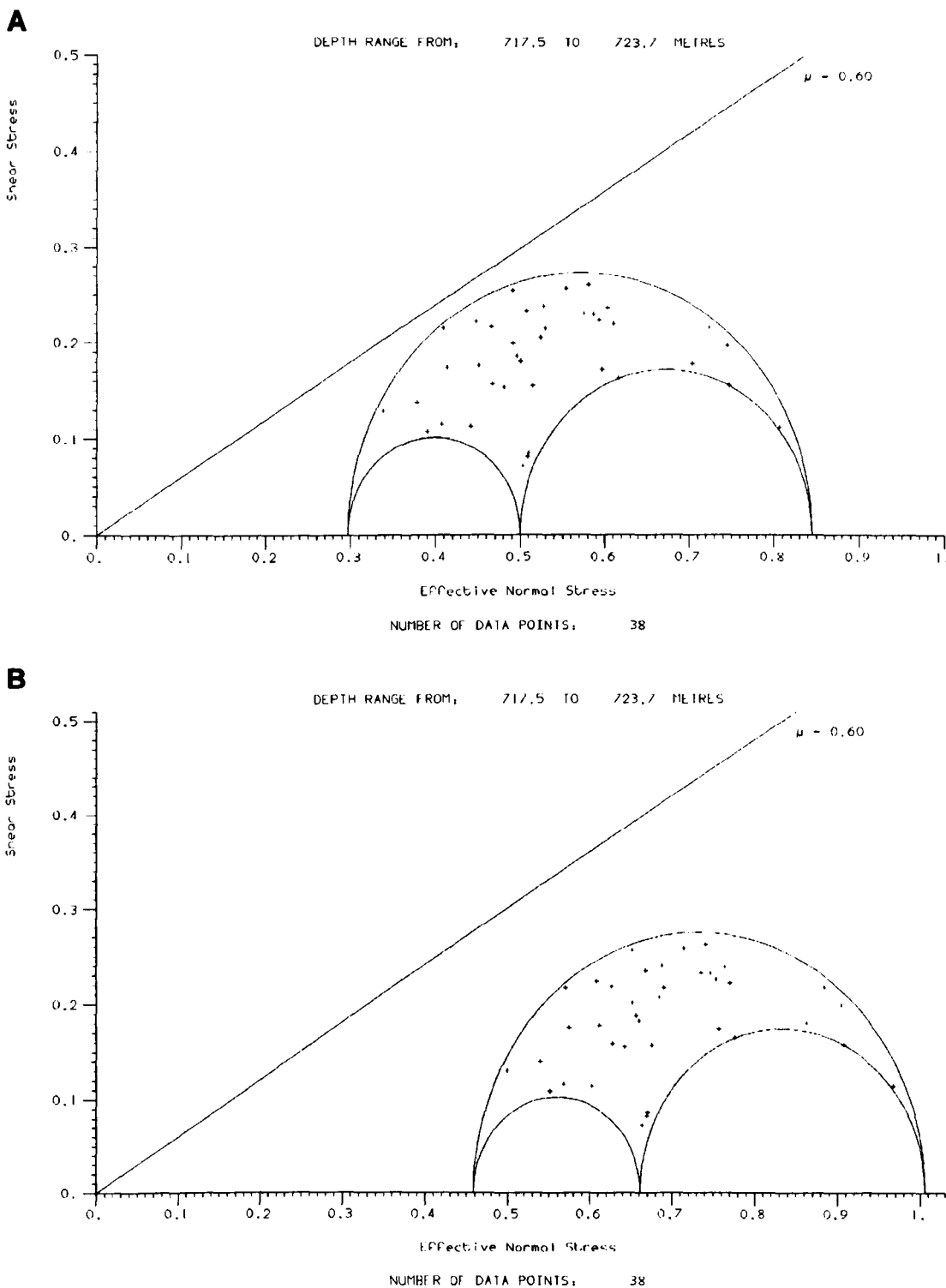


Figure 6.4 a/b – Mohr's circle of stress diagram where a pore pressure (P_p) magnitude gradient of a) 0.0124 and b) 0.0084 was applied to SIT flowing area E.

There are a few papers (notably Keys, 1979; McEwen *et al.*, 1985; Paillet, 1991b; Bremer *et al.*, 1992), that also discuss petrophysical characterisation and evaluation of rock properties from geophysical wireline logs in igneous and metamorphic rocks investigated during radioactive waste investigations.

During Nirex's investigations at Sellafield (section 1.2), a number of different types and styles of composite logs were created for differing projects:-

- A set of composite logs (Appendix 11) was presented in (NIREX, 1995f) to summarize the results from the geological, geophysical, groundwater monitoring, rock material properties and geochemical studies undertaken in all of the Sellafield boreholes.
- The geological and structural discontinuity information, gathered from the analysis of the borehole core and the geophysical borehole imagery logs, was presented in (NIREX, 1996e) as a suite of summary logs and charts (Appendix 11) for the Sellafield boreholes contained within the PRZ area (Boreholes 2, 4, 5, RCF1, RCF2, RCF3, RCM1, RCM2, RCM3, PRZ2 & PRZ3).

A additional specialist study of the spatial heterogeneity of the rocks mass at Sellafield was undertaken by Nirex and is presented in NIREX (1997i), NIREX (1997j) and Brereton *et al.* (1998). This research was undertaken mainly by the BGS who investigated how rock mass and hydrogeological properties could be synthetically generated by combining geophysical wireline log and borehole core-derived data (Brereton *et al.*, 1998). This investigation aimed to identify the physical factors that might influence groundwater flow through the site and the spatial variability of rock quality within the PRZ (NIREX, 1997j). Using the information and ideas developed in NIREX (1997i), NIREX (1997j) and Brereton *et al.* (1998), composite logs are produced here integrating the geological, geophysical, geotechnical and hydrogeological data collected during Nirex's scientific investigations at Sellafield.

The composite logs were produced in order to help in the recognition of patterns and relationships between data and aid in the identification of flowing and non-flowing discontinuities within the fractured rock mass of the BVG.

6.3.2 Production of Log(s)

The composite logs produced relate only to the BVG within Sellafield borehole RCF3 (525.0–991.5 mbRT). This example was chosen based on the large amount of geological, geophysical, geotechnical and hydrogeological information (Appendix 11) that was available for this borehole, and because the specialist meter scale hydrogeological SIT (section 5.2) was undertaken here (630.0–790.0 mbRT). A software routine called *Wellog* developed by Andy Lee, of the BGS was used to create the composite logs. A systematic guide of how to use *Wellog* to produce the logs is presented in section 2.6, Appendix 2.

It was thought appropriate that of the geophysical logs available, the gamma and resistivity (LLD, LLS & MSFL – refer to Table 6.5 for nomenclature) needed to be present on the composite log, as these logs are good at identifying variations in lithology within the borehole (Rider, 1996). The LLD, LLS and MSFL resistivity logs were all used as they represent the full depth and breadth capabilities of the resistivity tools available. The caliper log was also used as it gives an excellent indication of the condition, shape and orientation of the borehole, which is important when you are dealing with fractured rock masses such as the BVG (section 2.2.3). One of the most important geophysical log used was the acoustic Stoneley waveform log (REFC – refer to Table 6.5 for nomenclature). This log, in the right conditions, has been found to detect open fractures, their aperture and to additionally detect their permeability (Paillet, 1980; Zoback *et al.*, 1986; Hardin *et al.*, 1987; Hornby *et al.*, 1989; Paillet, 1991a; Tang *et al.*, 1991 & Hornby and Luthi, 1992), something which this investigation was trying to achieve.

Geophysical Logs	Synthetic Geotechnical Core Derived Logs	Hydrogeological Logs	Single Point Data
Gamma (GR)	Rock Quality Design (RQD)	Hydraulic conductivity from EPM tests (EPMK)	Flow zone locations (FLZN)
Caliper (CALI)	Rock Mass Rating (RMR)	Hydraulic conductivity from SIT (TBSK)	Potential Flowing Features locations (PFF)
Deep Laterlog (LLD)	Q-system (Q)		
Shallow Laterlog (LLS)			
Micro Spherically Focused Log (MSFL)			
Stoneley Wave Reflection Coefficient (REFC)			

Table 6.5 - Various logs and data used as the basis for the development and production of the composite logs.

The geotechnical logs used in the composite log were generated from investigations of the borehole core. The RQD (Rock Quality Design) log is derived from the measurements of the solid rock core and the determination of the percentage of solid core pieces that are greater than 100 mm between natural fractures expressed as a percentage of the total core length (Deere, 1964). The RMR (Rock Mass Rating) log was calculated by assessing six parameters: uniaxial compressive strength of the intact rock; RQD; spacing of the discontinuities; condition of the discontinuities; groundwater conditions and the orientation of the discontinuities within the borehole core (Bieniawski, 1976; Bieniawski, 1989). The RMR aims to give a sense of the relative quality of the rock mass on a scale between zero and one hundred. The Q-system log is based on a numerical assessment of the rock mass quality using six parameters: RQD; number of joint sets; roughness of the most unfavourable discontinuity; degree of alteration or filling along the weakest discontinuity; water inflow and stress conditions within the borehole (Barton *et al.*, 1974). The Q-system has values ranging from 0.001 to 1000. These geotechnical logs give a unique assessment into the engineering quality of the rocks mass, as a rating, which incorporates a number of geological parameters and are therefore a great advantage when assessing the rock mass.

There are two types of hydrogeological logs used in the assessment. The hydraulic conductivity logs (TBSK, EPMK – refer to Table 6.5 for nomenclature) and single point depth related data (FLZN & PFF – refer to Table 6.5 for nomenclature). The Short Interval Test (SIT – section 5.2) is represented by the hydraulic conductivity log TBSK and the Environmental Pressure Measurement (EPM – section 5.2) is represented by the hydraulic conductivity log EPMK. Both these logs measure the hydraulic conductivity of the rock mass and, by numerical assessment, the transmissivity (flow of fluid) within the rock mass. The SIT samples the borehole on a meter scale compared to the EPM that samples on at 50 m intervals.

Both logs identify the locations of flowing features within the borehole, to a certain degree of accuracy depending on the length scale of the test. The logs thus identify the areas of flowing and non-flowing features. The flow zone (FLZN) single point depth related locations are very similar to the hydrogeological conductivity test. They identify the locations of flowing features within the borehole, from production tests (section 5.2). The production tests do not quantify the amount of flow, only the location. The Potential Flowing Features (PFF - section 3.2.2.1) single point depth related data were also presented in the logs, as they are interesting when compared to the SIT and EPM logs, due to the suggestion that they are indicators of areas where groundwater flow occurred in past and in the current hydrogeological regime (section 3.2.2.1).

6.3.3 Presentation of Composite Log

Using the logs and data referred to above (Table 6.5), a composite log of the whole of the BVG (Figure 6.5a, Appendix 1B – Oversized Figures) and of the SIT zone (Figure 6.5b, Appendix 1B – Oversized Figures) in Sellafield borehole RCF3 were produced.

6.3.4 Assessment of Log

From the composite log produced (Figure 6.5 a/b, Appendix 1B), it appears that the MSFL did not detect any interesting features or patterns in association with any of the other logs. It was initially thought that it would be appropriate to place the MSFL in the same track as the two other resistivity logs (LLS & LLD). However, this caused problems due to the differing scales of resolution that reflected the varying rates that the tools sample at. The MSFL also had much more noise associated with the data compared to the LLS and LLD logs, which caused some masking to the LLS and LLD data particularly when looking at the detailed SIT zone (Figure 6.5 b, Appendix 1B). It was therefore decided to eliminate this log from the rest of the investigation. A new set of composite logs was then produced (Figures 6.6 a/b, Appendix 1B) using the same method as described in section 6.2.2.

Looking at Figures 6.6 a/b (Appendix 1B), it is apparent that the locations of the more transmissive ('flowing') areas in the SIT log (TBSK) correlate with the clustering of the PFF points. To aid in this observation a synthetic line log was created from the PFF data (Table 10.2, Appendix 10). To help in the visualisation of the 'clustering effect' of the PFF point data, it was smoothed using a moving average window. A number of differing window sizes and size increments were applied to the data. Table 6.6 sets out the varying levels of 'smoothing', which were applied to the PFF synthetic line log. A double track log demonstrating the SIT log (TBSK) and flow zone data (FLZN) against the various 'smoothed' synthetic PFF line logs (Table 6.6) was produced and is presented in Figure 6.7 (Appendix 1B). From Figure 6.7 (Appendix 1B – Oversized Figures), it is clear that the original 'clustering' point PFF data (blue-purple dots) are best represented by the PFFy log (Table 6.6). The PFFy log had a two-meter window applied to the original PFF point data, with an increment of 0.5 meters. For the rest of this thesis, this log will now be called the PFF smoothed log (PFFS). To enable the PFFS log to have a similar histogram style of representation as that observed in the TBSK log it had to be slightly adapted. This was accomplished by using the same rate of sampling as found in the TBSK log data (6 inch/0.1524m). From Figure 6.8 (Appendix 1B – Oversized Figures), it is easy to recognise the correlation between more transmissive ('flowing') areas in the SIT log (TBSK) and the PFF data. This new PFFS log was then added to the composite log (Figure 6.9 a/b, Appendix 1B). Further investigations and adaptations to the composite log were carried out, but with no further success. σ_{Hmax} stress data generated in section 5.3.2 (Table 5.4) were added to form a synthetic σ_{Hmax} stress log (SHMX). This log was added to the SIT zone composite log, as there was only stress data generated for this section of the borehole (section 5.3.2) and this is presented in Figure 6.10 (Appendix 1B). The stress log produced was very variable and was thought to be of little help in any pattern analysis. It is suspected that this detailed analysis is beyond the resolution capabilities of the image tools used to analyse the stress regime and of Breaking. This data will therefore be disregarded in any further analysis.

Log Name	Window Size (m)	Increment (m)
PFFw	5	2
PFFx	10	1
PFFy	2	0.5
PFFz	5	1

Table 6.6 – Table showing the various smoothing amounts used on the PFF data.

From this brief investigation into composite logs, it is hoped that the benefit of this method of visualisation and integration of geological, geophysical, hydrogeological and geotechnical data has been demonstrated successfully, despite the complexities of the geological setting and data set at Sellafield. One of the benefits of this technique is the ability to aid in the identification of patterns that may exist within data sets. This was hopefully evident in the relationship identified between the SIT log (TBSK) and the PFF data. One other idea that emerged from the identification of the relationship between the SIT log (TBSK) and the PFF data is that due care and consideration is needed when dealing with various sets of unrelated data. This is particularly, true where data have varying scales and different measurement techniques have been used.

7. - Discussion & Synthesis

7.1 Introduction

Nirex's Sellafield data set was used to investigate the relationship between the current stress field, discontinuities and the flow of fluid through a fractured rock mass. The object was to attempt to develop a diagnostic technique to identify fluid flow through discontinuities within a rock mass.

The Potential Repository Zone (PRZ) at Sellafield (Figure 1.3) is arguably the most extensively characterised sub-surface rock mass in the world in terms of the sheer volume and detail of the geological, geotechnical and hydrogeological data. In Nirex's extensive investigation, 29 deep boreholes were drilled (Table 1.1); continuously cored and geologically, geotechnically, geophysically and hydrogeologically logged and sampled. One major problem with the Sellafield data is the complexity of the geological setting. The Sellafield region is located in the transitional structural zone between the western margin of the Lower Palaeozoic volcanoclastic basement and the adjacent East Irish Sea Permian-Triassic sedimentary basin. Geologically these two areas are very different in origin. The Lower Palaeozoic volcanoclastic basement, the Borrowdale Volcanic Group (BVG), are a predominantly subaerial, subduction-related, calc-alkaline volcanic unit that formed due to the closure of the Iapetus Ocean. The BVG has a complex structural history, with multiphase deformation and reactivation leading to the development of an anisotropic, heterogeneous and fractured rock mass. The younger Permian-Triassic East Irish Sea basin rocks are a mixture of interbedded sedimentary breccias, evaporates, mudstones, siltstones and sandstones. These Permian-Triassic rocks were deposited during fault-controlled extensional subsidence (rifting), that began during the early Permian and continued periodically throughout the Triassic into Jurassic times causing an anisotropic and heterogeneous rock mass to develop. Due to the complex geological setting of the Sellafield region it can be very difficult to characterise the rock mass (Reeves, 1996 & Smythe, 1996).

The interaction between discontinuities and the current stress field and how these relate to the flow of fluid through the rock mass is also a very complex geological system. Ideally, a geologically continuous, isotropic and homogeneous rock mass, such as a granite, would be more favourable to analyse (e.g. Paterson, 1978).

This chapter will now discuss the main issues arising from the investigation of regional stress regime within the BVG at Sellafield and the characterisation and interaction of *in situ* stress, discontinuities and the flow of fluid through the BVG and Permian-Triassic rocks encountered at Sellafield.

7.2 Regional stress regime within the BVG at Sellafield

The stress regime at Sellafield was analysed using down-hole geophysical imagery logs (section 2.2.3.3) to identify borehole breakouts (minimum horizontal stress- σ_{Hmin}), within the top one hundred meters of the BVG in the vertical Sellafield boreholes. This gave a stress regime at Sellafield that was broadly compatible (Table 4.4, Figure 4.2a/b and Figure 4.3a/b) with the UK regional stress study undertaken by Evans (1987). Evans concluded that a NW-SE (135/315°) maximum horizontal stress (σ_{Hmax}) orientation is characteristic for the UK (section 2.3.4). Data from the current study are also in agreement with the σ_{Hmax} orientation derived from Nirex's hydrofrac test (section 2.2.3.3) results, which concluded that the mean orientation of σ_{Hmax} was 159/339°, ranging from 118/298° to 190/010° (NIREX, 1996a).

7.2.1 Assessment of tools used for breakout analysis

A preliminary investigation into the ability of various image logs to detect borehole breakout within a vertical crystalline BVG borehole was undertaken. The acoustic UBI (AMWF – amplitude of reflected signal waveform and TTWF – two-way travel time waveform) and conductivity FMI down-hole geophysical image logs were assessed (section 2.2.3.3). It was concluded that UBI AMWF image log is the most sensitive, for detecting borehole breakout within the BVG at Sellafield.

These conclusions are in agreement with the views of other workers studying equivalent problems in subsurface settings (e.g. Newmark *et al.*, 1984; Plumb and Hickman, 1985; Rider, 1996 and Prenskey, 1999).

The BHTV/UBI AMWF log generated a well-defined uniaxial breakout rose, orientated in a direction of $067.3^{\circ} \pm 24.0^{\circ}$ (ENE-WSW). The TTWF data generated a more circular shaped, less well defined breakout rose, orientated in a direction of $024.4^{\circ} \pm 24.8^{\circ}$ (NNE-SSW). The FMI conductivity data produced a breakout rose that was almost circular in shape, with a breakout orientated in a $135.2^{\circ} \pm 25.8^{\circ}$ direction (NW-SE). The BHTV/UBI logs are in broad agreement with the UK regional stress study undertaken by Evans (1987) and Nirex's hydrofrac test results. In contrast the FMI results are markedly anomalous. When looking at the breakout analysis and the image log in more detail, it was discovered that one of the pads on the FMI image tool was not functioning correctly. The FMI tool uses an array of electrodes on orientated pads and flaps to produce an electrical image of the borehole wall that can be interpreted as either conductive or resistive features (Standen, 1991). This tool does not cover the whole diameter of the borehole (Table 2.2), the electrical response from the four orthogonal pads and flaps is processed to produce four vertical 'strips' that cover $\sim 90\%$ of the borehole. A borehole breakout should be represented as areas of decreased resistivity, due to the increase in the discontinuities encountered within the borehole around a breakout on the FMI image log. This is due to the concentration of horizontal stress around the borehole causing the failure and spalling of the borehole wall, which is associated with borehole breakout (section 2.2.3.3). If the pads of the tool do not effectively contact the borehole wall then a decrease in resolution of the image occurs and it is possible that the imaging tool could miss small breakouts. Such small breakouts could occur within the BVG due to the high unconfined compressive rock strength (UCS) of the rock mass (Table 6.4). The resistivity of the rock matrix in crystalline formations (BVG) is known to be high (Pezard and Luthi, 1988).

As a result of the rock matrix being more resistive than the formation fluid, discontinuities may act as major conduits for the flow of electrical current. Resulting in a short-circuit pathway in the borehole (Jackson *et al.*, 1992). The FMS/FMI image tool was developed and designed by Schlumberger for use in sedimentary hydrocarbon reservoirs (Schlumberger, 1992) and not for high resistivity crystalline rock masses. Hence, the highly resistive rocks are beyond the remit of the tools specifications. Lovell *et al.*, 1995 suggested that the problem with the FMI's down hole imaging technique is that it uses a multiple single point resistance measurement to assess the fine changes in electrical resistivity at the surface of the borehole wall. The resistance measurements are essentially relative and cannot be converted to resistivities with great confidence. Each button is compensated by equalization techniques, which enhance the resistivity image, but such processes emphasize the non-quantitative nature of the measurement (Lovell *et al.*, 1995).

In comparison, the UBI provides a high-resolution detailed 360° record of a borehole's elongation. The tool uses a rapidly rotating pulsed sound source and a piezoelectric transducer to send and receive the waveforms (Rider, 1996, Prensky, 1999). Around a borehole breakout, the waveforms are distorted due to the borehole wall having an irregular surface (Figure 4.1b). This is due to the concentration of horizontal stress around the borehole causing the failure and spalling of the borehole wall, which is associated with borehole breakout (section 2.2.3.3). Within the crystalline rock mass of the BVG a high acoustic impedance contrast between the smooth unaltered surface and the highly distorted breakout zone in the borehole is identified. Unequal quality of signal around the borehole and variations in the resolution along the borehole of the BHTV/UBI image can occur from an uncentered tool, equipment noise and borehole wall roughness. In this analysis the use of the varying filter (section 4.2.1) and the technique used to calculate the eccentricity of the borehole wall (section 4.2) has reduced the effect of these unequal quality of signal and variations in the resolution.

The present investigation places further doubt into the ability of the FMS/FMI image tool to identify breakout effectively. The BHTV/UBI AMWF image log was subsequently used throughout the rest of this thesis to study breakout analysis.

7.2.2 Filtering of raw image log data

During the regional stress field analysis for the top one hundred meters of the BVG, a new filtering technique was applied to try to reduce the effect of noise generated in the breakout analysis due to discontinuities. A previous regional stress field study in the same area by Brereton *et al.*, 1997 used down-hole geophysical image logs to locate borehole breakouts. As part of this study, image log data were reanalysed and filtered to reduce the effect of discontinuity noise. The breakout results achieved were uniaxial in shape and well defined (Figure 4.2a/b, Appendix 1B). This contrasts with the analysis of Brereton *et al.*, 1997 that produced circular and poorly defined breakout roses with an overall mean breakout orientation (σ_{Hmin}) of $074.3^\circ \pm 25.6^\circ$ (Figure 4.7). A cross-plot of the mean breakout orientation (σ_{Hmin}) against the mean discontinuity orientation for each of the boreholes analysed in this study (Figure 4.2a/b, Appendix 1B), concluded that there was no correlation between the data sets. This suggested that the filtering has worked and removed discontinuity noise to produce a 'cleaner' result (Figure 4.9a).

7.2.3 Distribution of breakout results

A clustering of breakout orientations around the assumed σ_{Hmin} orientation derived from Nirex's hydrofrac testing was observed in the flow zone breakout analysis (Figure 4.9a). This showed a greater degree of scatter, when the orientations of discontinuities fell close to the σ_{Hmax} orientation derived from Nirex hydrofrac testing. Such observations indicate a defocusing of the breakout orientation due to the dominant discontinuity pattern coinciding and interacting with the stress field (σ_{Hmax}). The interaction may have caused drilling induced tensile fractures (section 2.2.3.3) and

dilation of pre-existing discontinuities to form in the orientation of σ_{Hmax} . Clustering of breakout orientations (σ_{Hmin}) was also seen around the σ_{Hmax} orientation (assumed from the Nirex hydrofrac testing), indicating that hydrofrac-style, drilling induced tensile fractures were forming within some of the Sellafield boreholes causing the breakout direction (σ_{Hmin}) to be misinterpreted. This effect was also identified when the breakout results (σ_{Hmin}) for the top one hundred meters stress map differed ($\sim 90^\circ$) from the regional trend ($135/315^\circ$) and the Nirex Hydrofrac Test results ($159/339^\circ$). These boreholes were considered as being affected by stress perturbations/rotations originally (section 2.3.2). Stress profiles for each of the Sellafield boreholes analysed in the top one hundred meters of the BVG were created (Figures App 5.41-5.55). From this analysis, no consistent correlation between fault intersection with the boreholes and perturbations/rotations of the *in situ* stress field could be identified. It was concluded that these boreholes were often identifying hydrofrac-style, drilling induced tensile fractures (section 2.2.3.3) and dilation of pre-existing discontinuities (σ_{Hmax}) instead of the borehole breakouts (σ_{Hmin}). Thus in many situations great care must be taken when interpreting the orientation of apparent borehole breakout.

These observations place some doubts concerning the effectiveness of applying the statistical approach (Brereton, 1992) to breakout analysis, as is used in *Breaking*. This statistical approach recognises that non-breakout features will also be encompassed within the processing procedure, but by carrying out the analysis over a sufficiently large sample range then the orientations of the breakout features will become orientationally highlighted (Brereton, 1992). For most of the boreholes analysed at Sellafield, the statistical approach works effectively. When other non-breakout features (hydrofrac style drilling induced tensile fractures and dilation of pre-existing discontinuities) are encountered within a borehole and become the dominant feature, breakout orientations can be misinterpreted. Within areas of the BVG at Sellafield, drilling induced tensile fractures and dilation of pre-existing

discontinuities are sometimes encountered instead of borehole breakout. This is due to the circumferential stress encountered around the borehole being less than the tensile strength of the rock mass forming the borehole wall. This causes drilling induced tensile fractures to form in the σ_{Hmax} direction. Where the maximum circumferential stress exceeds the compressive strength of the rock mass forming the borehole wall, compressional shear failure occurs in the σ_{Hmin} direction, causing apparent borehole breakout (Hillis and Reynolds, 2000). Due care therefore needs to be taken when using Brereton (1992) statistical borehole breakout analysis to determine the orientation of σ_{Hmin} in variable anisotropic, heterogeneous rock masses like the BVG at Sellafield. Similar observations were observed by Kessels (1989) and Vernik and Zoback (1989). Kessels (1989) observed that over virtually the entire Kontinentales Tiefbohrprogramm Bundesrepublik Deutschland (KTB) borehole in Bavaria, Southern Germany, enlargement of the borehole took place in the dip direction of the discontinuities (foliation). This was considered to be because the rock foliation within the KTB dips steeply and strikes approximately parallel to σ_{Hmax} . In the Kola borehole in the former Soviet Union, Vernik and Zoback (1989) encountered a similar enlargement of the borehole due to the interaction of the rock foliation and σ_{Hmax} .

The use of hydrofracture testing to identify accurately σ_{Hmax} in the BVG and similar heavily fractured rock masses is also questionable, as pre-existing flaws and discontinuities are likely to be re-opened by this technique instead of a new hydrofracture being generated. This could therefore give an inaccurate σ_{Hmax} orientation. However, the σ_{Hmax} Nirex Hydrofracture Testing results (159/339° lie within a range from 118/298° to 190/010°) and are comparable with the regional trend (135/315°) derived from Evans (1987) for the UK.

7.3 Characterisation & Interaction of *In Situ* Stresses, Discontinuities & the Flow of Fluid Through the BVG and Permian-Triassic Rocks at Sellafield

7.3.1 Characterisation

A number of data sets of varying scales were collected by Nirex to assess the hydrogeological conditions within the Sellafield boreholes and identify areas where fluid flow and non-flow through discontinuities within a rock mass were occurring. The two main data sets used in this research were the Full Sector Tests (production logging), which identified areas of fluid flow into a borehole (Flow Zones) on the tens of meter scale. These were carried out in all of the Sellafield boreholes. Short Interval Tests (SIT) were carried out in a 160 m (630-790 mbRT) zone within Sellafield borehole RCF3 to identify and measure areas of fluid in flow on the meter scale. In areas where flow was identified, discontinuity orientation data and *in situ* stress breakout analysis were carried out over these regions.

The British Geological Survey (BGS) produced the discontinuity orientation data used in this research. The BGS used the FMS/FMI resistivity image logs (section 2.4) to identify the sinusoidal traces that represent discontinuities within the Sellafield boreholes. To ensure that the discontinuity data sets produced by the BGS were a representative data set, a validation exercise was undertaken. From this study it was concluded that the BGS produced discontinuity data set correlated with the discontinuities encountered within the FMS/FMI imagery logs and therefore within the Sellafield boreholes. Out of the acoustic (BHTV /UBI - AMWF and TTWF) and resistivity (FMS/FMI) image logs available, it was also concluded that the FMS/FMI image tools were more sensitive (detected more discontinuities) and resolved finer scale features than the BHTV/UBI tools. This is due to the FMS/FMI tools ability to probe a small volume beyond the borehole wall, whilst the BHTV/UBI only 'sees' the intersection of the discontinuity within the borehole wall. The resistivity tools can also detect much smaller fractures than the acoustic tools if fractures are filled with highly conductive fluid (Paillet *et al.*, 1990).

The resistivity imaging tools scans and probes the electrical conductivity that is a function of the porosity, pore fluid, pore geometry, cementation and mineral infilling conductivity. This compares to the acoustic tools that probes the acoustic impedance of the rock mass, which is a function of the seismic velocity and density of the rock.

However, the BHTV/UBI AMWF image log were able to discriminate the sinusoidal length of the discontinuities better than the FMS/FMI image log, due to the BHTV/UBI tool being able to image the full borehole compared to the FMS/FMI's 50-90% coverage (Table 2.2). Although, the FMS/FMI tool may have more problems with imaging the high resistivity crystalline rock mass (section 7.2.1) and the ability to image the full borehole, it is capable of detecting finer scale features. Within the BVG there are a large number of hairline, minute discontinuities and therefore the imaging capabilities of the FMS/FMI tool are advantageous.

An *in situ* stress breakout analysis was undertaken over the FZ and SIT zone. Breakout (σ_{Hmin}) orientations were again in broad agreement with the results derived from the Nirex hydrofrac test results (mean σ_{Hmax} orientation 159/339° (NIREX, 1996a)). The *in situ* stress breakout analysis of the FZ also identified the defocusing effect of σ_{Hmin} , when discontinuities were orientated close to σ_{Hmax} and interacted with the stress field (Figure 5.6). Drilling induced tensile fractures (section 2.2.3.3) and the dilation of pre-existing discontinuities were also identified, causing the breakout (σ_{Hmin}) direction to be misinterpreted in the σ_{Hmax} direction.

7.3.2 Interaction of *In Situ* Stress, Discontinuities & the Flow of Fluid

The relationship between the flow of fluid through a fractured rock mass and the prevailing stress field in the Sellafield region is not straightforward. The classical hypothesis of discontinuity fluid flow states that discontinuities orientated parallel to σ_{Hmax} are assumed to be the most conductive (Jolly *et al.*, 2000). This theory relies on tensile failure and dilation of discontinuities.

In Sellafield, the dominant flowing discontinuities are not orientated parallel to σ_{Hmax} : in fact, the opposite can be observed with non-flowing discontinuities orientated parallel to σ_{Hmax} (Figure 5.9b).

Barton *et al.* (1995) developed a new theory suggesting that it is discontinuities actively undergoing shear, which are the most conductive. These discontinuities are classed as being 'critically stressed' where the ratios of the shear to effective normal stress acting on a discontinuity plane are close to shear failure (assuming the Coulomb failure criterion – Figure 2.19). When a discontinuity undergoes localised shear failure, the asperities will ride up and over each other resulting in dilation of the discontinuity's aperture (Figure 2.20). This would in turn cause an increase in the permeability of the discontinuity. The work of Barton *et al.* (1995) suggests therefore that discontinuity permeability will be stress dependant, because of the interplay between a discontinuity orientation and the full stress tensor.

The Barton *et al.* (1995) model was applied to the Sellafield data set. No 'critically stressed' flowing discontinuities were identified within the FZ data. However, within the SIT zone, in Sellafield borehole RCF3, flowing discontinuities generally formed a distinct subset in the upper portion of the Mohr diagram (Figure 6.3a), when compared to the non-flowing discontinuities (Figure 6.3b/c) that were more randomly orientated in the lower portions of the Mohr diagram. Although this result does not help to identify the precise discontinuities that are contributing to flow, it indicates ones that are *more likely to* contribute to the flow of fluid. It is suggested therefore, that this technique can be used as a characterization tool that allows discontinuities 'at risk' of becoming 'critically stressed' and hence more likely to allow fluid flow, to be highlighted. The postulated current stress regime at Sellafield does not enable 'critically stressed' discontinuities to form. A 'local' change in the magnitudes of the principal stresses or pore pressure within the rock mass needs to happen for discontinuities to become 'critically stressed' (Bell and Nur, 1978; Schmitt, 1981).

It was observed from the SIT flowing areas that discontinuities contained within these regions were orientated at $\sim 30\text{--}45^\circ$ to $\sigma_{H\max}$ and $\sigma_{H\min}$ (Figure 5.9b and Figure 5.10). Studies on geomaterials show that shear localisation and brittle faulting in initially low porosity rocks typically localise into a shear zone angled at 30° to the axial load (Rutter, 1993). Thus it seems possible that shear failure does seem to relate in some way to the flow of fluid within discontinuities at Sellafield. The relationship between the flow of fluid through a fractured rock mass and the prevailing stress field in the Sellafield region is not straightforward. Some discontinuities within areas identified contribute to the flow of fluid through a fractured rock mass whilst others don't. The effect of short-circuiting of the discontinuity network or the self-healing of a discontinuity due to shear-enhanced compaction can alter the flow of fluid through the rock mass and hence the discontinuities that demonstrate fluid flow. It is also possible that the differences of scale and resolution in the measurements of the various parameters (*in situ* stress magnitudes, maximum stress orientation, discontinuity orientation and hydrogeological tests (FZ and SIT)) used and correlated in the 'critical stress' analysis could affect the identification of fluid flow through the rock mass. The stress measurements are taken over a range of ~ 10 metres and the stress around a discontinuity is measured on the centimetre scale. Resolution of the tools also varies. The BHTV/UBI AMWF image log was used in the stress analysis and has a resolution of 0.83 cm (Rider, 1996). The FMS/FMI image log was used in the identification and orientation of discontinuities and has a resolution of 0.5/0.25 cm (Ekstrom *et al.*, 1987/Schlumberger, 1992). A modern and advanced interpretation must be able to combine both quantitative and qualitative information from different sources, of different natures and at different scales (Seera *et al.*, 1993). Up-scaling or down-scaling of values can cause problems and errors to develop.

The 'critical stress' analysis has a number of fundamental assumptions. The most significant is the assumption that the rock mass analysed is an isotropic and homogeneous rock mass. The BVG and Permian-Triassic rocks are quite clearly anisotropic and heterogeneous, even within the same lithology. Very few natural rocks are isotropic and homogeneous (Paterson, 1978). At the Rosemanowes Quarry, Cornwall, a large *in situ* stress study of the relatively homogeneous Carnmenellis Granite was undertaken by the Camborne School of Mines Hot Dry rock program (Pine *et al.*, 1983a; Batchelor and Pine, 1986). Here sixteen hydraulic fracture tests (section 2.2.3.3) were carried out from the near surface of the test borehole to a maximum depth of 2550 meters. During these tests, instead of the expected tensile failure of the rock mass in the σ_{Hmax} direction, shear failure at $\sim 30^\circ$ to σ_{Hmax} was observed from microseismic detection. This result is explained by Pine *et al.*, 1983a to have occurred due to the anisotropic *in situ* stress field interacting with critically aligned discontinuities. The Rosemanowes Quarry investigation originally assumed that all discontinuities parallel to σ_{Hmax} would allow fluid to flow through them. Pine, 1986 concluded from modeling of the Carnmenellis Granite Camborne School of Mines Hot Dry rock reservoir that there were no highly conductive singular fluid flow paths but large swept areas, and the possibility of ribbon-like flow channel geometries. This investigation demonstrates how a granitic rock mass that was thought to be relatively isotropic and homogeneous, certainly compared to the BVG and Permian-Triassic rocks, still contains heterogeneities that complicate and interact with the rock mass.

The second assumption is the assumed failure criterion. The Mohr-Coulomb failure criterion has been widely used to predict rock failure in rock masses. Scofield, 1998 emphasises the over-application of the theory to materials that do not show a linear relationship between the confining pressure and differential stress. Ohnaka, 1973 and Byerlee, 1967 showed that shear failure of igneous rocks and granite respectively did not show a linear relationship between confining pressure and differential stress.

Byerlee, 1975 also showed that a non-linear relationship exists for fracture strength with effective confining pressure for the Webber Sandstone. The use of the linear Mohr-Coulomb relationship in mathematical models of geological problems, such as borehole failure, has been shown to introduce significant errors (Wang, 1994). The non-linear relationship of strength to confining pressure has led to many theoretical and empirical failure criteria, such as the modified Griffith-type (McLintock and Walsh, 1962), Hoek-Brown (Hoek and Brown, 1980a) or non-linear Mohr-Coulomb (Wong *et al.*, 1997), which may more accurately model the geological problem of critical stress than Mohr-Coulomb.

The third most important assumption is the value that is assigned to the coefficient of friction (μ). The coefficient of friction defines which discontinuities are classed as being indirectly 'critically stressed'. In Barton *et al.*, 1995 a μ value of ≥ 0.6 was assumed. This value was based on the work by Byerlee, 1978, who compiled a wealth of shear test data involving a wide range of rocks and discontinuity types. Byerlee, 1978 concluded from his research that discontinuities experiencing a normal stress of greater than 200 MPa (i.e. 5-6 km depth) were well constrained by using a μ of between 0.6 and 1.0. At Sellafield the 'critical stress' analysis was applied to borehole data that was no deeper than 2 km. The Sellafield investigations were also undertaken at much shallower depths than the study undertaken by Barton *et al.*, 1995, at Cajon Pass, California (~ 3.5 km). Similar studies (Barton *et al.*, 1997; Finkbeiner *et al.*, 1997; Hickman *et al.*, 1997; Ito and Zoback, 2000) to investigate the 'critical stressed' theory, again all identify 'critically stressed' flowing discontinuities at depths exceeding 2 km. Furthermore most of these studies were undertaken in tectonically active regions. Sellafield is not a tectonically active region, although Akhurst *et al.*, 1998 have suggested that recent displacements have occurred on the Lake District Boundary Fault. This is based on the presence of small steps of a few meters in the height of the rock head surface around the Lake District Boundary Fault, which have been detected by high-resolution seismic reflection data.

From direct shear tests (DST) the peak friction angles (ϕ_p) were measured in the St Bees Sandstone; mudstone beds within the St Bees Sandstone; the Brockram and the BVG (NIREX, 1995e). From the direct shear tests the peak friction angle (ϕ_{peak}) was used to calculate the μ for each unit ($\mu = \tan \phi_{peak}$ Table 7.1). It is evident that μ is variable across the geological units encountered at Sellafield. The μ presented in Table 7.1 are consistent with the values that Barton *et al.*, 1995 assumed from Byerlee, 1978. This confirms that the stress regime at Sellafield may be restricting critically stressed discontinuities from forming. Paterson, 1978 assumes that igneous and high grade metamorphic rocks, with uniaxial compressive strengths (UCS) in the range of 100-200 MPa (confining pressure of 100 MPa), have differential stresses at fracture of around 500-800 MPa. In low-porosity sedimentary and low to medium grade metamorphic rocks, with uniaxial compressive strengths (UCS) in the range of 50-100 MPa (confining pressure of 100 MPa), Paterson, 1978 assumes differential stresses at fracture of around 200-300 MPa. At Sellafield the UCS for the BVG is ~ 128-157 MPa (Table 6.4) and the Permian-Triassic is ~ 36-100 MPa. At Sellafield the presumed differential stress magnitude between σ_{Hmax} (~ 65 MPa) and σ_{Hmin} (~ 40 MPa) at 2 km depth (maximum possible differential stress encountered within the Sellafield boreholes) is ~ 25 MPa (Figure 6.1). The differential stress at Sellafield is nowhere near the suggested differential stresses at fracture for igneous and high grade metamorphic or low-porosity sedimentary and low to medium grade metamorphic rocks described by Paterson, 1978. This suggests that the rocks have been either exhumed, which has caused relaxation in the stress field (and in turn the rock mass) or that changes in the stress field have happened since the fracturing of the rock mass.

A number of additional areas of complexity are also not considered in the 'critical stress' analysis. Many of the discontinuities that are identified as contributing to the flow of fluid contain mineral infillings at Sellafield. Mineral coatings/infillings, clay or fault gouge infillings can alter the coefficient of friction required for frictional failure along the discontinuity.

Rock Type (Number of results)	Mean ϕ_{peak}	Mean μ ($\tan \phi_{\text{peak}}$)
St Bees Sandstone (10 DST results)	37.8	0.78
Mudstone beds within St Bees Sandstone (3 DST results)	15.6	0.28
Brockram (2 DST results)	27.2	0.54
BVG (17 DST results)	32.2	0.63

Table 7.1 – Summary of the peak friction angles (ϕ_{peak}) from the Direct Shear Tests (DST) and the derived coefficients of friction (μ) (adapted from NIREX, 1995e).

Discontinuities containing mineral infillings at Sellafield are called Potentially Flowing Features (PFF – section 3.2.2.1), and are associated with the fluid flowing areas within the SIT zone (Figure 6.9a/b). PFF have been characterised by the identification of late-stage calcite mineralisation, known as ME9 mineralisation, within a discontinuity combined with open porosity (NIREX, 1997d). ME9 mineralisation is inferred to have occurred close to chemical equilibrium with the present-day groundwaters and may be actively precipitating, at least in parts of the present-day groundwater system (NIREX, 1997d). When comparing the orientation of the PFF to the postulated stress field it becomes apparent that an increased clustering of PFF occurs $\sim 30\text{--}45^\circ$ to the orientation of σ_{Hmax} and σ_{Hmin} (Figure 7.1). These results also mimic the observations from the SIT flowing areas (Figure 5.9b). Looking at the PFF orientation (dip azimuth) data (Table 7.2), PFF orientated at $\sim 40\text{--}45^\circ$ to σ_{Hmax} and σ_{Hmin} contain both discontinuities that are flowing and non-flowing, and no distinct relationship can be identified. This result is consistent with NIREX, 1997d observations, which state that no single association of PFF or clusters of PFF occur within the geological structure of the BVG, although there appears to be a partial correlation with fault damage zones.

It is also important to realise that shear failure (the basis for critical stress theory) is not the only failure process that can occur in intact rock, as demonstrated by the breakout analysis results. Tensile failure can also occur depending on the amount of circumferential stress that develops around a borehole when it is drilled and the properties of the rock mass (tensile and compressive rock strength). When heavily fractured rock masses like the BVG are drilled, it is more likely that tensile failure will occur along pre-existing flaws and discontinuities.

Within any analysis there is a certain degree of error, which can develop in calculations. Critical stress analysis is no different and encompasses a number of calculations that contain errors. For example, if you consider the principal stress orientations that were generated from borehole breakout

analysis of image logs (section 5.3), they have calculated errors varying from ± 3.3 to 27.1° (Table 5.2 & 5.3). The stress magnitudes (Figure 6.1) were also statistically determined through linear regression analysis of best fit, a method that is open to error. Even small errors can have a great effect on the very sensitive calculation used in *Stressit*. The location and shape of the Mohr circle will alter if one of the stress or pressure magnitude gradients changes. For example, if you altered the pore pressure (P_p) magnitude gradient by ± 0.002 when using *Stressit* to analyse Sellafield borehole RCF3 SIT flowing area E (717.50 – 723.71 mbRT), it causes the Mohr circle to move either closer to the origin of the graph (Figures 6.4a) when increased by 0.002, or to move away from the origin (Figures 6.4b) when decreased by 0.002. This occurs because the changes in the pore pressure (P_p) magnitude gradient alter the values of σ_1 , σ_2 and σ_3 . It appears, therefore, that an in depth investigation into the size of errors that are generated from the critical stress analysis is required, so that its limitations are more fully appreciated.

Critical stress analysis maybe a good characterisation tool that allows discontinuities 'at risk' of becoming 'critically stressed' and hence more likely to allow fluid flow, to be highlighted at Sellafield. There are a number of assumptions and complexities, which have been identified within this discussion and cause some doubt to be placed over this analysis. A controlled and rigorous laboratory based analysis of Barton *et al.*, 1995 'critical stress' analysis is required to assess the ability of this technique to identify discontinuities that are actively undergoing shear, and assess whether they are the most conductive.

**PAGE
NUMBERING
AS ORIGINAL**

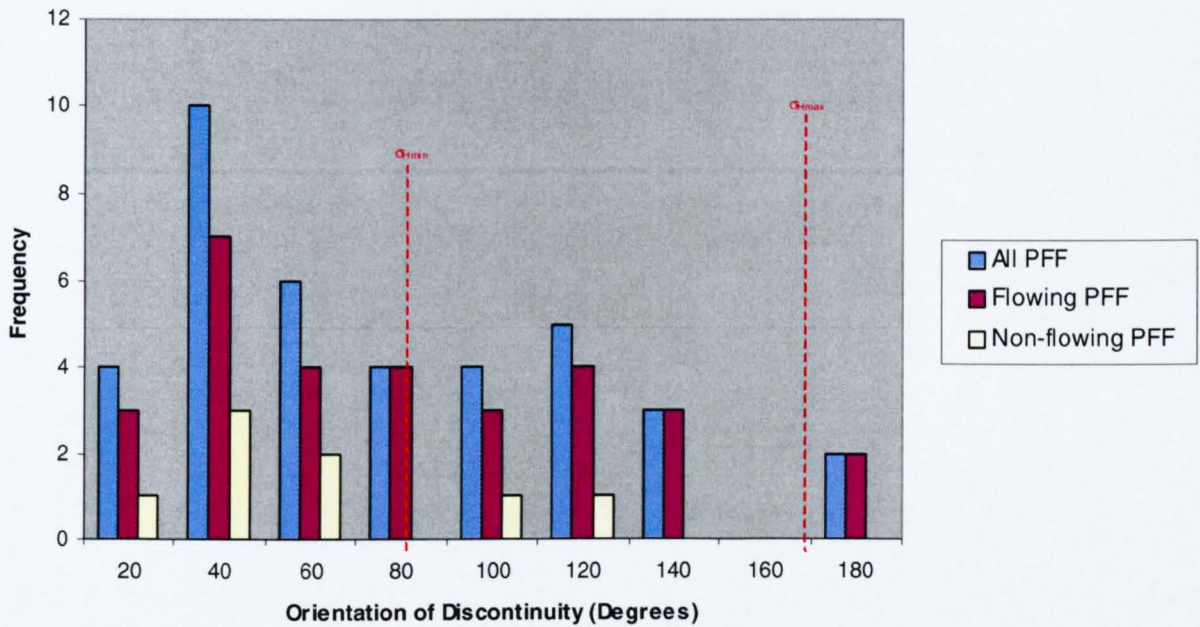


Figure 7.1 – Frequency plot of the orientation of PFF within the flowing and non-flowing areas analysed in the SIT zone in Sellafield borehole RCF3.

Depth (mbRT)	Dip Azimuth (Degrees)	Dip (Degrees)	σ_{Hmin}
652.31	46.62	51.99	79.20
652.49	135.23	40.29	79.20
652.71	86.19	64.95	79.20
669.37	96.93	66.86	26.60
669.69	2.81	67.54	26.60
670.05	42.94	35.00	26.60
670.13	172.88	65.37	26.60
696.64	32.42	33.00	40.10
696.77	127.38	45.39	40.10
696.87	80.12	55.03	40.10
699.85	113.27	76.59	52.20
707.65	109.13	64.65	21.60
709.06	15.87	65.83	21.60
718.90	36.15	41.02	60.80
719.02	15.96	70.83	60.80
719.25	138.03	24.82	60.80
719.28	115.41	72.56	60.80
719.28	165.93	78.36	60.80
719.30	115.22	62.56	60.80
721.17	74.50	88.96	60.80
724.27	85.66	52.96	84.80
739.00	30.75	66.04	84.80
745.71	47.58	65.19	84.80
756.55	37.36	53.14	82.30
757.07	105.74	35.83	82.30
757.80	29.69	54.08	82.30
758.68	23.18	60.00	58.70
759.22	29.04	66.07	58.70
759.75	72.32	34.21	51.90
760.39	46.03	42.21	51.90
761.95	40.27	36.18	62.00
763.59	17.69	42.94	62.00
765.68	21.91	53.02	55.60
765.70	31.65	61.13	55.60
766.28	56.40	36.27	55.60
766.28	66.45	53.74	55.60
766.38	26.78	57.08	55.60
766.78	66.25	65.26	55.60

Key	
	Flowing PFF
	Non-flowing PFF
	PFF's orientated in shear direction (20-40 & 100-120)

Table 7.2 – PFF depths, orientation and σ_{Hmin} values for the flowing and non-flowing PFF identified within the SIT zone in Sellafield borehole RCF3.

8. - Conclusions

The principal observations and conclusions to come from this thesis are listed below.

- The Potential Repository Zone at Sellafield is arguably the most extensively characterised sub-surface rock mass in the world in terms of the sheer volume and detail of the geological, geotechnical and hydrogeological data collected.
- The Sellafield region was identified as being located in a complex geological setting, which caused difficulty when trying to characterise the rock mass.
- The regional stress regime identified by borehole breakouts at Sellafield was found to be in broad agreement with the UK regional stress study undertaken by Evans, 1987) and hydrofrac test results (Nirex, 1996a). The stress regime in the Sellafield boreholes was deduced from down-hole geophysical imagery logs to identify borehole breakouts (minimum horizontal stress- σ_{Hmin}) within the top one hundred meters of the Borrowdale Volcanics Group.
- The ability of the acoustic (amplitude and travel time) and conductivity down-hole geophysical imagery to detect borehole breakouts within the crystalline Borrowdale Volcanics Group was investigated. From this study the acoustic amplitude image log was identified as the most sensitive for detecting borehole breakout within the Borrowdale Volcanics Group at Sellafield.

-
- A new filtering technique was applied when borehole breakouts were analysed. The aim of this filtering was to reduce the effect of noise generated in the breakout analysis by discontinuities. The filtered breakout results generally produced a focused, well-defined breakout rose direction.
 - From the regional stress analysis, no consistent correlation could be identified between faults intersecting a borehole and rotation/perturbation of the regional stress field by analysis of stress profiles created.
 - In both the regional and *in situ* stress analyses a significant spread in the breakout results was identified. It was concluded that the dominant discontinuity pattern within this region was coinciding and interacting with the stress field (σ_{Hmax}). It was determined that this interaction could have caused drilling induced tensile fractures and dilation of pre-existing discontinuities to form in the orientation of σ_{Hmax} . This idea was confirmed by the clustering of breakout orientations around the σ_{Hmax} orientation (obtained from the Nirex hydrofrac testing). Hydrofrac-style, drilling induced tensile fractures were formed within some of the Sellafield boreholes causing the breakout direction (σ_{Hmin}) to be misinterpreted.
 - Observations from both the regional and *in situ* stress analyses place some doubts over the effectiveness of applying a simple statistical approach (Brereton, 1992) to breakout analysis. The statistical approach used in this thesis recognises that non-breakout features will be identified within the processing procedure, but by carrying out the analysis over a sufficiently large sample range the orientations of the breakout features will become orientationally highlighted (Brereton, 1992). For most of the boreholes analysed at Sellafield, the statistical approach worked effectively, but where the dominant discontinuity pattern coincided and interacted with the stress field, the breakout direction (σ_{Hmin}) could be misinterpreted.

- From both the regional and *in situ* stress analyses of the Borrowdale Volcanics Group at Sellafield, the use of hydrofracture testing to identify accurately σ_{Hmax} has been questioned. It is concluded that when heavily fractured rock masses like the Borrowdale Volcanics Group are drilled tensile failure could occur along pre-existing flaws and discontinuities. The pre-existing flaws and discontinuities are likely to re-opened during hydrofracture testing instead of a new hydrofracture being generated.
- Discontinuities have been effectively analysed and orientated in the Sellafield boreholes by down-hole geophysical borehole image logs. Image tools have varying abilities of detection, which depend on the rock types and borehole conditions encountered. Overall, it can be concluded from the acoustic and conductivity tools used in the Borrowdale Volcanics Group at Sellafield, that the conductivity tools were more sensitive (detected more discontinuities) and resolved finer scale features than the acoustic tools. Within the Borrowdale Volcanics Group there are a large number of hairline, minute discontinuities and therefore the imaging capabilities of the conductivity tool are advantageous. The acoustic amplitude image logs discriminated the discontinuity trace far better than conductivity image logs but do not resolve as many minute discontinuities.
- The British Geological Survey produced the discontinuity orientation data used in this research from the analysis of borehole imagery logs. The prime directive of this data set was to orientate the borehole core and not to identify all the discontinuities identified by the imagery logs. To ensure that the British Geological Survey's data set was a true representation of the discontinuities encountered in the imagery logs it was necessary to undertake a validation exercise. From this study it was concluded that the British Geological Survey's discontinuity data set correlated with the discontinuities encountered within the conductivity imagery logs.

-
- The relationship between the flow of fluid through a fractured rock mass and the prevailing stress field in the Sellafield region is complex. In Sellafield, the dominant flowing discontinuities are not orientated parallel to σ_{Hmax} . In fact, the opposite can be observed with non-flowing discontinuities orientated parallel to σ_{Hmax} .
 - The critical stress' analysis of Barton et al. (1995) provided an indicative tool to highlight discontinuities that are likely to enable the flow of fluid within a rock mass at Sellafield. Although no 'critically stressed' flowing discontinuities were identified, flowing discontinuities within the short interval test zone generally formed a distinct subset compared to the non-flowing discontinuities that were more randomly orientated. These short interval test zone flowing discontinuities were orientated at $\sim 30-45^\circ$ to σ_{Hmax} and σ_{Hmin} . This observation suggests that shear localisation and brittle faulting occurs in a shear zone angled at $\sim 30^\circ$ to the axial load and does relate in some way to the flow of fluid within discontinuities at Sellafield. Regionally there doesn't seem to be 'critically stressed' discontinuities at Sellafield, but at a local (in situ) level a slight change in the magnitudes of the principal stresses or pore pressure within the rock mass could allow discontinuities 'locally' to be 'critically stressed'. In geologically complex and tectonically stable terrains, such as encountered at Sellafield, there are many complexities that are not considered or simplified by this analysis, which can affect the results (e.g. use of Mohr-Coulomb failure criterion; assume rock mass is anisotropic and homogeneous; coefficient of friction assumed to be ≥ 0.6).
 - Paterson, 1978) states that the differential stress at fracture for igneous and high grade metamorphic rocks with uniaxial compressive strengths in the range of 100-200 MPa (confining pressure of 100 MPa), have differential stresses at fracture of around 500-800 MPa. In low-porosity sedimentary and low to medium grade metamorphic rocks, with uniaxial compressive strengths in the range of 50-100 MPa (confining pressure of

100 MPa), Paterson, 1978) assumes differential stresses at fracture of around 200-300 MPa. At Sellafield the uniaxial compressive strengths for the Borrowdale Volcanics Group is ~ 128-157 MPa and the Permian-Triassic is ~ 36-100 MPa. At Sellafield the presumed differential stress magnitude between σ_{Hmax} (~ 65 MPa) and σ_{Hmin} (~ 40 MPa) at 2 km depth (maximum possible differential stress encountered within the Sellafield boreholes) is ~ 25 MPa. This suggests that at Sellafield the rocks have been either exhumed, which has caused relaxation in the stress field (and in turn the rock mass) or that changes in the stress field have happened since the fracturing of the rock mass.

- Discontinuities containing the latest phase of mineral infillings at Sellafield were identified by the British Geological Survey, these discontinuities were termed Potentially Flowing Features and appeared to be associated with fluid flow within a discontinuity with open porosity and calcite mineralisation. Within the short interval test zone a correlation was identified between the orientation of the Potentially Flowing Features and the postulated stress field. Potentially Flowing Features were identified as clustering ~ 30-45° to the orientation of σ_{Hmax} and σ_{Hmin} . These observations also mimic the areas identified as flowing from the short interval test flowing zone analysis. When looking at the Potentially Flowing Features that cluster ~ 30-45° to the orientation of σ_{Hmax} and σ_{Hmin} , some are flowing and others are not flowing. No distinct relationship between the flowing and non flowing Potentially Flowing Features could be identified.

9. - Recommendations for Further Work.

The aim of this thesis was to 1) investigate the regional stress regime within the Borrowdale Volcanic Group (BVG) at Sellafield and 2) investigate the flow of fluid within the fractured rock mass of the BVG and Permian-Triassic rocks at Sellafield. By applying the ideas developed by Barton *et al.*, 1995, with a view to being able to develop a diagnostic technique to identify fluid flowing discontinuities. Although this investigation has effectively analysed and modelled the regional stress regime at Sellafield, a less conclusive result was obtained for the analysis of fluid flow within the fractured rock mass of the BVG and Permian-Triassic rocks at Sellafield. This study has highlighted a number of areas where further investigation and research can be made to aid future research into this problem:-

- Further analysis into the degradation of breakout analysis where the dominant discontinuity pattern coincides with the orientation of σ_{Hmax} .
- Investigate and compare the minimum horizontal stress (σ_{Hmin}) orientation obtained from breakout analysis of the pre and post hydrofrac test image logs in Sellafield boreholes 2, 3, 5, 8A & 10A. This will enable comparison between pre and post hydrofrac stress orientations and assess how successful the hydrofrac results were at Sellafield in distinguishing the true value for σ_{Hmax} .
- Investigate the relationship between the trajectory of a borehole and the borehole breakout that is observed. How does a borehole trajectory affect the borehole breakout produced? Is there a way of compensating for it during breakout analysis?
- Carry out a controlled, detailed laboratory investigation of Barton *et al.*, 1995 'critical stress' theory to confirm whether discontinuities that are actively undergoing shear are in fact the most hydraulically conductive in the rock mass.

- Carry out a controlled, detailed laboratory shear failure investigation of the Potentially Flowing Features (PFF) to determine the actual PFF coefficient of friction. Compare this result to the values used by Barton *et al.*, 1995
- Go back to the core and look at the exact PFF in the Short Interval Test zone. See if there are any distinguishing features, which help to identify them and effect whether they can allow fluid to flow.
- Investigate the capabilities of modern down-hole geochemical tools to see if it is possible to identify PFF, because of their distinctive chemical composition (ME9 late stage calcite).

References

- Aadnoy, B. S. and Bell, J. S. (1998). Classification of drilling-induced fractures and their relationship to in situ stress directions. *Log Analyst*, **39** (6), 27-42.
- Akhurst, M. C., Barnes, R. P., Chadwick, R. A., Millward, D., Norton, M. G., Maddock, R. H., Kimbell, G. S. and Milodowski, A. E. (1998). Structural evolution of the Lake District Boundary Fault Zone in West Cumbria, UK. *Proceeding of the Yorkshire Geological Society*, **52** (2), 139-158.
- Anderson, E. M. (1951). *The dynamics of faulting and dyke formation with application to Britain*. Oliver and Boyd, Edinburgh.
- Anon (1988). Engineering geophysics: Report by the Geological Society Engineering Group Working Party. *Quarterly Journal of the Geological Society*, **21** (3), 207-272.
- Anon (1989). *Guide to geophysical logging of boreholes for hydrogeological purposes*. British Standards. Report No. BS 7022.
- Anon (1996). *Rock Fractures and Fluid Flow: Contemporary Understanding and Applications*. National Academy Press, Washington, D.C.
- Armitage, P., Holton, D., Jefferies, N. L., Myatt, B. J. and Wilcock, P. M. (1996). *Groundwater flow through fractured rock at Sellafield*. European Commission - Nuclear Science and Technology. Report No. EUR 16870.
- Babcock, E. A. (1978). Measurement of subsurface fractures from dipmeter logs. *American Association of Petroleum Geologists Bulletin*, **62**, 1111-1126.
- Baecher, G. B. (1983). Statistical analysis of rock mass fracturing. *Journal of Mathematical Geology*, **15** (2), 329-347.
- Barclay, W. J., Riley, N. J. and Strong, G. E. (1994). The Dinantian rocks of the Sellafield area, West Cumbria. *Proceedings of the Yorkshire Geological Society*, **50** (1), 37-49.
- Barnes, R. P., Ambrose, K., Holliday, D. W. and Jones, N. S. (1994). Lithostratigraphical subdivision of the Triassic Sherwood Sandstone Group in West Cumbria. *Proceeding of the Yorkshire Geological Society*, **50** (1), 51-60.
- Barton, C. A. (1988). Development of in-situ stress measurement techniques for deep drill holes. *Unpublished Ph.D. Thesis, Stanford University*.
- Barton, C. A., Moos, D., Peska, P. and Zoback, M. D. (1997). Utilizing wellbore image data to determine the complete stress tensor: Application to permeability anisotropy and wellbore stability. *The Log Analyst*, **38** (6), 21-33.

Barton, C. A. and Zoback, M. D. (1994). Stress perturbations associated with active faults penetrated by boreholes - possible evidence for near-complete stress drop and a new technique for stress magnitude measurements. *Journal of Geophysical Research-Solid Earth*, **99** (B5), 9373-9390.

Barton, C. A., Zoback, M. D. and Burns, K. L. (1988). In situ stress orientation and magnitude at the Fenton Geothermal Site, New Mexico, determined from wellbore breakouts. *Geophysical Research Letters*, **15** (5), 467-470.

Barton, C. A., Zoback, M. D. and Moos, D. (1995). Fluid-flow along potentially active faults in crystalline rock. *Geology*, **23** (8), 683-686.

Barton, N., Lien, R. and Lunde, J. (1974). Engineering classifications of rock masses for the design of tunnel support. *Rock Mechanics*, **6**, 183-239.

Batchelor, A. S. and Pine, R. J. (1986). The results of in situ stress determinations by seven methods to depths of 2500 m in the Cammenellis Granite. In: *Proceedings of the International Symposium on Rock Stress Measurements, Stockholm, Sweden*. 467-478.

Bath, A. H., McCartney, R. A., Richards, H. G., Metcalfe, R. and Crawford, M. B. (1996). Groundwater chemistry in the Sellafield area: A preliminary interpretation. *Quarterly Journal of Engineering Geology, London*, **29** (Suppl. 1), S39-57.

Bell, J. S. (1989). The stress regime of the Scotian Shelf off-shore Eastern Canada to 6 kilometers depth and implications for rock mechanics and hydrocarbon migration. In: *V. Maury and D. Fourmaintraux (Eds) Proceedings ISRM-SPE International Symposium: Rock at Great Depth, Pau*. A.A. Balkema, Rotterdam. 1243-1265.

Bell, J. S. (1990). Investigating stress regimes in sedimentary basins using information from oil industry wireline logs and drill records. In: *A. Hurst, M. A. Lovell and A. C. Morton (Eds) Geological Applications of Wireline Logs*. Geological Society of London, Special Publications, London, 305-325.

Bell, J. S. (1996). Petro Geoscience 2. In situ stresses in sedimentary rocks:- Applications of stress measurements. *Geoscience Canada*, **23** (3), 135-153.

Bell, J. S. and Gough, D. I. (1979). North East - South West compressive stresses in Alberta: evidence from oil wells. *Earth and Planetary Science Letters*, **45**, 475-482.

Bell, L. M. and Nur, A. (1978). Strength changes due to reservoir-induced pore pressure and stresses and application to Lake Oroville. *Journal of Geophysical Research*, **83** (B9), 4469-4483.

BGS (1997). *Geology of the West Cumbria district*. Memoir of the Geological Survey of Great Britain. Sheet 28 Whitehaven, 37 Gosforth and 47 Bootle (England and Wales).

Bieniawski, Z. T. (1976). Rock mass classification in rock engineering. *In: Proceedings of the Symposium on Exploration for Rock Engineering*. A.A. Balkema, Rotterdam. 1, 97-106.

Bieniawski, Z. T. (1989). *Engineering Rock Mass Classifications: A Complete Manual for Engineers and Geologists in Mining, Civil and Petroleum Engineering*. Wiley-Interscience, New York.

Black, J. H. and Brightman, M. A. (1996). Conceptual model of the hydrogeology of Sellafield. *Quarterly Journal of Engineering Geology, London*, 29 (Suppl. 1), S83-S93.

Blenkinsop, T. G., Hunt, C. and Kuszniir, N. J. (1986). *In situ stress measurements*. British Earthquake Research Group.

Bourke, L. T. (1989). Recognizing artifact images of the formation microscanner. *In: 30th Annual Logging Symposium Transactions: Society of Professional Well Log Analysts*. SPWLA, Denver, Paper WW.

Bowden, R. A., Bumpus, C. and Littleboy, A. K. (1998). An overview and update of the site characterization studies at Sellafield. *Proceeding of the Yorkshire Geological Society*, 52 (2), 125-137.

Bremer, M. H., Kulenkampff, J. and Schopper, J. R. (1992). Lithological and fracture response of common logs in crystalline rocks. *In: A. Hurst, C. M. Griffiths and P. F. Worthington (Eds) Geological Applications of Wireline Logs II*. Geological Society of London, Special Publications, London. 65, 221-234.

Brereton, N. R. (1992). *Rock stress orientation measurements in Sellafield boreholes 2, 3 and 4*. British Geological Survey. Report No. WK/92/13C.

Brereton, N. R., Cornet, F. H., Cowgill, S. M., Evans, C. J., Golke, M., Peart, R. J., Royles, C. P., Scotti, O. and Jianmin, Y. (1993). *European rock stress - Compilations and interpretations (Final Report)*. British Geological Survey. Report No. WK/93/17R.

Brereton, N. R., Evans, C. J. and Kingdon, A. (1998). Hydrogeological and geotechnical rock property characterisation from geophysics. *Proceeding of the Yorkshire Geological Society*, 52 (2), 199-214.

Brereton, N. R., Evans, C. J., Peart, R. J. and Hyett, A. J. (1990). *Mechanisms and theoretical basis governing the creation and development of borehole breakouts*. British Geological Survey. Report No. WK/90/18.

Brereton, N. R., Evans, C. J., Rogers, S. F., Kingdon, A. and Heaven, R. E. (1997). *Geomechanical modelling and anisotropy at the reservoir scale*. British Geological Survey. Report No. WK/97/2C.

Brereton, N. R. and Mueller, B. (1991). European stress: contributions from borehole breakouts. *Philosophical Transactions of the Royal Society*, **337**, 165-179.

Byerlee, J. (1978). Friction of rocks. *Pure and Applied Geophysics*, **116**, 615-626.

Byerlee, J. D. (1967). Frictional characteristics of granite under high confining pressure. *Journal of Geophysical Research*, **72**, 3639-3648.

Byerlee, J. D. (1975). The fracture strength of the Webber Sandstone. *International Journal of Rock Mechanics, Mineral Science & Geomechanical Abstracts*, **12**, 1-4.

Chaplow, R. (1996). The geology and hydrogeology of Sellafield: An overview. *Quarterly Journal of Engineering Geology, London*, **29** (Suppl. 1), S1-S12.

Cooling, C. M. and Hudson, J. A., Eds. (1986). The importance of in situ rock stress in repository design. In: O. Stephansson (Eds) *Proceedings of the International Symposium on Rock Stress and Rock Stress Measurements, Stockholm*. 647-656.

Cowgill, S. M. (1994). The Orientation of Crustal Stresses in the North Sea Basin and their Geological Origin. *Unpublished Ph.D. Thesis, University College London*.

Cox, J. W. (1970). The high resolution dipmeter reveals dip-related borehole and formation characteristics. In: *11th Annual Logging Symposium Transactions: Society of Professional Well Log Analysts*. SPWLA. 1-25.

Cuss, R. J. (1998). An Experimental Investigation of the Mechanical Behaviour of Sandstones with Reference to Borehole Stability. *Unpublished Ph.D. Thesis, University of Manchester*.

Deere, D. U. (1964). Technical description of rock cores for engineering purposes. *Rock Mechanics & Engineering Geology*, **1**, 16-22.

Dennis, B., Standen, E., Georgi, D. T. and Callow, G. O. (1987). Fracture identification and productivity predictions in a carbonate reef complex. *Society of Petroleum Engineers, Paper 16808*, 579-588.

Doveton, J. H. (1986). *Log Analysis of Subsurface Geology - Concepts and Computer Methods*. John Wiley & Sons, New York.

- Doveton, J. H. and Prenskey, S. E. (1992). Geological applications of wireline logs - A synopsis of developments and trends. *The Log Analyst*, **33** (3), 286-301.
- Dudley, J. W. I. (1993). Quantitative fracture identification with the borehole televiewer. In: *34th Annual Logging Symposium Transactions: Society of Professional Well Log Analysts*. Paper LL.
- Edwards, S. T. (1997). A Study of In-situ Stress Magnitudes in the North Sea Basin from Borehole Measurements. *Unpublished Ph.D. Thesis, Birkbeck College and University College London*.
- Ekstrom, M. P., Dahan, C. A., Chen, M. Y., Lloyd, P. M. and Rossi, D. J. (1987). Formation imaging with microelectrical scanning arrays. *The Log Analyst*, **28** (3), 294-306.
- Engelder, T. (1993). *Stress Regimes in the Lithosphere*. Princeton University Press, Princeton.
- Evans, C. J. (1987). *Crustal stress in the United Kingdom*. British Geological Survey.
- Finkbeiner, T., Barton, C. A. and Zoback, M. D. (1997). Relationships among in-situ stress, fractures and faults, and fluid flow: Monterey formation, Santa Maria Basin, California. *AAPG Bulletin-American Association of Petroleum Geologists*, **81** (12), 1975-1999.
- Gay, N. C. (1980). The state of stress in the plates. In: A. W. Bally, P. L. Penden, T. R. McGetchin and R. I. Walcott (Eds) *Dynamics of Plate Interiors*. American Geophysical Union/Geological Society of America, 145-154.
- Gentier, S. S. and Hopkins, D. L. (1997). Mapping fracture aperture as a function of normal stress using a combination of casting, image analysis and modelling techniques. *International Journal of Rock Mechanics and Mineral Sciences & Geomechanics Abstracts.*, **34** (3/4), 359.
- Gough, D. I. and Bell, J. S. (1982). Stress orientations from oil-well fractures in Alberta and Texas. *Canadian Journal of Earth Sciences*, **19**, 1358-1370.
- Gough, D. I. and Gough, W. I. (1987). Stress near the surface of the earth. *Annual Review of Earth and Planetary Sciences*, **15**, 545-566.
- Griffith, A. A. (1921). The phenomena of rupture and flow in solids. *Philosophical Transactions of the Royal Society*, **221**, 163-198.

- Gutmanis, J. C., Lanyon, G. W., Wynn, T. J. and Watson, C. R. (1998). Fluid flow in faults: A study of fault hydrogeology in the Triassic Sandstone and Ordovician Volcaniclastic rocks at Sellafield, North-West England. *Proceeding of the Yorkshire Geological Society*, **52** (2), 159-176.
- Haimson, B. C. (1978). The hydrofracturing stress measuring method and recent field results. *International Journal of Rock Mechanics, Mineral Science & Geomechanical Abstracts*, **15**, 167-178.
- Haimson, B. C. (1982). *A comparative study of deep hydrofracturing and overcoring at six locations with particular interest to the Nevada Test Site*. United States Geological Survey. Open File Report No. 82-1075.
- Hardin, E. L., Cheng, C. H., Paillet, F. L. and Mendelson, J. D. (1987). Fracture characterisation by means of attenuation and generation of tube waves in fractured crystalline rock at Mirror Lake, New Hampshire. *Journal of Geophysical Research*, **92** (B8), 7989-8006.
- Harker, S. D., McCann, G. J., Bourke, L. T. and Adams, J. T. (1990). Methodology of Formation MicroScanner Image interpretation in Claymore and Scappa fields (North Sea). In: A. Hurst, M. A. Lovell and A. C. Morton (Eds) *Geological Applications of well logs*. Geological Society of London, Special Publications, London. **48**, 11-25.
- Hearst, J. R. and Nelson, P. H. (1985). *Well Logging for Physical Properties*. McGraw-Hill, New York.
- Heffer, K. J. and Koutsabeloulis, N. C. (1995). Stress effects on reservoir flow:- numerical modelling used to produce field data. In: H. J. De Hann (Eds) *New Developments in Improved Oil Recovery*. Geological Society of London, Special Publications, London. **84**, 81-88.
- Heffer, K. J. and Lean, J. C. (1993). Earth stress orientation - a control on, and guide to, flooding directionality in a major reservoir. In: W. Linville (Eds) *Reservoir Characterisation III*. PennWell Books, Tulsa.
- Heliot, D., Etchecopar, A. and Cheung, P. (1989). New developments in fracture characterisation from logs. In: V. Maury and D. Fourmaintraux (Eds) *Proceedings ISRM-SPE International Symposium: Rock at Great Depth, Pau*. A.A. Balkema, Rotterdam. 1471-1478.
- Hickman, S. H., Barton, C. A., Zoback, M. D., Morin, R., Sass, J. and Benoit, R. (1997). In situ stress and fracture permeability along the Stillwater Fault Zone, Dixie Valley, Nevada. *International Journal of Rock Mechanics and Mineral Sciences & Geomechanics Abstracts.*, **34** (3/4), 414.

- Hickman, S. H., Healy, J. H. and Zoback, M. D. (1985). In situ stress, natural fracture distribution, and borehole elongation in the Auburn Geothermal Well, Auburn, New-York. *Journal of Geophysical Research-Solid Earth and Planets*, **90** (B7), 5497-5512.
- Hillis, R. R. and Reynolds, S. D. (2000). The Australian stress map. *Journal of the Geological Society.*, **157**, 915-921.
- Hoek, E. and Brown, E. T. (1980a). Empirical strength criterion for rock masses. *Journal of the Geotechnical Engineering Division*, **106**, 1013-1036.
- Hoek, E. and Brown, E. T. (1980b). *Underground Excavations in Rock*. Institution of Mining and Metallurgy, London.
- Hornby, B. E., Johnson, D. L. and Plumb, R. A. (1989). Fracture evaluation using reflected stoneley-wave arrivals. *Geophysics*, **54** (10), 1274-1288.
- Hornby, B. E. and Luthi, S. M. (1992). An Integrated interpretation of fracture apertures computed from electrical borehole scans and reflected stoneley waves. In: A. Hurst, C. M. Griffiths and P. F. Worthington (Eds) *Geological Applications of Wireline Logs II*. Geological Society of London, Special Publications, London. **65**, 185-198.
- Hornby, B. E., Luthi, S. M. and Plumb, R. A. (1992). Comparison of fracture apertures computed from electrical borehole scans and reflected stoneley waves: An integrated interpretation. *The Log Analyst*, **33** (1), 50-66.
- Hottman, C. E., Smith, J. H. and Purcell, W. R. (1979). Relationship among earth stresses, pore pressure and drilling problems offshore Gulf of Alaska. *Journal of Petroleum Technology*, **31**, 1477-1484.
- Hubbert, M. and Willis, D. G. (1957). Mechanics of hydraulic fracturing. *Transactions of the Petroleum Engineers of AIME*, **210**, 153-166.
- Ito, T. and Zoback, M. D. (2000). Fracture permeability and in situ stress to 7 km depth in the KTB Scientific Drillhole. *Geophysical Research Letters*, **27** (7), 1045-1048.
- Jackson, P. D., Shedlock, S., Willis-Richards, J. and Green, A. S. P. (1992). Enhanced resolution resistivity logging for fracture studies. In: A. Hurst, C. M. Griffiths and P. F. Worthington (Eds) *Geological Applications of Wireline Logs II*. Geological Society of London, Special Publications, London. **65**, 265-274.
- Jaeger, J. C. (1969). *Elasticity, Fracture and Flow: With Engineering and Geological Applications*. Chapman & Hall, New York.
- Jaeger, J. C. and Cook, N. G. W. (1984). *Fundamentals of Rock Mechanics*. Chapman & Hall, London.

Jolly, R. J. H., Wei, L. and Pine, R. J. (2000). Stress-sensitive fracture-flow modelling in fractured reservoirs. *In: Proceedings of the 2000 SPE International Petroleum Conference, Villahermosa, Mexico*. Society of Petroleum Engineers.

Kessels, W. (1989). Observation and interpretation of time dependant behaviour of borehole stability in the continental deep drilling pilot borehole. *In: V. Maury and D. Fourmaintraux (Eds) Proceedings ISRM-SPE International Symposium: Rock at Great Depth, Pau*. A.A. Balkema, Rotterdam.

Keys, W. S. (1979). Borehole geophysics in igneous and metamorphic rocks. *In: 20th Annual Logging Symposium Transactions: Society of Professional Well Log Analysts, Tulsa*. SPWLA. Paper OO.

Keys, W. S. (1988). *Borehole geophysics applied to ground-water hydrogeology*. United States Geological Survey. Open-File Report No 87-539.

Keys, W. S. (1990). *Borehole geophysics applied to groundwater investigations*. United States Geological Survey. Book 2, Chapter E2.

Keys, W. S. and MacCary, L. M. (1971). *Application of borehole geophysics to water resources investigations*. United States Geological Survey. Book 2, Chapter E1.

Kirsch, G. (1898). Die theorie der elastizitat und die bednurnisse der festigeitslehre. *Zietschrift der Veriens Deutscher Ingenieure*, **42**, 797-807.

Klein, R. J. and Brown, E. T. (1983). *The state of stress in British rocks*. Department of the Environment. Report No. DOE/RW/83.8.

Laubach, S. E., Baumgardner, R. W., Monson, E. R., Hunt, E. and Meador, K. J. (1988). Fracture detection in low-permeability reservoir sandstone: A comparison of BHTV and FMS logs to core. *Society of Petroleum Engineers, Paper 18119*, 129-139.

Lehne, K. A. (1990). Fracture detection from logs of North Sea Chalk. *In: A. Hurst, M. A. Lovell and A. C. Morton (Eds) Geological Applications of Wireline Logs*. Geological Society of London, Special Publications, London, 263-271.

Leman, E. R. (1964). The measurement of stress in rock - Part 1- The principles of rock stress measurements. *Journal of the South African Institute of Mining and Metallurgy*, **65**, 45-81.

- Lincecum, T. A. M. V., Reinmiller, R. and Mattner, J. (1993). Natural and induced fracture classification using image analysis. *In: 34th Annual Logging Symposium Transactions: Society of Professional Well Log Analysts*. Paper J.
- Lofts, J. C. and Bourke, L. T. (1999). The recognition of artifacts from acoustic and resistivity borehole imaging devices. *In: M. A. Lovell, G. Williamson and P. K. Harvey (Eds) Borehole Imaging: Applications and Case Histories*. Geological Society of London, Special Publications, London. **159**, 59-76.
- Long, J. C. S., Karasaki, K., Davey, A., Peterson, J., Landsfield, M., Kemeny, J. and Martel, S. (1991). An inverse approach to the construction of fracture hydrogeology models conditioned by geophysical data: An example from the validation exercises at the Stripa Mine. *International Journal of Rock Mechanics and Mineral Sciences & Geomechanics Abstracts*, **28** (2/3), 121-142.
- Lovell, M. A., Harvey, P. K., Brewer, T. S., Williams, C., Jackson, P. D. and Williamson, G. (1997). Application of FMS images in the Ocean Drilling Program - An overview. *In: A. Cramp, C. J. McLeod, S. V. Lee and E. J. W. Jones (Eds) Geological evolution of ocean basins - results from the Ocean Drilling Program*. Geological Society of London, Special Publications, London. **131**, 287-303.
- Lovell, M. A., Harvey, P. K., Jackson, P. D., Flint, R., Gunn, D., Williamson, G., Ball, J. K., Ashu, A. P. and Williams, C. (1995). Electrical resistivity core imaging II: Investigation of fabric and fluid flow characteristics. *Scientific Drilling*, **5** (4), 153-164.
- Luthi, S. M. and Souhaite, P. (1990). Fracture apertures from electrical borehole scans. *Geophysics*, **55** (7), 821-833.
- Mastin, L. G. (1988). Effect of borehole deviation on breakout orientations. *Journal of Geophysical Research*, **93** (B8), 9187-9195.
- Mastin, L. G., Heinemann, B. B., Fuchs, K. and Zoback, M. D. (1989). Preliminary results of breakout analysis below 500m depth in the KTB pilot hole. *In: V. Maury and D. Fourmaintraux (Eds) Proceedings ISRM-SPE International Symposium: Rock at Great Depth, Pau*. A.A. Balkema, Rotterdam. 1491-1499.
- McEwen, T. J., McCann, D. M. and Shedlock, S. (1985). Fracture analysis from borehole geophysical techniques in crystalline rocks. *Quarterly Journal of Engineering Geology, London*, **18**, 413-436.
- McGarr, A. and Gay, N. C. (1978). State of Stress in the Earth's Crust. *Annual Review of Earth and Planetary Sciences*, **6**, 405-436.

-
- McL. Michie, U. (1996). The geological framework of the Sellafield area and its relationship to hydrogeology. *Quarterly Journal of Engineering Geology, London*, **29** (Suppl. 1), S13-S27.
- McL. Michie, U. and Bowden, R. A. (1994). UK NIREX geological investigations at Sellafield. *Proceeding of the Yorkshire Geological Society*, **50** (1), 5-10.
- McLintock, F. A. and Walsh, J. B. (1962). Friction on Griffith cracks in rock under pressure. In: *Proceedings of the 4th US National Congress on Application Mechanics, New York*. American Society of Mechanical Engineers.
- Millward, D., Beddoe-Stephens, B., Williamson, I. T., Young, S. R. and Petterson, M. G. (1994). Lithostratigraphy of a concealed calders-related ignimbrite sequence within the Borrowdale Volcanic Group of West Cumbria. *Proceeding of the Yorkshire Geological Society*, **50** (1), 25-36.
- Mueller, B., Reinecker, J., Heidbach, O. and Fuchs, K. (2000). *The 2000 release of the World Stress Map*, available online at www.world-stress-map.org.
- Newmark, R. L., Zoback, M. D. and Anderson, R. N. (1984). Orientation of in situ stresses in the oceanic-crust. *Nature*, **311** (5985), 424-428.
- NIREX (1993a). *The geological structure of the Sellafield area: December 1993 update*. UK NIREX Ltd. Report No. 520.
- NIREX (1993b). *The geology and hydrogeology of the Sellafield area: Interim Assessment December 1993*. UK NIREX Ltd. Report No. 524.
- NIREX (1994). *Modelling groundwater flow and radionuclide transport*. UK NIREX Ltd. Report No. S/94/004.
- NIREX (1995a). *The 3-D geological structure of the PRZ: Summary report*. UK NIREX Ltd. Report No. S/95/005.
- NIREX (1995b). *The 3-D geology and hydrogeology of the RCF South Shaft location: Summary report*. UK NIREX Ltd. Report No. S/95/007.
- NIREX (1995c). *The Flow zone characterisation of the RCF area: Summary report*. UK NIREX Ltd. Report No. S/95/006.
- NIREX (1995d). *Generation of an orientated discontinuity data set for borehole RCF3*. UK NIREX Ltd. Report No. 545.
- NIREX (1995e). *Geotechnical studies at Sellafield: Executive summary of NGI/WSA work from 1990 to 1994*. UK NIREX Ltd. Report No. 801.

NIREX (1995f). *Sellafield geological and hydrogeological investigations: Factual report - compilation of maps and drawings*. UK NIREX Ltd. Report No. SA/95/002.

NIREX (1996a). *Assessment of the in-situ stress field at Sellafield - Main report*. UK NIREX Ltd. Report No. SA/96/004.

NIREX (1996b). *The borehole RCF3 pump test*. UK NIREX Ltd. Report No. S/96/003.

NIREX (1996c). *The NIREX Digital Geoscience Database - An overview*. UK NIREX Ltd. Report No. S/96/001.

NIREX (1996d). *The RCF Longlands Farm, West Cumbria: Report on baseline groundwater pressure and hydrochemistry, summary report*. UK NIREX Ltd. Report No. S/96/004.

NIREX (1996e). *Structural atlas of the Sellafield boreholes*. UK NIREX Ltd. Report No. SA/96/005.

NIREX (1997a). *Assessment of the in-situ stress field at Sellafield*. UK NIREX Ltd. Report No. S/97/003.

NIREX (1997b). *Data summary sheets in support of gross geotechnical predictions*. UK NIREX Ltd. Report No. SA/97/052.

NIREX (1997c). *The geological structure of the Sellafield site*. UK NIREX Ltd. Report No. S/97/007.

NIREX (1997d). *The hydrochemistry of Sellafield: 1997 update*. UK NIREX Ltd. Report No. SA/97/089.

NIREX (1997e). *The hydrogeology of the Sellafield area: 1997 update*. UK NIREX Ltd. Report No. S/97/008.

NIREX (1997f). *Locations of flow zones in Sellafield deep boreholes*. UK NIREX Ltd. Report No. SA/97/073.

NIREX (1997g). *Planning the scientific programme for the Rock Characterisation Facility*. UK NIREX Ltd. Report No. S/97/006.

NIREX (1997h). *The Quaternary of the Sellafield area*. UK NIREX Ltd. Report No. S/97/002.

NIREX (1997i). *Spatial heterogeneity of rock mass properties*. UK NIREX Ltd. Report No. SA/97/021.

NIREX (1997j). *Spatial heterogeneity of the rock mass within the Potential Repository Zone*. UK NIREX Ltd. Report No. S/97/005.

NIREX (1997k). *Summary data compilation for the location, distribution and orientation of potential flowing features in the Sellafield boreholes*. UK NIREX Ltd. Report No. SA/97/031.

Ohnaka, M. (1973). The quantitative effect of hydrostatic confining pressure on the compressive strength of crystalline rocks. *Journal of Physics of the Earth*, **21**, 125-140.

Paillet, F., Barton, C., Luthi, S., Rombow, F. and Zemanek, J. (1990). Borehole imaging and its application in well logging - An overview. In: F. Paillet, C. Barton, S. Luthi, F. Rombow and J. Zemanek (Eds) *Borehole Imaging*. SPWLA Reprint Series, Houston, 1-23.

Paillet, F. L. (1980). Acoustic propagation in the vicinity of fractures which intersect a fluid-filled borehole. In: *21st Annual Logging Symposium Transactions: Society of Professional Well Log Analysts*. SPWLA, Paper DD.

Paillet, F. L. (1991a). Acoustic full-waveform logs and fracture permeability. *The Log Analyst*, **32** (3), 256-270.

Paillet, F. L. (1991b). Use of geophysical well logs in evaluating crystalline rocks for siting of radioactive-waste repositories. *The Log Analyst*, **32** (2), 85-107.

Paillet, F. L., Keys, W. S. and Hess, A. E. (1985). Effects of lithology on televiwer-log quality and fracture interpretation. In: *27th Annual Logging Symposium Transactions: Society of Professional Well Log Analysts*. SPWLA, Dallas, Paper JJJ.

Paillet, F. L. and Kim, K. (1987). Character and distribution of borehole breakouts and their relationship to in situ stresses in Deep Columbia River Basalts. *Journal of Geophysical Research*, **92** (B7), 6223-6234.

Paterson, M. S. (1978). *Experimental Rock Deformation - The Brittle Field*. Springer-Verlag, Berlin.

Peska, P. and Zoback, M. D. (1995). Compressive and tensile failure of inclined well bores and determination of in-situ stress and rock strength. *Journal of Geophysical Research-Solid Earth*, **100** (B7), 12791-12811.

Pezard, P. A., Hiscott, R. N., Lovell, M. A., Collela, A. and Malinverno, A. (1992). Evolution of the Izu-Bonin intraoceanic forearc Basin, Western Pacific, from cores and FMS images. In: A. Hurst, C. M. Griffiths and P. F. Worthington (Eds) *Geological Applications of Wireline Logs II*. Geological Society London, Special Publications, London. **65**, 43-69.

Pezard, P. A. and Luthi, S. M. (1988). Borehole electrical images in the basement of the Cajon Pass Scientific Drillhole, California: fracture identification and tectonic implications. *Geophysical Research Letters*, **15** (9), 1017-1020.

Pine, R. J. (1986). Rock Joint and Rock Mass Behaviour during Pressurised Hydraulic Injections. *Unpublished Ph.D. Thesis, Camborne School of Mines*.

Pine, R. J., Ledingham, P. and Merrifield, C. M. (1983a). In-situ stress measurement in the Carnmenellis Granite - II Hydrofracture tests at Rosemanowes Quarry to depths of 2000 m. *International Journal of Rock Mechanics, Mineral Science & Geomechanical Abstracts*, **20** (2), 63-72.

Pine, R. J., Tunbridge, L. W. and Kwakwa, K. (1983b). In-situ stress measurement in the Carnmenellis Granite - I Overcoring tests at South Crofty Mine at depth of 790 m. *International Journal of Rock Mechanics, Mineral Science & Geomechanical Abstracts*, **20** (2), 51-62.

Plumb, R. A. (1989). Fracture patterns associated with incipient wellbore breakouts. In: V. Maury and D. Fourmaintraux (Eds) *Rocks at great depths*. A.A. Balkema, Rotterdam. **2**, 761-768.

Plumb, R. A., Brie, A. and Hsu, K. (1985). Fracture detection and evaluation using new wireline methods. In: *Proceedings of the 26th U.S Symposium on Rock Mechanics - Research and Engineering Applications in Rock Masses.*, Rapid City. Boston: A.A. Balkema.

Plumb, R. A. and Hickman, S. H. (1985). Stress-induced borehole elongation: A comparison between the four-arm dipmeter and the borehole televiewer in the Auburn Geothermal Well. *Journal of Geophysical Research*, **90** (B7), 5513-5521.

Plumb, R. A. and Luthi, S. M. (1989). Analysis of borehole images and their application to geologic modelling of an aeolian reservoir. In: *Proceedings of the 61st Annual Technical Conference of the Society of Petroleum Engineers, New Orleans*. Society of Petroleum Engineers. 505-514.

Prensky, S. E. (1994). *Bibliography of well-log applications.*, SPWLA.

Prensky, S. E. (1999). Advances in borehole imaging technology and applications. In: M. A. Lovell, G. Williamson and P. K. Harvey (Eds) *Borehole Imaging: Applications and Case Histories*. Geological Society of London, Special Publications, London. **159**, 1-43.

Priest, S. D. (1985). *Hemispherical Projection Methods in Rock Mechanics*. George Allen and Unwin, London.

Priest, S. D. (1993). *Discontinuity Analysis for Rock Engineering*. Chapman & Hall, London.

Prosser, J., Buck, S., Saddler, S. and Hilton, V. (1999). Methodologies for multi-well sequence analysis using borehole image and dipmeter data. *In: M. A. Lovell, G. Williamson and P. K. Harvey (Eds) Borehole imaging: Applications and case histories*. Geological Society of London, Special Publications, London, 91-121.

Rawnsley, K. D., Rives, T., Petit, J. P., Hencher, S. R. and Lumsden, A. C. (1992). Joint development in perturbed stress fields near faults. 939-951.

Reeves, G. M. (1996). Hydrogeological investigation programmes: Best practice. *In: R. S. Hazeldine and D. K. Smythe (Eds) Radioactive Waste Disposal at Sellafield, UK - Site Selection Geological and Engineering Problems*. University of Glasgow, Glasgow, 279-310.

Rider, M. (1996). *The Geological Interpretation of Well Logs*. Whittles, Caithness.

Rogers, S. F. (2000). Stress-related flow - Are we looking the right way? *DiaLog*. October 2000,

Rogers, S. F. and Evans, C. J. (in press). Stress dependent flow in the fractured rocks of Sellafield, UK. *In: M.A. Lovell and N. Parkinson (Eds) Geological Applications of Wireline Logs III: AAPG Methods in Exploration*. 13, 241-250.

Rutter, E. (1993). The mechanics of natural rock deformation. *In: G. Hudson (Eds) Comprehensive Rock Engineering*. Pergamon Press. 1, 63-92.

Schafer, J. N. (1980). A practical method of well evaluation and acreage development for the naturally fractured Austin Chalk formation. *Log Analysts*, 21, 10-23.

Schlumberger (1989). Log interpretation principles/applications.

Schlumberger (1992). *FMI Fullbore Formation MicroImager*. Schlumberger. Document No SMP-9210.

Schmitt, T. J. (1981). The West Europe stress field: New data and interpretation. *Journal of Structural Geology*, 3 (3), 309-315.

Scofield, A. (1998). Mohr Coulomb correction error. *Ground Engineering*, 31, 30-32.

Seera, O., Stowe, I. and Motet, D. (1993). True integrated interpretation. *In: 34th Annual Logging Symposium Transactions Society of Professional Well Log Analysts, Calgary*. SPLWA. Paper Z.

Shamir, G. and Zoback, M. D. (1989). The stress orientation profile in the Cajon Pass, California, scientific drillhole, based on detailed analysis of stress induced borehole breakouts. *In: V. Maury and D. Fourmaintraux (Eds) Proceedings ISRM-SPE International Symposium: Rock at Great Depth, Pau.* A.A. Balkema, Rotterdam.

Shamir, G., Zoback, M. D. and Barton, C. A. (1988). In situ stress orientation near the San-Andreas Fault - Preliminary-results to 2.1 Km depth from the Cajon Pass Scientific Drillhole. *Geophysical Research Letters*, **15** (9), 989-992.

Smythe, D. K. (1996). The 3-D structural geology of the PRZ. *In: R. S. Hazeldine and D. K. Smythe (Eds) Radioactive Waste Disposal at Sellafield, UK - Site Selection Geological and Engineering Problems.* University of Glasgow, Glasgow, 237-265.

Springer, J. E. (1987). Stress orientations from wellbore breakouts in Coalinga Region. *Tectonics*, **6** (5), 667-676.

Standen, E. (1991). Tips for analyzing fractures on electrical wellbore images. *World Oil*, **April**, 99-118.

Strong, G. E., Milodowski, A. E., Pearce, J. M., Kemp, S. J., Prior, S. V. and Morton, A. C. (1994). The petrology and diagenesis of Permo-Triassic rocks of the Sellafield area, Cumbria. *Proceedings of the Yorkshire Geological Society*, **50** (1), 77-90.

Sutton, J. S. (1996). Hydrogeological testing in the Sellafield area. *Quarterly Journal of Engineering Geology, London*, **29** (Suppl. 1), S29-S23.

Sutton, J. S., Solely, R., Jeffery, R., Chackrabarty, C. and McLeod, R. (1996). *Cross hole hydraulic testing between deep borehole 2 and 4 at Sellafield.* European Commission - Nuclear Science and Technology. Report No. EUR 16967.

Talbot, C. J. and Sirat, M. (2001). Stress control of hydraulic conductivity in fracture-saturated Swedish bedrock. *Engineering Geology*, **61**, 145-153.

Tang, X. M., Cheng, C. H. and Toksoz, M. N. (1991). Stoneley-wave propagation in a fluid-filled borehole with a vertical fracture. *Geophysics*, **56** (4), 447-460.

Taylor, T. J. (1991). A method for identifying fault related fracture systems using the borehole televiewer. *In: 32nd Annual Logging Symposium Transactions: Society of Professional Well Log Analysts.* Paper JJ.

Terzaghi, R. D. (1965). Sources of error in joint surveys. *Geotechnique*, **15**, 287-303.

Teufel, L. W. (1983). Determination of in situ stress from anelastic strain recovery measurements of oriented core. *In: Proceedings of the SPE/DOE Symposium on Low Permeability., Denver, Colorado.* Society of Petroleum Engineers. 421-430.

Timoshenko, S. P. and Goodier, J. N. (1970). *Theory of Elasticity.* McGraw-Hill Kogakusha, Tokyo.

Torres, D., Strickland, R. and Gianzero, M. (1990). A new approach to determining dip and strike using borehole images. *In: 31st Annual Logging Symposium Transactions: Society of Professional Well Log Analysts.* SPWLA. Paper K, 1-20.

Twiss, R. J. and Moores, E. M. (1992). *Structural Geology.* W.H. Freeman and Company, New York.

Vernik, L. and Zoback, M. D. (1989). Effects of rock elastic and strength properties in estimations of the state of stress at depth. *In: V. Maury and D. Fourmaintraux (Eds) Proceedings ISRM-SPE International Symposium: Rock at Great Depth, Pau.* A.A. Balkema, Rotterdam. 1033-1040.

Wang, Y. (1994). The effect of nonlinear Mohr-Coulomb criterion on borehole stresses and damage zone estimate. *Canadian Geotechnical Journal*, **31**, 104-109.

Wilbur, C. and Amedei, B. (1990). Flow pump measurement of fracture transmissivity as a function of normal stress. *In: G. A. Johnson (Eds) Rock Mechanics and Challenges.* A.A. Balkema, Rotterdam, 621-627.

Wiprut, D., Zoback, M. D., Hanssen, T. H. and Peska, P. (1997). Constraining the full stress tensor from observations of drilling-induced tensile fractures and leak-off tests: Application to borehole stability and sand production on the Norwegian Margin. *International Journal of Rock Mechanics and Mineral Sciences & Geomechanics Abstracts.*, **34** (3/4), 417.

Wong, T. F., David, C. and Zhu, W. (1997). The transition from brittle faulting to cataclastic flow in porous sandstones: mechanical deformation. *Journal of Geophysical Research, B, Solid Earth and Planets*, **102**, 3009-3025.

Yeo, I. W., De Freitas, M. H. and Zimmerman, R. W. (1998). Effect of shear displacement on the aperture and permeability of a rock fracture. *International Journal of Rock Mechanics and Mining Sciences & Geomechanics Abstracts*, **35** (8), 1051-1070.

Zemanek, J., Caldwell, R. L., Glenn, E. E., Holcomb, S. V., Norton, L. J. and Straus, A. J. D. (1969). The borehole televiewer - a new logging concept for fracture location and other types of borehole inspection. *Journal of Petroleum Technology*, **21**, 762-774.

Zemanek, J., Glenn, E. E., Norton, L. J. and Cadwell, R. L. (1970). Formation inspection with the borehole televiewer. *Geophysics*, **35**, 254-269.

Zheng, Z., Kemeny, J. and Cook, N. G. W. (1989). Analysis of borehole breakouts. *Journal of Geophysical Research*, **94** (B6), 7171-7182.

Zoback, M. D., Mastin, L. and Barton, C. A. (1986). In-situ stress measurements in deep boreholes using hydraulic fracturing, wellbore breakouts, and stoneley wave polarization. In: *Proceedings of the International Symposium on Rock Stress Measurements, Stockholm*. 280-299.

Zoback, M. D., Moos, D., Mastin, L. and Anderson, R. N. (1985). Well bore breakouts and in situ stress. *Journal of Geophysical Research-Solid Earth and Planets*, **90** (B7), 5523-5530.

Zoback, M. L. (1992). First and second-order patterns of stress in the lithosphere: The World stress map project. *Journal of Geophysical Research*, **97** (B8), 11,703-11,728.

Zoback, M. L. and Zoback, M. D. (1980). State of stress in the conterminous United States. *Journal of Geophysical Research*, **85** (B11), 6113-6156.

Zoback, M. L., Zoback, M. D., Adams, J., Assumpcao, M., Bell, S., Bergman, E. A., Blumling, P., Brereton, N. R., Denham, D., Ding, J., Fuchs, K., Gay, N., Gregerson, S., Gupta, H. K., Gvishiani, A., Jacoc, K., Klein, R., Knoll, P., Magee, M., Mercier, J. L., Muller, B. C., Paquin, C., Rajendran, K., Stephansson, O., Suarez, G., Suter, M., Udias, A., Xu, Z. H. and Zhizhin, M. (1989). Global patterns of tectonic stress. *Nature*, **341**, 291-298.

Appendix 1

Over Sized A) Tables & B) Figures

Borehole	Depth (mbRT)	Any rotation in stress profile observed	Approx depth rotation encountered (mbRT)	Average range of orientation (Degrees) of σ_{Hmin} (σ_{Hmin}) across stress profile	Range of orientation (Degrees) of σ_{Hmin} (σ_{Hmin}) across rotation	Number of faults encountered in Stress Profile	Number of faults found in rotation	Type of stress profile produced	Comment on type of stress profile produced with respect to breakout rose produced	Figure (Appendix 5)
BH2	487 - 587	Yes	510 - 540	100 - 170	30 - 40	3	1	Variable	Rotation explains why biaxial breakout rose produced	App 5.41
BH3	1621 - 1721	Yes	1684 - 1721	100 - 160	20 - 70	7	4	Variable	Rotations explains why more circular biaxial breakout rose produced	App 5.42
BH5	490 - 590	Yes	532 - 553	20 - 100	60 - 90	1	1	Variable	Rotations explains why more circular biaxial breakout rose produced	App 5.43
BH7A	578 - 678	Yes	610 - 678	70 - 80	30 - 140	8	7	Consistent + Kick	Rotations explains why biaxial breakout rose produced	App 5.44
BH8A	203.1 - 303.1	Yes	203 - 231	150 - 165	50 - 140	13	5	Consistent + Kick	Rotation explains why generally uniaxial breakout rose produced with small biaxial component	App 5.45
BH9A	29 - 119	Yes	52 - 67	40 - 65	55 - 150	9	0	Consistent + Kick	Rotation explains why generally uniaxial breakout rose produced with small biaxial component	App 5.46
BH9B	24.7 - 124.7	Yes	63 - 88	50 - 80	70 - 90	16	4	Consistent + Kick	Rotation explains why generally uniaxial breakout rose produced with small biaxial component	App 5.47
BH10A	1052 - 1152	Yes	1052 - 1075	70 - 80	60 - 90	6	6	Consistent + Kick	Rotation within average range of orientation explains why uniaxial breakout rose produced	App 5.48
BH11A	1024 - 1124	Yes	1024 - 1067	150 - 175	50 - 160	5	0	Variable	Rotations explains why more circular uniaxial breakout rose produced	App 5.49
BH12A	930.75 - 980.75	No	N/A	80 - 100	N/A	4	N/A	Consistent	Biaxial breakout rose, not consistent with type of stress profile produced - anomalous result	App 5.50
BH13A	1620 - 1720	Yes (2)	1620 - 1638	75 - 110	20 - 100	4	2	Variable	Rotations explains why more circular biaxial breakout rose produced	App 5.51
"	"	"	1693 - 1720	"	60 - 160	"	0	"	"	"
BH14A	721 - 821	Yes	793 - 821	80 - 100	90 - 110	1	1	Consistent + Kick	Rotation explains why generally uniaxial breakout rose produced with small biaxial component	App 5.52
RCF3	525 - 630	Yes	548 - 578	50 - 100	65 - 95	13	5	Consistent + Kick	Rotations explains why more circular uniaxial breakout rose produced	App 5.53
RCM1	525 - 625	Yes	525 - 568	80	80 - 125	15	7	Consistent + Kick	Rotation explains why generally uniaxial breakout rose produced with small biaxial component	App 5.54
RCM2	530 - 630	Yes	530 - 558	70 - 75	65 - 125	10	5	Consistent + Kick	Uniaxial breakout rose, not consistent with type of stress profile produced - anomalous result	App 5.55

Table 4.8 – Summary of type of stress profile concluded for each borehole and the number of faults encountered within the profile.

Table 5.2 – Results of flow zone stress analysis.

Borehole ID	Production Log Flow Zone ID	Production Log Flow Zone Top Depth (mbRT)	Production Log Flow Zone Bottom Depth (mbRT)	Flow Zone Separation (m)	Depth Stress / Fracture orientation calculated over (mbRT)	σ_{Hmin} (Degrees)	σ_{Hmax} (Degrees)	Stress Confidence (+/-)	No. Data Points	Max Stress Rose Value	Stress Figure (Appendix 8)	Mean Fracture Orientation (Degrees)	Mean Fracture Confidence (+/-)	Discontinuity Figure (Appendix 8)
2	1	198			193.0 - 203.0	127.3	217.3	13.5	984	0.37	App 8.1	132.7	13.5	App 8.133
2	2	205	210	7.0	202.5 - 212.5	102.8	192.8	10.0	984	0.46	App 8.2	137.3	15.5	App 8.134
2	3	211		6.0	206.0 - 216.0	94.5	184.5	8.7	984	0.38	App 8.3	138.6	17.1	App 8.135
2	4	216.5		5.5	211.5 - 221.5	82.4	172.4	8.7	984	0.43	App 8.4	138	17.9	App 8.136
2	5	233		16.5	228.0 - 238.0	43.4	133.4	11.9	984	0.50	App 8.5	138.3	22.0	App 8.137
2	6	242		9.0	237.0 - 247.0	20.8	110.8	9.8	984	0.40	App 8.6	134.7	15.7	App 8.138
2	11	384.0		142.0	379.0 - 389.0	0.5	90.5	18.2	984	0.20	App 8.7	132.6	12.9	App 8.139
2	12	547.0		163.0	539.0 - 550.0	158.4	248.4	8.6	1082	0.26	App 8.8	161.2	12.4	App 8.140
2	13	573.0		26.0	568.0 - 575.5	88.7	178.7	15.1	738	0.26	App 8.9	139.7	18.9	App 8.141
2	14	607		34.0	605.0 - 610.0	6.9	96.9	8.9	492	0.27	App 8.10	143.6	21.7	App 8.142
2	15	622.5		15.5	615.0 - 622.5	144.2	234.2	10.8	738	0.22	App 8.11	7.4	5.8	App 8.143
2	15	622.5		0.0	622.5 - 627.0	94.5	184.5	24.2	442	0.23	App 8.12	152.5	13.8	App 8.144
2	15	622.5		0.0	615.0 - 627.0	94.9	184.9	27.1	1180	0.15	App 8.13	13.9	13.4	App 8.145
2	17	735.5		113.0	732.0 - 742.0	67.6	157.6	17.1	984	0.23	App 8.14	150.1	18.9	App 8.146
2	18	743.5		8.0	733.5 - 753.5	61.7	151.7	16.2	1968	0.26	App 8.15	145.9	22.0	App 8.147
2	19	803.0		59.5	800.0 - 803.98	124.0	214.0	18.5	392	0.26	App 8.16	139.6	12.9	App 8.148
2	19	803.0		0.0	801.5 - 804.0	132.5	222.5	19.1	246	0.25	App 8.17	142.8	17.3	App 8.149
2	19	803.0		0.0	804.0 - 813.0	41.9	131.9	15.6	886	0.33	App 8.18	76.9	22.6	App 8.150
2	20	933	942	130.0	932.0 - 941.0	37.2	127.2	13.2	886	0.24	App 8.19	78.2	26.7	App 8.151
2	21	963	971	30.0	961.5 - 974.0	69.9	159.9	15.7	1230	0.28	App 8.20	134	25.8	App 8.152
2	22	1011	1020	48.0	1005.5 - 1025.5	49.7	139.7	22.4	1968	0.14	App 8.21	154.5	17.5	App 8.153
2	24	1143	1153	132.0	1142.0 - 1158.0	99.3	189.3	21.1	1576	0.15	App 8.22	157.2	14.1	App 8.154
2	24	1143	1153		1148.5 - 1153.0	28.7	118.7	17.4	444	0.19	App 8.23	157.1	10.1	App 8.155
2	25	1594	1600	451.0	1590.0 - 1602.0	113.2	203.2	17.2	1574	0.20	App 8.24	137	22.5	App 8.156
2	25	1594	1600		1590.0 - 1594.5	105.7	195.7	8.1	590	0.48	App 8.25	139	19.8	App 8.157
2	25	1594	1600		1594.5 - 1602.0	130.3	220.3	23.0	984	0.13	App 8.26	138.8	21.8	App 8.158
5	1	540	545		537.5 - 547.5	81.7	171.7	22.7	984	0.19	App 8.27	79	21.5	App 8.159
5	2	593	599	53.0	591.0 - 601.0	61.1	151.1	23.5	984	0.19	App 8.28	75.3	23.8	App 8.160
5	3	743	750	150.0	736.5 - 756.5	57.4	147.4	20.3	1968	0.20	App 8.29	17	15.2	App 8.161

Highlighted data denotes FZ in sedimentary Permo-Triassic rocks.

Table 5.2 – Results of flow zone stress analysis.

Borehole ID	Production Log Flow Zone ID	Production Log Flow Zone Top Depth (mbRT)	Production Log Flow Zone Bottom Depth (mbRT)	Flow Zone Separation (m)	Depth Stress / Fracture orientation calculated over (mbRT)	σ_{Hmin} (Degrees)	σ_{Hmax} (Degrees)	Stress Confidence (+/-)	No. Data Points	Max Stress Rose Value	Stress Figure (Appendix 8)	Mean Fracture Orientation (Degrees)	Mean Fracture Confidence (+/-)	Discontinuity Figure (Appendix 8)
5	3	743	750		742.0 - 749.0	92.0	182.0	19.2	688	0.16	App 8.30	129.3	19.8	App 8.162
5	3	743	750		741.5 - 751.5	95.6	185.6	22.1	984	0.12	App 8.31	127.3	22.5	App 8.163
5	4	753	756	10.0	749.5 - 758.0	157.8	247.8	18.8	836	0.20	App 8.32	161.5	14.0	App 8.164
5	5	811	816	58.0	804.0 - 818.0	67.6	157.6	19.7	1378	0.21	App 8.33	81.8	19.8	App 8.165
5	6	840	843	29.0	836.5 - 846.5	86.8	176.8	22.8	984	0.20	App 8.34	114.1	24.8	App 8.166
5	7	883	892	43.0	882.5 - 892.5	28.9	118.9	19.5	984	0.21	App 8.35	36.9	20.5	App 8.167
8A	1	231			227.0 - 237.0	133.5	223.5	21.9	984	0.14	App 8.36	68.6	24.8	App 8.168
8A	2	344	362	113.0	339.0 - 364.5	163.9	253.9	22.4	2460	0.11	App 8.37	109.1	23.0	App 8.169
8A	3	695		351.0	692.0 - 701.0	28.8	118.8	17.1	886	0.20	App 8.38	140.6	21.7	App 8.170
8A	4	735		40.0	734.0 - 738.0	86.3	176.3	18.0	394	0.24	App 8.39	147.0	21.8	App 8.171
8A	5	758		23.0	755.2 - 760.0	174.7	264.7	21.8	474	0.17	App 8.40	85.0	24.3	App 8.172
8A	6	892		134.0	883.0 - 895.5	165.6	255.6	21.4	1230	0.15	App 8.41	157.4	14.4	App 8.173
8A	7	954		62.0	952.0 - 956.0	102.2	192.2	18.6	394	0.20	App 8.42	75.7	19.8	App 8.174
11A	13	880		83.0	878.5 - 885.0	5.6	95.6	18.3	640	0.17	App 8.43	21.8	19.9	App 8.175
11A	13	880			869.0 - 889.0	17.5	107.5	20.4	1970	0.16	App 8.44	84.7	17.5	App 8.176
11A	14	979		99.0	973.0 - 978.0	121.1	211.1	21.0	490	0.17	App 8.45	111.7	23.6	App 8.177
11A	14	979			978.0 - 978.5	169.5	259.5	4.2	48	0.55	App 8.46	32.0	0.0	App 8.178
11A	14	979			978.0 - 978.6	170.9	260.9	5.5	58	0.54	App 8.47	32.0	0.0	App 8.179
11A	14	979			978.5 - 983.0	109.3	199.3	25.3	432	0.16	App 8.48	70.2	19.5	App 8.180
11A	14	979			973.0 - 983.0	108.6	198.6	24.0	982	0.11	App 8.49	106.1	23.8	App 8.181
11A	15	995		16.0	993.0 - 997.5	164.8	254.8	19.9	444	0.15	App 8.50	26.3	16.1	App 8.182
11A	16	1004		9.0	999.0 - 1009.0	11.5	101.5	21.1	986	0.10	App 8.51	118.1	19.3	App 8.183
11A	17	1010		6.0	1006.5 - 1013.5	16.5	106.5	23.7	690	0.13	App 8.52	137.9	19.4	App 8.184
11A	18	1017		7.0	1016.2 - 1025.0	11.6	101.6	23.6	866	0.13	App 8.53	146.4	16.8	App 8.185
11A	19	1075		58.0	1070.0 - 1080.0	141.8	231.8	21.4	984	0.14	App 8.54	115.5	23.1	App 8.186
11A	20	1109		34.0	1104 - 1114	6.6	96.6	19.2	984	0.18	App 8.55	139.2	21.8	App 8.187
RCF3	1	215	219		211.0 - 221.0	44.5	134.5	15.4	984	0.41	App 8.56	133.1	14.1	App 8.188
RCF3	10	431			428.1 - 433.0	148.4	238.4	21.5	482	0.19	App 8.57	130.7	16.0	App 8.189
RCF3	11	440		9.0	436.5 - 442.9	133.7	223.7	18.8	630	0.18	App 8.58	121.6	19.3	App 8.190

Highlighted data denotes FZ in sedimentary Permo-Triassic rocks.

Table 5.2 – Results of flow zone stress analysis.

Borehole ID	Production Log Flow Zone ID	Production Log Flow Zone Top Depth (mbRT)	Production Log Flow Zone Bottom Depth (mbRT)	Flow Zone Separation (m)	Depth Stress / Fracture orientation calculated over (mbRT)	σ_{Hmin} (Degrees)	σ_{Hmax} (Degrees)	Stress Confidence (+/-)	No. Data Points	Max Stress Rose Value	Stress Figure (Appendix 8)	Mean Fracture Orientation (Degrees)	Mean Fracture Confidence (+/-)	Discontinuity Figure (Appendix 8)
RCF3	11	440			439.05 - 442.9	50.8	140.8	13.6	378	0.28	App 8.59	114.4	18.3	App 8.191
RCF3	12	463		23.0	454.0 - 464.6	63.2	153.2	20.4	1042	0.21	App 8.60	101.7	17.9	App 8.192
RCF3	12	463			454.0 - 473.0	65.5	155.5	21.4	1870	0.12	App 8.61	110.4	19.1	App 8.193
RCF3	13	476		13.0	473.0 - 481.0	27.4	117.4	19.6	786	0.18	App 8.62	116.6	13.9	App 8.194
RCF3	13	476			473.0 - 479.0	32.6	122.6	21.3	590	0.15	App 8.63	114.9	15.0	App 8.195
RCF3	14	525		49.0	520.0 - 530.0	110.9	200.9	25.7	984	0.12	App 8.64	108.2	18.5	App 8.196
RCF3	15	535		10.0	526.0 - 542.0	66.3	156.3	21.9	15574	0.15	App 8.65	104.1	26.2	App 8.197
RCF3	16	556		21.0	546.0 - 566.0	80.8	170.8	23.3	1968	0.13	App 8.66	110.6	22.9	App 8.198
RCF3	17	578		22.0	575.5 - 581.5	82.4	172.4	16.6	590	0.20	App 8.67	90.7	22.8	App 8.199
RCF3	17	583			576.0 - 580.0	85.5	175.5	15.2	394	0.21	App 8.68	12.4	5.2	App 8.200
RCF3	18	583		0.0	578.0 - 588.0	68.0	158.0	19.5	984	0.23	App 8.69	21.1	17.8	App 8.201
RCF3	19	670		87.0	663.0 - 675.0	46.6	136.6	16.4	1182	0.29	App 8.70	167.9	9.0	App 8.202
RCF3	x	702		32.0	697.0 - 706.0	53.3	143.3	20.0	886	0.22	App 8.71	90.6	16.5	App 8.203
RCF3	y	708		6.0	704.0 - 711.0	37.6	127.6	23.1	688	0.12	App 8.72	26.2	19.2	App 8.204
RCF3	20	757		49.0	747.0 - 767.0	76.3	166.3	17.8	1970	0.24	App 8.73	117.7	22.6	App 8.205
RCF3	21	761		4.0	757.6 - 765.0	53.0	143.0	14.9	728	0.28	App 8.74	123.4	13.7	App 8.206
RCF3	z	915		154.0	911.0 - 919.0	84.9	174.9	17.0	788	0.24	App 8.75	96.5	22.7	App 8.207
RCF3	22	953		38.0	948.0 - 963.0	74.1	164.1	11.6	1476	0.33	App 8.76	36.9	20.1	App 8.208
RCM1	3	85			80.0 - 90.0	134.6	224.6	18.8	984	0.22	App 8.77	134.8	17.8	App 8.209
RCM1	4	106		21.0	101.0 - 111.0	29.9	119.9	15.0	986	0.25	App 8.78	140.2	17.3	App 8.210
RCM1	5	112		6.0	107.0 - 117.0	5.1	95.1	17.5	984	0.26	App 8.79	149.5	16.8	App 8.211
RCM1	6	117		5.0	112.0 - 122.0	145.6	235.6	17.8	984	0.22	App 8.80	140.9	18.3	App 8.212
RCM1	7	125		8.0	120.0 - 130.0	112.5	202.5	17.7	984	0.23	App 8.81	142.3	17.4	App 8.213
RCM1	10	155		30.0	150.0 - 160.0	171.7	261.7	15.2	984	0.23	App 8.82	137.1	15.1	App 8.214
RCM1	11	166	168	11.0	162.0 - 172.0	104.9	194.9	17.2	986	0.23	App 8.83	134.8	14.9	App 8.215
RCM1	12	273		107.0	270.0 - 275.0	77.4	167.4	19.7	492	0.21	App 8.84	137.3	18.7	App 8.216
RCM1	13	279		6.0	275.0 - 283.0	178.5	268.5	14.9	788	0.27	App 8.85	144.4	16.4	App 8.217
RCM1	14	308		29.0	303.0 - 313.0	81.8	171.8	19.5	984	0.20	App 8.86	141.7	19.3	App 8.218
RCM1	15	325	332	17.0	324.0 - 332.0	41.5	131.5	25.3	788	0.19	App 8.87	135.7	19.1	App 8.219

Highlighted data denotes FZ in sedimentary Permo-Triassic rocks.

Table 5.2 – Results of flow zone stress analysis.

Borehole ID	Production Log Flow Zone ID	Production Log Flow Zone Top Depth (mbRT)	Production Log Flow Zone Bottom Depth (mbRT)	Flow Zone Separation (m)	Depth Stress / Fracture orientation calculated over (mbRT)	σ_{Hmin} (Degrees)	σ_{Hmax} (Degrees)	Stress Confidence (+/-)	No. Data Points	Max Stress Rose Value	Stress Figure (Appendix 8)	Mean Fracture Orientation (Degrees)	Mean Fracture Confidence (+/-)	Discontinuity Figure (Appendix 8)
RCM1	17	358	362	33.0	355.0 - 365.0	11.0	101.0	15.4	984	0.28	App 8.88	137.7	20.2	App 8.220
RCM1	18	384		26.0	379.0 - 389.0	82.4	172.4	19.2	984	0.22	App 8.89	140.2	17.4	App 8.221
RCM1	19	388	390	4.0	384.0 - 394.0	62.2	152.2	16.1	984	0.22	App 8.90	133.1	18.8	App 8.222
RCM1	21	403	404	15.0	398.5 - 408.5	166.1	256.1	22.8	984	0.16	App 8.91	133.4	19.1	App 8.223
RCM1	21	403	404		399.5 - 402.0	74.5	164.5	6.5	246	0.39	App 8.92	131.8	20.3	App 8.224
RCM1	21	403	404		402.0 - 404.3	161.3	251.3	10.8	226	0.62	App 8.93	131.4	15.9	App 8.225
RCM1	21	403	404		404.3 - 409.5	43.8	133.8	18.8	512	0.21	App 8.94	133.0	16.2	App 8.226
RCM1	22	414		11.0	409.0 - 419.0	158.9	248.9	19.3	986	0.19	App 8.95	127.6	14.8	App 8.227
RCM1	23	422		8.0	417.0 - 427.0	139.2	229.2	18.5	984	0.23	App 8.96	130.4	13.9	App 8.228
RCM1	24	468		46.0	465.5 - 470.0	39.7	129.7	20.5	444	0.19	App 8.97	134.0	23.5	App 8.229
RCM1	25	500		32.0	496.0 - 504.0	132.5	222.5	22.4	788	0.12	App 8.98	121.0	20.9	App 8.230
RCM1	26	693		193.0	685.0 - 700.0	59.7	149.7	21.6	1476	0.15	App 8.99	109.4	23.2	App 8.231
RCM1	27	838		145.0	833.0 - 843.0	71.1	161.1	19.7	984	0.20	App 8.100	81.1	21.6	App 8.232
RCM1	28	938		100.0	932.0 - 946.0	71.4	161.4	12.6	1378	0.32	App 8.101	143.8	19.9	App 8.233
RCM1	29	947		9.0	938.0 - 957.0	68.1	158.1	13.3	1870	0.30	App 8.102	43.1	23.9	App 8.234
RCM1	30	963		16.0	958.0 - 968.0	77.9	167.9	11.0	984	0.33	App 8.103	59.3	24.2	App 8.235
RCM2	1	66	68		62.0 - 72.0	52.3	142.3	20.2	984	0.25	App 8.104	127.5	11.8	App 8.236
RCM2	2	75	76	9.0	70.5 - 80.5	39.8	129.8	16.0	986	0.21	App 8.105	124.7	19.5	App 8.237
RCM2	3	107		32.0	97.0 - 117.0	46.8	136.8	16.3	1968	0.31	App 8.106	130.3	15.9	App 8.238
RCM2	5	128	129	21.0	124.0 - 138.5	54.3	144.3	10.4	1428	0.53	App 8.107	133.2	14.9	App 8.239
RCM2	6	134	135	6.0	130.0 - 138.5	55.5	145.5	9.2	836	0.67	App 8.108	135.2	17.0	App 8.240
RCM2	7	146	148	12.0	143.0 - 153.0	54.7	144.7	18.6	986	0.32	App 8.109	150.0	17.9	App 8.241
RCM2	8	155	156	9.0	150.5 - 160.5	51.1	141.1	16.4	986	0.33	App 8.110	138.5	18.6	App 8.242
RCM2	11	228.5		73.5	218.5 - 230.0	56.3	146.3	15.8	1132	0.28	App 8.111	132.4	19.6	App 8.243
RCM2	11	228.5			229.7 - 236.0	15.7	105.7	9.4	620	0.36	App 8.112	135.1	20.8	App 8.244
RCM2	12	227	230		238.0 - 248.0	77.1	167.1	17.1	984	0.27	App 8.113	121.1	14.5	App 8.245
RCM2	13	243		16.0	261.0 - 271.0	151.1	241.1	3.3	986	0.61	App 8.114	142.7	15.5	App 8.246
RCM2	14	266		23.0	271.0 - 281.0	144.9	234.9	3.8	984	0.78	App 8.115	138.7	11.8	App 8.247
RCM2	15	276		10.0	300.0 - 308.5	56.9	146.9	5.8	836	0.50	App 8.116	146.2	20.2	App 8.248

Highlighted data denotes FZ in sedimentary Permo-Triassic rocks.

Table 5.2 – Results of flow zone stress analysis.

Borehole ID	Production Log Flow Zone ID	Production Log Flow Zone Top Depth (mbRT)	Production Log Flow Zone Bottom Depth (mbRT)	Flow Zone Separation (m)	Depth Stress / Fracture orientation calculated over (mbRT)	σ_{Hmin} (Degrees)	σ_{Hmax} (Degrees)	Stress Confidence (+/-)	No. Data Points	Max Stress Rose Value	Stress Figure (Appendix 8)	Mean Fracture Orientation (Degrees)	Mean Fracture Confidence (+/-)	Discontinuity Figure (Appendix 8)
RCM2	15	276			301.0 - 304.3	139.1	229.1	17.1	324	0.31	App 8.117	147.8	17.8	App 8.249
RCM2	16	302	305	26.0	333.0 - 343.0	24.6	114.6	15.5	984	0.37	App 8.118	127.4	17.9	App 8.250
RCM2	17	338		36.0	371.0 - 381.0	20.0	110.0	18.7	986	0.19	App 8.119	130.1	15.1	App 8.251
RCM2	19	386		48.0	404.5 - 414.0	161.1	251.1	26.6	936	0.14	App 8.120	131.0	17.0	App 8.252
RCM2	20	408	410	22.0	416.0 - 422.0	78.2	168.2	24.3	590	0.20	App 8.121	122.9	18.3	App 8.253
RCM2	21	418	420	10.0	444.0 - 455.0	111.7	201.7	20.7	1082	0.27	App 8.122	116.5	21.0	App 8.254
RCM2	22	448	450	30.0	490.2 - 498.0	151.9	241.9	20.5	766	0.19	App 8.123	90.8	19.2	App 8.255
RCM2	23	494	495	46.0	518.0 - 523.5	160.2	250.2	18.6	540	0.14	App 8.124	71.5	16.0	App 8.256
RCM2	24	520	522	26.0	540.0 - 542.0	128.5	218.5	20.8	198	0.27	App 8.125	45.8	15.6	App 8.257
RCM2	25	541		21.0	540.0 - 545.0	134.3	224.3	19.5	492	0.16	App 8.126	52.6	18.3	App 8.258
RCM2	25	541			543.2 - 545.0	140.7	230.7	17.4	176	0.26	App 8.127	67.8	16.0	App 8.259
RCM2	26	544		3.0	693.0 - 703.0	164.6	254.6	23.2	984	0.13	App 8.128	141.9	18.7	App 8.260
RCM2	26	544			697.5 - 700.0	140.5	230.5	19.6	246	0.25	App 8.129	64.4	24.4	App 8.261
RCM2	27	698		154.0	713.0 - 724.0	75.5	165.5	17.3	1082	0.26	App 8.130	142.9	21.1	App 8.262
RCM2	28	717		19.0	884.0 - 904.0	75.2	165.2	16.0	1970	0.23	App 8.131	159.3	14.3	App 8.263
RCM2	29	894		177.0	919.0 - 929.0	83.2	173.2	10.2	984	0.35	App 8.132	81.5	21.1	App 8.264

Highlighted data denotes FZ in sedimentary Permo-Triassic rocks.

Flow Zone ID	low Zone Depth (mbR)	Depth (mbRT)	σ_{Hmax}	Stressit Output Data File	No. Data Points	Stressit Output Plot File
1	198.0	193.0 - 203.0	217.3	s2_fz1_ssit_193_203.dat	70	Figure App 10.1
2	207.5	202.5 - 212.5	192.8	s2_fz2_ssit_202_212.dat	60	Figure App 10.2
3	211.0	206.0 - 216.0	184.5	s2_fz3_ssit_206_216.dat	59	Figure App 10.3
4	216.5	211.5 - 221.5	172.4	s2_fz4_ssit_211_221.dat	66	Figure App 10.4
5	233.0	228.0 - 238.0	133.4	s2_fz5_ssit_228_238.dat	50	Figure App 10.5
6	242.0	237.0 - 247.0	110.8	s2_fz6_ssit_237_247.dat	39	Figure App 10.6
11	384.0	379.0 - 389.0	90.5	s2_fz11_ssit_379_389.dat	77	Figure App 10.7
12	547.0	539.0 - 550.0	248.4	s2_fz12_ssit_539_550.dat	61	Figure App 10.8
13	573.0	568.0 - 575.5	178.7	s2_fz13_ssit_568_575.dat	38	Figure App 10.9
14	607.0	605.0 - 610.0	96.9	s2_fz14_ssit_605_610.dat	38	Figure App 10.10
15	622.5	615.0 - 622.5	234.2	s2_fz15_ssit_615_622.dat	50	Figure App 10.11
15	622.5	622.5 - 627.0	184.5	s2_fz15_ssit_622_627.dat	35	Figure App 10.12
15	622.5	615.0 - 627.0	184.9	s2_fz15_ssit_615_627.dat	85	Figure App 10.13
17	735.5	732.0 - 742.0	157.6	s2_fz17_ssit_732_742.dat	62	Figure App 10.14
18	743.5	733.5 - 753.5	151.7	s2_fz18_ssit_733_753.dat	130	Figure App 10.15
19	803.0	800.0 - 803.98	214.0	s2_fz19_ssit_800_804.dat	27	Figure App 10.16
19	803.0	801.5 - 804.0	222.5	s2_fz19_ssit_801_804.dat	18	Figure App 10.17
19	803.0	804.0 - 813.0	131.9	s2_fz19_ssit_804_813.dat	38	Figure App 10.18
20	937.5	932.0 - 941.0	127.2	s2_fz20_ssit_932_941.dat	63	Figure App 10.19
21	967.0	961.5 - 974.0	159.9	s2_fz21_ssit_961_974.dat	72	Figure App 10.20
22	1015.5	1005.5 - 1025.5	139.7	s2_fz22_ssit_1005_1025.dat	86	Figure App 10.21
24	1148.0	1142.0 - 1158.0	189.3	s2_fz24_ssit_1142_1158.dat	109	Figure App 10.22
24	1148.0	1148.5 - 1153.0	118.7	s2_fz24_ssit_1148_1153.dat	35	Figure App 10.23
25	1597.0	1590.0 - 1602.0	203.2	s2_fz25_ssit_1590_1602.dat	95	Figure App 10.24
25	1597.0	1590.0 - 1594.5	195.7	s2_fz25_ssit_1590_1594.dat	41	Figure App 10.25
25	1597.0	1594.5 - 1602.0	220.3	s2_fz25_ssit_1594_1602.dat	54	Figure App 10.26

Table 6.2a – Result of Flow Zone Stressit analysis for Sellafield borehole 2.

Flow Zone ID	Flow Zone Depth (mbRT)	Depth (mbRT)	σ_{tmax}	Stressit Output Data File	No. Data Points	Stressit Output Plot File
1	542.5	537.5 - 547.5	171.7	s5_fz1_ssit_537_547.dat	56	Figure App 10.27
2	596.0	591.0 - 601.0	151.1	s5_fz2_ssit_591_601.dat	59	Figure App 10.28
3	746.5	736.5 - 756.5	147.4	s5_fz3_ssit_736_756.dat	92	Figure App 10.29
3	746.5	742.0 - 749.0	182.0	s5_fz3_ssit_742_749.dat	29	Figure App 10.30
3	746.5	741.5 - 751.5	185.6	s5_fz3_ssit_741_751.dat	38	Figure App 10.31
4	754.8	749.5 - 758.0	247.8	s5_fz4_ssit_749_758.dat	31	Figure App 10.32
5	813.5	804.0 - 818.0	157.6	s5_fz5_ssit_804_818.dat	44	Figure App 10.33
6	841.5	836.5 - 846.5	176.8	s5_fz6_ssit_836_846.dat	31	Figure App 10.34
7	887.5	882.5 - 892.5	118.9	s5_fz7_ssit_882_892.dat	35	Figure App 10.35

Table 6.2b – Result of Flow Zone Stressit analysis for Sellafield borehole 5.

Flow Zone ID	Flow Zone Depth (mbRT)	Depth (mbRT)	σ_{Hmax}	Stressit Output Data File	No. Data Points	Stressit Output Plot File
1	232.0	227.0 - 237.0	223.5	s8a_fz1_ssit_227_237.dat	47	Figure App 10.36
2	352.0	339.0 - 364.5	253.9	s8a_fz2_ssit_339_364.dat	255	Figure App 10.37
3	696.0	692.0 - 701.0	118.8	s8a_fz3_ssit_692_701.dat	62	Figure App 10.38
4	736.0	734.0 - 738.0	176.3	s8a_fz4_ssit_734_738.dat	22	Figure App 10.39
5	758.0	755.2 - 760.0	264.7	s8a_fz5_ssit_755_760.dat	40	Figure App 10.40
6	892.0	883.0 - 895.5	255.6	s8a_fz6_ssit_883_895.dat	105	Figure App 10.41
7	952.0	952.0 - 956.0	192.2	s8a_fz7_ssit_952_956.dat	18	Figure App 10.42

Table 6.2c – Result of Flow Zone Stressit analysis for Sellafield borehole 8A.

Flow Zone ID	Flow Zone Depth (mbRT)	Depth (mbRT)	σ_{Hmax}	Stressit Output Data File	No. Data Points	Stressit Output Plot File
13	879.0	878.5 - 885.0	95.6	s11a_fz16_ssit_878_885.dat	12	Figure App 10.43
13	879.0	869.0 - 889.0	107.5	s11a_fz16_ssit_869_889.dat	26	Figure App 10.44
14	979.0	973.0 - 978.0	211.1	s11a_fz17_ssit_973_978.dat	17	Figure App 10.45
14	979.0	978.0 - 978.5	259.5	s11a_fz17_ssit_978_978.dat	4	Figure App 10.46
14	979.0	978.0 - 978.6	260.9	s11a_fz17_ssit_978_979.dat	4	Figure App 10.47
14	979.0	978.5 - 983.0	199.3	s11a_fz17_ssit_978_983.dat	16	Figure App 10.48
14	979.0	973.0 - 983.0	198.6	s11a_fz17_ssit_973_983.dat	37	Figure App 10.49
15	995.0	993.0 - 997.5	254.8	s11a_fz18_ssit_993_997.dat	13	Figure App 10.50
16	1004.0	999.0 - 1009.0	101.5	s11a_fz19_ssit_999_1009.dat	47	Figure App 10.51
17	1010.0	1006.5 - 1013.5	106.5	s11a_fz20_ssit_1006_1013.dat	44	Figure App 10.52
18	1017.0	1016.2 - 1025.0	101.6	s11a_fz21_ssit_1016_1025.dat	36	Figure App 10.53
19	1075.0	1070.0 - 1080.0	231.8	s11a_fz22_ssit_1070_1080.dat	41	Figure App 10.54
20	1109.0	1104 - 1114	96.6	s11a_fz23_ssit_1104_1114.dat	61	Figure App 10.55

Table 6.2d – Result of Flow Zone Stressit analysis for Sellafeld borehole 11A.

Flow Zone ID	Flow Zone Depth (mbRT)	Depth (mbRT)	σ_{Tmax}	Stressit Output Data File	No. Data Points	Stressit Output Plot File
1	217.0	211.0 - 221.0	134.5	rcf3_fz1_ssit_211_221.dat	14	Figure App 10.56
10	431.0	428.1 - 433.0	238.4	rcf3_fz10_ssit_428_433.dat	28	Figure App 10.57
11	440.0	436.5 - 442.9	223.7	rcf3_fz11_ssit_436_442.dat	44	Figure App 10.58
11	440.0	439.05 - 442.9	140.8	rcf3_fz11_ssit_439_442.dat	24	Figure App 10.59
12	463.0	454.0 - 464.6	153.2	rcf3_fz12_ssit_454_464.dat	17	Figure App 10.60
12	463.0	454.0 - 473.0	155.5	rcf3_fz12_ssit_454_473.dat	42	Figure App 10.61
13	476.0	473.0 - 481.0	117.4	rcf3_fz13_ssit_473_481.dat	24	Figure App 10.62
13	476.0	473.0 - 479.0	122.6	rcf3_fz13_ssit_473_479.dat	18	Figure App 10.63
14	525.0	520.0 - 530.0	200.9	rcf3_fz14_ssit_520_530.dat	33	Figure App 10.64
15	535.0	528.0 - 542.0	158.3	rcf3_fz15_ssit_526_542.dat	80	Figure App 10.65
16	556.0	546.0 - 566.0	170.8	rcf3_fz16_ssit_546_566.dat	92	Figure App 10.66
17	578.0	575.5 - 581.5	172.4	rcf3_fz17_ssit_575_581.dat	34	Figure App 10.67
17	578.0	576.0 - 580.0	175.5	rcf3_fz17_ssit_576_580.dat	22	Figure App 10.68
18	583.0	578.0 - 588.0	158.0	rcf3_fz18_ssit_578_588.dat	49	Figure App 10.69
19	670.0	663.0 - 675.0	136.6	rcf3_fz19_ssit_663_675.dat	69	Figure App 10.70
x	702.0	697.0 - 706.0	143.3	rcf3_fzx_ssit_697_706.dat	39	Figure App 10.71
y	708.0	704.0 - 711.0	127.6	rcf3_fzy_ssit_704_711.dat	38	Figure App 10.72
20	757.0	747.0 - 767.0	166.3	rcf3_fz20_ssit_747_767.dat	66	Figure App 10.73
21	781.0	757.6 - 765.0	143.0	rcf3_fz21_ssit_757_765.dat	31	Figure App 10.74
z	915.0	911.0 - 919.0	174.9	rcf3_fzz_ssit_911_919.dat	45	Figure App 10.75
22	953.0	948.0 - 963.0	164.1	rcf3_fz22_ssit_948_963.dat	62	Figure App 10.76

Table 6.2e – Result of Flow Zone Stressit analysis for Sellafield borehole RCF3.

Flow Zone ID	Flow Zone Depth (mbRT)	Depth (mbRT)	σ_{Hmax}	Stressit Output Data File	No. Data Points	Stressit Output Plot File
3	85.0	80.0 - 90.0	224.6	rcm1_fz3_ssit_80_90.dat	74	Figure App 10.77
4	106.0	101.0 - 111.0	119.9	rcm1_fz4_ssit_101_111.dat	85	Figure App 10.78
5	112.0	107.0 - 117.0	95.1	rcm1_fz5_ssit_107_117.dat	77	Figure App 10.79
6	117.0	112.0 - 122.0	235.6	rcm1_fz6_ssit_112_122.dat	81	Figure App 10.80
7	125.0	120.0 - 130.0	202.5	rcm1_fz7_ssit_120_130.dat	85	Figure App 10.81
10	155.0	150.0 - 160.0	261.7	rcm1_fz10_ssit_150_160.dat	77	Figure App 10.82
11	167.0	162.0 - 172.0	194.9	rcm1_fz11_ssit_162_172.dat	92	Figure App 10.83
12	273.0	270.0 - 275.0	167.4	rcm1_fz12_ssit_270_275.dat	47	Figure App 10.84
13	279.0	275.0 - 283.0	268.5	rcm1_fz13_ssit_275_283.dat	70	Figure App 10.85
14	308.0	303.0 - 313.0	171.8	rcm1_fz14_ssit_303_313.dat	86	Figure App 10.86
15	328.5	324.0 - 332.0	131.5	rcm1_fz15_ssit_324_332.dat	61	Figure App 10.87
17	360.0	355.0 - 365.0	101.0	rcm1_fz17_ssit_355_365.dat	86	Figure App 10.88
18	384.0	379.0 - 389.0	172.4	rcm1_fz18_ssit_379_389.dat	72	Figure App 10.89
19	389.0	384.0 - 394.0	152.2	rcm1_fz19_ssit_384_394.dat	68	Figure App 10.90
21	403.5	398.5 - 408.5	256.1	rcm1_fz21_ssit_398_408.dat	67	Figure App 10.91
21	403.5	399.5 - 402.0	164.5	rcm1_fz21_ssit_399_402.dat	15	Figure App 10.92
21	403.5	402.0 - 404.3	251.3	rcm1_fz21_ssit_402_409.dat	18	Figure App 10.93
21	403.5	404.3 - 409.5	133.8	rcm1_fz21_ssit_404_409.dat	36	Figure App 10.94
22	414.0	409.0 - 419.0	248.9	rcm1_fz22_ssit_409_419.dat	73	Figure App 10.95
23	422.0	417.0 - 427.0	229.2	rcm1_fz23_ssit_417_427.dat	72	Figure App 10.96
24	468.0	465.5 - 470.0	129.7	rcm1_fz24_ssit_465_470.dat	10	Figure App 10.97
25	500.0	496.0 - 504.0	222.5	rcm1_fz25_ssit_496_504.dat	26	Figure App 10.98
26	693.0	685.0 - 700.0	149.7	rcm1_fz26_ssit_685_700.dat	153	Figure App 10.99
27	838.0	833.0 - 843.0	161.1	rcm1_fz27_ssit_833_843.dat	88	Figure App 10.100
28	938.0	932.0 - 946.0	161.4	rcm1_fz28_ssit_932_946.dat	122	Figure App 10.101
29	947.0	938.0 - 957.0	158.1	rcm1_fz29_ssit_938_957.dat	161	Figure App 10.102
30	963.0	958.0 - 968.0	167.9	rcm1_fz30_ssit_958_968.dat	80	Figure App 10.103

Table 6.2f – Result of Flow Zone Stressit analysis for Sellafeld borehole RCM1.

Flow Zone ID	Flow Zone Depth (mbRT)	Depth (mbRT)	σ_{Hmax}	Stressit Output Data File	No. Data Points	Stressit Output Plot File
1	67.0	62.0 - 72.0	142.3	rcm2_fz1_ssit_62_72.dat	47	Figure App 10.104
2	75.5	70.5 - 80.5	129.8	rcm2_fz2_ssit_70_80.dat	51	Figure App 10.105
3	107.0	97.0 - 117.0	136.8	rcm2_fz3_ssit_97_117.dat	91	Figure App 10.106
5	128.5	124.0 - 138.5	144.3	rcm2_fz5_ssit_124_138.dat	69	Figure App 10.107
6	134.5	130.0 - 138.5	145.5	rcm2_fz6_ssit_130_138.dat	40	Figure App 10.108
7	147.0	143.0 - 153.0	144.7	rcm2_fz7_ssit_143_153.dat	44	Figure App 10.109
8	155.5	150.5 - 160.5	141.1	rcm2_fz8_ssit_150_160.dat	50	Figure App 10.110
11	228.5	218.5 - 230.0	146.3	rcm2_fz11_ssit_218_230.dat	72	Figure App 10.111
11	228.5	229.7 - 236.0	105.7	rcm2_fz11_ssit_229_236.dat	29	Figure App 10.112
12	243.0	238.0 - 248.0	167.1	rcm2_fz12_ssit_238_248.dat	59	Figure App 10.113
13	266.0	261.0 - 271.0	241.1	rcm2_fz13_ssit_261_271.dat	42	Figure App 10.114
14	276.0	271.0 - 281.0	234.9	rcm2_fz14_ssit_271_281.dat	46	Figure App 10.115
15	303.5	300.0 - 308.5	146.9	rcm2_fz15_ssit_300_308.dat	38	Figure App 10.116
15	303.5	301.0 - 304.3	229.1	rcm2_fz15_ssit_301_304.dat	14	Figure App 10.117
16	338.0	333.0 - 343.0	114.6	rcm2_fz16_ssit_333_343.dat	51	Figure App 10.118
17	376.0	371.0 - 381.0	110.0	rcm2_fz17_ssit_371_381.dat	59	Figure App 10.119
19	409.0	404.5 - 414.0	251.1	rcm2_fz19_ssit_404_414.dat	60	Figure App 10.120
20	419.0	416.0 - 422.0	168.2	rcm2_fz20_ssit_416_422.dat	28	Figure App 10.121
21	449.0	444.0 - 455.0	201.7	rcm2_fz21_ssit_444_455.dat	55	Figure App 10.122
22	494.5	490.2 - 498.0	241.9	rcm2_fz22_ssit_490_498.dat	14	Figure App 10.123
23	521.0	518.0 - 523.5	250.2	rcm2_fz23_ssit_518_523.dat	10	Figure App 10.124
24	541.0	540.0 - 542.0	218.5	rcm2_fz24_ssit_540_542.dat	9	Figure App 10.125
25	544.0	540.0 - 545.0	224.3	rcm2_fz25_ssit_540_545.dat	15	Figure App 10.126
25	544.0	543.2 - 545.0	230.7	rcm2_fz25_ssit_543_545.dat	5	Figure App 10.127
26	698.0	693.0 - 703.0	254.6	rcm2_fz26_ssit_693_703.dat	72	Figure App 10.128
26	698.0	697.5 - 700.0	230.5	rcm2_fz26_ssit_697_700.dat	13	Figure App 10.129
27	717.0	713.0 - 724.0	165.5	rcm2_fz27_ssit_713_724.dat	70	Figure App 10.130
28	894.0	884.0 - 904.0	165.2	rcm2_fz28_ssit_884_904.dat	165	Figure App 10.131
29	924.0	919.0 - 929.0	173.2	rcm2_fz29_ssit_919_929.dat	50	Figure App 10.132

Table 6.2g – Result of Flow Zone Stressit analysis for Sellafield borehole RCM2.

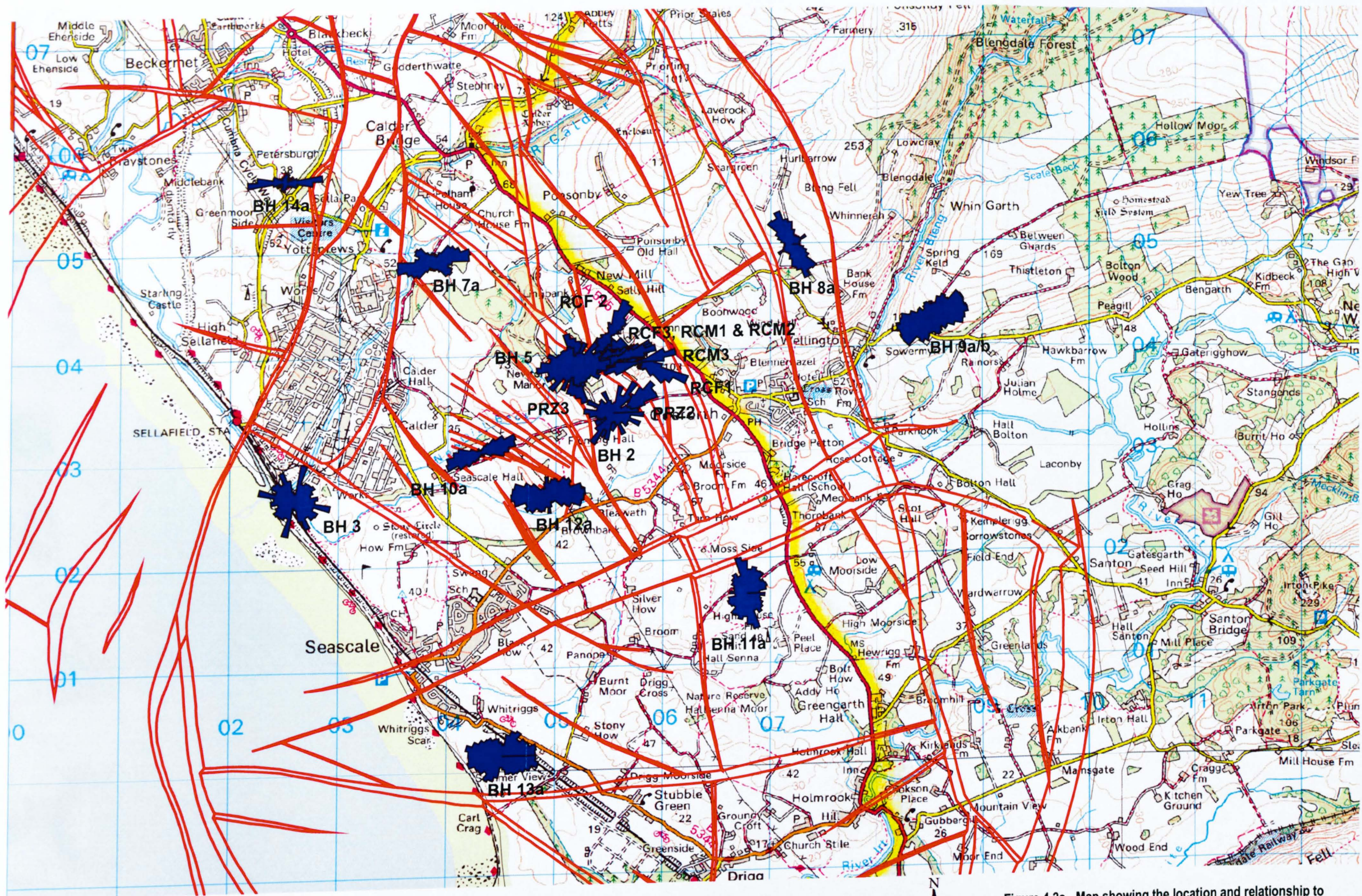


Figure 4.2a - Map showing the location and relationship to the geological structure of the breakout (σ_{min}) results from the in situ stress investigation of the top one hundred meters of the BVG in the site area at Sellafield.

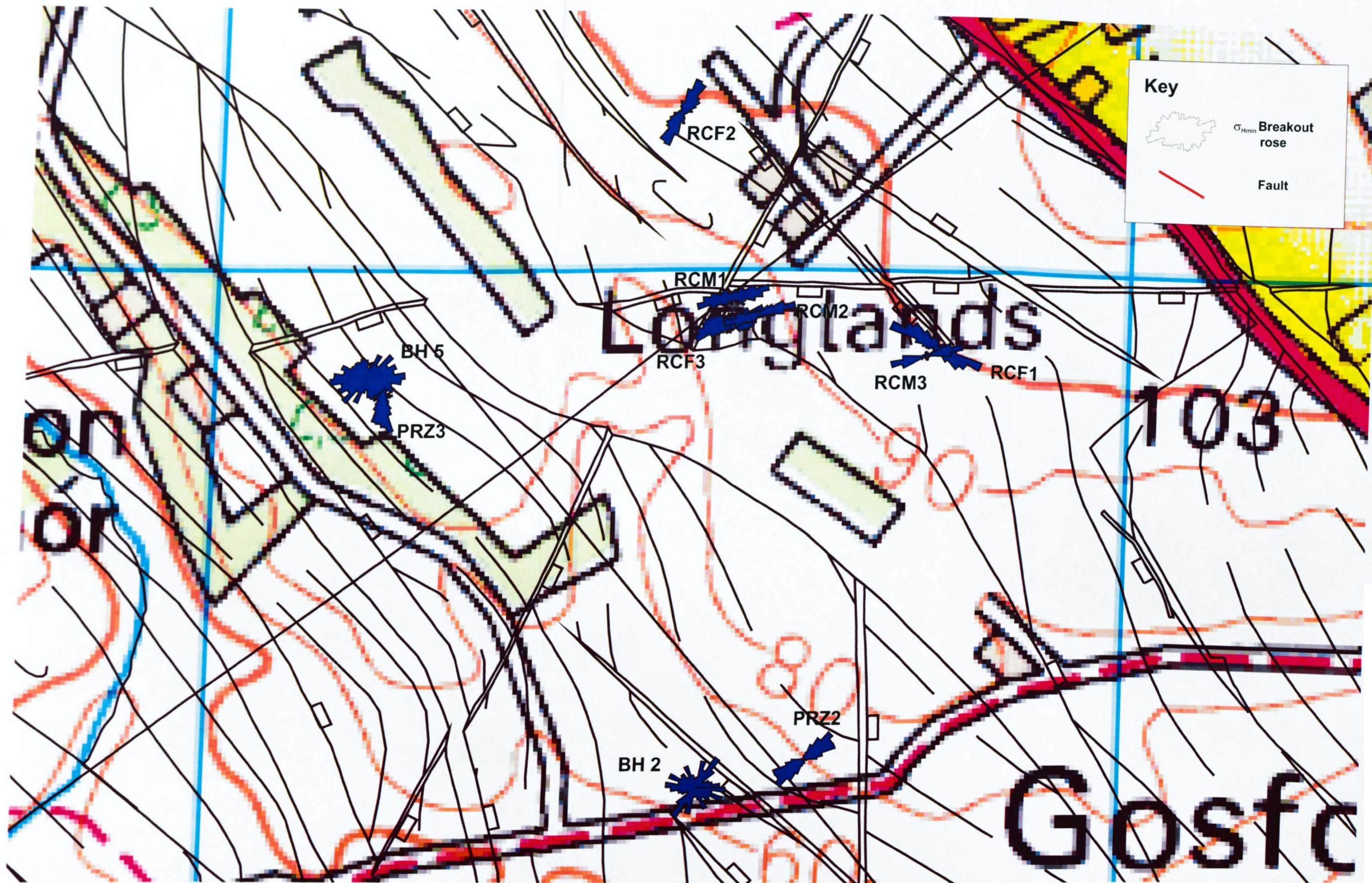
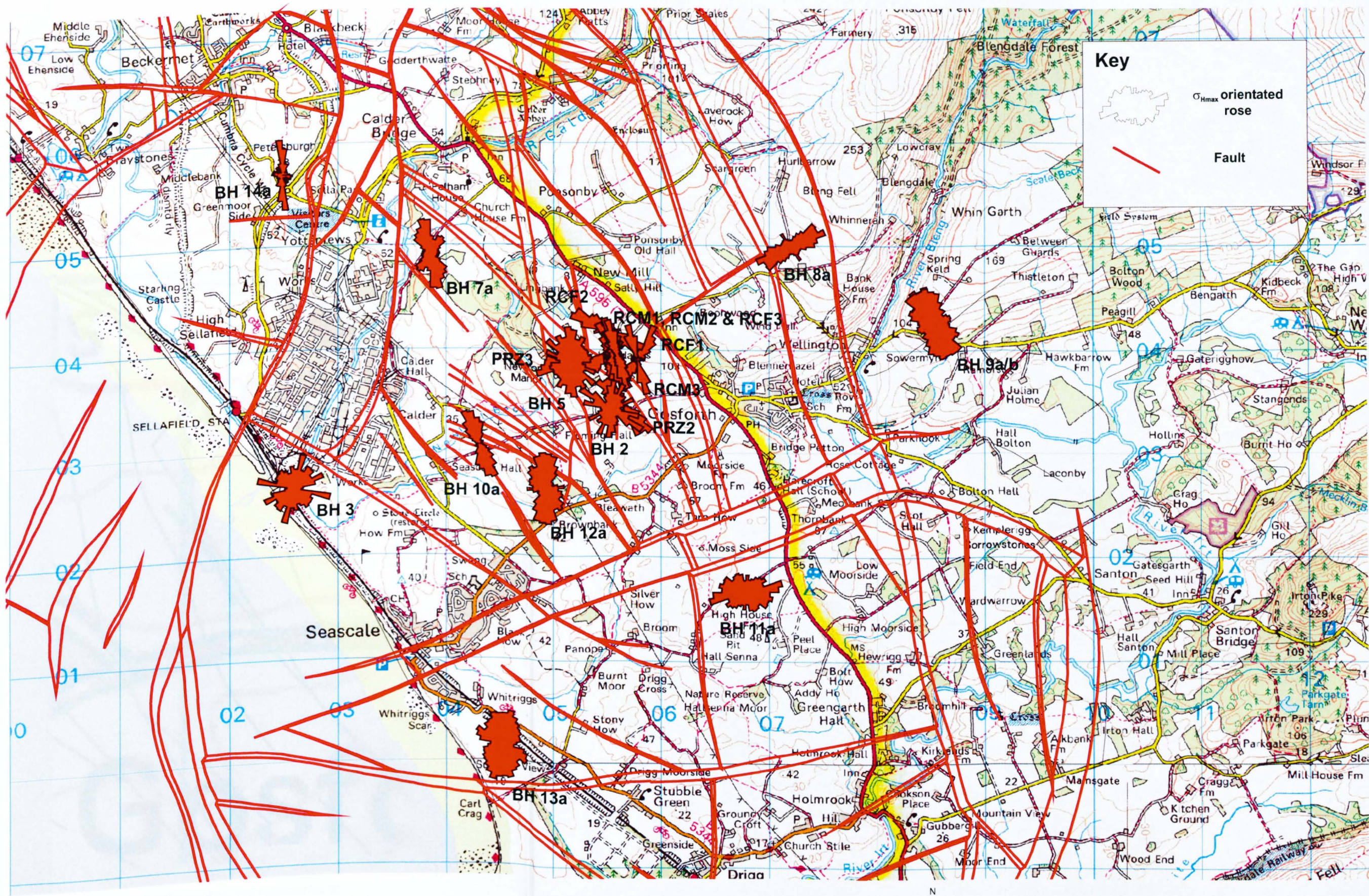


Figure 4.2b - Map showing the location and relationship to the geological structure of the breakout (σ_{Hmin}) results from the *in situ* stress investigation of the top one hundred meters of the BVG in the PRZ area.



Key

 σ_{Hmax} orientated rose

 Fault

Figure 4.3a - Map showing the location and relationship to the geological structure of the σ_{Hmax} orientated breakout results from the *in situ* stress investigation of the top one hundred meters of the BVG in the site area.

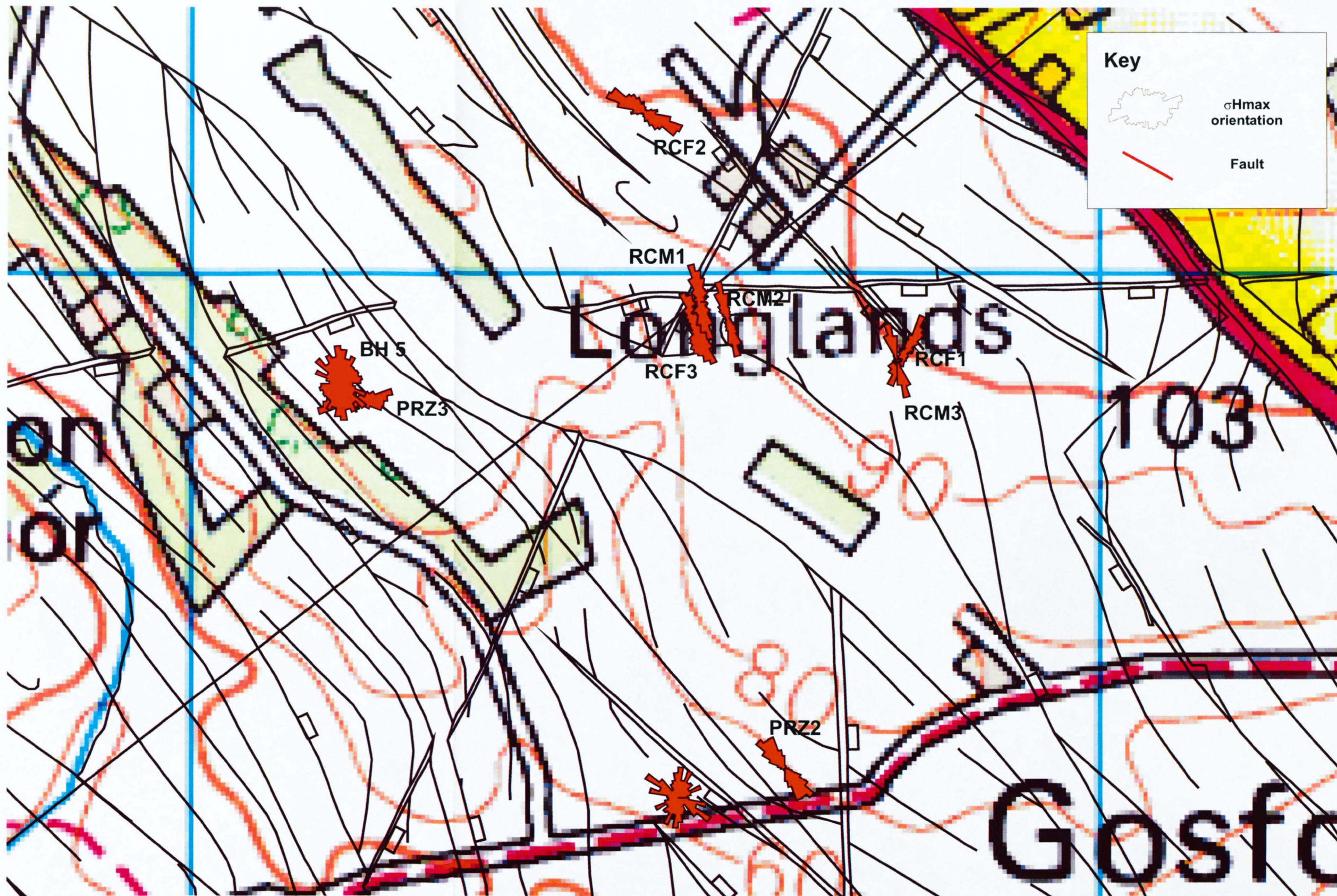


Figure 4.3b - Map showing the location and relationship to the geological structure of the σ_{Hmax} orientated breakout results from the *in situ* stress investigation of the top one hundred meters of the BVG in the PRZ area.

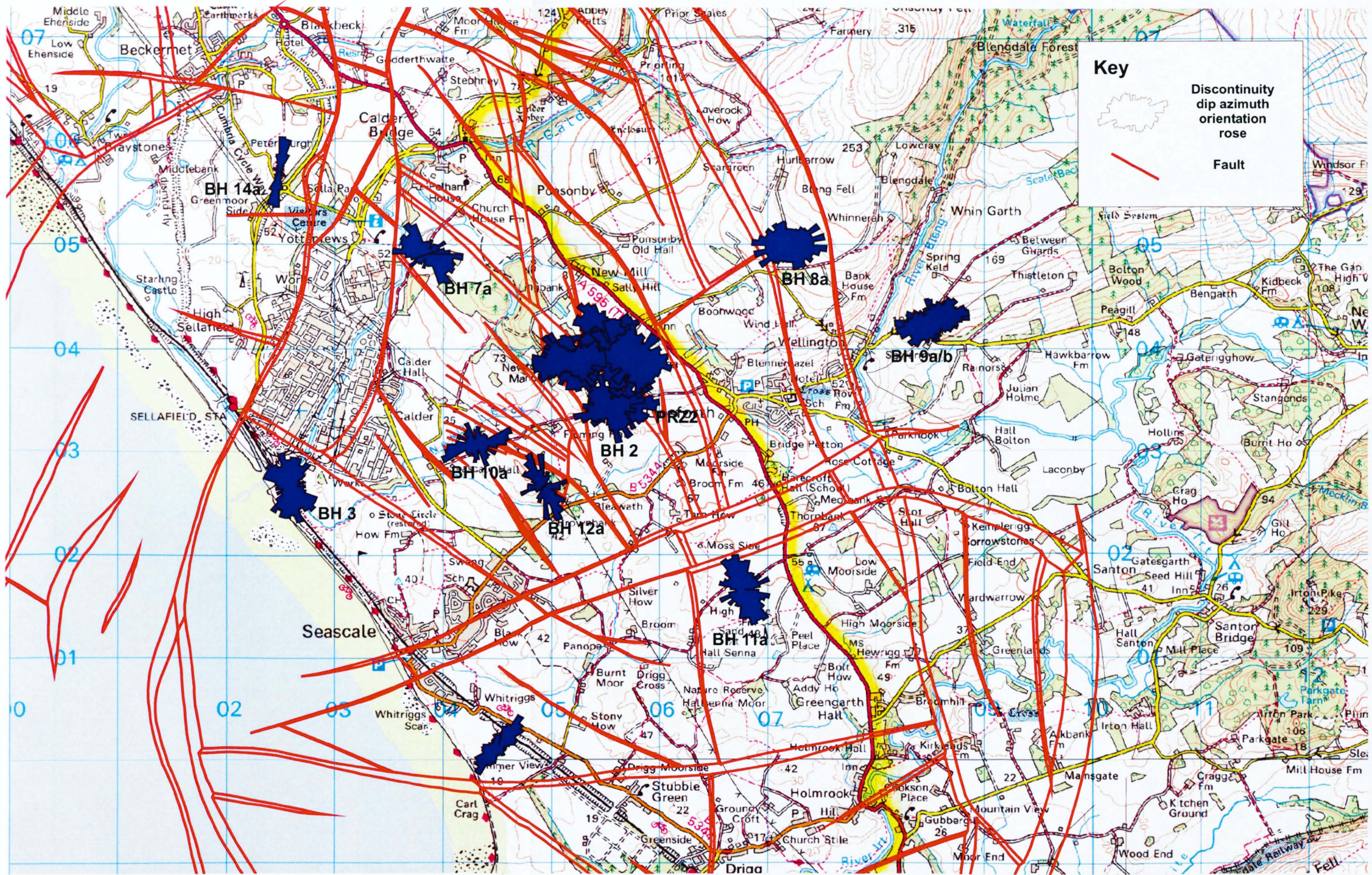


Figure 4.4a - Map showing the location and relationship to the geological structure of the discontinuity dip azimuth orientation rose plots from the main investigation of the top one hundred meters of the BVG in the site area.

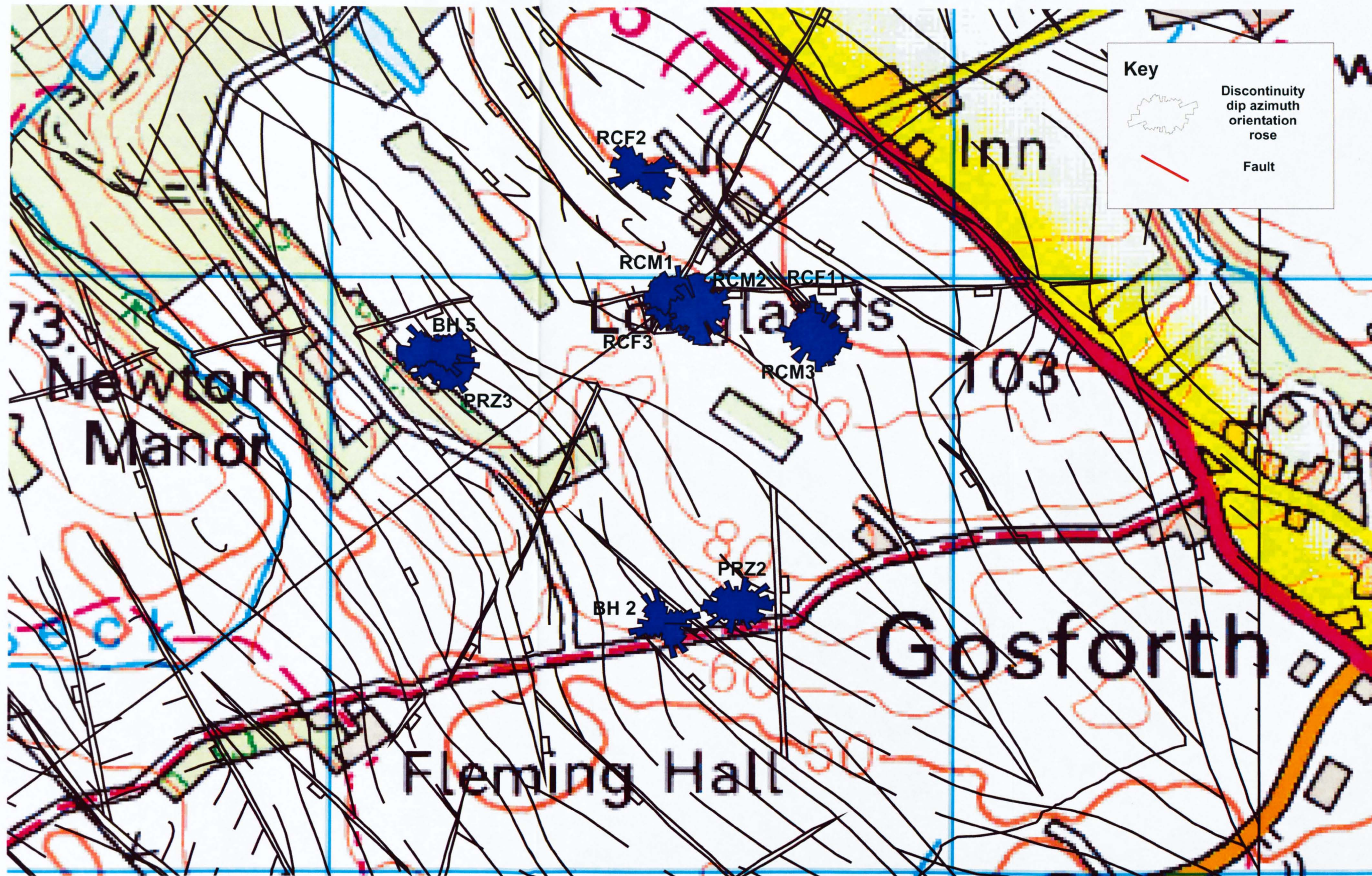


Figure 4.4b - Map showing the location and relationship to the geological structure of the discontinuity dip azimuth orientation rose plots from the investigation of the top one hundred meters of the BVG in the PRZ area.

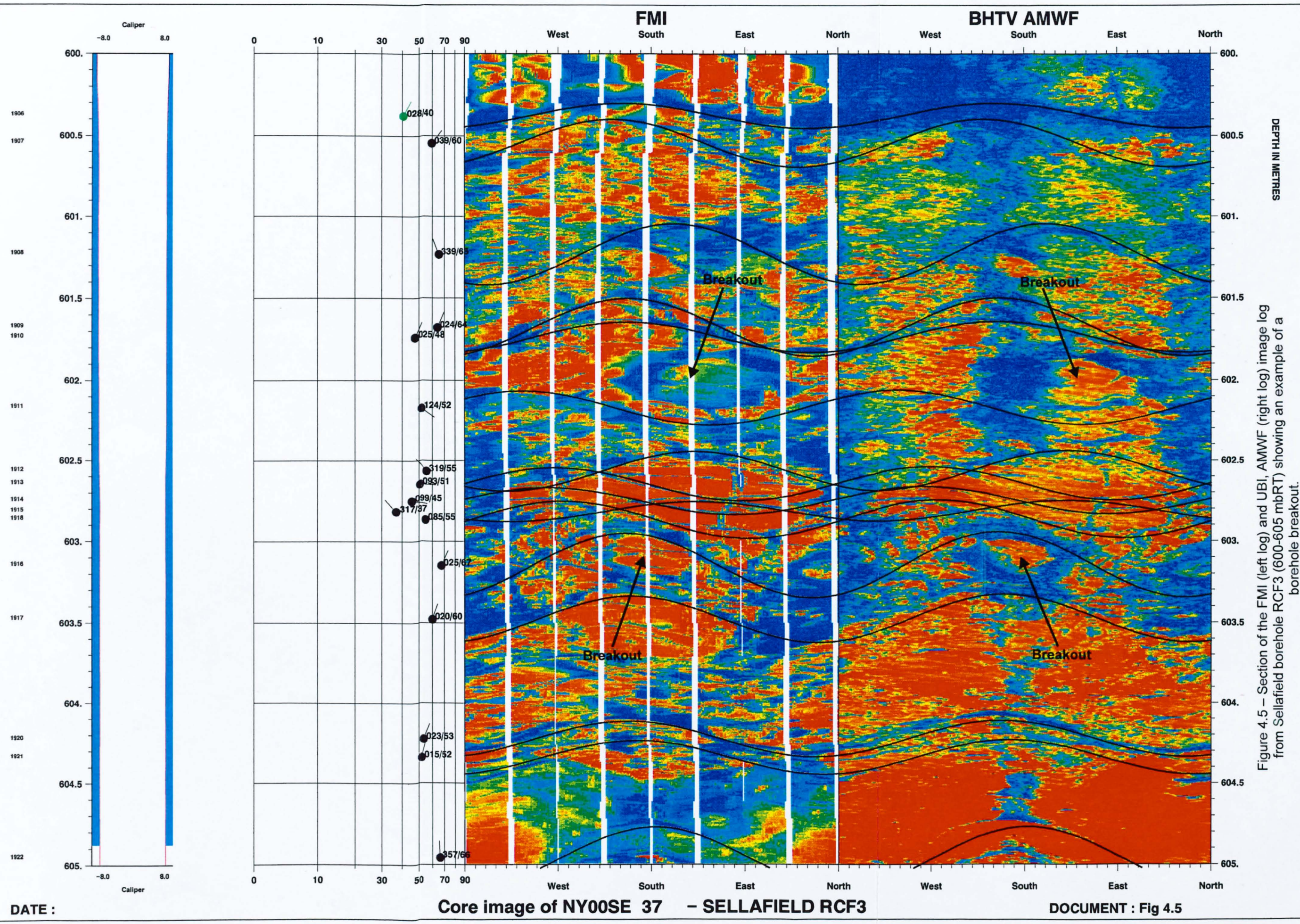


Figure 4.5 – Section of the FMI (left log) and UBI, AMWF (right log) image log from Sellafield borehole RCF3 (600-605 mbRT) showing an example of a borehole breakout.

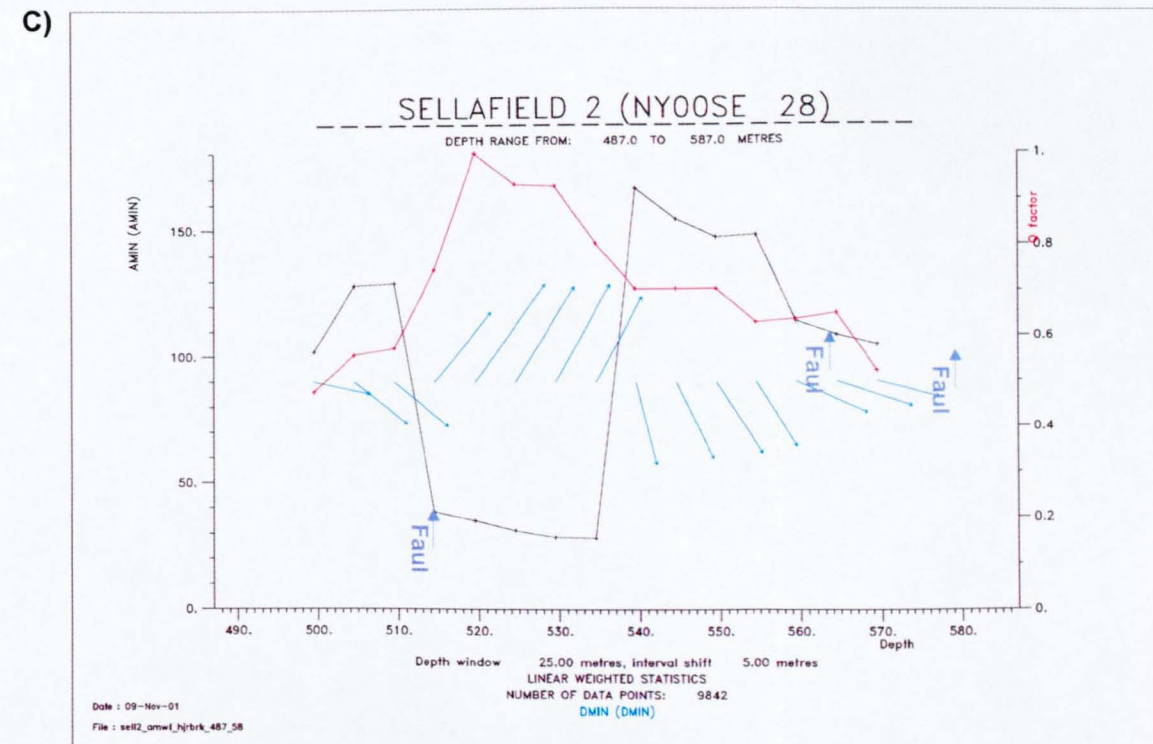
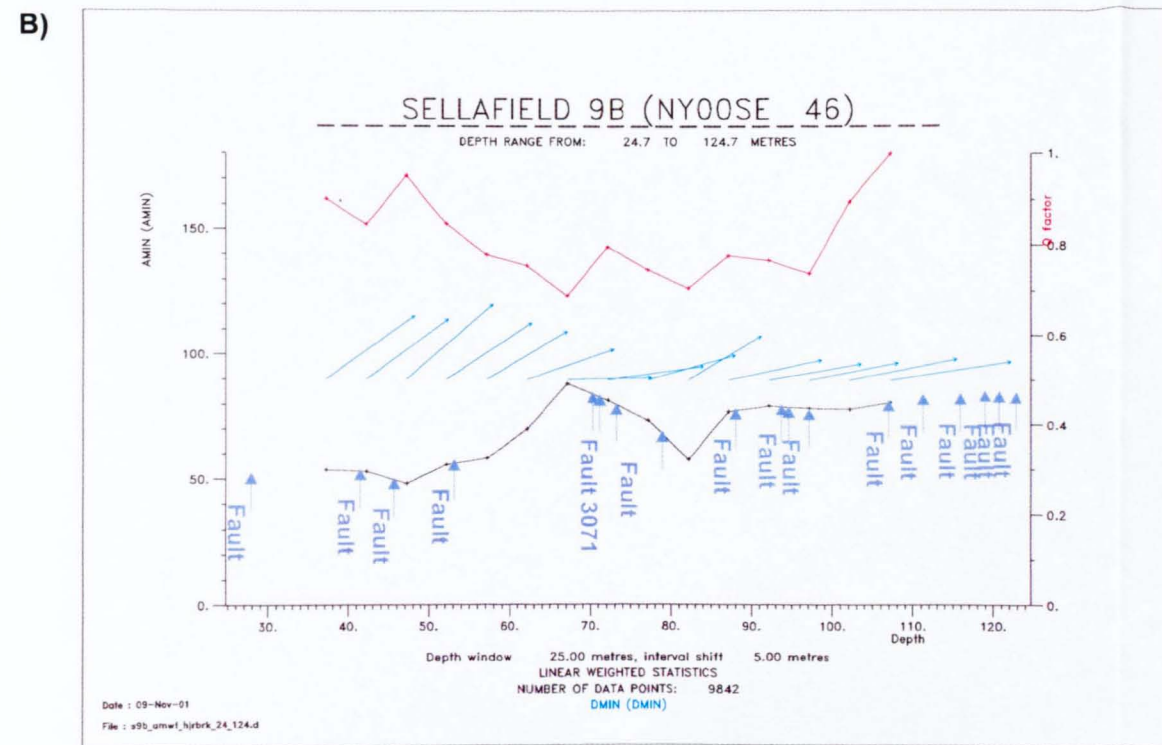
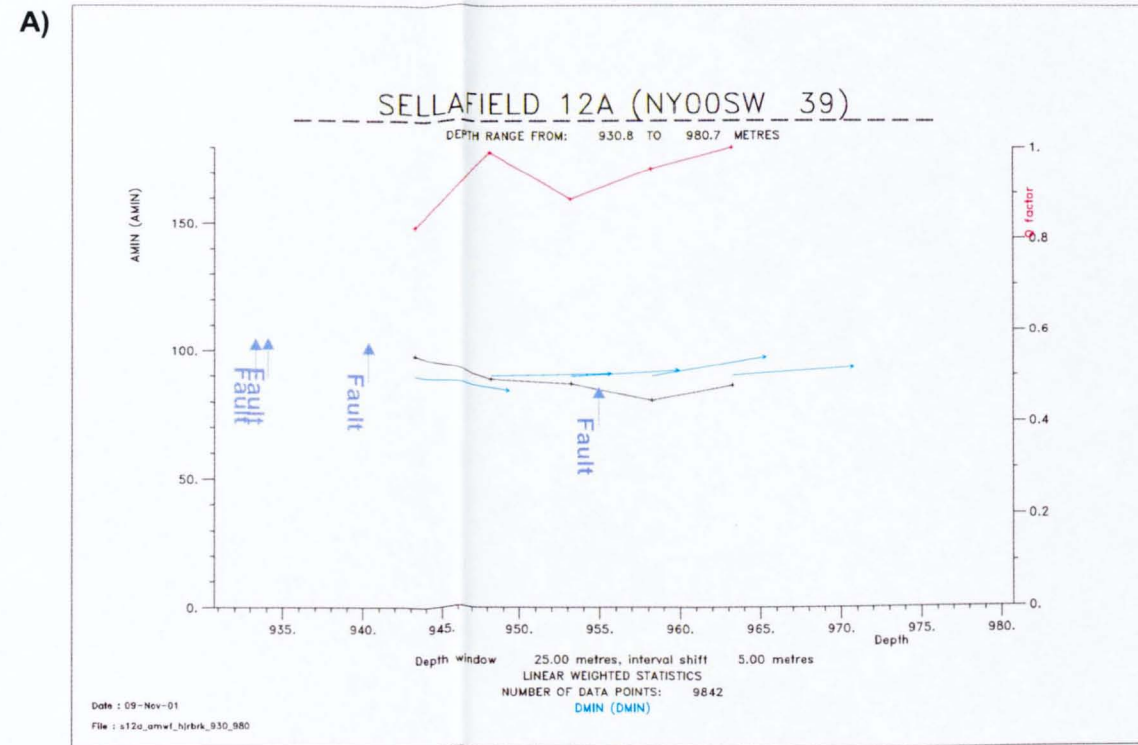


Figure 4.10a/b/c - Examples of the three types of stress profiles identified a) consistent σ_{Hmin} e.g. borehole 12A, b) area of change, but overall consistent σ_{Hmin} e.g. borehole 9B and c) variable σ_{Hmin} e.g. borehole 2.

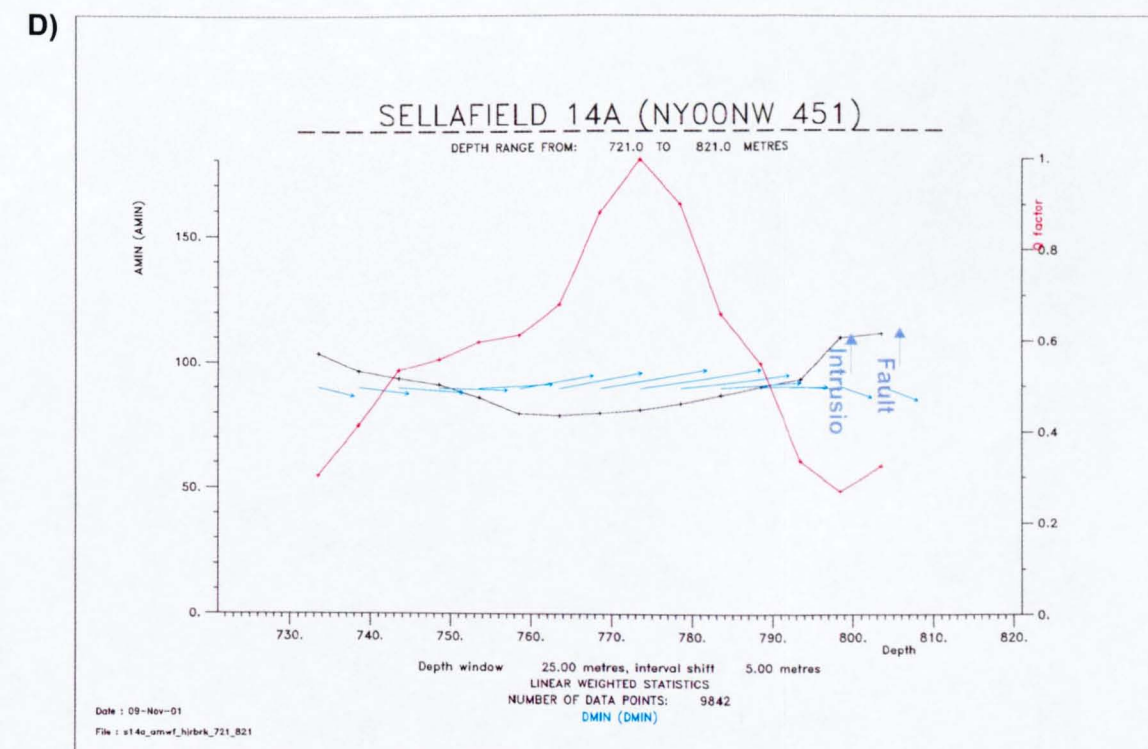
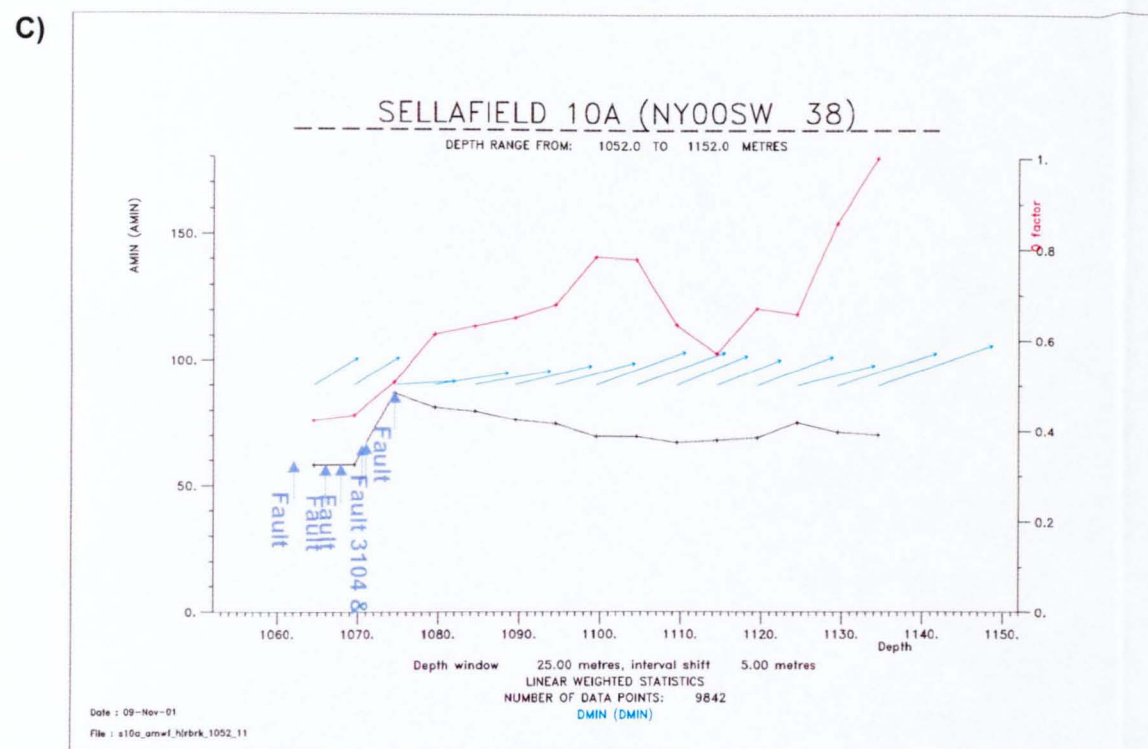
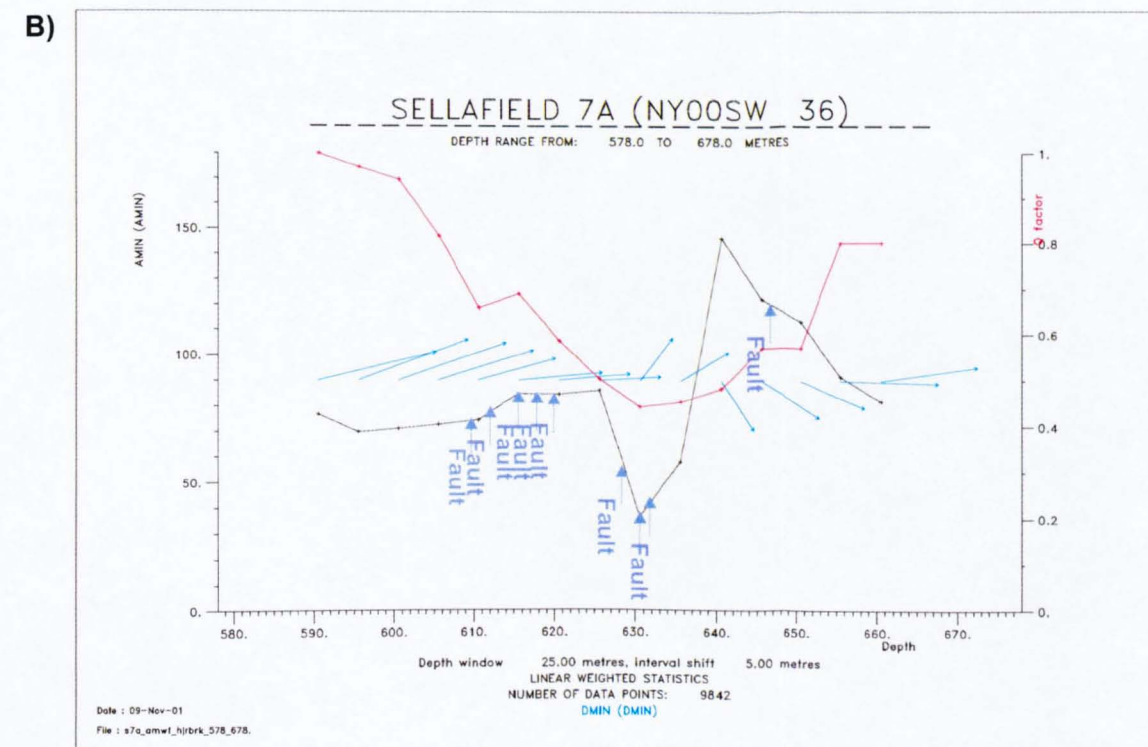
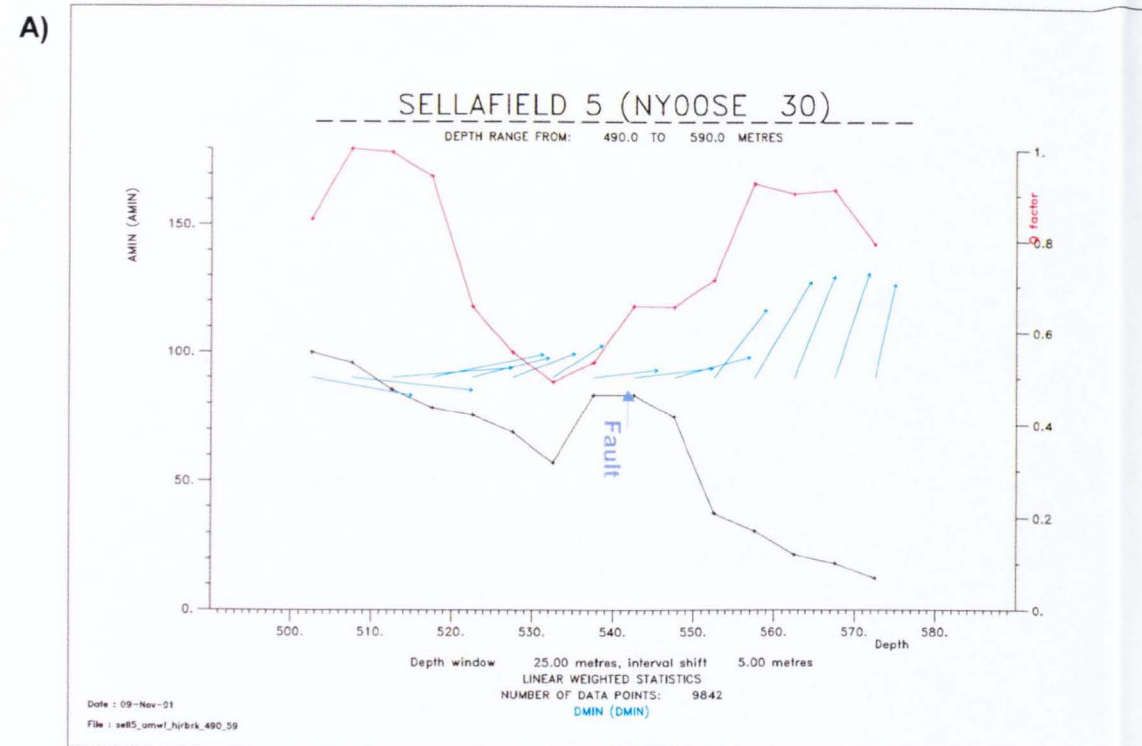


Figure 4.11a/b/c/d - Stress profiles of the boreholes where the locations of the faults and rotation of the stress field was identified a) borehole 5, b) borehole 7A, c) borehole 10A and d) borehole 14A.

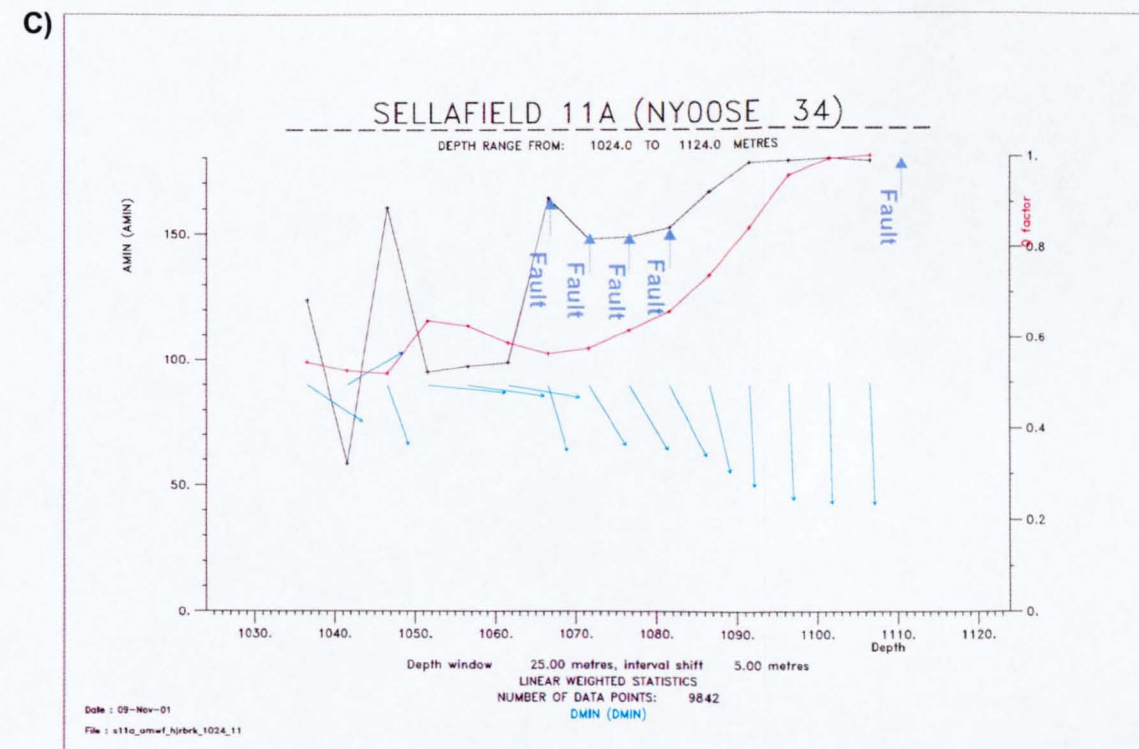
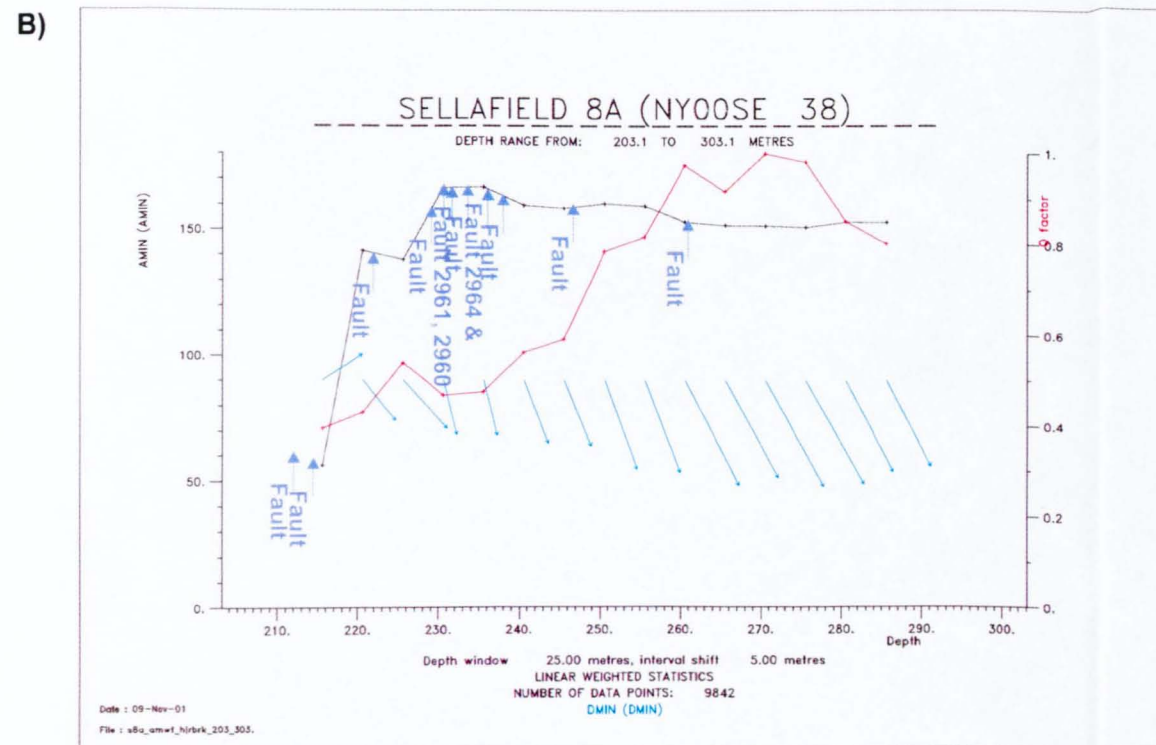
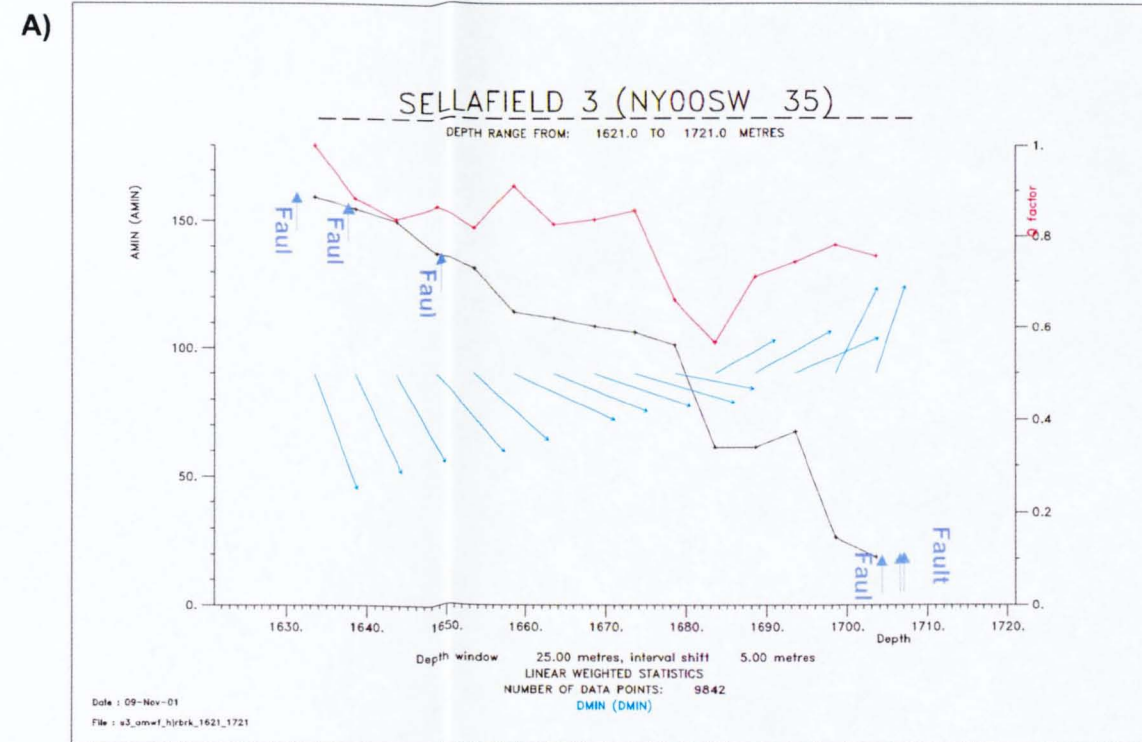
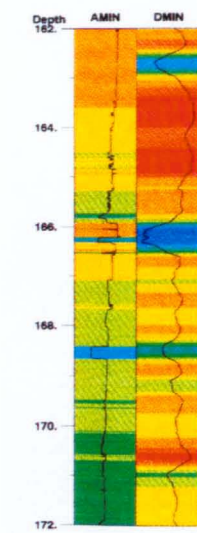


Figure 4.12a/b/c - Stress profiles of the boreholes that showed rotation in Figure 4.2a and 4.8 a) borehole 3, b) borehole 8A and c) borehole 11A.

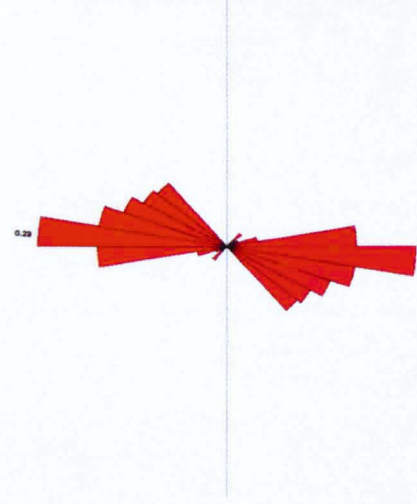
A)



Date : 08-Aug-00
File : rpt1_ammf_nYork_M0_580

SELLAFIELD RCM1 (NY00SE 41)

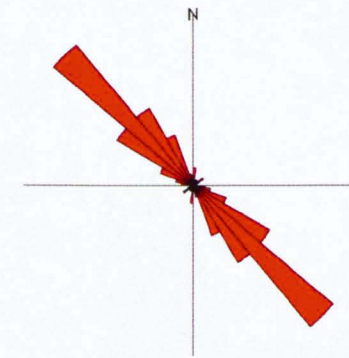
DEPTH RANGE FROM: 162.0 TO 172.0 METRES



Min stress = 104.9 +- 17.2 Class 1
LINEAR WEIGHTED STATISTICS
NUMBER OF DATA POINTS: 986

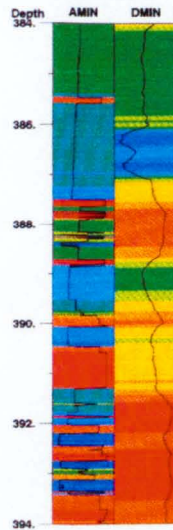
B)

RCM 1 Flow Zone
DEPTH RANGE FROM: 162.0 TO 172.0 METRES



Mean direction = 134.8 +- 14.9 Class 1
NO OF DATA POINTS 7126

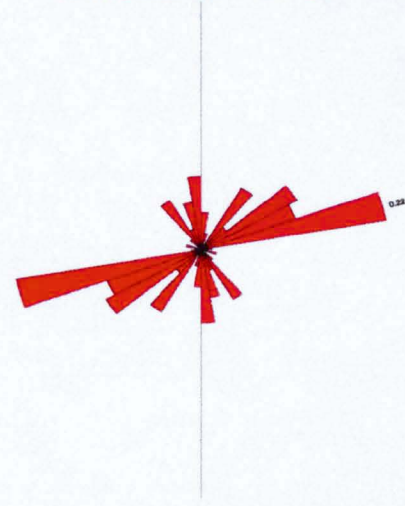
C)



Date : 08-Aug-00
File : rpt1_ammf_nYork_M0_580

SELLAFIELD RCM1 (NY00SE 41)

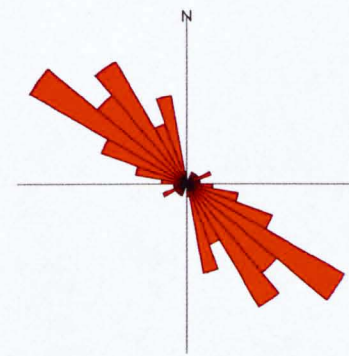
DEPTH RANGE FROM: 384.0 TO 394.0 METRES



Min stress = 62.2 +- 16.1 Class 2
LINEAR WEIGHTED STATISTICS
NUMBER OF DATA POINTS: 984

D)

RCM 1 Flow Zone
DEPTH RANGE FROM: 384.0 TO 394.0 METRES



Mean direction = 133.1 +- 18.8 Class 1
NO OF DATA POINTS 7126

Figure 5.4a/b/c/d/e/f - A selection of the Permian-Triassic breakout (σ_{Hmin}) and discontinuity results in borehole RCM1 for production log flow zones a/b) 11, c/d) 19 & e/f) 22 (Table 5.2, Appendix 1A).

E)



F)

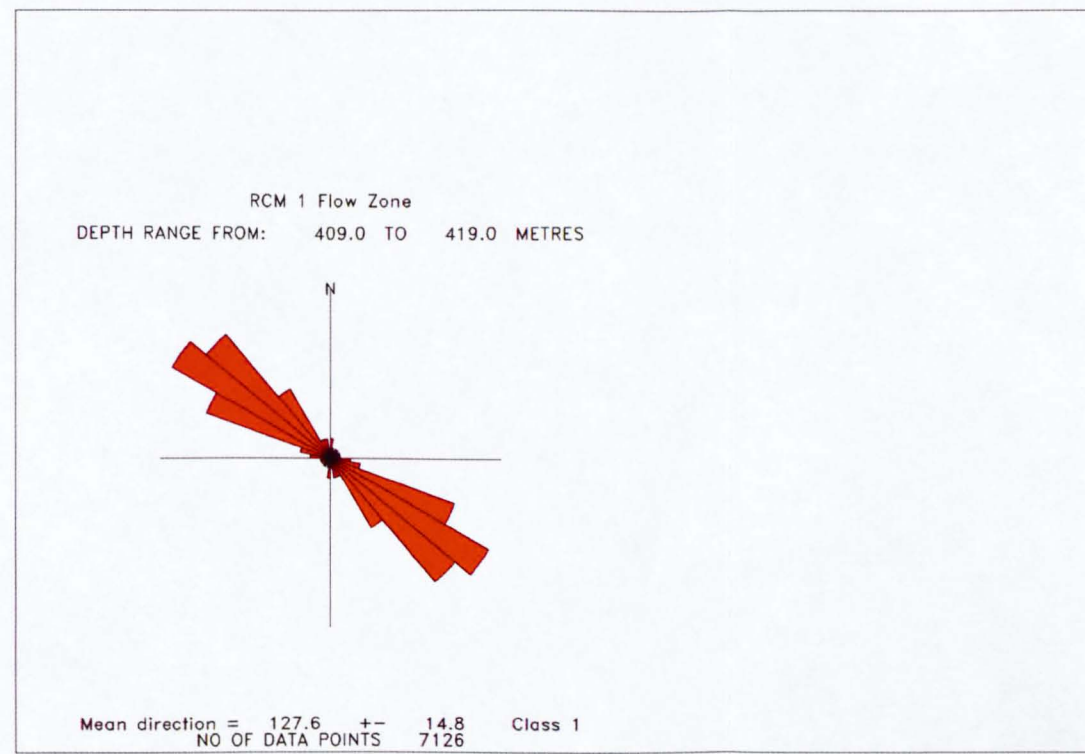
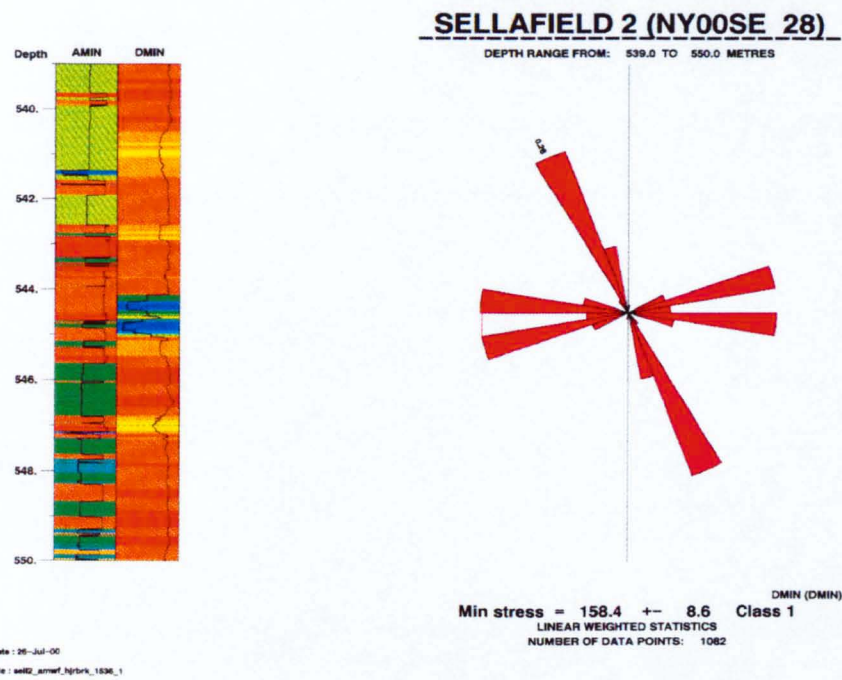
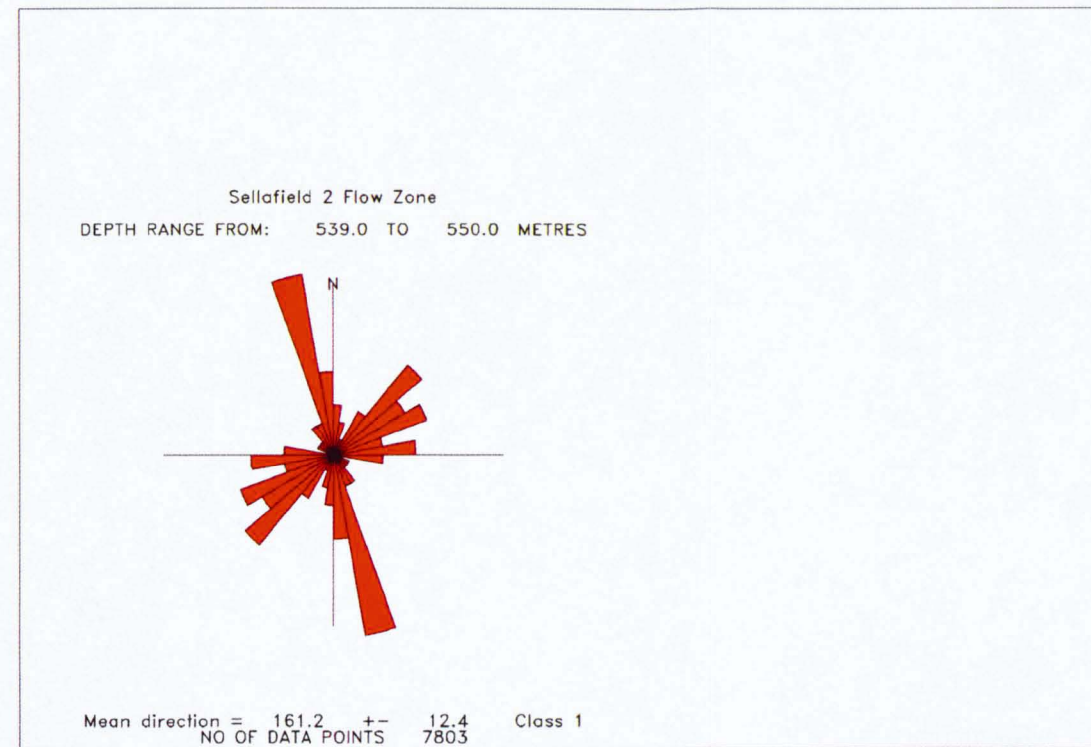


Figure 5.4a/b/c/d/e/f - A selection of the Permian-Triassic breakout (σ_{Hmin}) and discontinuity results in borehole RCM1 for production log flow zones a/b) 11, c/d) 19 & e/f) 22 (Table 5.2, Appendix 1A).

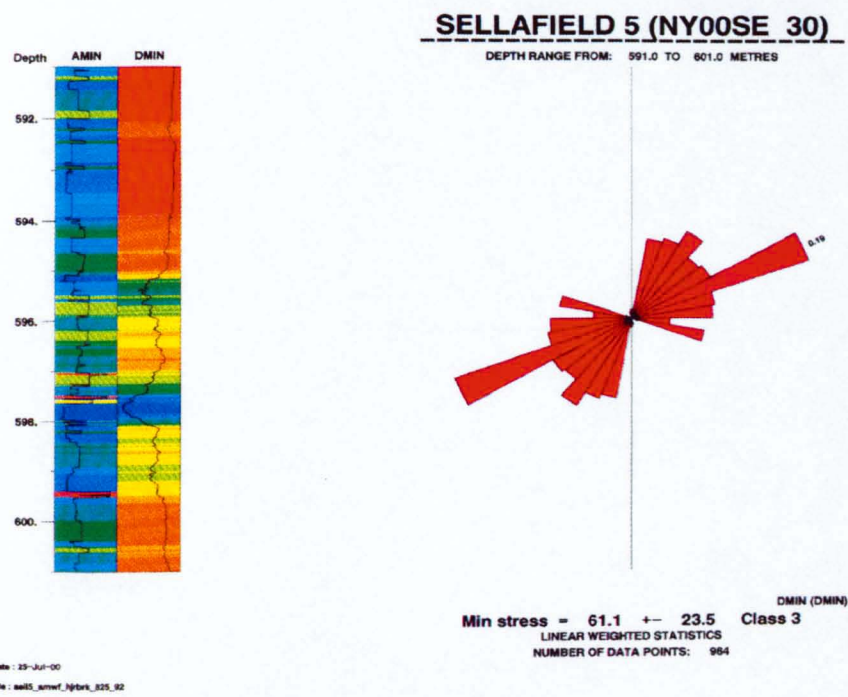
A)



B)



C)



D)

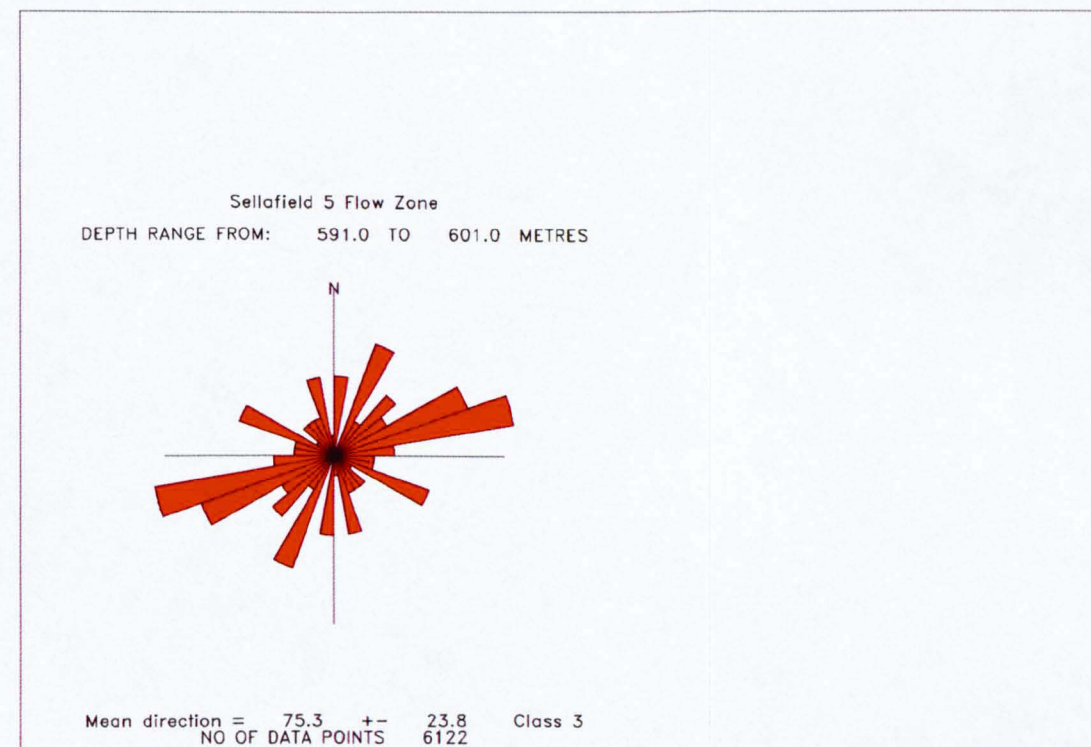
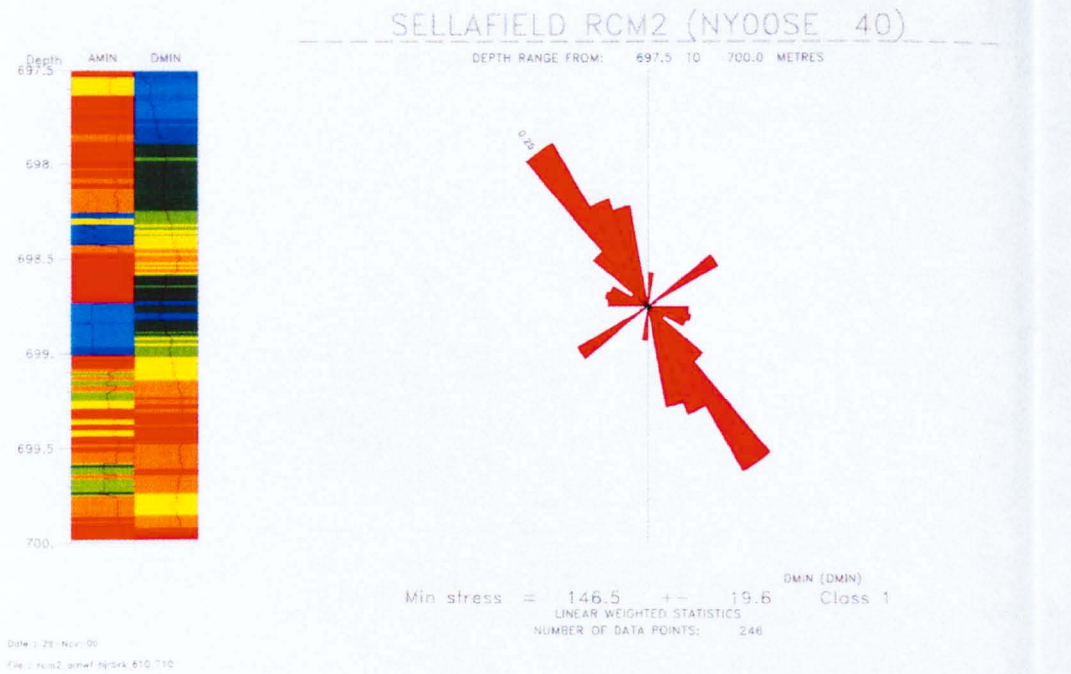
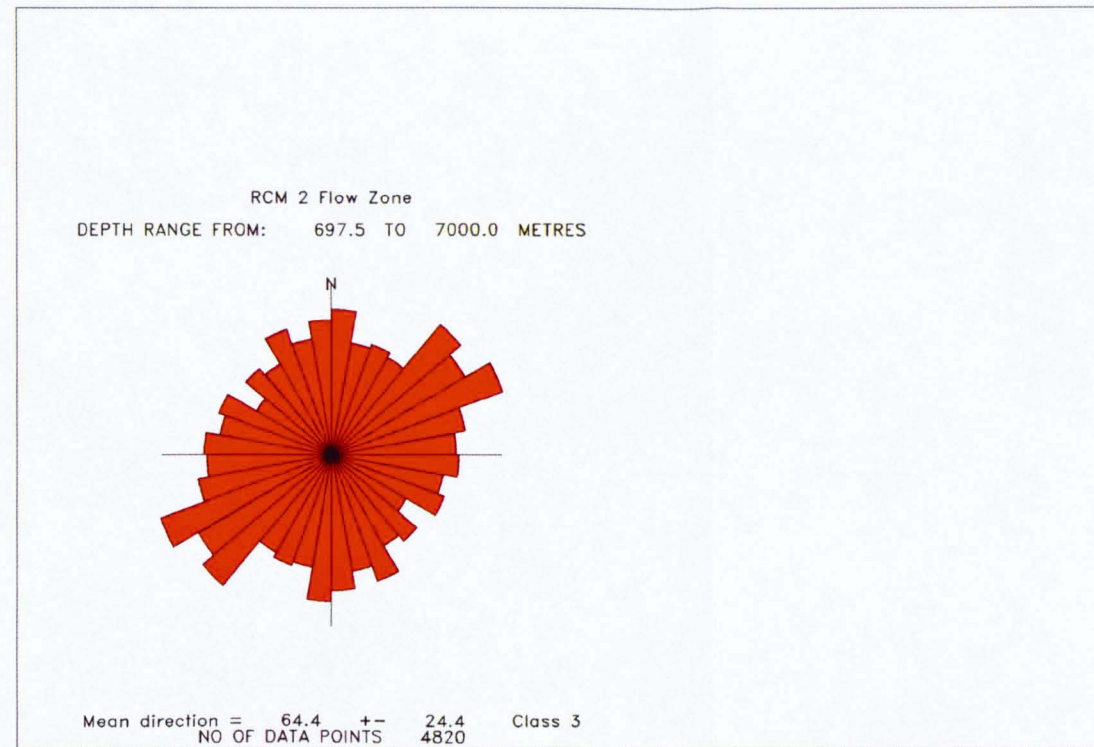


Figure 5.5a/b/c/d/e/f/g/h - A selection of the BVG breakout (σ_{Hmin}) and discontinuity results for boreholes/production log flow zone a/b) 2/12, c/d) 5/2, e/f) RCM2/26 & g/h) RCM2/28 (Table 5.2, Appendix 1A).

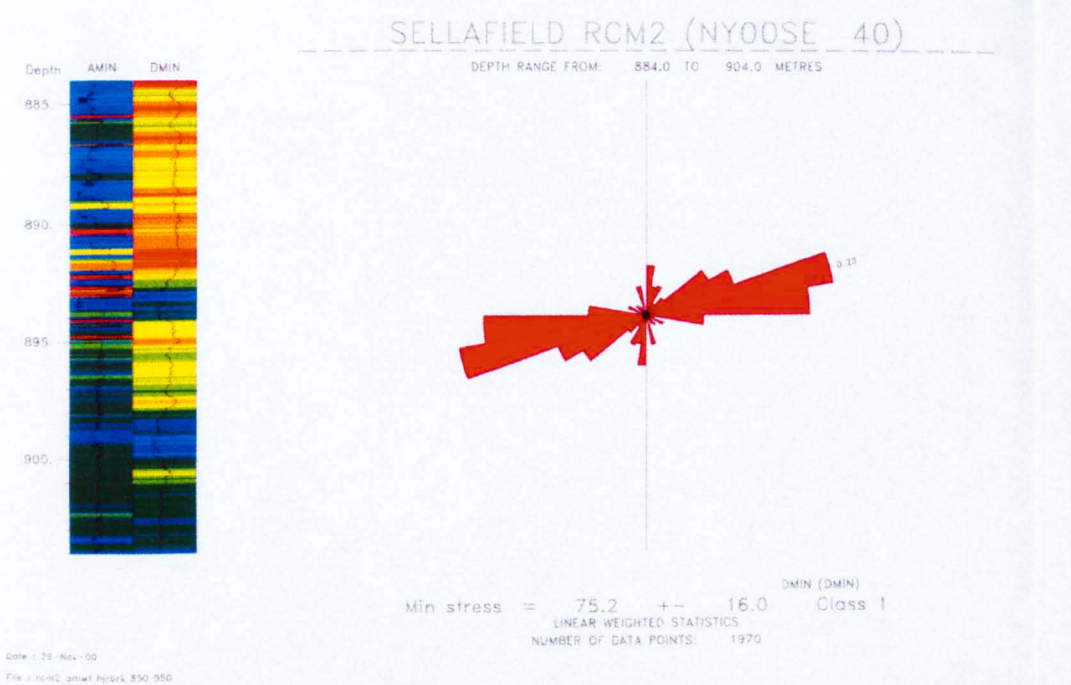
E)



F)



G)



H)

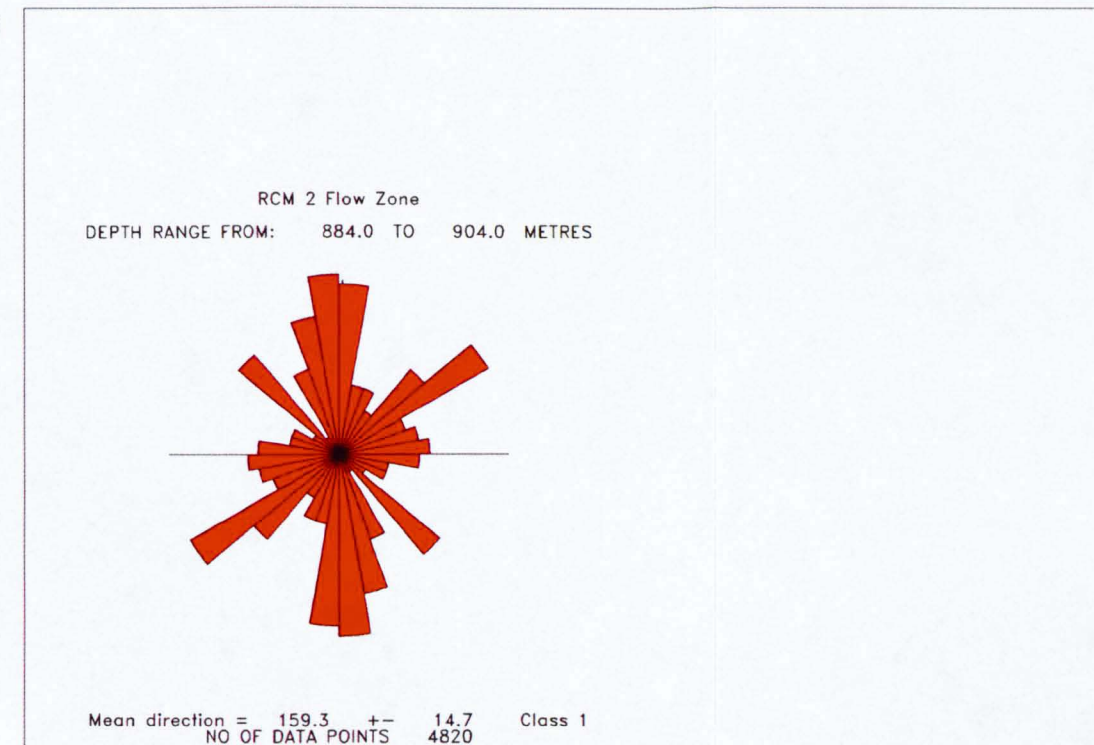
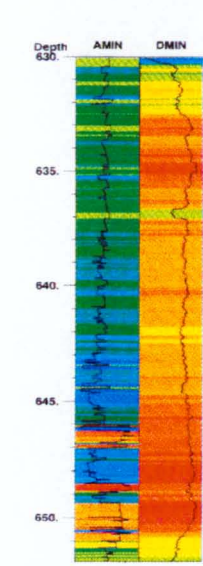


Figure 5.5a/b/c/d/e/f/g/h - A selection of the BVG breakout (σ_{Hmin}) and discontinuity results for boreholes/production log flow zone a/b) 2/12, c/d) 5/2, e/f) RCM2/26 & g/h) RCM2/28 (Table 5.2, Appendix 1A).

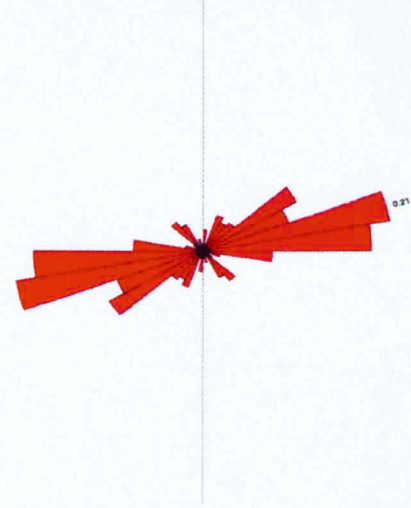
A)



Date: 23-Jul-01
File: rcf3_sitref_nybrk_630_735

SELLAFIELD RCF3 (NY00SE 37)

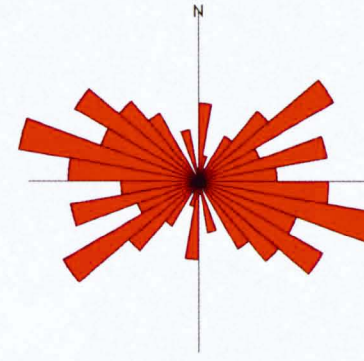
DEPTH RANGE FROM: 630.0 TO 651.9 METRES



Min stress = 72.3 +- 16.9 Class 1
LINEAR WEIGHTED STATISTICS
NUMBER OF DATA POINTS: 1720
DMIN (DMIN)
SIT FZ Analysis.

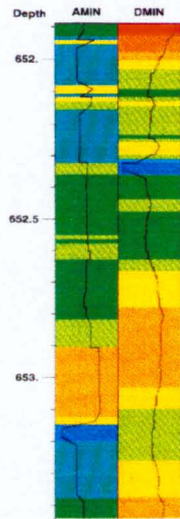
B)

RCF3 SIT
DEPTH RANGE FROM: 630.0 TO 651.9 METRES



Mean direction = 105.7 +- 23.5 Class 3
NO OF DATA POINTS 3712

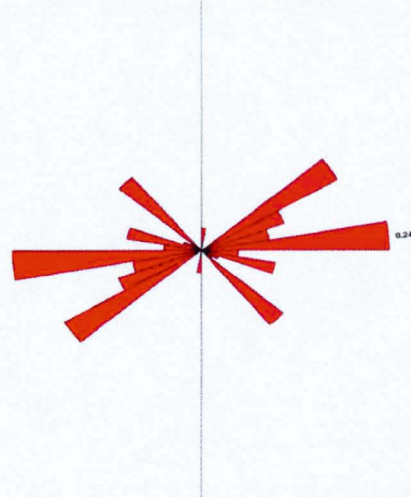
C)



Date: 23-Jul-01
File: rcf3_sitref_nybrk_630_735

SELLAFIELD RCF3 (NY00SE 37)

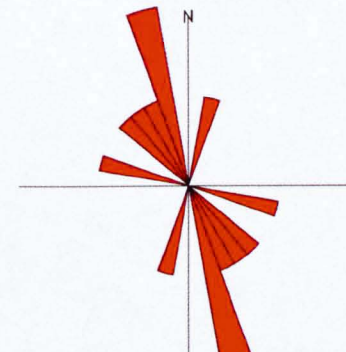
DEPTH RANGE FROM: 651.9 TO 653.5 METRES



Min stress = 79.2 +- 18.7 Class 1
LINEAR WEIGHTED STATISTICS
NUMBER OF DATA POINTS: 124
DMIN (DMIN)
SIT FZ Analysis.

D)

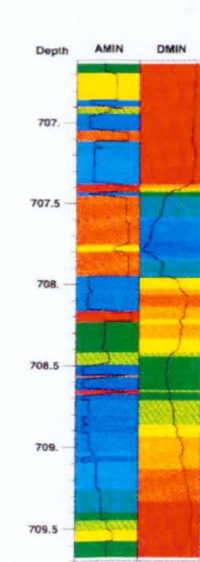
RCF3 SIT
DEPTH RANGE FROM: 651.9 TO 653.5 METRES



Mean direction = 154.9 +- 11.2 Class 1
NO OF DATA POINTS 3712

Figure 5.8a/b/c/d/e/f/g/h/i/j/k/l/m/n/o/p - A selection of the breakout (σ_{Hmin}) and discontinuity results for borehole RCF3 SIT flowing and no-flowing zones (Table 5.3) a/b) NA, c/d) A, e/f) D, g/h) NE, i/j) E, k/l) F, m/n) NG & o/p) NI .

E)



Date: 23-Jul-01
File: rcf3_amin_np01k_830_736

SELLAFIELD RCF3 (NY00SE 37)

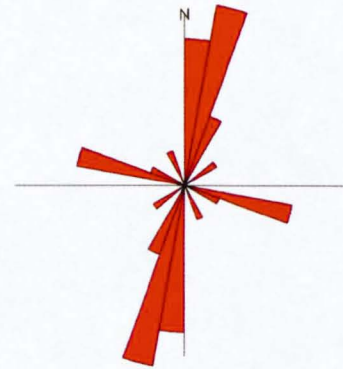
DEPTH RANGE FROM: 706.6 TO 709.7 METRES



Min stress = 21.6 +- 25.8 Class 2
LINEAR WEIGHTED STATISTICS
NUMBER OF DATA POINTS: 242
DMIN (DMIN)
SIT FZ Analysis.

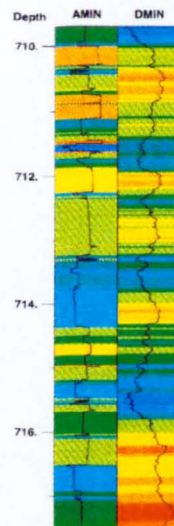
F)

RCF3 SIT Zone
DEPTH RANGE FROM: 706.6 TO 709.7 METRES



Mean direction = 16.9 +- 14.5 Class 1
NO OF DATA POINTS 3712

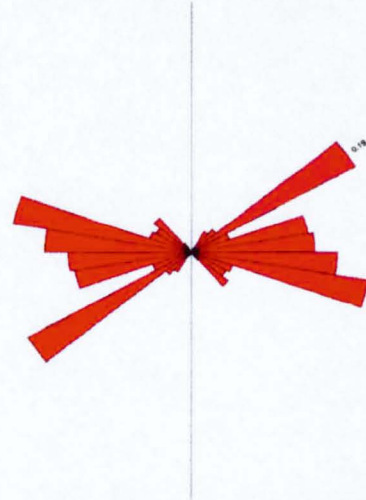
G)



Date: 23-Jul-01
File: rcf3_amin_np01k_830_736

SELLAFIELD RCF3 (NY00SE 37)

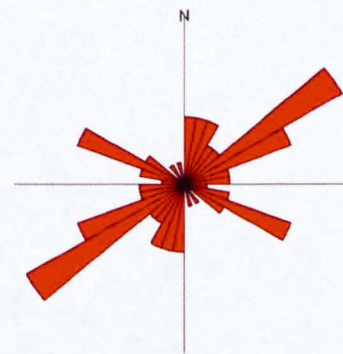
DEPTH RANGE FROM: 709.7 TO 717.5 METRES



Min stress = 71.1 +- 19.6 Class 1
LINEAR WEIGHTED STATISTICS
NUMBER OF DATA POINTS: 616
DMIN (DMIN)
SIT FZ Analysis.

H)

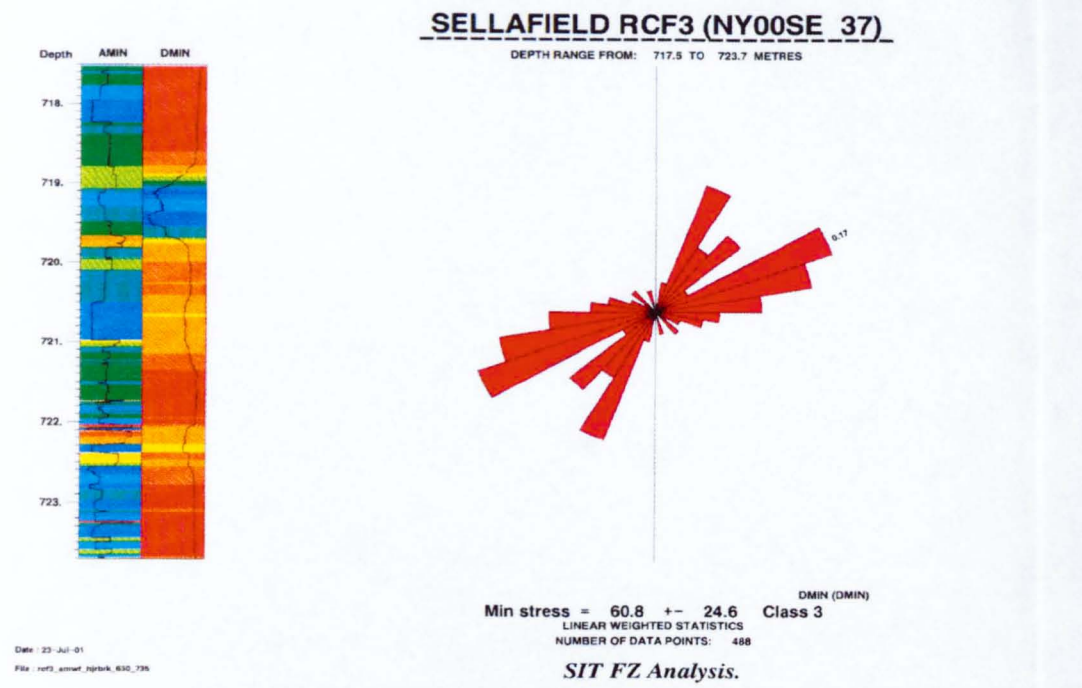
RCF3 SIT Zone
DEPTH RANGE FROM: 709.7 TO 717.5 METRES



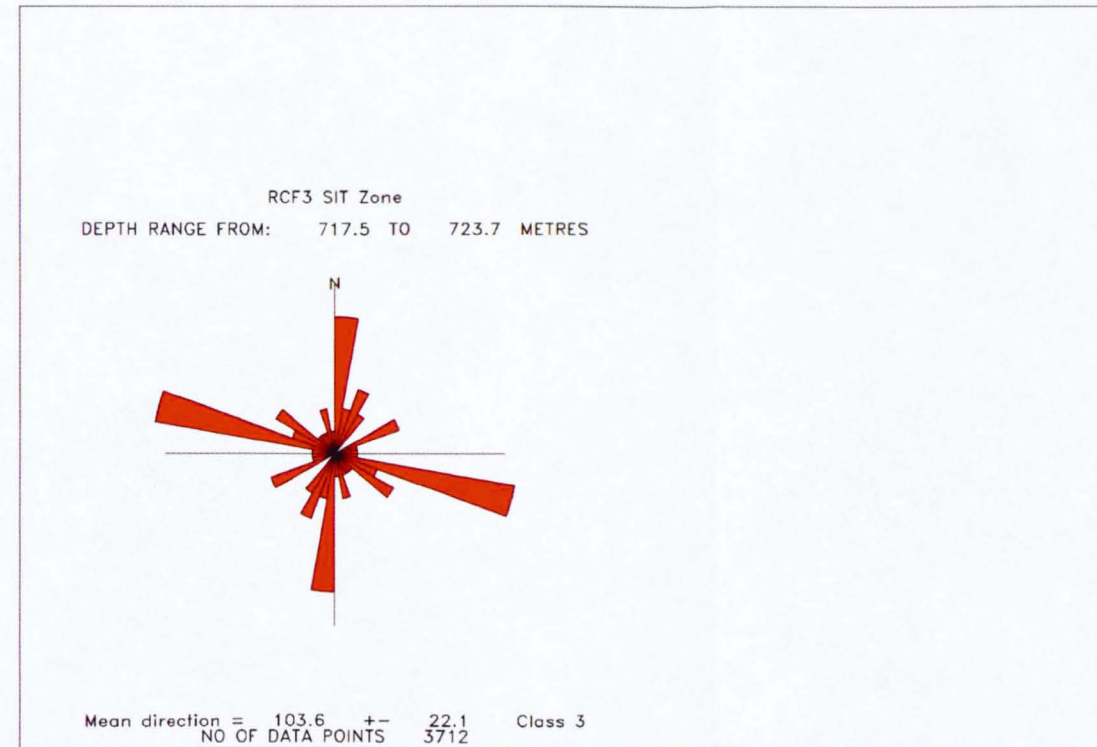
Mean direction = 52.8 +- 21.5 Class 3
NO OF DATA POINTS 3712

Figure 5.8a/b/c/d/e/f/g/h/i/j/k/l/m/n/o/p - A selection of the breakout (σ_{Hmin}) and discontinuity results for borehole RCF3 SIT flowing and no-flowing zones (Table 5.3)
a/b) NA, c/d) A, e/f) D, g/h) NE, i/j) E, k/l) F, m/n) NG & o/p) NI .

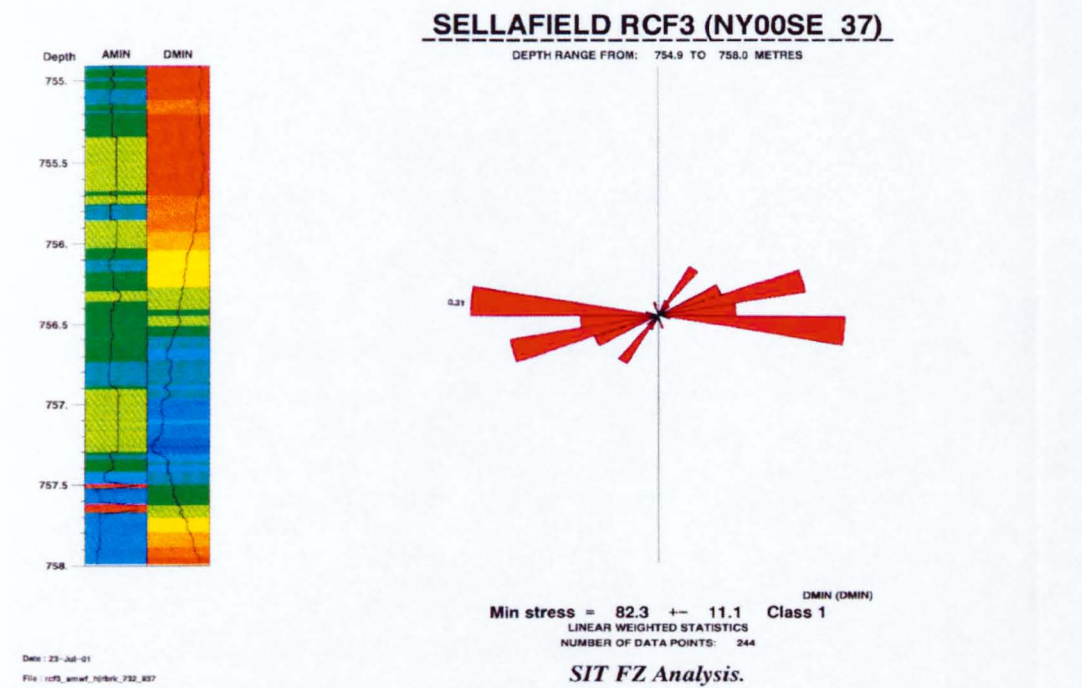
I)



J)



K)



L)

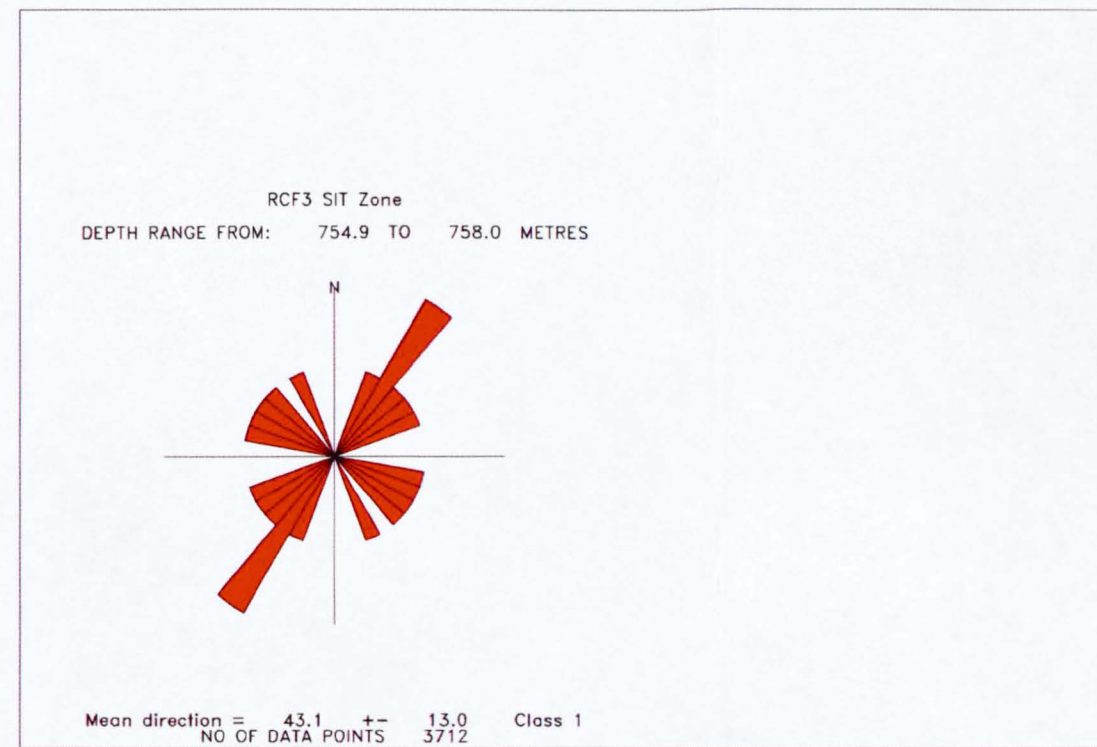
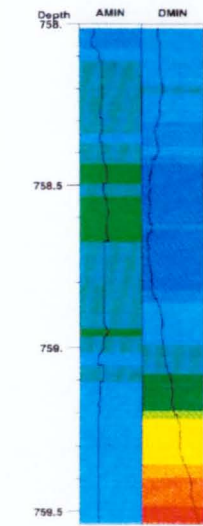


Figure 5.8a/b/c/d/e/f/g/h/i/j/k/l/m/n/o/p - A selection of the breakout (σ_{Hmin}) and discontinuity results for borehole RCF3 SIT flowing and no-flowing zones (Table 5.3)
 a/b) NA, c/d) A, e/f) D, g/h) NE, i/j) E, k/l) F, m/n) NG & o/p) NI .

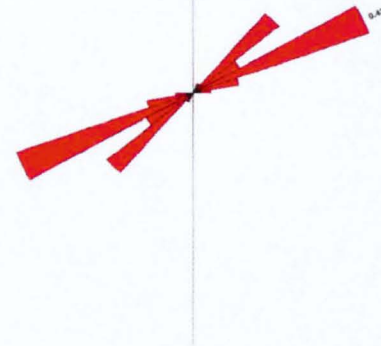
M)



Date: 23-Jul-01
File: rcf3_amin_dmin_758_837

SELLAFIELD RCF3 (NY00SE 37)

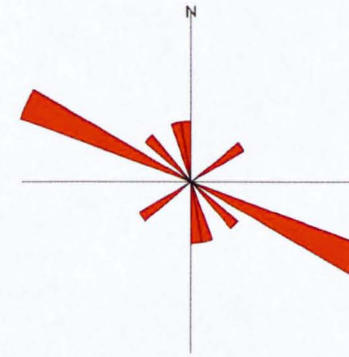
DEPTH RANGE FROM: 758.0 TO 759.5 METRES



Min stress = 58.7 +- 12.1 Class 1
LINEAR WEIGHTED STATISTICS
NUMBER OF DATA POINTS: 122
SIT FZ Analysis.

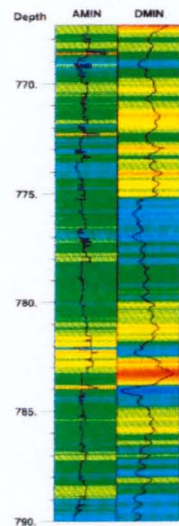
N)

RCF3 SIT Zone
DEPTH RANGE FROM: 758.0 TO 759.5 METRES



Mean direction = 121.5 +- 8.8 Class 1
NO OF DATA POINTS 3712

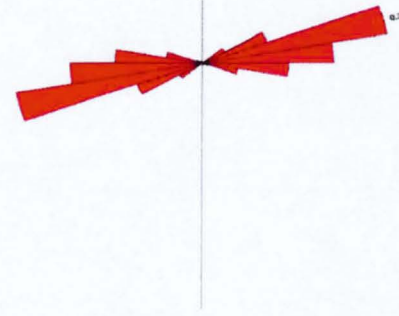
O)



Date: 23-Jul-01
File: rcf3_amin_dmin_767_837

SELLAFIELD RCF3 (NY00SE 37)

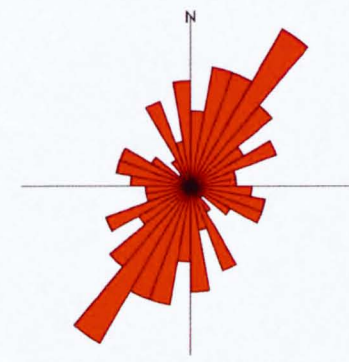
DEPTH RANGE FROM: 767.4 TO 790.0 METRES



Min stress = 81.0 +- 12.9 Class 1
LINEAR WEIGHTED STATISTICS
NUMBER OF DATA POINTS: 1780
SIT FZ Analysis.

P)

RCF3 SIT Zone
DEPTH RANGE FROM: 767.4 TO 790.0 METRES



Mean direction = 36.0 +- 20.3 Class 3
NO OF DATA POINTS 3712

Figure 5.8a/b/c/d/e/f/g/h/i/j/k/l/m/n/o/p - A selection of the breakout (σ_{Hmin}) and discontinuity results for borehole RCF3 SIT flowing and no-flowing zones (Table 5.3)
a/b) NA, c/d) A, e/f) D, g/h) NE, i/j) E, k/l) F, m/n) NG & o/p) NI .

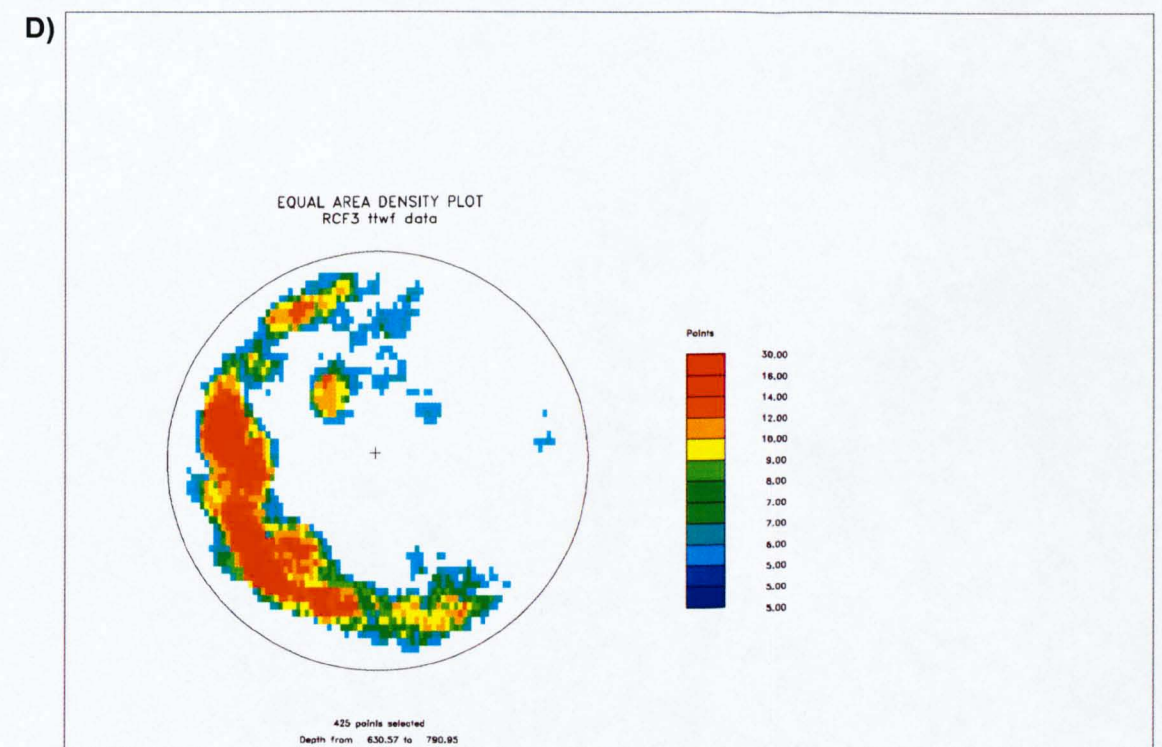
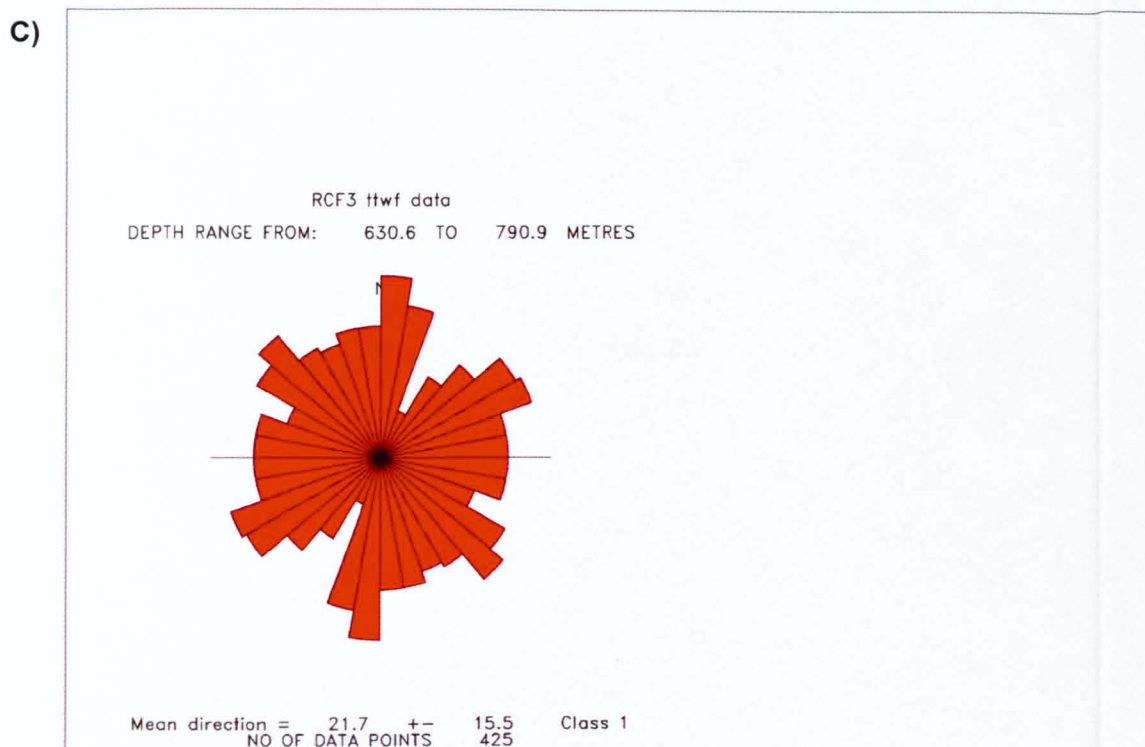
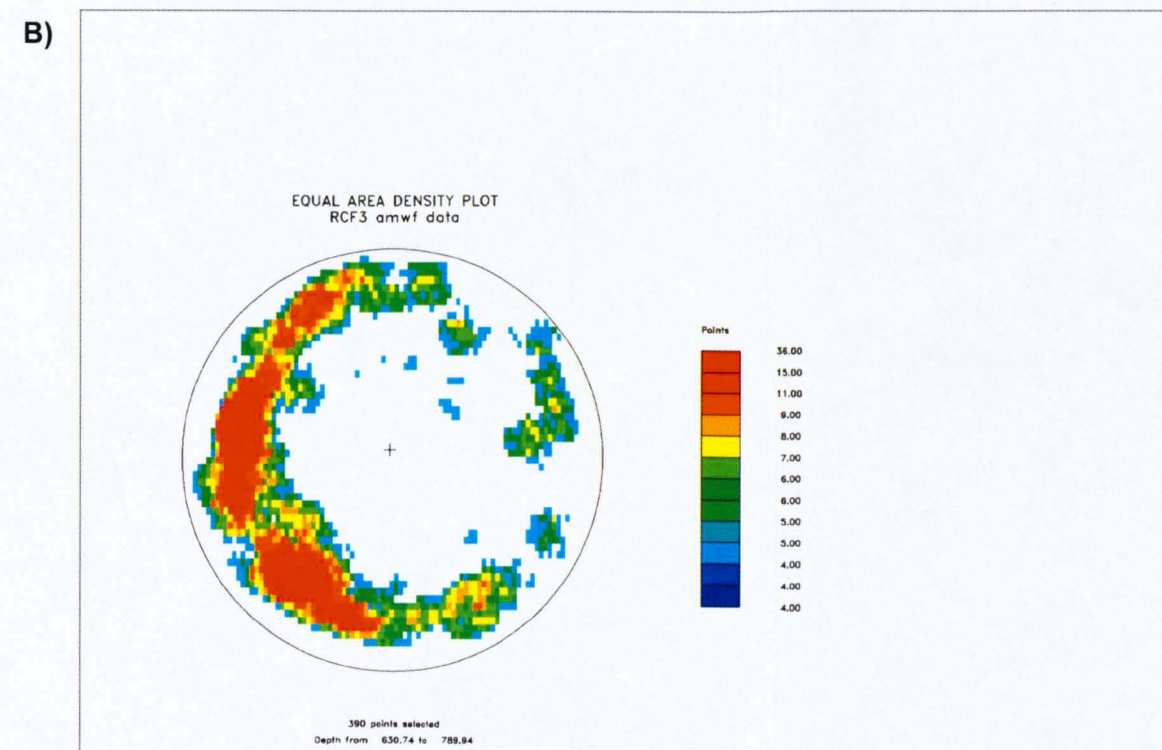
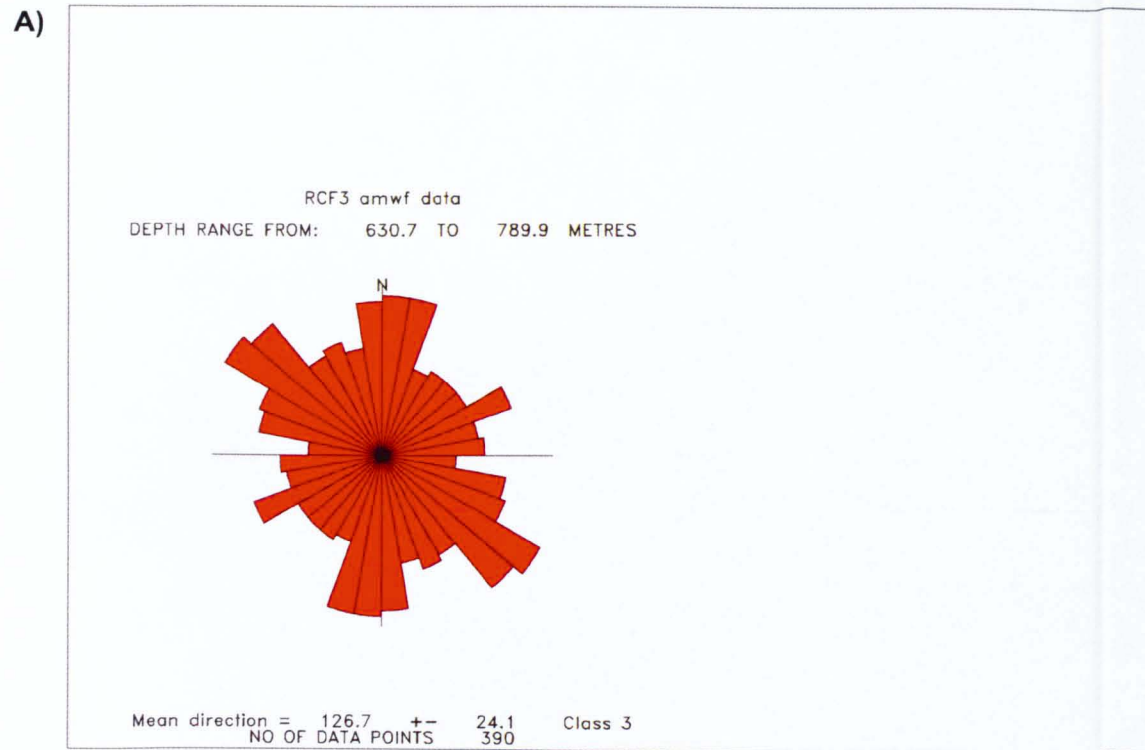


Figure 5.11a/b/c/d/e/f/g/h - The orientation rose plots and lower hemisphere equal area density stereographic projections produced from the discontinuity data generated by the a/b) UBI (AMWF), c/d) UBI (TTWF), e/f) FMI & g/h) FMI/UBI (NIREX) imagery logs from Sellafield borehole RCF3.

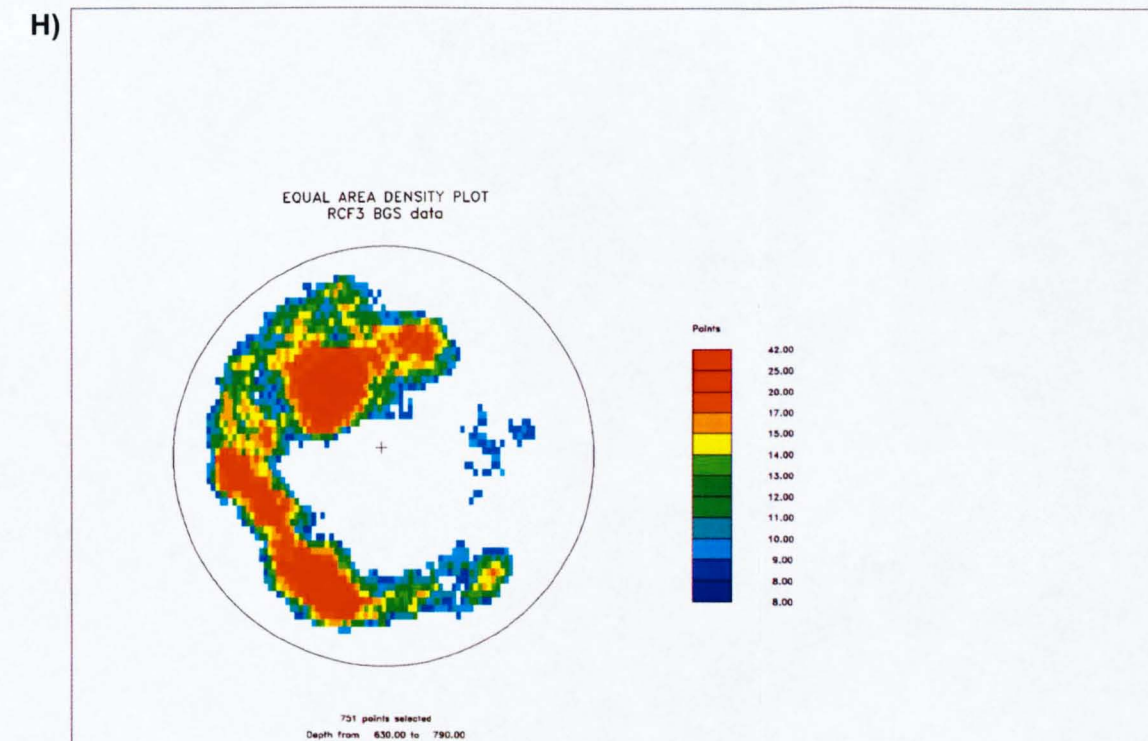
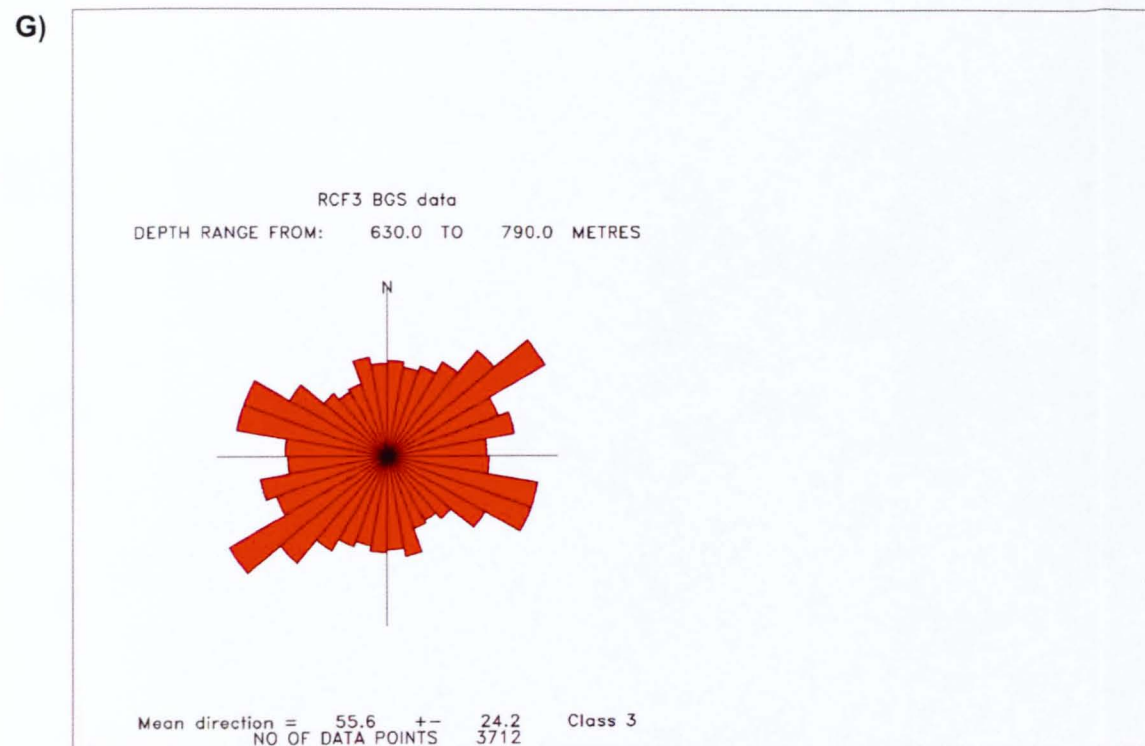
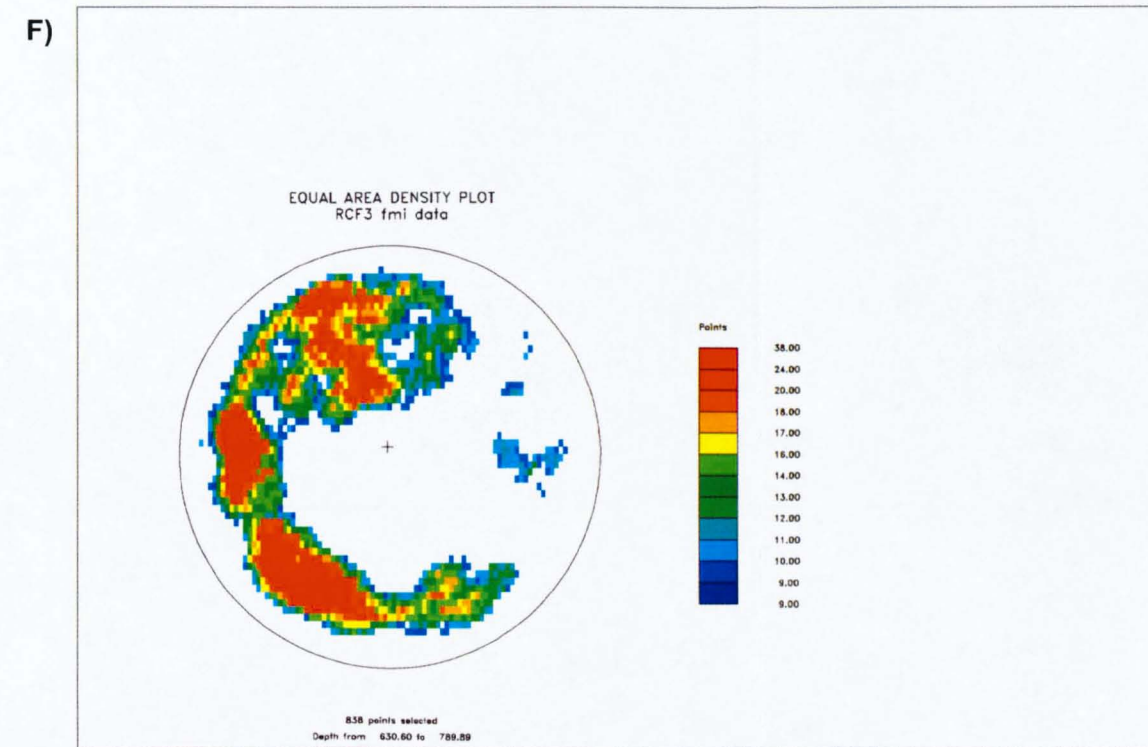
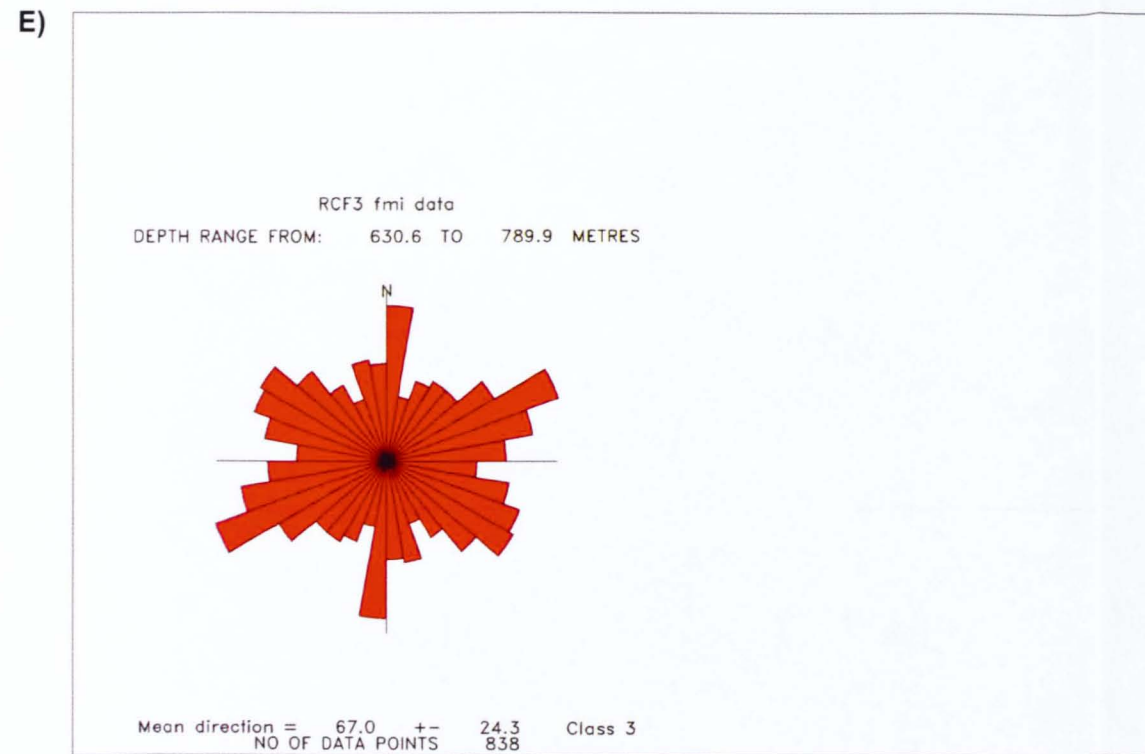


Figure 5.11a/b/c/d/e/f/g/h - The orientation rose plots and lower hemisphere equal area density stereographic projections produced from the discontinuity data generated by the a/b) UBI (AMWF), c/d) UBI (TTWF), e/f) FMI & g/h) FMI/UBI (NIREX) imagery logs from Sellafeld borehole RCF3.



SELLAFIELD RCF3

NY00SE 37

1: 500

Grid East 305565 North 503932

Latitude 54 25 18.85

Longitude -3 27 20.21

Datum RT 88.27 maOD

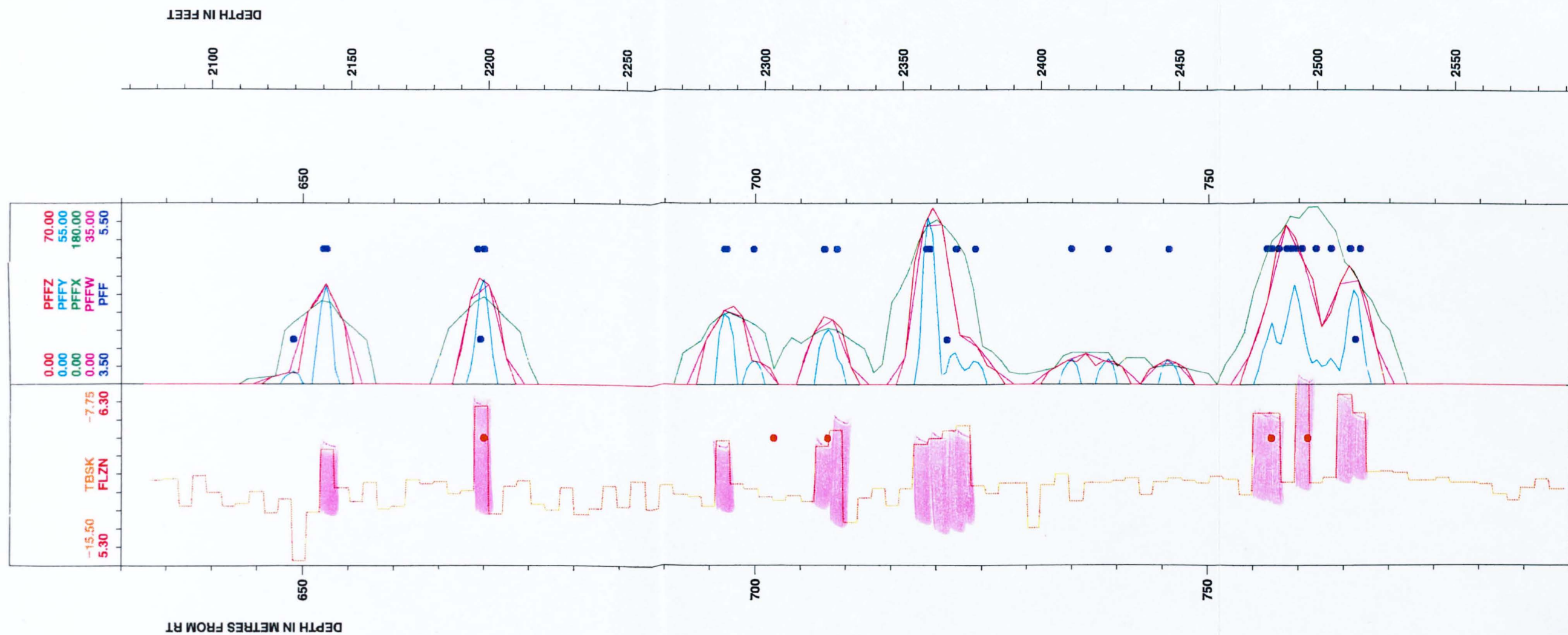
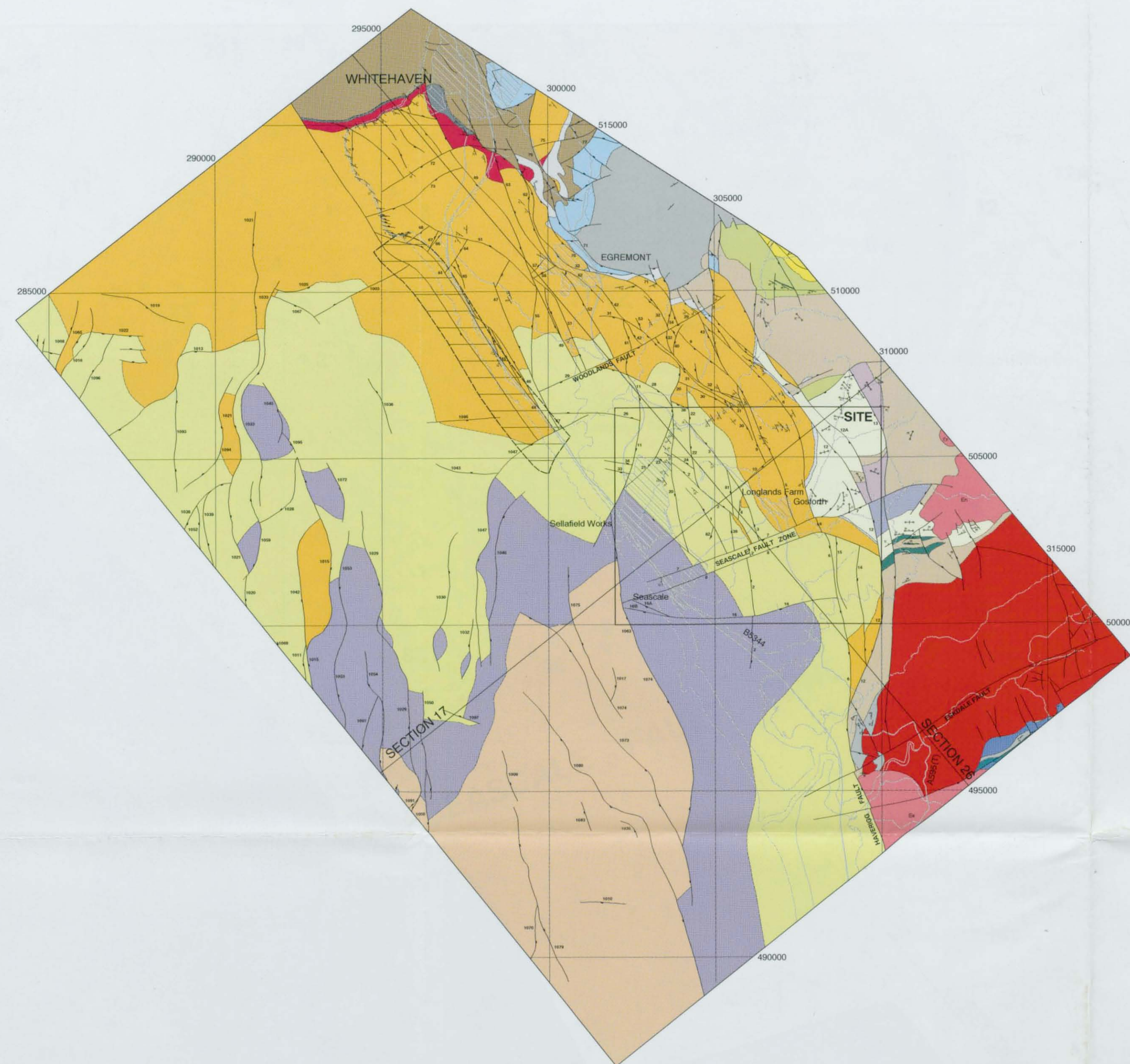


Figure 6.7 – Test log of PFF point data and all smoothed PFF synthetic logs.



KEY

- Mercia Mudstone Group
 - Ormskirk Sandstone
 - Calder Sandstone
 - St. Bees Sandstone
 - St. Bees Shale
 - St. Bees Evaporite
 - Brockram
- PERMIAN AND TRIASSIC
- Hensingham Group and Coal Measures
 - Carboniferous Limestone, undivided
- CARBONIFEROUS
- Wraithow Basalt
 - Craghouse Tuff
 - Seatallan Dacite
 - Bedded Tuffs and reworked volcanic rocks
 - Andesite
 - Mottled Tuff
 - Birkby Fell Member (Basalt)
 - Devoke Water Tuff (Basalt)
- (BORROWDALE VOLCANIC GROUP) ORDOVICIAN
- Latterbarrow Sandstone
 - Skiddaw Group, undivided
- ORDOVICIAN
- INTRUSIVE IGNEOUS ROCKS**
- En Granite; Ennerdale Intrusion
 - Granite; Eskdale Intrusion
 - Es Granodiorite; Eskdale Intrusion
- ORDOVICIAN-DEVONIAN

- Area of conjectural structure
- Geological boundary, Solid
- Fault, crossmark on downthrow side
- Fault Number
- Inclined strata, dip in degrees
- Vertical strata
- Inclined igneous foliation, dip in degrees
- Vertical igneous foliation

For details of Region area see Drawing Number 010030
 For details of Site area see Drawing Number 010032
 The geology of the PRZ has been revised since production of Nirex Report Number 524. The revised geology is presented in Nirex Report Number S/95/005 Sellafeld Geological Investigations: The 3D Geological Structure of the PRZ: Summary Report and in Drawing Number 010033
 For details of cross section 17 see Drawing Number 010057
 For details of cross section 26 see Drawing Number 010058

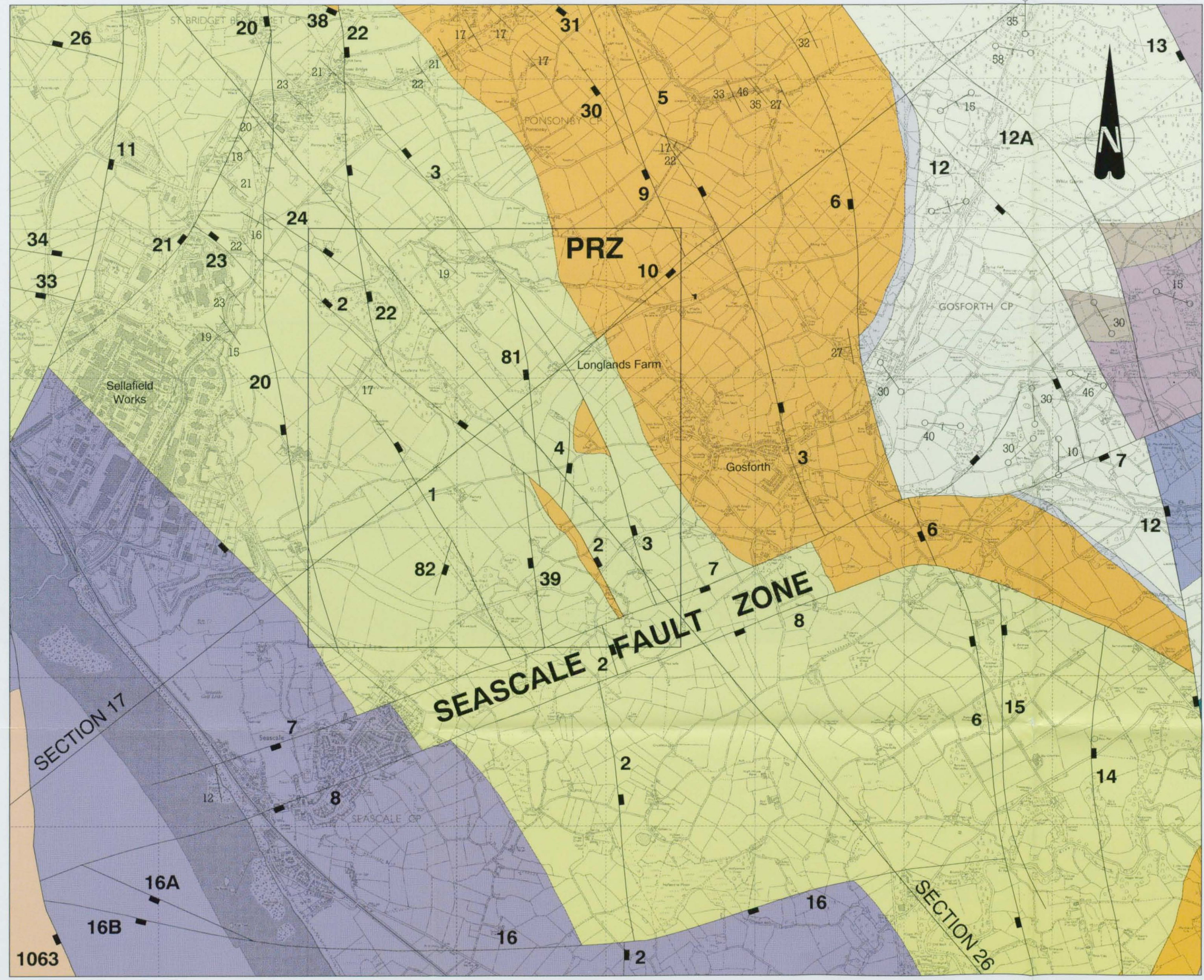
The information on this map has been derived from the following report(s):
 Nirex Report Number 524 Volume 2 Enclosure 9



Topographical base map derived from Ordnance Survey Landranger Series
 © Crown copyright reserved

Figure 3.1b – Map showing the district geological and structural setting of Sellafeld (from NIREX, 1995g).

MOD:												DRAWING PRODUCED BY: SECURITY CLASS												DRAWN PT		PHASE		ROCK CHARACTERISATION FACILITY											
AUTHORISED BY NIREX												British Geological Survey												CHECKED RJP		LOCATION		DISTRICT: SUB-QUATERNARY											
DRAWN CHKD. APPD. DATE												FOR UK NIREX LTD UNDER CONTRACT No. SCRS/1511												APPROVED CAG		SYSTEM		Figure 3.1b GEOLOGY											
AUTHORISED BY NIREX												NIREX												APPROVED DWH		STATUS P.I.		AO SIZE DRG. No. 010031 MOD.											
DRAWN CHKD. APPD. DATE												DATE JUNE 95												AUTHORISED BY NIREX		UNITS													
DRAWN CHKD. APPD. DATE																								DATE JUNE 95		SCALE 1:50 000													



KEY

- Mercia Mudstone Group
- Ormskirk Sandstone
- Calder Sandstone
- St. Bees Sandstone
- Brockram
- Wrighthow Basalt
- Craghouse Tuff
- Seatallan Dacite
- Bedded Tuffs and reworked volcanic rocks
- Andesite

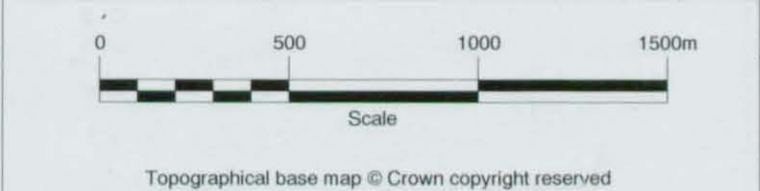
PERMIAN AND TRIASSIC (BORROMALE VOLCANIC GROUP)

ORDOVICIAN

- Geological boundary, Solid
- Fault, crossmark on downthrow side
- 13** Fault Number
- Inclined strata, dip in degrees
- Inclined igneous foliation, dip in degrees
- Vertical igneous foliation

For details of Region see Drawing Number 010030
 For details of District see Drawing Number 010031
 The geology of the PRZ has been revised since production of Nirex Report Number 524. The revised geology is presented in Nirex Report Number S/95/005 Sellafield Geological Investigations: The 3D Geological Structure of the PRZ: Summary Report and in Drawing Number 010033
 For details of cross-section 17 see Drawing Number 010059
 For details of cross-section 26 see Drawing Number 010060
 The information on this map has been derived from the following report(s):
 Nirex Report Number 524 Volume 2 Enclosure 9

Figures 3.3a – Site scale Sub-Quaternary Geological map of Sellafield (from NIREX, 1995g).



MOD:	MOD:	MOD:	MOD:	MOD:
AUTHORISED BY NIREX				
DRAWN	CHKD	APPD	DATE	DRAWN
CHKD	APPD	DATE	DRAWN	CHKD
APPD	DATE	DRAWN	CHKD	APPD
DATE	DRAWN	CHKD	APPD	DATE

DRAWING PRODUCED BY:

 British Geological Survey
 FOR UK NIREX LTD UNDER CONTRACT No. SCRS/1511

SECURITY CLASS
 DRAWN PT
 CHECKED RJP
 APPROVED CAG
 APPROVED DWH
 AUTHORIZED BY NIREX RC/MD
 DATE JUNE 95

PHASE
 LOCATION
 SYSTEM
 STATUS P.I.
 UNITS
 SCALE 1:10 000

NIREX



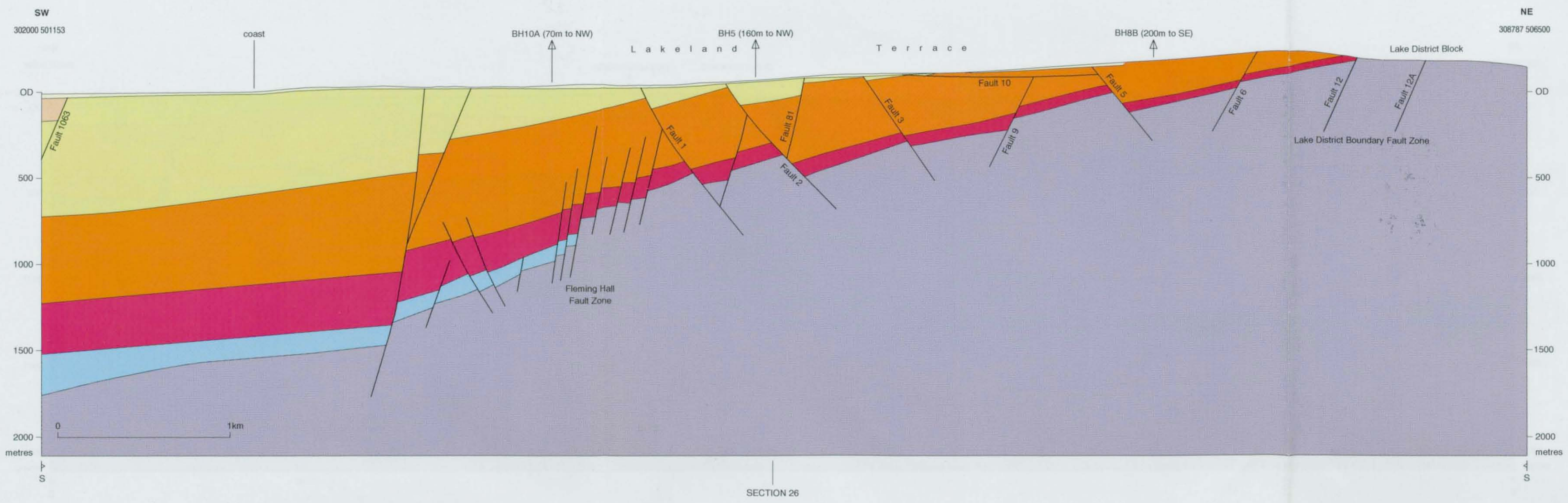
ROCK CHARACTERISATION FACILITY
 SITE: SUB-QUATERNARY GEOLOGY
 AO SIZE DRG. No. 010032 MOD

KEY

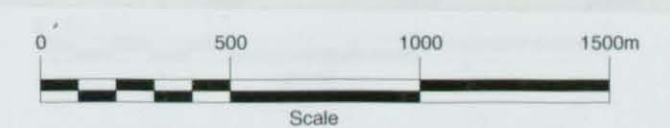
-  Site Boundary
-  Quaternary strata
-  Mercia Mudstone Group
-  Ormskirk and Calder Sandstone formations
-  St. Bees Sandstone Formation
-  Cumbrian Coast Group
-  Carboniferous strata
-  Pre-Carboniferous (Caledonian) basement rocks

For details of Region area see Drawing Number 010055
 For details of District area see Drawing Number 010057
 The geology of the PRZ has been revised since production of Nirex Report Numbers 346 and 524. The revised geology is presented in Nirex Report Number S/95/005 Sellafield Geological Investigations: The 3D Geological Structure of the PRZ: Summary Report and in Drawing Number 010061
 For details of cross-section 26 see Drawing Number 010060

The information on this drawing has been derived from the following report(s):
 Nirex Report Number 346
 Nirex Report Number 524 Volumes 2 & 4



Figures 3.3b – Site scale Sub-Quaternary cross-section of Sellafield, drawn from Figure 3.3a, section line 17 (from NIREX, 1995g).



Topographical base map © Crown copyright reserved

MOD:	MOD:	MOD:	MOD:	MOD:
AUTHORISED BY NIREX				
DRAWN	CHKD.	APPD.	DATE	DRAWN
CHKD.	APPD.	DATE	DRAWN	CHKD.
APPD.	DATE	DRAWN	CHKD.	APPD.
DATE	DRAWN	CHKD.	APPD.	DATE

DRAWING PRODUCED BY: **British Geological Survey**

FOR UK NIREX LTD UNDER CONTRACT No. SCRS/1511

SECURITY CLASS

DRAWN

CHECKED

APPROVED

APPROVED

AUTHORISED BY NIREX

DATE JUNE 95

NIREX

PHASE

LOCATION

SYSTEM

STATUS P.I.

UNITS

SCALE 1:10 000

ROCK CHARACTERISATION FACILITY

SITE: CROSS-SECTION 17

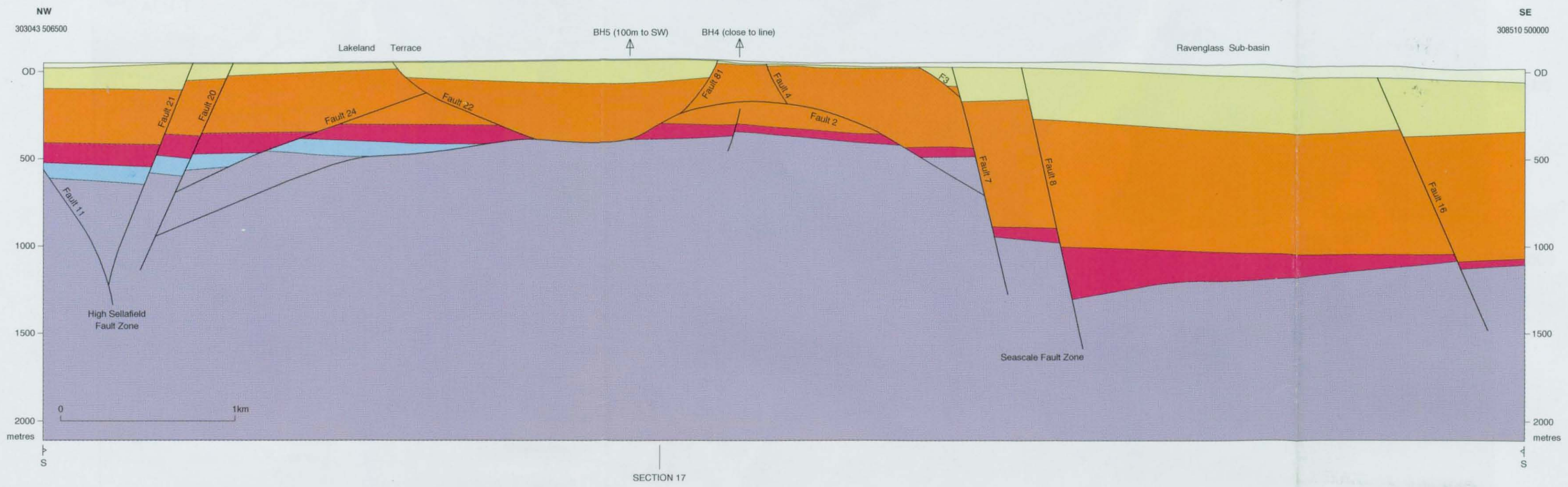
AO SIZE No. 010059 MOD.

KEY

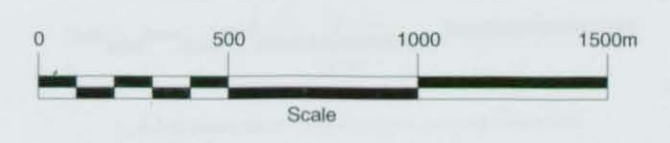
- Site Boundary
- Quaternary strata
- Ormskirk and Calder Sandstone formations
- St. Bees Sandstone Formation
- Cumbrian Coast Group
- Carboniferous strata
- Pre-Carboniferous (Caledonian) basement rocks

For details of Region area see Drawing Number 010056
 For details of District area see Drawing Number 010058
 The geology of the PRZ has been revised since production of Nirex Report Numbers 346 and 524. The revised geology is presented in Nirex Report Number S/95/005 Sellafield Geological Investigations: The 3D Geological Structure of the PRZ: Summary Report and in Drawing Number 010062
 For details of cross-section 17 see Drawing Number 010059

The information on this drawing has been derived from the following report(s):
 Nirex Report Number 346
 Nirex Report Number 524 Volumes 2 & 4



Figures 3.3c – Site scale Sub-Quaternary cross-section of Sellafield, drawn from Figure 3.3a, section line 26 (from NIREX, 1995g).



Topographical base map © Crown copyright reserved

MOD:	MOD:	MOD:	MOD:	MOD:
AUTHORISED BY NIREX				
DRAWN	CHKD.	APPD.	DATE	DRAWN
CHKD.	APPD.	DATE	DRAWN	CHKD.
APPD.	DATE	DRAWN	CHKD.	APPD.
DATE	DRAWN	CHKD.	APPD.	DATE

DRAWING PRODUCED BY: **British Geological Survey**
 FOR UK NIREX LTD UNDER CONTRACT No. SCRS/1511

SECURITY CLASS

DRAWN	PT
CHECKED	RJP
APPROVED	CAG
APPROVED	DWH
AUTHORISED BY NIREX	RC/MD
DATE	JUNE 95

PHASE	
LOCATION	
SYSTEM	
STATUS	P.I.
UNITS	
SCALE	1:10 000

ROCK CHARACTERISATION FACILITY

SITE: CROSS-SECTION 26

AO SIZE DRG. No. 010060 MOD.



SELLAFIELD RCF3

NY00SE 37



1: 500

Grid East 305565 North 503932

Latitude 54 25 18.85

Longitude -3 27 20.21

Datum RT 88.27 maOD

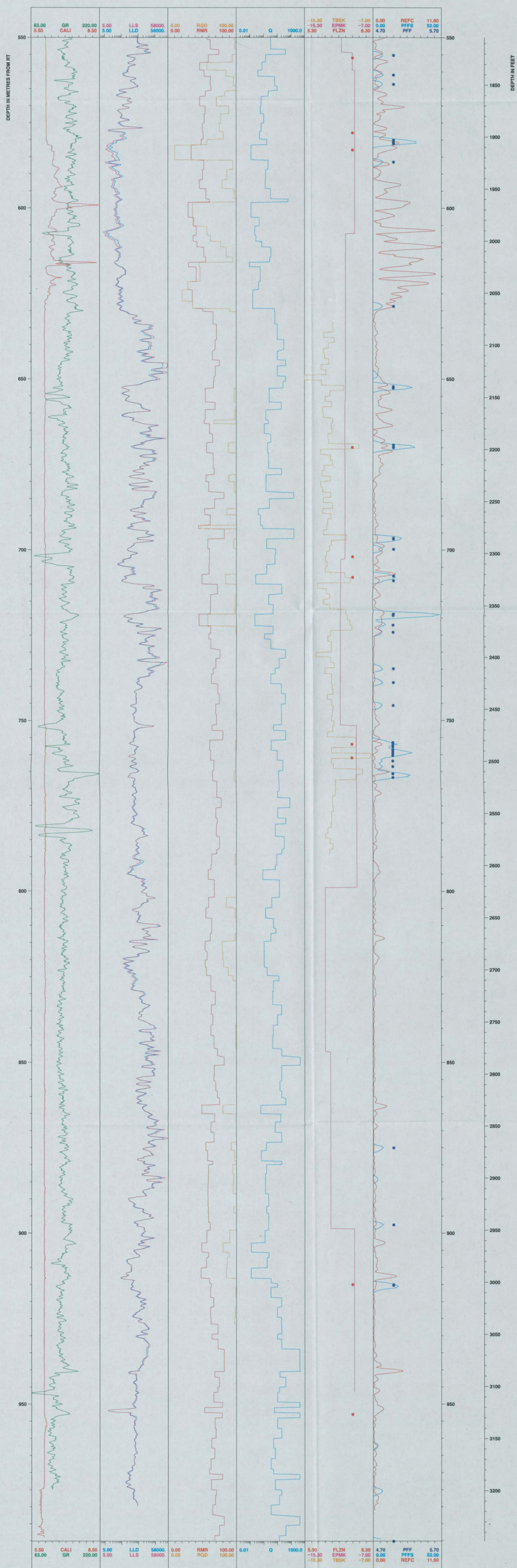


Figure 6.9a - Composite log of all BVG with PFFS log.

SELLAFIELD RCF3

NY00SE 37

1: 500

Grid East 305565 North 503932

Latitude 54 25 18.85

Longitude -3 27 20.21

Datum RT 88.27 maOD

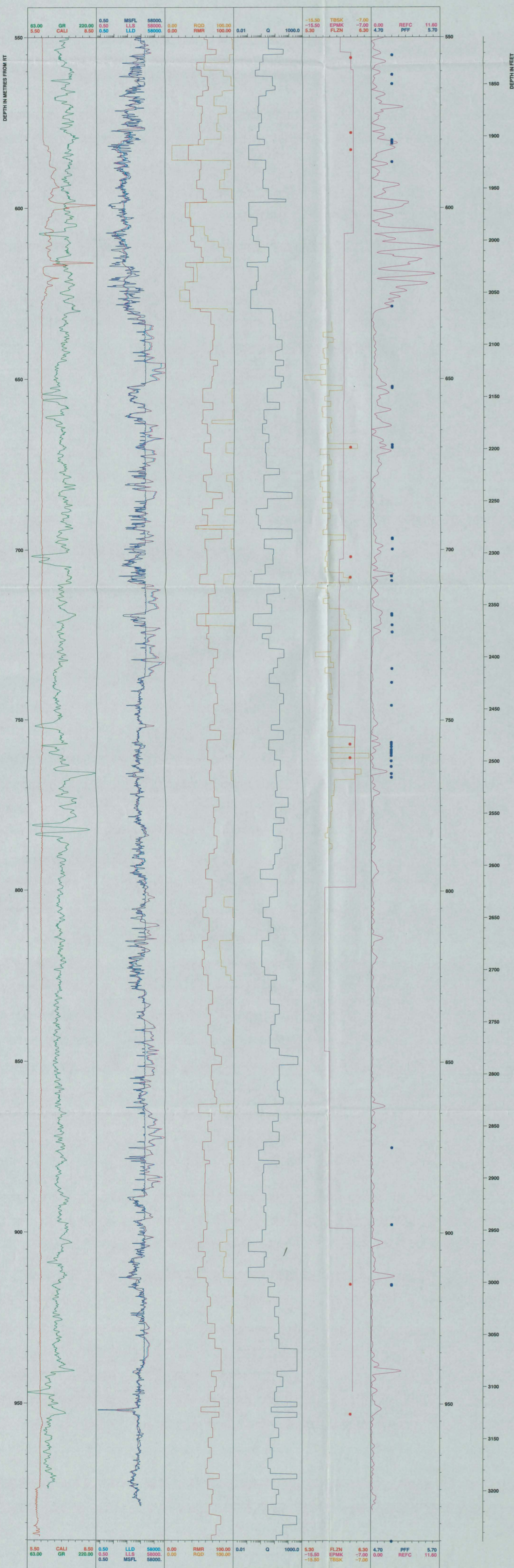


Figure 6.5a - Composite log of all BVG in Sellafield RCF3.



SELLAFIELD RCF3

NY00SE 37

1: 500

Grid East 305565 North 503932

Latitude 54 25 18.85

Longitude -3 27 20.21

Datum RT 88.27 maOD



Sandstone	Set Breccia	Tuff	Lapilli Tuff Py.B
Sand Clay clasts	Breccia	Lapilli Tuff	Lapilli Tuff Tuff/Ph.B
Claystone	No Core	Lithic Lapilli Tuff	Pyroclastic Breccia
Siltstone	Fault	Tuff/L. Tuff (airfall)	Banded Rhyolite
Green Bed	Set with extracasts	Tuff/L. Tuff (ignimbrite)	Basic Intrusion
Mdst Breccia	Tuff	L. Tuff Tuff Breccia	Acid Intrusion

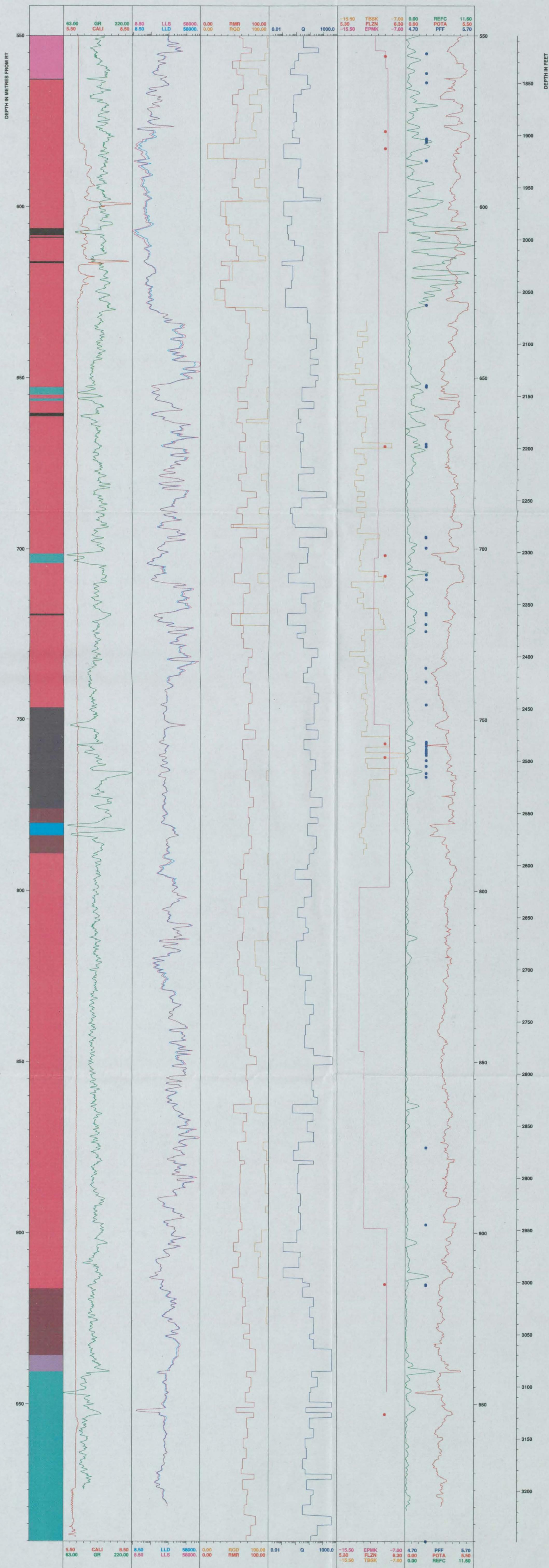


Figure 6.6a - Composite log of all BVG in Sellafield RCF3.



SELLAFIELD RCF3

NY00SE 37

1: 500

Grid East 305565 North 503932

Latitude 54 25 18.85

Longitude -3 27 20.21

Datum RT 88.27 maOD



Sandstone	Sst Breccia	Tuff	Lapilli Tuff /Py.B
Sandstone / Clay clasts	Breccia	Lapilli Tuff	Lapilli Tuff /Tuff/Py.B
Claystone	No Core	Lithic Lapilli Tuff	Pyroclastic Breccia
Siltstone	Fault	Tuff/L.Tuff (airfall)	Banded Rhyolite
Green Bed	Sst with extraclasts	Tuff/L.Tuff (Ignimbrite)	Basic Intrusion
Mdst Breccia	Tuff	L.tuff/ Tuff Breccia	Acid Intrusion

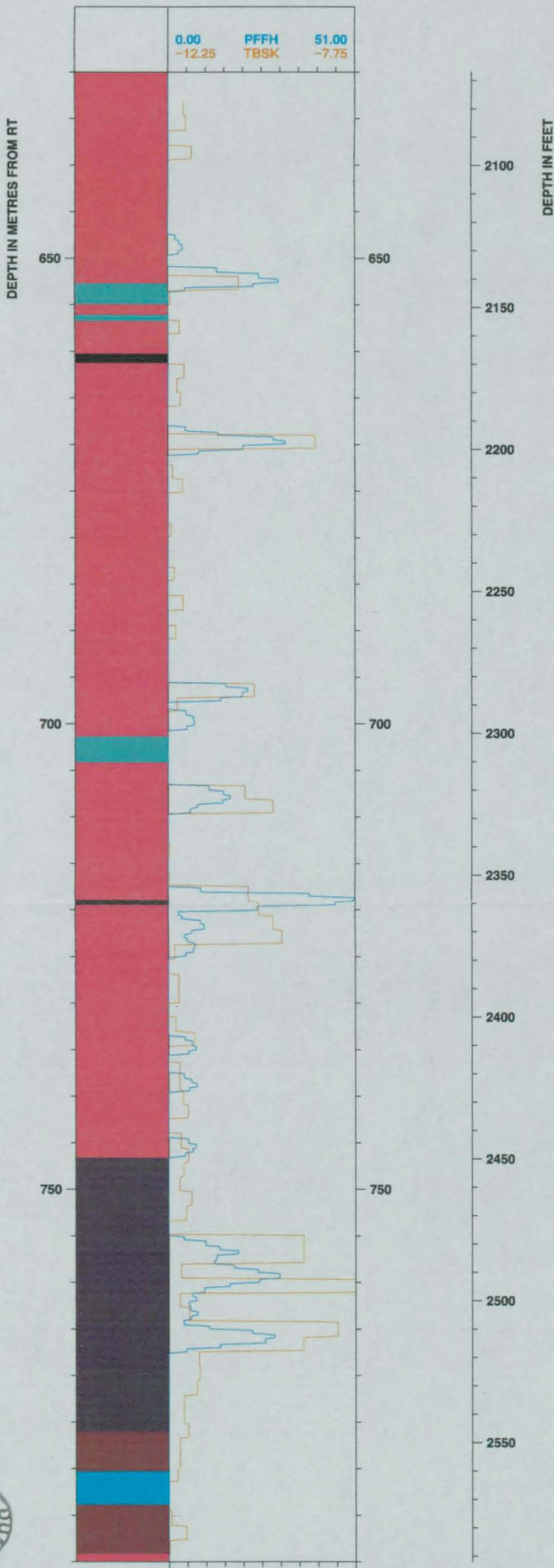


Figure 6.8 – Log of PFFS presented in TBSK log style.

SELLAFIELD RCF3

NY00SE 37

1: 500

Grid East 305565 North 503932

Latitude 54 25 18.85

Longitude -3 27 20.21

Datum RT 88.27 maOD

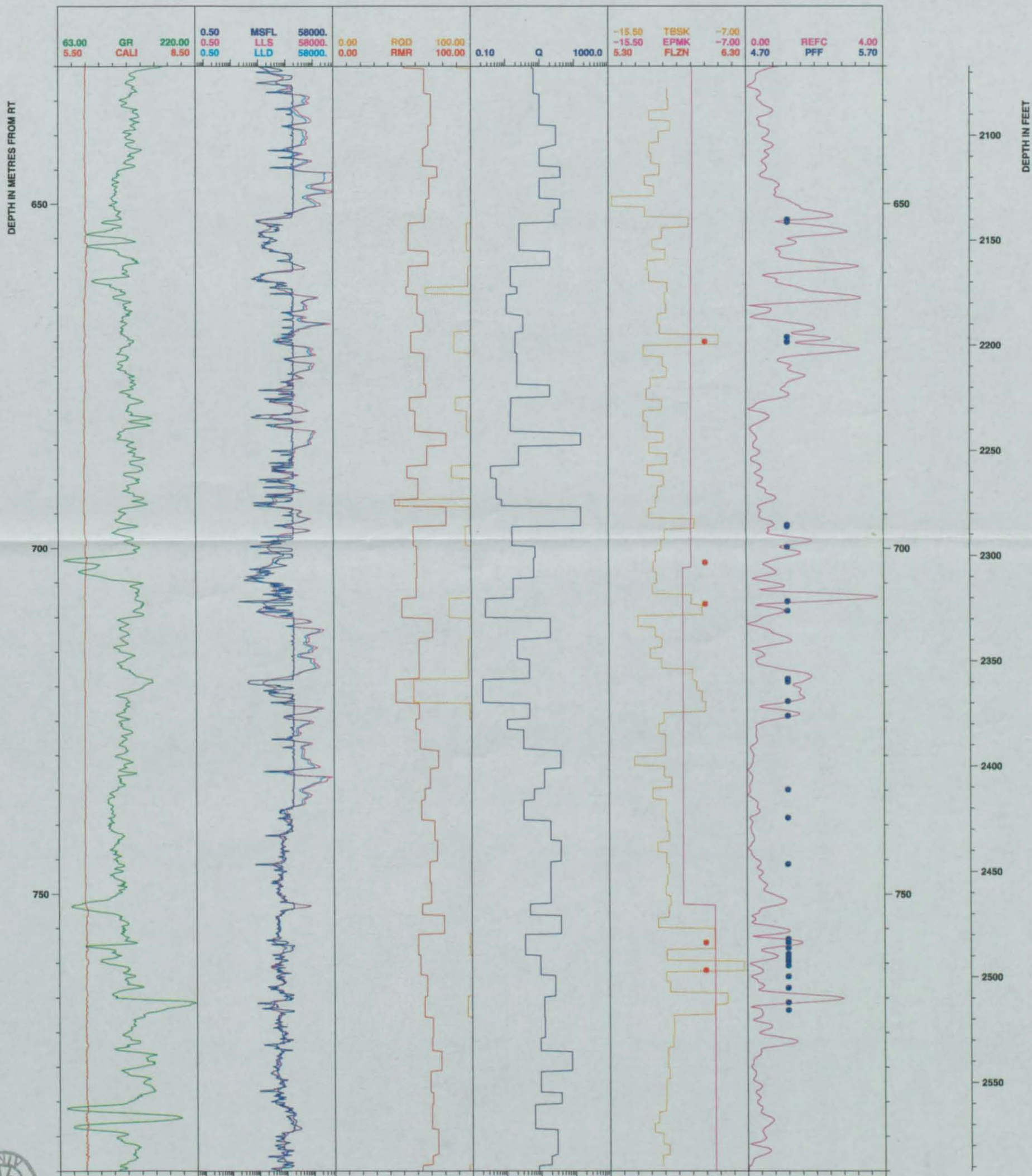


Figure 6.5b – Composite log of SIT zone in Sellafield RCF3.

SELLAFIELD RCF3

NY00SE 37

1: 500

Grid East 305565 North 503932

Latitude 54 25 18.85

Longitude -3 27 20.21

Datum RT 88.27 maOD

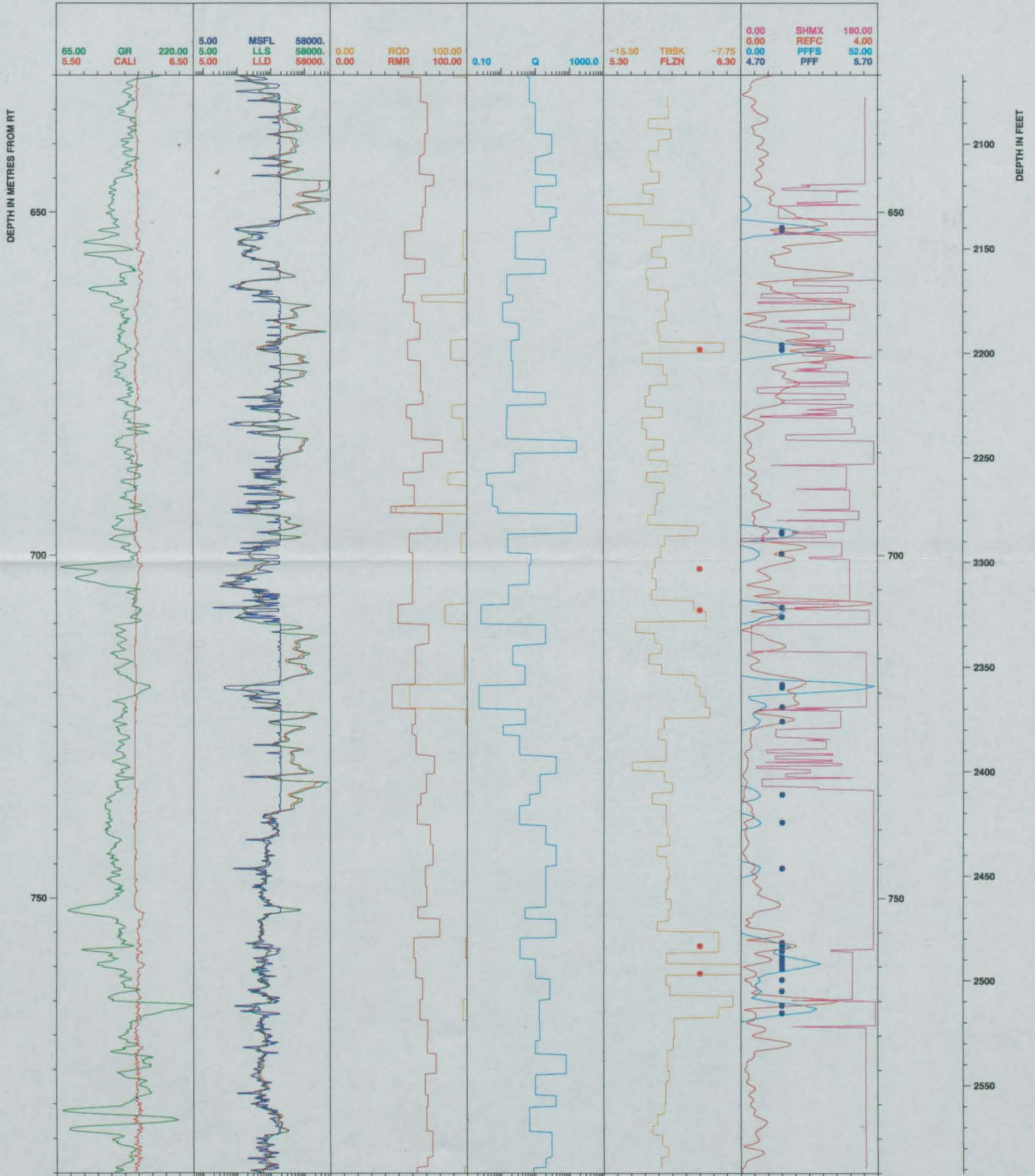


Figure 6.10 – Composite log of SIT zone with SHMX.



ANEL 1 OF 2

SELLAFIELD RCF3

NY00SE 37

1: 500

Grid East 305565 North 503932

Latitude 54 25 18.85

Longitude -3 27 20.21

Datum RT 88.27 maOD

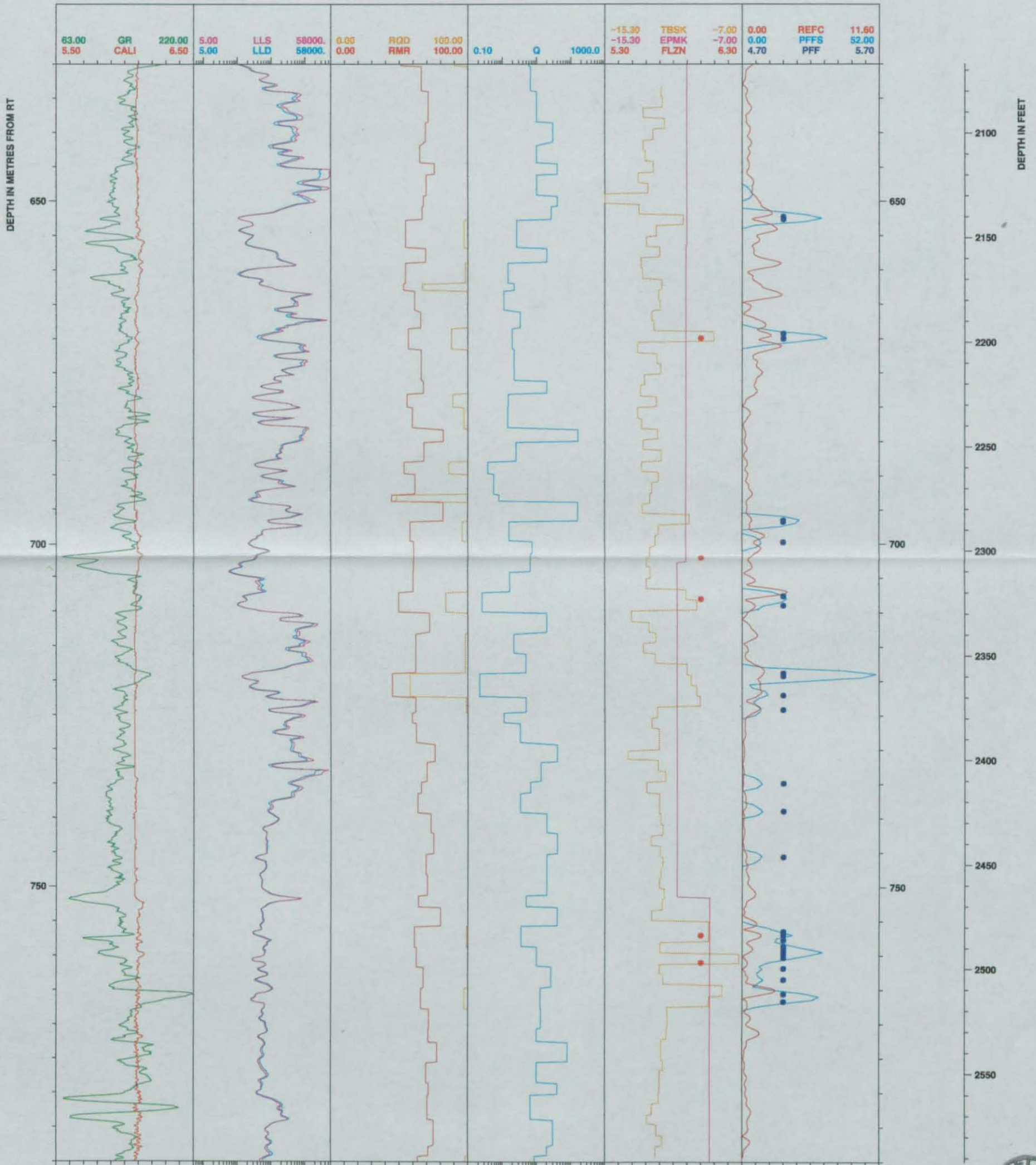


Figure 6.9b – Composite log of SIT zone with PFFS log.



SELLAFIELD RCF3

NY00SE 37

1: 500

Grid East 305565 North 503932

Latitude 54 25 18.85

Longitude -3 27 20.21

Datum RT 88.27 maOD



Sandstone	Set Breccia	Tuff	Lapilli Tuff Py.B
Sand Clay clasts	Breccia	Lapilli Tuff	Lapilli Tuff /Tuff/Ph.B
Claystone	No Core	Lithic Lapilli Tuff	Pyroclastic Breccia
Siltstone	Fault	Tuff/L. Tuff (airfall)	Banded Rhyolite
Green Bed	Set with extraclasts	Tuff/L. Tuff (ignimbrite)	Basic Intrusion
Mdat Breccia	Tuff	L. Tuff Tuff Breccia	Acid Intrusion

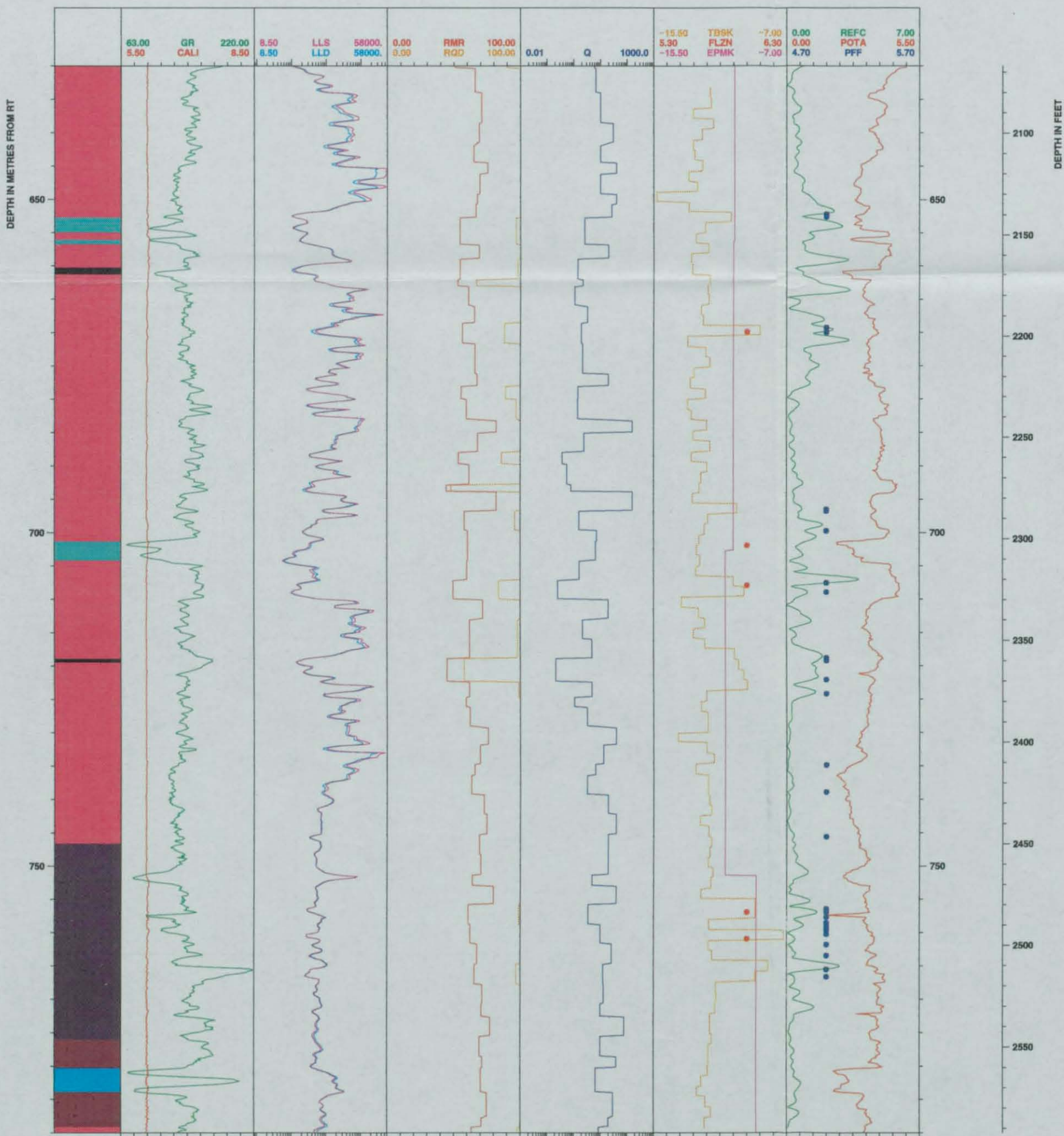


Figure 6.6b – Composite log of SIT zone in Sellafield RCF3.